AEROTHERMODYNAMICS OF TURBULENT SPOTS AND WEDGES AT HYPERSONIC SPEEDS

by

Abderrahmane Fiala

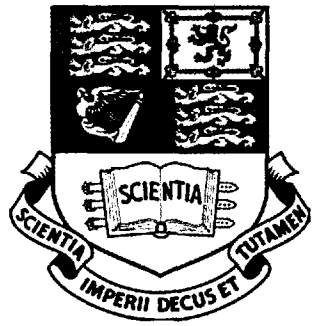

A thesis submitted for the degree of
Doctor of Philosophy of the University of London
and for the
Diploma of Imperial College

November 2004

Department of Aeronautics
Imperial College of Science, Technology and Medicine
London

Abstract

The aerothermodynamic characteristics of turbulent spots and wedges in a hypersonic transitional boundary layer were studied experimentally. A blunt cylindrical model was tested in a Mach 8.9 tunnel freestream at a unit Reynolds number of 47.4 million per metre. The corresponding boundary layer edge conditions were estimated from the laminar CFD computations at $M_e \approx 3.7$ and $Re_e \approx 2.7 \times 10^6/m$, within the region of measurements, significantly lower than the freestream conditions, a direct consequence of the entropy layer effect associated with the blunt nose. Two different sets of measurements were carried out on naturally-occurring transition (individual turbulent spots) and discrete roughness-induced transition (turbulent wedges). Surface heat transfer measurements were made using axial and circumferential multiple arrays of thin-film platinum resistance gauges. Time-dependent and time-averaged heat transfer data revealed the presence of turbulent events with different intermittency levels up to 100% for the fully developed wedges. Although the measurements did not cover the whole intermittent-transition region, the extent of the latter was found to be substantial. Conditional data sampling was used to acquire information on spot propagation speeds, geometrical characteristics, and spatial development at the model surface. The average spot speed compared very well with previous studies at incompressible, subsonic, and low supersonic speeds. Surface thermal footprints of the spots enabled the average geometrical and growth characteristics—namely planform shape, width, length, apex half-angle, streamwise growth and spanwise spreading rates—to be obtained. The result showed considerable similarities with low speed studies. Turbulent wedge experiments, using a discrete roughness element, allowed wedge characteristics such as heat transfer level, shape, and spanwise spreading rate to be acquired. The latter compared extremely well with previous predictions at hypersonic speeds. The wedge was found to form by the succession of a high number of individual spots which quickly coalesce within a small distance downstream of the roughness trip.

Dedicated to

...my dear Mum,
family and friends.

Acknowledgements

Special acknowledgements go to the Algerian Ministry of Higher Education and Scientific Research for their postgraduate scholarship and the Universities UK *ORS* scheme for their research award,

My full gratitude goes to my supervisor Professor Richard Hillier without whom none of this would have been possible,

Special thanks go to the Hypersonics Laboratory technicians Roland Hutchins and in particular Stephen Johnson for their technical expertise in running the Gun Tunnel facility,

At last but not least, my special thanks go to my family and friends for their continuous support during my six year's stay in the United Kingdom.

Contents

Nomenclature

d	Experimental model afterbody diameter
dM_∞/dx	Tunnel freestream axial Mach number gradient
I, $I(t)$	Intermittency square function of time
I_{avg}	Time-average of intermittency square function
i	Body-tangent computational mesh direction
j	Body-normal computational mesh direction
k	Roughness-trip height
l_s	Turbulent spot length
l_s^+	l_s expressed in computed fully turbulent wall scale units
M_∞	Freestream Mach number
M_e	Computed laminar boundary layer edge Mach number
M_k	Computed laminar Mach number at the trip height location
p	Pressure
p_∞	Freestream static pressure
p_{0_∞}	Freestream total pressure
q_{lam}	Computed laminar heat flux
q_{tur}	Computed fully turbulent heat flux
q_w	Measured heat flux
R	Experimental model nose radius
R_b	Experimental model blending region radius
$R_{ij}(\tau)$	Cross-correlation function between two i and j gauge locations
Re_∞	Freestream unit Reynolds number
Re_e	Computed laminar boundary layer edge unit Reynolds number
Re_{kk}	Computed laminar Reynolds number based on the trip height k
Re_{tr}	Transition Reynolds number
$Re_{\delta,\ \delta_1,\ \delta_2}$	Reynolds number based on laminar boundary layer thicknesses
t	Time
T	Temperature
T_∞	Freestream static temperature
T_{0_∞}	Freestream total temperature
T_s	Turbulent spot time-history in heat transfer signal
T_w	Wall temperature
U_∞	Freestream velocity

U_b, $U_{t.e}$	Turbulent spot back (trailing edge) average convection speed
U_c, U_{mean}	Turbulent spot average (mean) convection speed
U_e	Computed laminar boundary layer edge velocity
U_f, $U_{l.e}$	Turbulent spot front (leading edge) average convection speed
U_k	Computed laminar velocity at the trip height location
w_c	Turbulent wedge core width
w_e	Turbulent wedge outer width
w_k	Roughness-trip width
w_s	Turbulent spot width
w_s^+	w_s expressed in computed fully turbulent wall scale units
x	Axial distance from the model apex
x_k	x-position of the roughness-trip
y_w	Normal distance from the model surface
z	Spanwise (circumferential) location with respect to roughness-trip

Greek letters

α	Spanwise spreading half-angle
α_c	Turbulent wedge core spanwise spreading half-angle
α_e	Turbulent wedge outer spanwise spreading half-angle
α_s	Turbulent spot spanwise spreading half-angle
$\alpha_r\sqrt{\rho_r}$	Platinum thin-film figure of merit
γ	Intermittency factor
γ_∞	Ratio of specific heats
δ	Computed laminar boundary layer thickness
δ_1	Computed laminar boundary layer displacement thickness
δ_2	Computed laminar boundary layer momentum thickness
ϵ	Laminar-turbulent threshold coefficient
θ_s	Turbulent spot apex half-angle
λ_s	Turbulent spot internal structure parameter
λ_s^+	λ_s expressed in computed fully turbulent wall scale units
μ_e	Computed laminar boundary layer edge molecular viscosity
μ_k	Computed laminar molecular viscosity at the trip height location
ρ_∞	Freestream density
ρ_e	Computed laminar boundary layer edge density
ρ_k	Computed laminar density at the trip height location

List of Figures

List of Tables

Chapter 1

Introduction

1.1 Motivations

The new perspective of future space transportation has most importantly required an increase in safety and reliability with considerable reduction in cost. Thus, the precise determination of the aerothermodynamic environment around the space-plane is essential and necessitates the understanding of fundamental physical phenomena such as shock waves, vortical flows, boundary layers, and real gas effects. Figure 1.1 illustrates some of the space-plane concepts and prototypes that have been made most recently. The design of these vehicles most importantly aims to reduce surface heating and drag and provide good flow intake characteristics (for air-breathing applications), which are mainly governed by the body shape, amount of nose bluntness, and state of the boundary layer, be it laminar, transitional or fully turbulent.

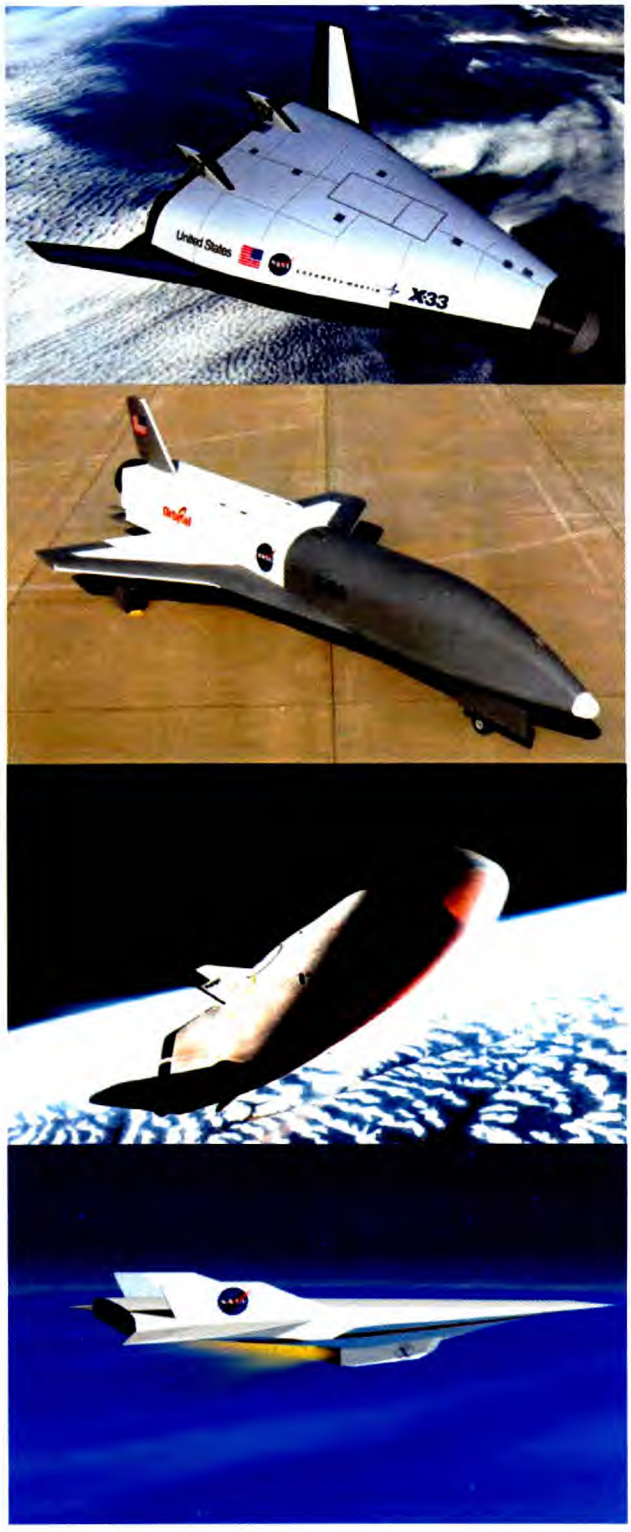

Figure 1.1: Space-plane concepts. From top to bottom; (a) Reusable Launch Vehicle *RLV*, X-33; (b) RLV, X-34; (c) emergency Crew Return Vehicle *CRV*, X-38; (d) hypersonic air-breathing transport vehicle, X-43 (courtesy of NASA).

Transition is an unsteady process through which a laminar boundary layer receives external disturbances (either freestream or body-related) that subsequently grow in space and time yielding eventually to turbulence, a process which is yet to be fully understood.[83] From an 'engineering/design' viewpoint, transition onset is defined by the location where time-averaged surface heat transfer and skin friction start to deviate from the laminar value and gradually increase to the fully turbulent value across the *intermittent-transition* zone. The latter extends from the location of initial breakdown of the laminar flow into *turbulent spots* up to the location where the spots are entirely coalesced to form a fully turbulent flow (defined in more detail in section 1.3.1). The extent of this region is governed by the rate of formation, propagation, growth, and amalgamation of turbulent spots. In roughness-induced transition, where the roughness trip is of sufficiently large size (typically about half the local laminar boundary layer thickness or greater), turbulence occurs right behind the roughness trip in the form of a *turbulent wedge.*

Transition has been one of the most intricate subjects in aerodynamics research, particularly so at hypersonic speeds due to the large uncertainties associated with the determination of flow properties (e.g., heat transfer and skin friction), large physical extent of the intermittent-transition region, and significant number of the parameters that affect the transition process. The substantial length of the intermittent-transition zone, which can range between 20% and 80% of a vehicle length,[83] results in many important flow phenomena, such as flow compression (as for engine intakes), shock wave impingement (at the body-wing/fin intersections) and flow separation, to probably take place within this zone. It also generates large uncertainties in the estimates of the minimum and maximum heat fluxes and skin friction coefficients locations, which can yield variations in the design vehicle 'gross take-off weight' by at least 100%.[83]

The significant number of factors affecting the transition onset and process makes their prediction very difficult. Anderson[2] pointed out that the transition Reynolds number, Re_{tr}, depends upon several factors such as boundary layer edge Mach

number, wall temperature, body shape, angle of attack, surface roughness, disturbance environment, body vibration, body curvature, pressure gradients, leading edge bluntness, total temperature, cross flow instabilities, and real gas effects at high enough Mach numbers (figure 1.2). Clearly, the determination of an analytical expression for the transition Reynolds number is virtually impossible and therefore a good understanding of the physics involved is the key for better transition prediction and modelling.

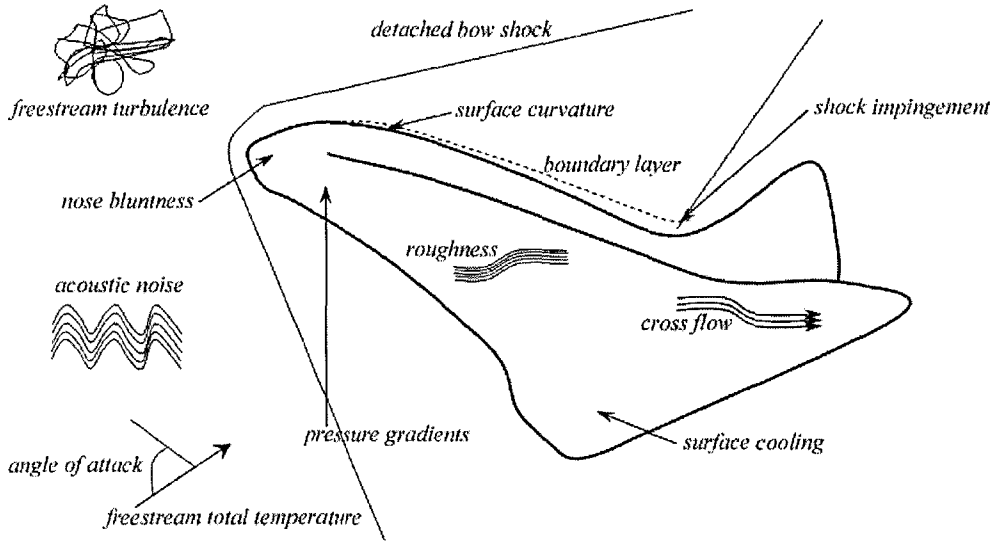

Figure 1.2: Illustration of the factors affecting transition; these comprise freestream and body-related parameters.

The particular driving force behind the present study on the aerothermodynamics of turbulent spots and wedges, in addition to the points mentioned earlier, is the work of Zanchetta and Hillier[111,112] on blunt cone kinetic heating in the Imperial College gun tunnel. They obtained very significant lengths of intermittent flow for the largest nose radius in the flow regime prior to 'transition reversal'. This presented a good opportunity for investigating in more depth the geometrical, convective, growth and structural characteristics of turbulent spots which form, develop and merge across the intermittent-transition zone. Some of the results obtained suggested

a possible relationship, in terms of dynamic characteristics and structure, between turbulent spots and wedges, providing the incentive for the study of turbulent wedges (discussed in more detail in chapter 7).

In the present study, the aerodynamic heating into the body surface is the primary property being investigated, since it is considered as a critical design parameter for hypersonic vehicles and excellent transition detector. This is performed through experimentation and laminar flow computation that assists the analysis of the experimental data. The remainder of this chapter will present the necessary definitions followed by a review of the recent state of transition research. The following chapters (chapters 2 and 3) will describe the experimental facility, models and procedures, together with the laminar CFD methodology and simulations. The experimental data will then be presented in chapters 4 to 7, including full analysis and discussion of the result, highlighting the contribution of the present study to the general understanding of hypersonic transition.

1.2 Hypersonic flow characteristics

The transition from supersonic to hypersonic flow does not implicate a sudden change in flow properties as for that from subsonic to supersonic. Instead, the flow is said to be hypersonic when certain flow phenomena start to occur and become increasingly more significant as the Mach number increases. As a rule of thumb,[2] a hypersonic flow is defined as a flow of a Mach number of 5 or greater. The following sections describe the physical phenomena which characterise hypersonic flows.

1.2.1 Thin shock layer

From the oblique shock relations,[2,3] for a given deflection angle, the shock wave angle is found to decrease as the Mach number increases. At hypersonic speeds, the *shock layer*—the region between the body surface and the shock wave—becomes increasingly *thin* with increasing Mach number.

1.2.2 Viscous interaction

As the surface of the body is approached, the flow is decelerated through viscous effects (across the boundary layer) and the kinetic energy of the gas is converted into thermal energy. At hypersonic speeds, the kinetic energy of the gas is significant and so therefore is the resulting thermal energy near the wall. This yields a temperature rise and density drop as the Mach number increases and thus, for a given mass flow rate (conservation of mass), the boundary layer thickness becomes more significant. Anderson[2] gives the following formula for the growth of the laminar boundary layer thickness, δ, as a function of the boundary layer edge Mach and Reynolds numbers:

$$\frac{\delta}{x} \propto \frac{M_e^2}{{Re_{e,x}}^{1/2}} \tag{1.1}$$

The dramatic increase in boundary layer thickness in hypersonic flows leads to large displacement of the inviscid flow associated with the presence of the boundary layer. This causes a change in the effective shape of the body and thus increases drag. Furthermore, the thick boundary layer interacts with the thin shock layer, particularly near the leading edge, causing what is known as *viscous interaction.*

1.2.3 Entropy layer

Frequently in hypersonic flow applications, the body apex, or nose, is blunted (the case of the present study) in order to reduce the aerodynamic heating into the surface. The introduction of nose blunting causes the shock wave to detach, such that streamlines behind the central part of the shock wave experience a large loss in total pressure and large increase in entropy, Δs_{shock}, across the shock. These high entropy streamlines constitute what is known as the *entropy layer.* The shock wave angle and thus the rate of entropy increase across it, Δs_{shock}, gradually decrease with distance from the axis to the equivalent sharp-body value. The boundary layer develops with the entropy layer controlling the boundary layer edge condition.

1.2.4 Real gas effects

In high total temperature hypersonic flows, at a given static pressure, some of the total energy of the gas is used for the vibration of the gas molecules once the appropriate characteristic static temperature of vibration, T_{vib}, has been reached. As the total temperature is increased further, the molecules of the gas start to dissociate when the characteristic static temperature of dissociation, T_{dis}, is attained, then ionise at the characteristic static temperature of ionisation, T_{ion}, ($T_{vib} < T_{dis} < T_{ion}$). The gas utilises appropriate fractions of the total energy available for the vibration, dissociation and ionisation processes, yielding a reduction in the flow temperature compared to the thermally and calorically ideal gas case. These types of flows are more precisely known as hypervelocity flows. In the present study, real gas effects are insignificant due to the modest total temperature used ($T_{0_\infty} = 1150$ K).

1.3 Boundary layer transition

1.3.1 The transition process and onset

The process of transition, according to the common literature such as Kuethe,[50] Schetz,[80] Schlichting[81] and White,[102] ensues in six different stages which take place successively downstream from a fully laminar to a fully turbulent motion (figure 1.3). These include; a laminar stable base flow (1); a linear region where 2D unstable Tollmien-Schlichting waves form (2); a non-linear region characterised by the formation of 3D waves and spanwise 'Λ/hairpin'-vortex structures (3) which decay and eventually breakdown (4); an intermittent-transition zone where turbulent spots form and develop (5); and finally a region of fully developed turbulent flow (6). More in-depth studies,[45,51,52,54,55,57,75–77,82,96,101] introduced the concept of receptivity, which in fact is crucial to the initiation of the transition process in the laminar flow region (1) (figure 1.3). There is another case where the various stages of the transition process are bypassed due to the flow and environmental distur-

bance conditions. This is known as *bypass transition* and is the case for the discrete roughness-induced transition (or turbulent wedges) which are examined in detail in chapter 7.

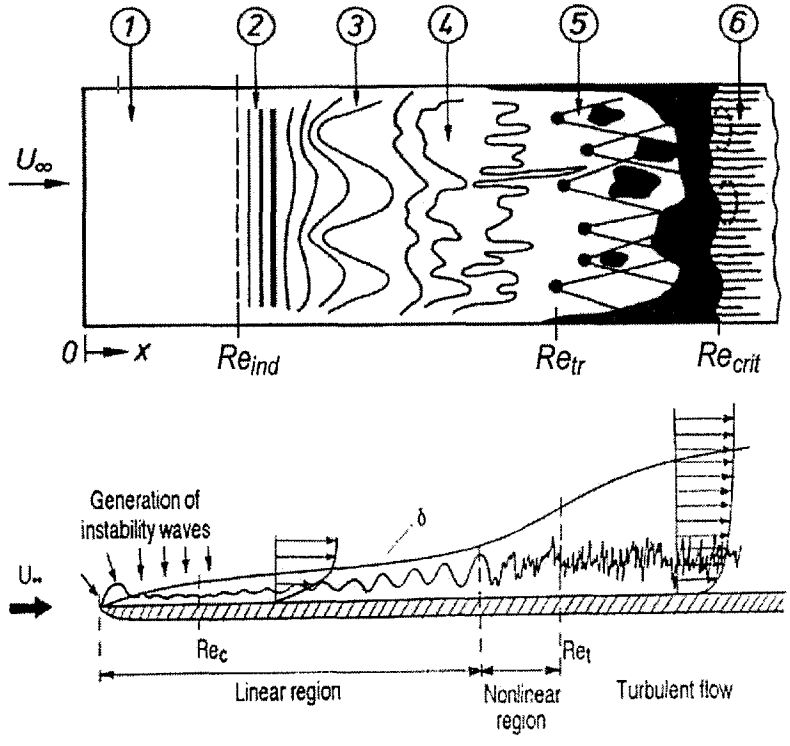

Figure 1.3: The transition process (top from Schlichting,[81] bottom from Kachanov[45]); (1) laminar stable base flow and receptivity region, (2) unstable 2D Tollmien-Schlichting waves, (3) 3D waves and vortex formation ('Λ/hairpin'-structure), (4) vortex decay and breakdown, (5) *intermittent region: turbulent spots formation, growth and coalescence*, (6) fully turbulent flow.

The onset of transition is defined from two different perspectives. The mathematical approach examines the different development stages—linear and non-linear growth in space and time—of a disturbance field within a laminar flow until its breakdown and initiation of turbulent spots. This covers the streamwise length of $[x_{ind}, x_{tr}]$, where x_{ind} is the position where the first unstable waves occur and x_{tr} is the position of initial spot formation. In this case, the transition onset is expressed by its location, x_{ind}, or more generally by the *indifference* Reynolds number,

Re_{ind} (figure 1.3-top). This approach aims to predict the onset process and location of turbulence spots. The engineering approach however, is concerned with the intermittent-transition region—covering the streamwise length of $[x_{tr}, x_{crit}]$, where x_{crit} is the location where the boundary layer is fully turbulent—to establish correlations between the intermittent-transition zone and freestream and body-related parameters. In this case, the transition onset is expressed by its location, x_{tr}, or more generally by the *transition* Reynolds number Re_{tr} (figure 1.3-top). In a time-averaged 'heat flux-streamwise distance' curve, the transition onset location corresponds to the point where the heat transfer starts to deviate from the laminar value (figure 1.4).

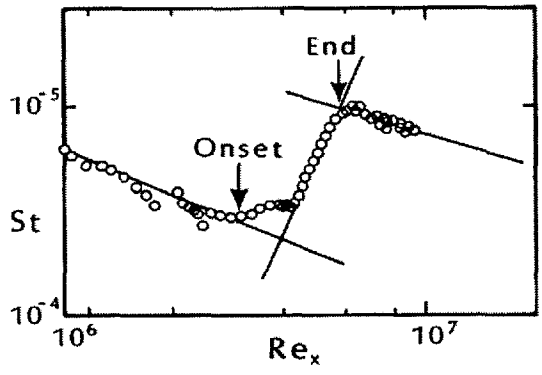

Figure 1.4: Intermittent-transition region (Bertin[11]); the transition onset from an engineering viewpoint.

In the following sections, the various stages of the transition process, as presented above, are described in more detail.

Receptivity

Reshotko[76] defines receptivity as follows:

> *'Receptivity is the process by which a particular forced disturbance enters the boundary layer, the nature of its signature in the disturbance flow, and the mechanism of exciting its corresponding free disturbance or normal mode in the boundary layer.'*

The disturbances mentioned here include freestream external and body-related disturbances. The former comprises acoustic disturbances (pressure fluctuations), entropy disturbances (temperature fluctuations), vorticity disturbances (turbulence), atmospheric disturbances, and particulate. The latter are formed within the boundary layer and comprise surface roughness and curvature, model vibration, nose bluntness, and wall temperature. The process of receptivity is generally initiated at the leading edge (the model nose in the present case) and at any downstream location where the boundary layer has to accommodate any changes in surface geometry or boundary conditions.[76,77]

Linear region

The disturbances within the laminar boundary layer, depending upon their frequency, wave number and amplitude, could either amplify in space and time and hence initiate the transition process—unstable boundary layer—or dwindle and thus maintain the stable flow.[50,81] The amplified disturbances cause the well-known 2D Tollmien-Schlichting waves (also known as the first instability mode) to form and develop in space and time. This stage of the transition process is well described by *Linear Stability Theory (LST)*, which is based on the principle that any flow can be decomposed into the laminar base flow (being examined) and a superimposed perturbation motion. Depending on the body geometry and flow type being investigated, a set of equations—which contain parameters such as frequency, wave number, amplitude and phase—is obtained and, once solved, determines whether the boundary layer is stable or unstable. In the simplest case of a 2D flat plate incompressible boundary layer, stability is defined by the well-known *Orr-Sommerfeld* equation that yields the Neutral stability curve, from which the transition Reynolds number is extracted and, depending on the disturbances parameters (i.e., frequency, wave number,...etc), the state of the boundary layer is defined.[81]

At hypersonic speeds, higher modes of instability, well known as *Mack modes*, take place in addition to the first mode.[45,53,57,67,76,77,81,96] This was discovered

by Mack[53] from his first successful formulation and resolution of the compressible stability equations which yielded an infinite number of solutions in the limit of infinite Mach numbers. At supersonic and low hypersonic Mach numbers, the second mode is considered the most unstable as it often presents the largest amplification rates, depending upon flow conditions and disturbance environment.

Non-linear region

Three-dimensionality appears in this region where Λ-shaped vortices form and distort with streamwise distance, causing their apex to move up to greater vorticity levels. These vortices are thus intensified and stretched until bursting.[50] The breakdown of the laminar boundary layer is still not fully understood as reported by Kachanov.[45] For weak non-linearity, the *Parabolised Stability Equations (PSE)* describe satisfactorily the disturbance field in the boundary layer.[6] However, for strong non-linearity (e.g., hypersonic boundary layers), PSE is not always applicable.

Intermittent-transition region

After breakdown of the laminar flow, high frequency regions identifying turbulent spots are formed.[50] These spots, of high heat transfer, high skin friction and arrowhead shape (figures 1.5 and 1.6), grow in space and time and eventually merge into a fully turbulent flow. In incompressible flows,[86] the propagation speed of the spot varies from approximately $0.50U_\infty$ at the spot trailing edge to approximately $0.88U_\infty$ at the spot leading edge, a difference that leads to their streamwise growth. The spots are contained in the intermittent-transition region which is characterised by an intermittency factor, γ, defined as the fraction in time that turbulent flow exists within a total time window of intermittent flow at a fixed location. This factor takes the value of 0 when the flow is fully laminar and the value of 1 when the flow is fully turbulent.[81]

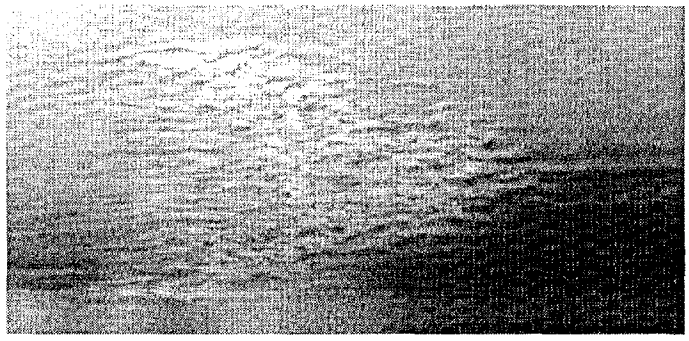

Figure 1.5: View of a turbulent spot in an incompressible flow (from Falco[26]).

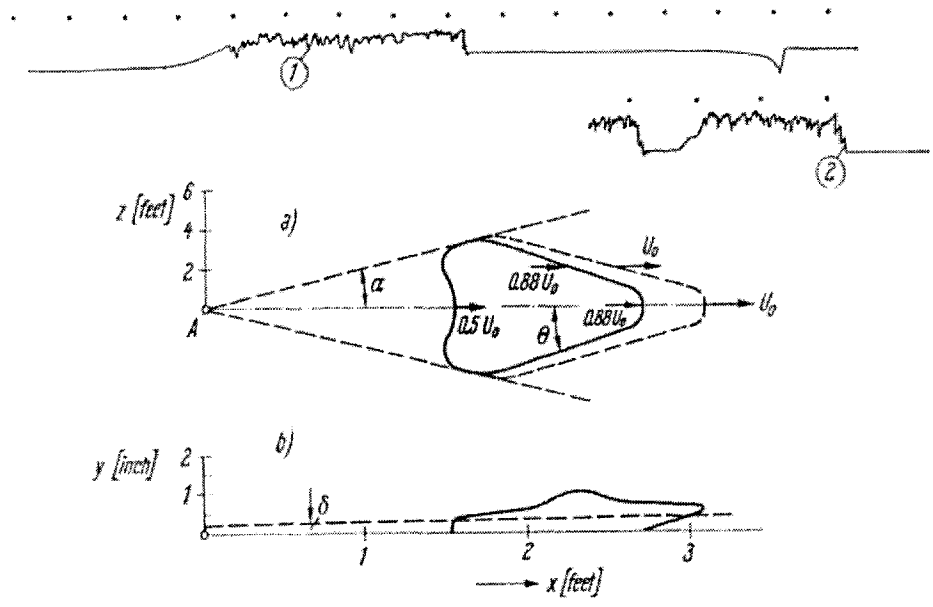

Figure 1.6: Turbulent spot in an incompressible flow (Schubauer and Klebanoff[86]). (top); hot-wire signal of an artificially-generated (1) and naturally-occurring (2) turbulent spot. (bottom); plan and elevation views of an artificially generated spot; lateral spreading half-angle, $\alpha = 11.3°$; spot apex half-angle, $\theta = 15.3°$; freestream velocity, $U_\infty = 10$ m/s; δ is the laminar boundary layer thickness.

1.3.2 Factors affecting transition

Pressure gradient

The presence of an adverse pressure gradient in the streamwise direction (i.e., $\partial p/\partial x > 0$, x being the axial direction) hastens transition. Schlichting[81] also reported a rise in instability level, within a boundary layer in the presence of a favourable pressure gradient ($\partial p/\partial x < 0$), with increasing pressure gradient level ($\partial^2 p/\partial x^2 > 0$).

Wall temperature

Anderson[2] suggested that wall cooling ($T_w < T_{aw}$, T_w being the wall temperature and T_{aw} the adiabatic wall temperature) stabilises the laminar boundary layer only for moderate supersonic speeds. However, Garry,[30] Kuethe,[50] and White[102] stated that the effect of wall cooling is reversed when surface roughness size increases. At hypersonic speeds, the transition-wall cooling relationship is less evident. Bertin[11] reported that for fixed freestream Mach and unit Reynolds numbers, cooling first stabilises the boundary layer then, as the wall temperature is further reduced, transition is hastened until certain values where the effected is re-reversed. Finally, at sufficiently low wall temperatures, no further effect is encountered on the stability of the laminar flow.

Freestream Mach number (compressibility effects)

Anderson[2] pointed out that the increase in boundary layer edge Mach number delays transition particularly for freestream Mach numbers greater than four. Furthermore, Kuethe[50] suggested that the boundary layer becomes more unstable for Mach numbers between 1.3 and 4.5.

Surface roughness

Surface roughness is a transition trigger in the way that transition is hastened as the roughness size is increased. Moreover, Reda[73] reported higher transition Reynolds number, based on roughness height, using isolated roughness compared with that obtained with distributed roughness.

Nose bluntness

Hypersonic flows around blunt bodies are characterised by the presence of a high vorticity layer (or entropy layer) which flows downstream of the blunt nose. The effect of this layer is to alter the boundary layer edge conditions and therefore the transition characteristics of the boundary layer. Many authors such as Anderson,[2] Bertin,[11] and Zanchetta[112] reported that nose blunting delays transition. The transition Reynolds number, Re_{tr}, increases with increasing Reynolds number based on nose radius, Re_n, up to a certain limit where the effect is reversed; the so-called transition reversal.

Unit Reynolds number and environmental effects

Unit Reynolds number is a flow property that is able to quantify the level of external disturbances which influence the onset and process of transition. Generally, as the unit Reynolds number increases, transition is moved upstream.[2,11,50,80,81,102] Bertin[11] however, made a comparison between flight and wind tunnel data and he ascertained that an increase in unit Reynolds number has a stabilising effect according to flight data and a destabilising effect according to wind tunnel data. He suggested as a result that the freestream environment plays a significant role as far as the stability of the laminar flow is concerned.

Cross flow instabilities

Although not considered in the present study, where axisymmetric configurations are used, cross flow instabilities generally present an inflection point in the boundary layer profile and hence the laminar flow is less stable.[81]

The description given above mainly presented the general trends in transition behaviour with these factors. In fact, the influence of each parameter on transition may change from case to another depending upon freestream, environmental and body-related conditions and the number of factors that are simultaneously involved.

1.4 Review of transition research

1.4.1 Boundary layer stability and transition prediction

Malik et al.[54,55] conducted in-depth studies on boundary layer stability and transition modelling and onset prediction in hypersonic flows. They used linear and non-linear stability theories together with *Large Eddy* and *Direct Numerical Simulations*, *LES* and *DNS* respectively. The results were then validated against 'quiet' tunnel data (i.e., obtained in a low freestream disturbance environment). They advocated that the application of the e^N method to high-speed flows ought to consider all instability modes (first and higher modes) due to the difference in their nature (viscous or inviscid) and growth rate with relation to the freestream Mach number. It was found that the e^N method (with $9 < N < 11$) yielded good agreement with the quiet tunnel data, yet it indicated strong sensitivity to freestream disturbances. Moreover, the application of simple engineering correlations such as the '$(Re_{\delta_2}/M_e)_{tr}$' method, where Re_{δ_2} and M_e are the boundary layer edge Reynolds number based on momentum thickness and Mach number respectively, is useful in very particular cases although it cannot be generalised, as they demonstrated from the comparison of 2D and axisymmetric cases.

Malik et al.[55] also discussed the effect of nose bluntness in delaying the onset of transition. The introduction of nose blunting generated a significant increase in the transition Reynolds number, Re_{tr}, however it remained lower than the predicted values using the e^N method. This discrepancy was associated with the fact that larger amplification rates for the e^N method were required since nose blunting caused rapid growth of the disturbances within the laminar boundary layer.

Malik[54] also examined the effect of favourable pressure gradient on transition onset and he discovered that, although it stabilises the first mode, it does not ensure the stability of the second mode. Moreover, Kimmel et al.[49] found that, in the presence of a favourable pressure gradient, the second mode has lower growth rates and shifts to lower frequencies .

The effect of wall temperature on transition was also investigated (see for example the work of Malik,[54] Reshotko[76] and Stetson[96]). It was discovered that wall cooling destabilises the higher modes, including the second mode that was found to be the transition trigger at hypersonic speeds. Malik[54] suggested that if the environment was free of high frequency disturbances the effect of wall cooling on hypersonic transition may be reversed.

One of the most critical issues in connection with the experimental study of boundary layer stability and transition is wind tunnel noise. In this respect, several studies were conducted[13,51,55,76,77,82,96] and reported the effect of environmental noise in reducing the transition Reynolds number Re_{tr}. It was also suggested that transition prediction using the e^N and *PSE* methods could only be validated against data obtained in tunnels with low disturbance level. Malik et al.[55] revealed that high freestream acoustic disturbances dramatically affects ground facility data, in particular transition location and trends. The extent of these effects was found to be geometry-dependent in relation with the receptivity mechanism, a fact which implied yet again that stability theory results can merely be useful in a low disturbance environment.

Perhaps one of the most popular studies on hypersonic transition prediction and testing is that due to Stetson et al.[96] In their paper, they suggested that ordinary (or noisy) tunnels could still provide good source of data comparison. Their argument is that, in the hypersonic regime, there are special considerations to the coupling between the environmental disturbances and boundary layer disturbances that are responsible for transition. It is noted from their paper[96] that:

> *'The critical environmental disturbances are those disturbances of the same frequency as the boundary layer disturbances responsible for transition. Therefore, it is important to identify the dominant boundary layer disturbances and the amplitudes of the corresponding environmental disturbances at the same frequency.'*

In other words, environmental disturbances have an effect on transition only if they excite the potentially dominant boundary layer disturbances, which are of relatively high frequencies. Stetson et al.[96] also highlighted the fact that boundary layer disturbance mechanisms are still not as well understood at hypersonic speeds as at subsonic/supersonic speeds. They reported the work of Mack[53] in establishing the existence of unstable higher modes and the characteristics of their growth and damping which were discovered to be frequency dependent.

Noise effect was also investigated by Schneider,[82] who pointed out that high in-flight transition Reynolds numbers are due to the low level of noise and well controlled body surface disturbances. He discovered that in some cases the trend in transition data obtained in conventional tunnels was the opposite of those obtained in quiet tunnels. The noise in question consists of temperature fluctuations, particulate, vorticity fluctuations, and acoustic disturbances of which a large fraction is radiated from the tunnel-wall turbulent boundary layer.[82] Schneider argued that these disturbances must be measured satisfactorily for good in-flight and ground test transition prediction. Schneider[83] presents an excellent review of the state of hypersonic transition—stability and laminar breakdown—research from an experimental point of view.

1.4.2 Intermittent-Transition Region

This section is concerned with the investigations of turbulent spot characteristics which have been conducted over the last fifty years since the pioneering work of Emmons.[25] His water-table experiment revealed isolated patches of turbulence that were identified as turbulent spots. As a result of this finding, he put forward the well known theory of transition which is based on the formation and growth of turbulent spots. Since then, tremendous amount of work has been carried out on turbulent spot characteristics.

Turbulent spot average characteristics in incompressible boundary layers with a zero pressure gradient

Schubauer et al.[86] were the first to establish the relationship between the behaviour of artificially generated and naturally-occurring turbulent spots in relation with the transition process. Using hot-wire anemometry to measure artificially produced spots in an incompressible flow, they obtained for the first time spot geometrical, convective, and growth characteristics (a typical spot is illustrated in figure 1.6). Since then, the universal shape of the turbulent spot—with an arrowhead shape in the plan-view and a stretched patch with an overhang leading edge and a hump in the elevation-view—was established. Their measurements yielded a constant spot trailing and leading edge velocities at the surface across the spanwise extent and were equal to $0.50U_\infty$ and $0.88U_\infty$ respectively for a freestream unit Reynolds number, Re_∞, of $6 \cdot 10^5$ m^{-1}. The spot apex half-angle was 15.3° whereas the lateral spreading half-angle was 10° and decreased to 8.6° as Re_∞ decreased to $2 \cdot 10^5$ m^{-1}. Schubauer et al. also found that the maximum thickness of the spot—defined by the distance to the wall of the top of the hump—increased with axial distance in the same manner as a fully turbulent boundary layer. They also suggested that the overhanging leading edge, with a tip velocity of U_∞, was created as a result of the slow laminar flow near the surface moving in the opposite direction, giving also rise to a 'calmed region' (or wake region) behind the spot.

More detailed velocity measurements on artificially produced spots in a Blasius boundary layer were made by Wygnanski et al.[106] They achieved, using the ensemble-averaged data, the characteristics of the average spot which was found to exhibit conical similarity far downstream of its initiation point. In these regions, the average spot had a universal shape that was independent of the type of fluid, Reynolds number, $Re_{\delta_1^*}$ (δ_1^* being the laminar boundary layer displacement thickness at the spot formation point), or the manner the spot was generated. In contrast to Schubauer et al.[86] study , the leading interface of the spot was slightly concave and propagated downstream at a velocity which varied between $0.89U_\infty$ at the spot centre-plane and $0.50U_\infty$ at the extreme spanwise location. On the other hand, the spot trailing edge velocity was constant throughout and was equal to $0.50U_\infty$. Wygnanski et al. also obtained a spot apex half-angle of 15.2° and a lateral spreading half-angle of 10°—constant with axial distance—in excellent agreement with Schubauer et al.[86] findings.

A similar investigation of artificial spots was carried out by Mautner et al.[59] using both velocity and surface pressure measurements. Most importantly, they obtained an ensemble surface-pressure signal which indicated that the spot surface pressure signature had a spanwise growth rate of about 12°, compared with 10° obtained from velocity disturbance measurement in the spot wing tip region, and did not depict conical similarity as for the velocity disturbance field. The geometry of the pressure field in fact evolved with axial distance and thus with the Reynolds number. Mautner et al. also obtained spot leading and trailing edge velocities at the spot plane of symmetry which were dependent on Re_∞ in such a way that, as the latter was increased, the spot leading edge velocity, $U_{l.e}$, rose whereas the trailing edge velocity, $U_{t.e}$, decreased. The values obtained are summarised in table 1.1.

Re_∞ ($\times 10^{-5}$ m^{-1})	$U_{l.e}/U_\infty$	$U_{t.e}/U_\infty$
5.1	0.820	0.55
6.6	0.845	0.54

Table 1.1: Spot leading and trailing edge velocities obtained by Mautner et al.[59]

The values shown above were somewhat lower than Schubauer et al.[86] and Wygnanski et al.[106] due to the fact that they represent the leading and trailing edges of the spot pressure disturbance field which do not exactly correspond to those of the spot velocity field.

It appeared from the Mautner et al.[59] study that some of the ensemble-averaged spot characteristics were Reynolds number-dependent. This result was confirmed by Wygnanski et al.[107] who discovered that the spot ensemble-average speed (or length-to-time scale ratio) and streamwise growth rate increased with increasing Re_∞. At the spot centreline near the surface, the leading edge velocity remained unchanged, whereas the trailing edge velocity decreased with increasing Re_∞. Furthermore, far downstream of its generation point, the spot was found to grow linearly with axial distance in the spanwise direction at a rate of 9.3° at $Re_\infty = 6.5 \cdot 10^5$ m^{-1} and increased to 10° at $Re_\infty = 12.4 \cdot 10^5$ m^{-1}, in good agreement with Schubauer et al.[86]

More recently, spot behaviour was examined at the body surface by means of heat transfer measurement[14,15] and thermochromic liquid crystal visualisation.[113] Ching et al.[14] obtained the temperature signature at the wall of naturally-occurring spots in an incompressible flow over a flat plate using thin-film heat transfer gauges. These allowed them to acquire information on spot dynamics and intermittency distributions across the intermittent-transition region. The spot mean, average leading edge and trailing edge velocities, U_{mean}, $U_{l.e}$ and $U_{t.e}$ respectively, were obtained by means of cross-correlation analysis for two Re_∞ conditions. The result is summarised in table 1.2.

Re_∞ ($\times 10^{-6}$ m^{-1})	$U_{l.e}/U_\infty$	$U_{t.e}/U_\infty$	U_{mean}/U_∞
2.4	0.81	0.50	0.68
4.2	0.86	0.48	0.63

Table 1.2: Turbulent spot mean, average leading edge and trailing edge velocities obtained by Ching et al.[14]

Zhong et al.[113] identified the initiation of the wake-induced transition process (as witnessed in turbomachine blades) with the formation of turbulent spots. The onset

point was found to move upstream with increasing level of freestream turbulence intensity. The spanwise growth rate of the spots in the region of their initiation was equal to 3.5°, compared to 6.5° further downstream of this region (as reported by the same authors[114,115]). This phenomenon was also encountered by several investigators such as Schubauer et al.,[86] Wygnanski et al.[106] and Mautner et al.[59]

Chong et al.[15] performed flow measurements at, and away from, the surface of a flat plate using simultaneously hot-wires and thin-film heat transfer gauges. Using velocity perturbation contours, they affirmed the existence of a spot spanwise overhang similarly to the spot leading edge in the streamwise direction. This finding was considered to be responsible for the smaller spot spanwise growth rates obtained at the surface using heat transfer measurement (see above, Zhong et al.[113]) compared with those obtained at a finite distance from the surface using velocity measurement (e.g., Schubauer et al.[86] and Wygnanski et al.[106]).

Turbulent spot average characteristics in incompressible boundary layers with pressure gradients

The effect of pressure gradient on turbulent spot behaviour was examined by several investigators such Katz et al.,[46] Zhong et al.[114,115] and Chong et al.[15] In their work on artificially generated turbulent spots in an incompressible flow over a flat plate with the presence of a favourable pressure gradient (*Falkner-Skan* parameter, $\beta = 1$) using hot-wire anemometry, Katz et al.[46] obtained reduced spot growth rates by more than 50% in both streamwise and spanwise directions compared with the zero pressure gradient case. The spot average shape transformed from the regular arrowhead shape into a rounded triangular shape with the trailing edge being nearly straight and perpendicular to the streamwise direction. Moreover, the average spot length, width and wake region extent were significantly reduced. Katz et al. also found that the spot leading and trailing edges propagated downstream at velocities, $U_{l.e}$ and $U_{t.e}$ respectively, approximately proportional to $\sqrt{x_0}$ (x_0 being the axial distance to the spot initiation point) while U_∞ varied linearly with x_0. This lead

them to conclude that no direct scaling of $U_{l.e}$ and $U_{t.e}$ with U_∞ was possible in the pressure gradient case as for the Blasius boundary layer case. The authors also suggested that the velocity profile and integral thicknesses within the spot compared well with their counterparts of a fully developed turbulent boundary layer and that the turbulent intensity inside the spot was higher than that of the zero pressure gradient case.

The effect of a favourable pressure gradient on spot behaviour was also investigated by Chong et al.[15] In their study of artificially generated spots in an incompressible boundary layer over a flat plat, they confirmed the effect of a favourable pressure gradient on reducing the streamwise growth rate of spots. They also found that both leading and trailing edge propagation rates were virtually the same at the surface and at the laminar boundary layer edge.

Zhong et al.[114,115] studied artificially produced spot characteristics in an incompressible water flow over a flat plate at $Re_\infty = 2 \cdot 10^5$ m^{-1} in the presence of three different levels of pressure gradients; 'zero', 'mild adverse' and 'strong adverse'. For the first time, pictures of the thermal footprint of the propagating spots were obtained using the thermochromic liquid crystal visualisation technique which allowed both qualitative and quantitative analysis of the results. Zhong et al. obtained an increasing spot spanwise growth rate, from 6.5° in the 'zero' case to 9° in the 'mild adverse' case and finally to 12° for the 'strong adverse' case. The authors suggested that the fact of these smaller values compared with previous published work was due to the difference between the temperature signature of the spot at the surface (using heat transfer measurement) and spot velocity disturbance field obtained at a certain distance away from the surface (hot-wire measurement), a fact which underlined a possible difference in the transition characteristics of momentum and thermal boundary layers. Zhong et al. also showed that the effect of increasing level of adverse pressure gradient was to increase and decrease the spot leading and trailing interface velocities respectively, a fact which resulted in an increase in the overall streamwise growth of the turbulent spot.

Turbulent spot substructure

The study of turbulent spot average characteristics revealed the existence of some structures within its interior. Increasingly detailed flow measurements and visualisations have been accordingly carried out to resolve these substructures in the attempt to understand the mechanisms yielding the growth of the spot across the intermittent-transition region. An exhaustive number of investigations have been conducted regarding this matter using experiment (e.g., Wygnanski et al.,[106,107] Perry et al.,[70] Antonia et al.,[5] Mautner et al.,[59] Itsweire et al.,[41] Barrow et al.,[7] Sankaran et al.,[79] Johnson et al.,[43] Sabatino et al.,[78] and Schröder et al.[85]) and most recently, with the advance in computer power, through CFD in particular *DNS* (e.g., Singer et al.,[93,94] Das et al.,[21] and Johnson[44]).

For some time, it was believed that the spot consisted of a singular flow-dominant arrowhead vortex tube that resided within the spot.[59,106] This vortex tube, which narrowed with spanwise distance from the spot plane of symmetry, had a maximum vorticity around the spot leading and trailing edge regions in the plane of symmetry. This was concluded from surface pressure and hot-wire velocity measurements made at, and away from, the wall. However, it was soon realised that the spot was composed of an increasingly more complex structure of vortices and streaks through entrainment of neighbouring laminar flow as it moved downstream.

In their experimental investigation of the internal structure of artificially generated turbulent spots within an incompressible flat plate boundary layer ($Re_\infty \approx 54000\ \mathrm{m}^{-1}$) using smoke visualisation, Perry et al.[70] discovered that the turbulent spot was composed of an array of 'Λ-shaped' vortices, which formed initially as one undulated vortex filament developed right behind the disturbance location (figure 1.7-a). This filament stretched and laterally induced a new undulation on each side, which in turn evolved and induced new undulations (figure 1.7-b). This cascade nature of the process lead to the formation and development of the turbulent spot as shown in figure 1.7-c. For a sufficiently grown spot, Perry et al. suggested a

near-constant λ_s (figure 1.7) with axial distance with a value $\lambda_s = 4.1\delta_1^*$, where δ_1^* is the laminar boundary layer displacement thickness at the location of spot initiation.

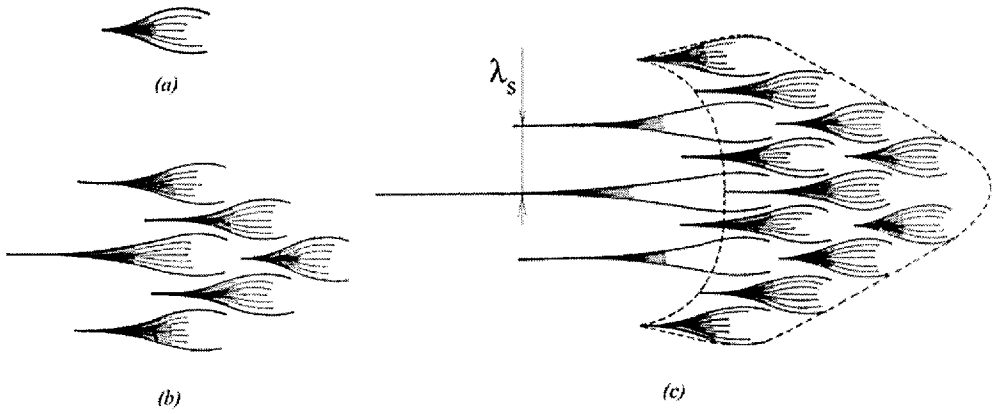

Figure 1.7: Turbulent spot substructure according to Perry et al.[70] λ_s is the distance between the centres of two adjacent vortices.

Wygnanski et al.,[107] through the examination of instantaneous velocity data, observed a deeply corrugated free interface separating the turbulent and non-turbulent fluids in the spot elevation plan of symmetry. They concluded that the spot comprised a finite number of large coherent eddies with trapped non-turbulent flow in between. In good agreement with Perry et al.[70] findings, they suggested that the spot contained several 'hairpin' eddies which were arranged in an arrowhead configuration and grew in number by destabilising and entraining the surrounding laminar flow, forming as a result more hairpin eddies at the rear end of the spot as it propagated downstream. This was the reason, according to the authors, behind the low velocity of the spot trailing interface compared with that of the leading edge. Similar entrainment mechanism and eddies generation occurred in the spot wing-tip regions, resulting in the spanwise growth of the spot. This result was also obtained by Itsweire et al.[41] through the analysis of the 'statistically most-probable' spot as opposed to the 'globally ensemble-averaged' spot, which caused the loss in detail of the spot substructure and was the reason behind previous perceptions of a single 'Λ-shaped' or 'horseshoe' vortex configuration.

More recently, Schröder et al.[85] used the *PIV* technique to determine detailed information on artificially generated spot substructures in an incompressible flow. In line with previous findings, The average spot substructure was established as 'hairpin-like' vortices and streaks of strong shear layers, essentially similar to, but more organised than, those of fully turbulent boundary layers. This structure was recognised to be responsible for the streamwise and spanwise growth of the spot and *self-similarity* of the arrowhead shape.

With the increase in computer power, more computational investigations of spot internal structure have been made in particular using *DNS*. Of particular interest is the work of Singer et al.[93,94] which focused on the early formation stages of the spot in an incompressible flat plate boundary layer. The result confirmed the existence of a substructure of hairpin-like vortices (figure 1.8), which were added near the trailing edge of the spot, in good agreement with previous experimental findings (e.g., Wygnanski et al.[107]). More importantly however, Singer et al. pointed out that the streamwise vortices were more intense and more frequent than the large spanwise vorticity structure whose importance had been overestimated by previous experimental results. The spot obtained showed the usual features that had been observed in experimental studies (figure 1.9).

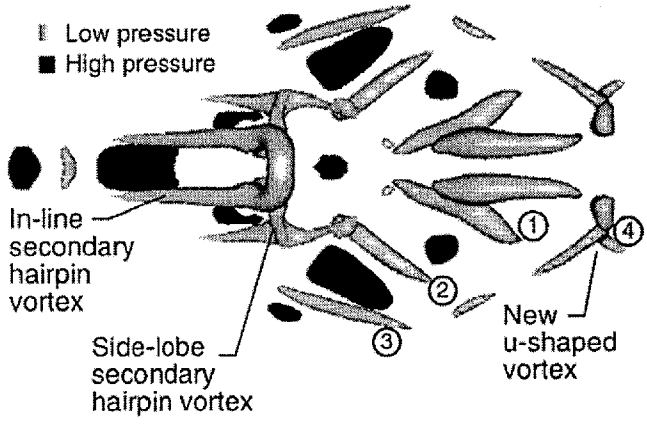

Figure 1.8: Plan view of a forming turbulent spot including the complex hairpin and quasi-streamwise vortex structures, numbered 1 to 4 according to the order of appearance (from Singer et al.[93]).

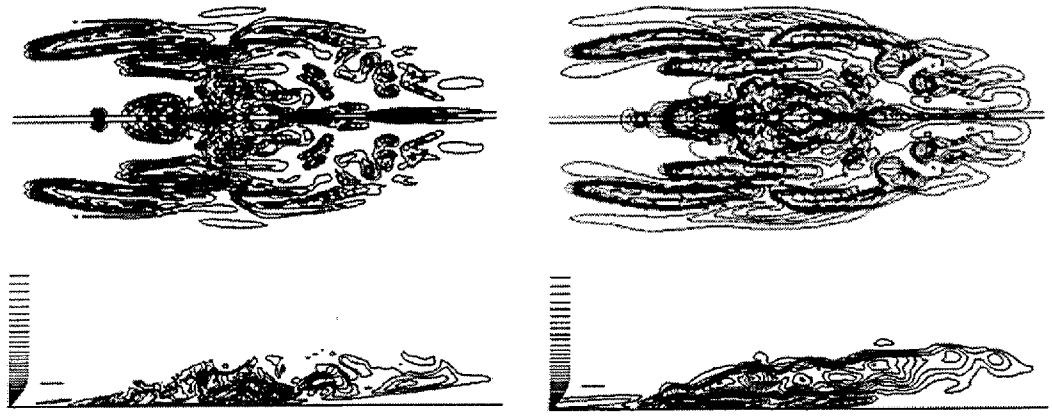

Figure 1.9: Plan and elevation (in the plane of symmetry) views of perturbation vertical vorticity and streamwise velocity contours (from Singer et.[93]). (left), vertical vorticity; (right) streamwise velocity. On the left side, the laminar velocity profile is indicated and the short horizontal line next to it shows the location of the plan view.

Turbulent spot average characteristics in low subsonic flows

De Lange et al.[22] carried out experiments on a flat plate boundary layer at a freestream Mach number, M_∞, of 0.33 and unit Reynolds number, Re_∞, of $1.1 \cdot 10^7$ m^{-1}. Using thin-film heat transfer gauges, they obtained turbulent spots—from different experiments and in different regions of the flow including those travelling in the wake region of preceding spots—which presented a heat flux profile that was self-similar. Furthermore, the heat transfer within the spot compared very well with the fully turbulent boundary layer level obtained in the same conditions. These findings interestingly agree with low speed results.

Schook et al.[84] investigated the effect of freestream turbulence intensity on turbulent spots in a Mach 0.36 flow over a flat plate. The spots were formed as a result of the turbulence present in the freestream, which was created by means of a grid positioned upstream of the plate leading edge. The spots were detected through their thermal footprints using heat transfer gauges. The analysis of the data using signal cross-correlation yielded spot mean speeds which were greatly affected by the level of freestream turbulence and higher than those of naturally-occurring spots.

Turbulent spot characteristics at hypersonic speeds

In hypersonic flows, studies on turbulent spot average characteristics are much more scarce (e.g., James,[42] Nagamatsu et al.,[68] Fischer,[28,29] Reda,[71,72] Mee et al.,[62] Mee,[63,64] Zanchetta et al.,[111] Zanchetta,[112] Wijesinghe,[103] and Huntley et al.[39]) and have been restricted to experiment, which is particularly complex and expensive. Full numerical simulation of the flow in the intermittent-transition zone, including turbulent spots, in high Mach and Reynolds numbers flows remains unfeasible with the computer power currently available. In the present author's knowledge, no type of investigation has been conducted up till now on spot substructure in these flow regimes. The experimental work has mostly been limited to the use of surface heat transfer measurement and flow visualisation with temperature sensitive coating and shadowgraph.

With reference to visualisation work, James[42] obtained shadowgraph images of roughness-induced turbulent spot planforms and elevation profiles on gun-launched slender transparent bodies in free flight. These images allowed the extraction of spot geometry, formation, propagation and growth rates in the range of freestream Mach number of $M_\infty = 2.7 - 10$, unit Reynolds number of $Re_\infty = 63 - 248$ million/m and various amounts of surface roughness. The geometry of the fully developed spots obtained (e.g., figure 1.10) compared well with those measured at low speeds and was found to be independent of the freestream Mach number, unit Reynolds number, and surface roughness. In contrast, these parameters, in addition to body shape, significantly affected the rate of formation, propagation, streamwise and spanwise growth of the spot. The spot leading and trailing edge velocities decreased with increasing roughness size and increased with increasing M_∞. The effect of the latter on these velocities depended greatly on the amount of roughness used. The spot apex half-angle was found to decrease with streamwise distance and the shape of the body leading edge had the most important effect on the rate of spot formation which was observed to increase with increasing Re_∞.

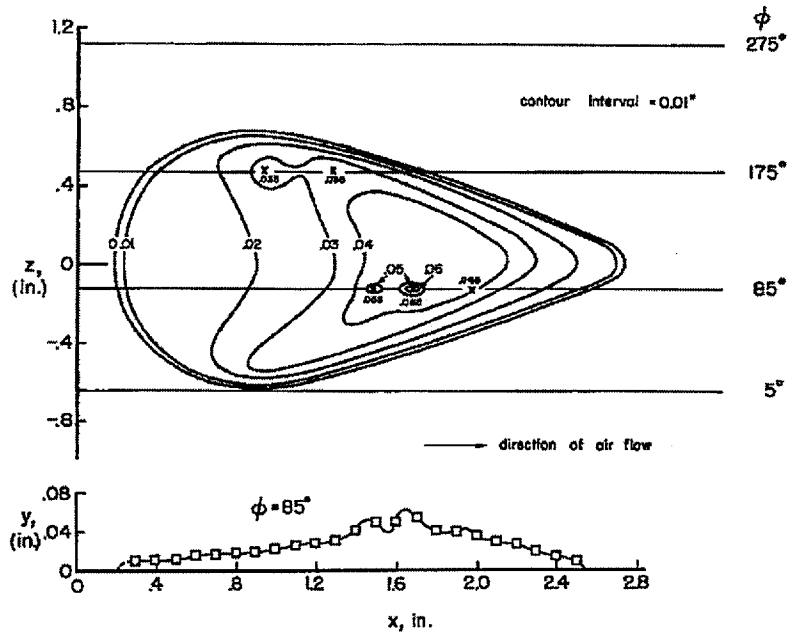

Figure 1.10: Turbulent spot geometry; (top) plan view; (bottom), elevation view. The laminar boundary layer edge Mach and unit Reynolds numbers are $M_e = 3.9$ and $Re_e = 9 \cdot 10^7$ m^{-1} respectively.

On his work on sharp slender cones at $M_\infty = 4.5$ in aeroballistics range, Reda[71,72] acquired simultaneous shadowgraph images of propagating spots within a laminar boundary layer and a fully developed turbulent wedge (figure 1.11, which is reported in Schneider's work[83]). On the top half of the model, the boundary layer is laminar with the presence of two distinct spots at different stages of their growth. The upstream spot on the right of the picture seems in its early formation phases, whereas the downstream spot on the left appears to have reached the fully developed stage with an elevation profile conforming with previous findings at similar speeds (e.g., James[42]) and low speeds (as reported throughout this section). The thickness of the downstream spot is clearly greater than the local laminar boundary layer thickness over a significant streamwise fraction. The surrounding laminar flow travels supersonically with respect to the upper portion of this spot, giving rise to the spot trailing edge shock wave (figure 1.11). The second shock wave which is visible around the spot leading edge location is in fact formed at the trailing edge

of an adjacent preceding spot. The maximum thickness of the spots compares very well with the thickness of the fully developed turbulent boundary layer (shown on the bottom half of the model) at the same streamwise location.

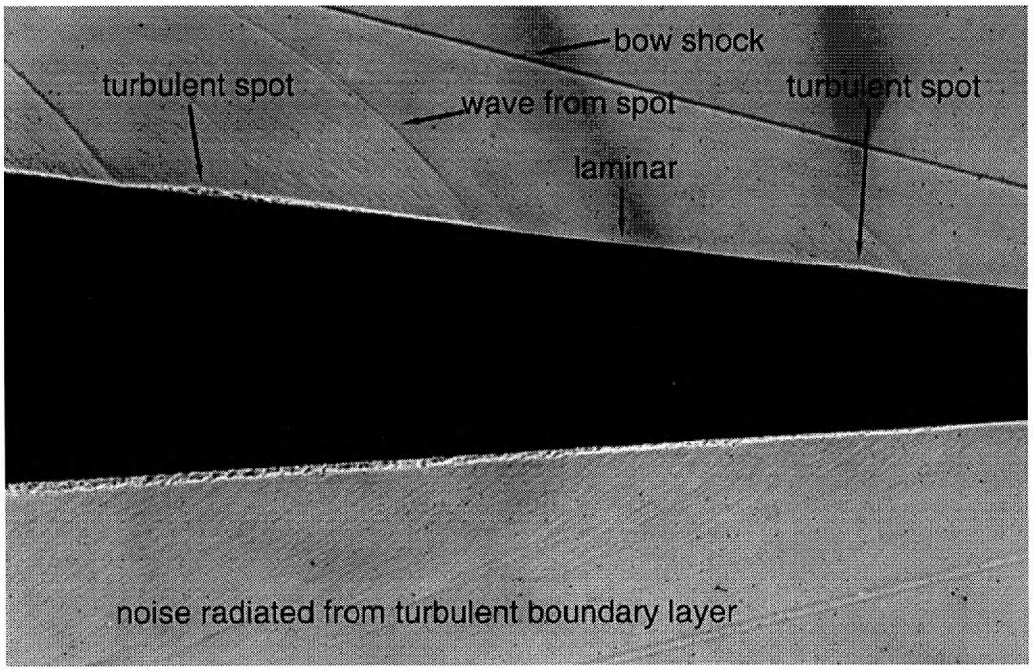

Figure 1.11: Shadowgraph of transition on a sharp cone at Mach 4.31 (reported by Schneider[83] from the work of Reda[71,72]).

More recently, new laser techniques have been developed and applied to flow visualisation, including the process of laminar-turbulent transition. Huntley et al.[39] investigated transition of a sharp-nosed elliptic cone boundary layer in a Mach 8 flow using *Filtered Rayleigh Scattering*. They obtained streamwise, spanwise, and simultaneous spanwise/planform images of the different stages of a transitional boundary layer, including laminar, unstable laminar with the presence of unstable waves, intermittent, and fully turbulent.

Nagamatsu et al.[68] conducted experiments on a 10° cone in the Mach number range of 9.1 to 16. Using thin-film platinum heat transfer gauges, he obtained information on spot mean propagation speed, which was found to vary between 0.8 to 0.9 of the freestream velocity.

Fischer[28] collected data that had been obtained from various types of experiments (individual turbulent spots, turbulent wedges, and unstable flows downstream of roughness trips) with a wide variation in tunnel disturbance environment and test model configuration, different natures of transition inception (naturally-occurring and roughness-induced), and different measurement/ visualisation techniques (hot-film, hot-wire, oil flow pattern,...etc). The result showed a reduction in the spot spanwise spreading rate with increasing boundary layer edge Mach number (figure 1.12), a fact which is responsible for the extensive lengths of intermittent-transition region in hypersonic flows.

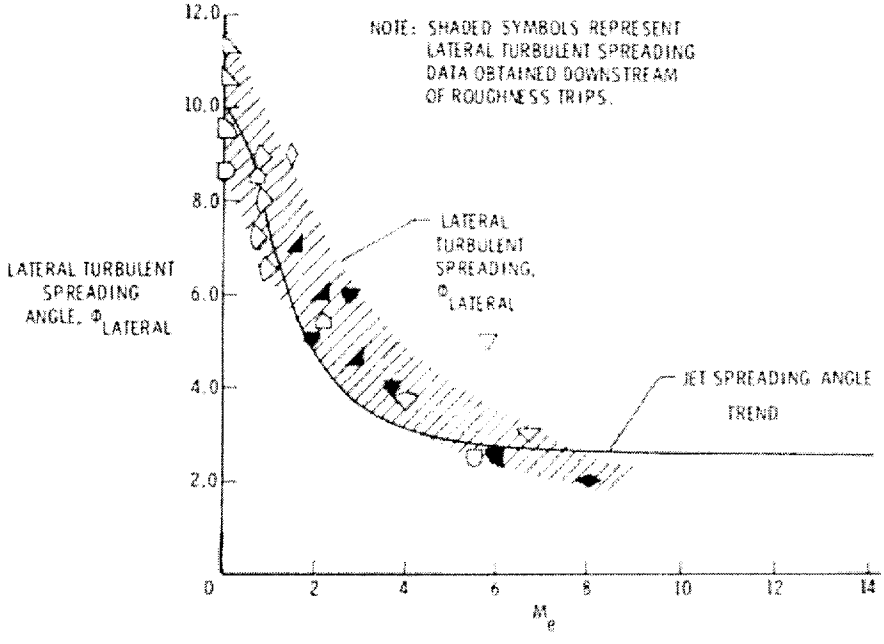

Figure 1.12: Fischer's collated data;[28] variation of turbulent spot and wedge lateral spreading rates with boundary layer edge Mach number M_e.

The theoretical prediction of Doorly and Smith[23] gave a power function for the spot spreading half-angle, α_s, with the boundary layer edge Mach number, M_e, as being $\alpha_s = tan^{-1}(3^{-3/2}2^{1/2}M_e^{-1})$. This is a hyperbolic function which yields a reduction in α_s with increasing M_e in good agreement with Fischer's collated experimental data.[28]

Mee et al.[62] obtained heat transfer signature of naturally-occurring turbulent spots in a flat plate boundary layer at Mach 5.6 in a hypervelocity shock tunnel using thin-film heat transfer gauges. They estimated the spot trailing edge propagation speed at 0.6 of the freestream value at a unit Reynolds number, Re_∞, of $2.5 \cdot 10^6$ m^{-1} and freestream enthalpy, H_s, of 9.3 MJ/kg. Mee et al. emphasised the necessity of a minimum averaging time window for satisfactory mean heat transfer distributions across the intermittent-transition zone to be acquired. This time window should be larger than that required for fully laminar and fully turbulent flows.

In later experiments on turbulent spots, Mee[63,64] measured a lower spot trailing edge propagation speed which was estimated at about 0.5 of the freestream value. The corresponding leading edge propagation speed was evaluated at approximately 0.9 of the freestream velocity. These values were obtained at $M_\infty = 6.2$, $Re_\infty = 2.6 \cdot 10^6$ m^{-1}, and $H_s = 6.2$ MJ/kg. The estimation of the spot lateral spreading rate at approximately 3.5°, in good agreement with much lower enthalpy results (e.g., Fischer[28]), suggested its dependency mainly on M_∞. The reasonable comparison of the transition length Reynolds numbers obtained with their low speed counterparts suggested possible higher spot production rates with increasing Mach number.

1.4.3 Roughness-induced transition and turbulent wedges

Work on roughness-induced transition has mostly focused on finding correlations between flow properties, roughness trip characteristics and transition onset location. This has generally been formulated as a transition Reynolds number based upon either boundary layer edge conditions ($Re_{ke,tr} = \rho_e U_e k/\mu_e$, where k is the roughness height) or flow properties at the roughness height location ($Re_{kk,tr} = \rho_k U_k k/\mu_k$), such as the work of Reda[72,73] and Mee.[63,64] Other investigators, such as Iliff et al.,[40] Berry et al.,[9,10] Horvath et al.[38] and Thompson,[98] established the $(Re_{\delta_2}/M_e)_{tr} = f(k/\delta)$ function for transition correlation (Re_{δ_2} being the laminar boundary layer (l.b.l.) edge Reynolds number based on momentum thickness, M_e the l.b.l. edge Mach number, and δ the l.b.l. thickness). Reda[73] presents a good

review of roughness-dominated transition correlations for hypersonic applications.

With reference to the turbulent wedge, which describes the transition region downstream of a discrete roughness element, it manifests itself as either a full patch of turbulence—a fully developed turbulent wedge—in which case the wedge shape can be identified at any planform station from the wall, or a cluster of individual turbulent spots, in which case the wedge shape is identified only at the wall through the signature of the propagating spots. The latter has already been covered in section 1.4.2, for the spots which were generated by means of a roughness trip. Regarding fully developed wedges, a few important points are briefly reported here.

In an incompressible flow with different amounts of favourable pressure gradients, Zhong et al.[116] obtained turbulent wedge lateral growth rates, α_s, using temperature-sensitive and shear-sensitive liquid crystals. The result showed similar α_s using both techniques in the zero pressure gradient case, however a discrepancy was identified as a favourable pressure gradient was introduced. The difference was estimated at about 30% with the highest gradient level. This result highlighted the difference in transition behaviour between the thermal and momentum boundary layers. Furthermore, Zhong et al. asserted the existence of a spanwise overhang in the wedge profile, which is the reason behind the reduction in spanwise growth rates obtained using surface heat transfer measurements compared with those obtained with hot-wire velocity measurements (which can be found in Zhong et al. work[115]).

In his work on blunt cone boundary layer transition at Mach 8.9, Zanchetta[112] examined the characteristics of turbulent wedges, which were produced by means of roughness trips of different shapes and sizes, using liquid crystal thermography. A typical result is shown in figure 1.13. Zanchetta discovered that the small distributed roughness ($k/\delta \approx 0.12$) produced axially aligned wake structures behind, which underwent transition at a certain downstream station. He also found that a triangular-shaped trip ($k/\delta \approx 0.33$) generated two wing-tip vortices which developed and underwent transition independently of each other possibly at different downstream locations. In contrast, a sand grain trip ($k/\delta \approx 0.33$) developed a

symmetrical wake flowfield and transition front downstream. The boundary layer located in the supersonic flow zone in the nose and rear-nose regions was established to be the most susceptible to roughness-induced transition.

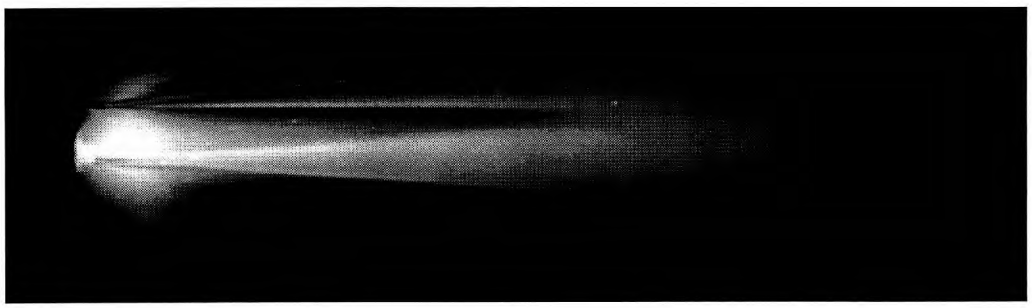

Figure 1.13: Turbulent wedge thermal footprint on a 5° semi-angle blunt-nosed cone at Mach 8.9, obtained using liquid crystal thermography (from Zanchetta[112]).

1.5 The present study

This present work is a result of continuing interest in the transition problem at the Imperial College Hypersonics Laboratory. This was initiated by Edwards[24] in 1981 with his work on the transition of a flat plate boundary layer. Thereafter in 1992, Sell[89] investigated the transition mechanisms on sharp and blunt-nosed cones using time-averaged heat transfer data. In 1996, Zanchetta[112] continued the work of Sell through detailed examination of nose blunting and surface roughness effects on transition onset location and region extent in cone flows. For his largest nose radius ($R = 25$ mm, $Re_n = 1,185,000$), Zanchetta obtained very extensive lengths of intermittent flow up to 400 mm chord length, only a fraction of the large lengths that occurred but not fully covered by his measurements. His time-dependent data revealed the presence of turbulent events of time-scales and frequencies that were within the range of resolution and accuracy of the experimental equipment available (sample frequency of 125 kHz and heat transfer gauge resolution of up to 0.3 mm^{-1}). Although the latter was not high enough for fine resolution of the spot interior—turbulence frequencies typically of 500 kHz, much higher than the average inter-

mittent event frequency—it presented a window of opportunity for the examination of individual turbulent spot average characteristics. In this respect, Wijesinghe[103] performed some experiments during his undergraduate final year in the Hypersonics Laboratory and the result was very encouraging. The present study aims to extend his work to a larger scale, in particular, to provide detailed information on spot planform geometry, growth and propagation rates. This would contribute to; (1) the extension of the sparse engineering database of turbulent spots; (2) the general understanding of the transition phenomenon at hypersonic speeds.

Chapter 2

Experimental Apparatus and Procedure

This chapter describes the apparatus utilised for the acquirement of the experimental data. This includes the gun tunnel facility, flow visualisation and measurement techniques, and experimental models. A full description of the experimental equipment used in the present study, including the full tunnel calibration exercise, can be found elsewhere.[56] A new high-accuracy system of measuring and monitoring tunnel pre-firing pressures has recently been incorporated. A detailed description of these most recent upgrades can be obtained from the work of Williams.[105]

2.1 Gun tunnel facility

2.1.1 Description

The experiments were carried out in the Imperial College gun tunnel (figure 2.1) which uses nitrogen as test gas. The total duration of a single run is 20 ms with a steady time window of approximately 6 ms. The tunnel operates at three different pressure conditions—low, medium, and high—providing a nominal Mach number of 8.9 and unit Reynolds numbers of up to 47 million per metre for the high pressure run condition (see table 2.1), which was used to obtain the present data. The repeatability of experimental runs is within $\pm 2\%$ and $\pm 4\%$ in terms of freestream

total pressure and total temperature, p_{0_∞} and T_{0_∞}, respectively.

M_∞	dM_∞/dx (%/m)	Re_∞ (/m)	γ_∞	p_{0_∞} (bar)	T_{0_∞} (K)
8.9 (±1%)	2.7	47.4×10^6 (±6%)	1.4	600 (±2%)	1150 (±4%)

Table 2.1: Gun tunnel test section flow conditions; high pressure run as described by Mallinson et al.[56]

The nozzle, with an exit diameter of 350 mm, generates a highly axisymmetric flow with a very slight flow angularity, but somewhat under expanded as a result of the turbulent boundary layer formed at the nozzle wall. This produces a test flow diamond which extends from the inside of the nozzle and across the test section, generating a slight axial gradient in the flow which is expressed as a 2.7% per metre increase in Mach number (see Mallinson et al.[56] and most recently Williams[105] for an extended description of the gun tunnel calibration). The test section is approximately 1 m in length and can incorporates model chord-lengths of up to 800 mm, very suitable for transition studies where intermittent-transitional zones extend over significant distances.

2.1.2 Operation

For reasons of safety, the gun tunnel is operated through a control panel located in a separated room. A rigorous procedure is followed in conducting a run to ensure safety and allow good repeatability of test conditions. The gun tunnel is composed of a driver and a barrel separated with a septum chamber, a nozzle at the downstream end of the barrel, and a test section which connects with a vacuum tank (figure 2.1). Three different diaphragms are used for the tunnel operation, of which two are inter-positioned at about 100 mm (septum boundaries)—a first (D_1 in figure 2.2) separating the driver from the septum and a second (D_2) separating the septum from the barrel—and a third diaphragm, D_3, made of *Melanex* separating the barrel from the nozzle inlet (figure 2.2).

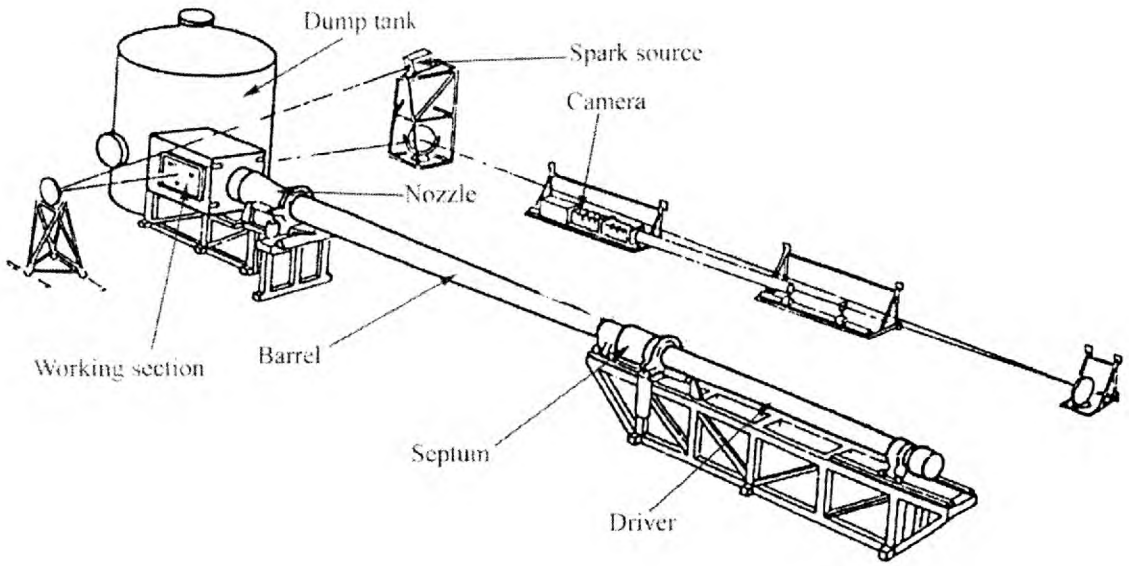

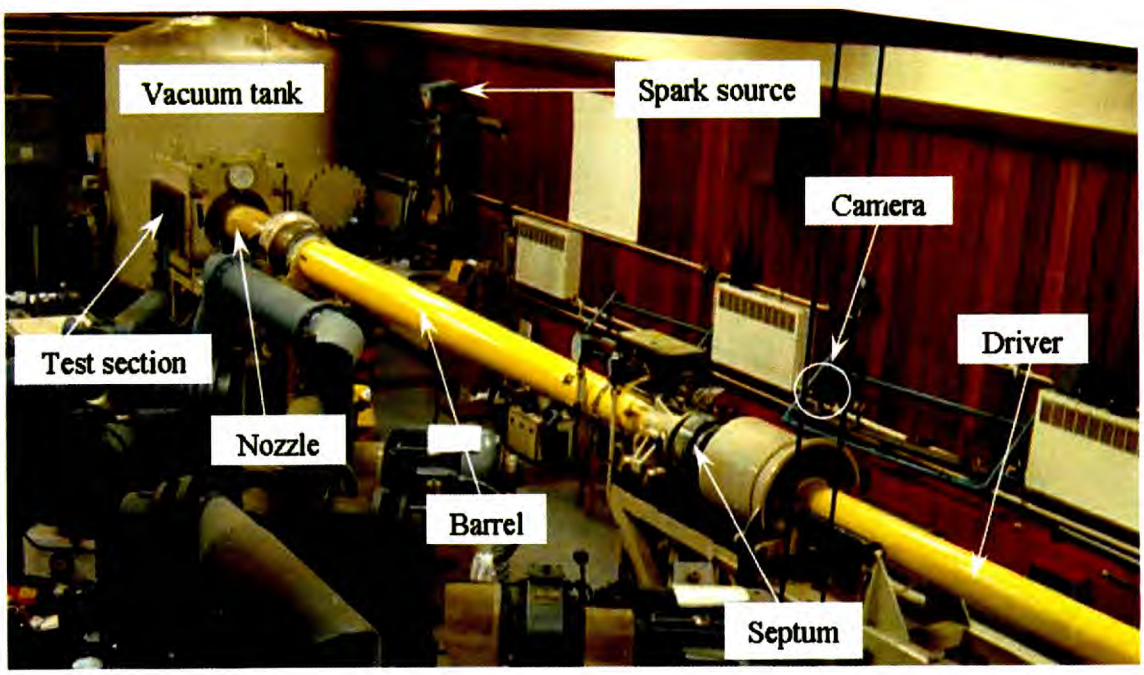

Figure 2.1: The Imperial College gun tunnel facility. (a) 3D Schematic of the facility including schlieren system set-up (Sell[89]); (b) Photograph of the tunnel.

Prior to each run, the inside of the barrel and the test section are thoroughly cleaned to provide uncontaminated test flow and three new diaphragms are mounted in the appropriate locations. The high pressure run takes about 40 minutes to carry out. At the start of a run, the driver, barrel, and 'nozzle/test section/dump tank'—referred to as *gas-expansion section*—are isolated from each other via the 3 diaphragms. The process starts with evacuating air from the dump tank section, to guarantee that the 'test flow' starts properly in the nozzle and that, after a run has been completed, the section remains at pressures below atmospheric. Normally, the dump tank pressure is reduced to about 240 to 293 Pa (1.8 to 2.2 Torr).

Once 'vacuum' has been achieved in the test section, the process of pressurising the driver and barrel—at this stage, the gas supply pipe valves V_4 and V_1 are open and V_s is closed (figure 2.2)—is initiated through the 4 stage-compressors unit. Each stage compressor has an upper operating pressure limit, which once attained, the next stage is activated. When the barrel pressure has reached $p_1 = 1055$ kPa (153 psi), the barrel valve, V_1, is closed and the driver pressure is continuously increased until it attains 44800 kPa (6500 psi), by which point the septum valve, V_s, is opened to pressurise the septum chamber to 46900 kPa (6800 psi). As soon as the driver pressure has attained $p_4 = 97500$ kPa (14140 psi), the pressurisation procedure is completed and the tunnel is ready to be fired. To do that, valve V_s is opened and the septum pressure is instantly increased (due to the large difference in volume between the driver and septum) resulting first in the rupture of diaphragm D_2 then diaphragm D_1 (figure 2.2); the tunnel is fired. The large driver-barrel pressure ratio, p_4/p_1, accelerates the piston located inside the barrel and the test gas is compressed through a system of reflected shocks to the reservoir pressure, $p_{4_{res}}$, of 53400 kPa, which causes the *Melanex* diaphragm D_3 to burst. The gas then expands through the nozzle and the 'test flow' is obtained; the run is now completed.

The tunnel reservoir condition is captured by means of a *Kistler* piezo-electric transducer positioned just upstream of the nozzle throat. Figure 2.3 shows a typical total pressure time history obtained from a high pressure run.

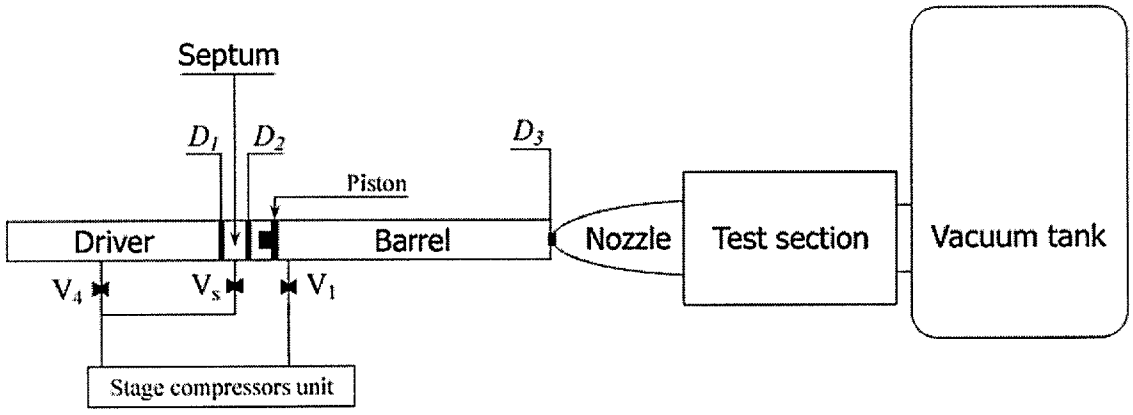

Figure 2.2: 2D simplified schematic of the tunnel various sections and positioning of the steel diaphragms, D_1 and D_2, and the *Melanex* diaphragm D_3. Also, a simplified sketch of the gas supply connection; V_4, driver valve; V_s, septum valve; V_1, Barrel valve.

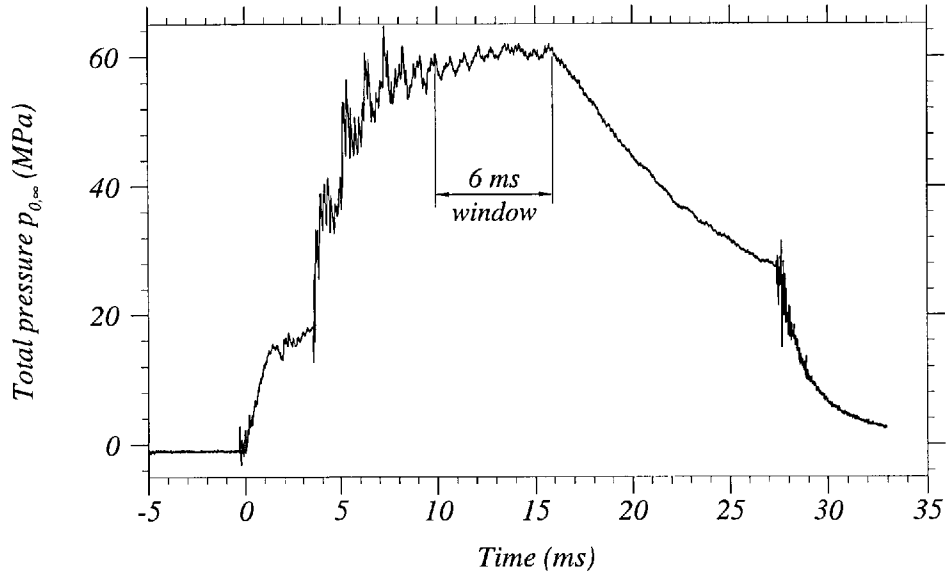

Figure 2.3: Time history for the total pressure signal obtained from a high pressure run. The 6 ms window represents the steady run-time.

2.2 Flow visualisation and measurement

The experimental result have been obtained by means of two well-established techniques namely schlieren and heat transfer measurement. The former is qualitative and was mainly used for the visualisation of the detached bow shock wave and boundary layer. The latter is quantitative and was used for the acquisition of detailed heat flux 2D distributions at the model surface and thus the detection of turbulent spot and wedge thermal footprints.

2.2.1 Schlieren visualisation

Schlieren is a non-intrusive optical method which is based on the fact that when a light beam travels through a flowfield with local density gradients, the rays in this beam are deflected towards higher levels of density gradient. The deflected light rays are then 'labelled' through either a change in contrast or colour, at a knife edge or colour-banded filter.

The experimental setup of the schlieren system in the gun tunnel facility is shown in figure 2.4. The system includes an argon spark source for illumination, two concave mirrors, m_1 and m_2, of 300 mm diameter and 6.1 m focal length, a 450 mm diameter flat mirror, a colour filter positioned at the second focal plane, and a 2 m focal length convex lens used for light focusing onto the camera plate. The latter is a Canon EOS and uses a 35 mm 200 ASA colour film. Several types of colour filters were used in an attempt to visualise the boundary layer and turbulent spots and wedges. However, this was unsuccessful at the low ambient densities and density differences across the boundary layer.

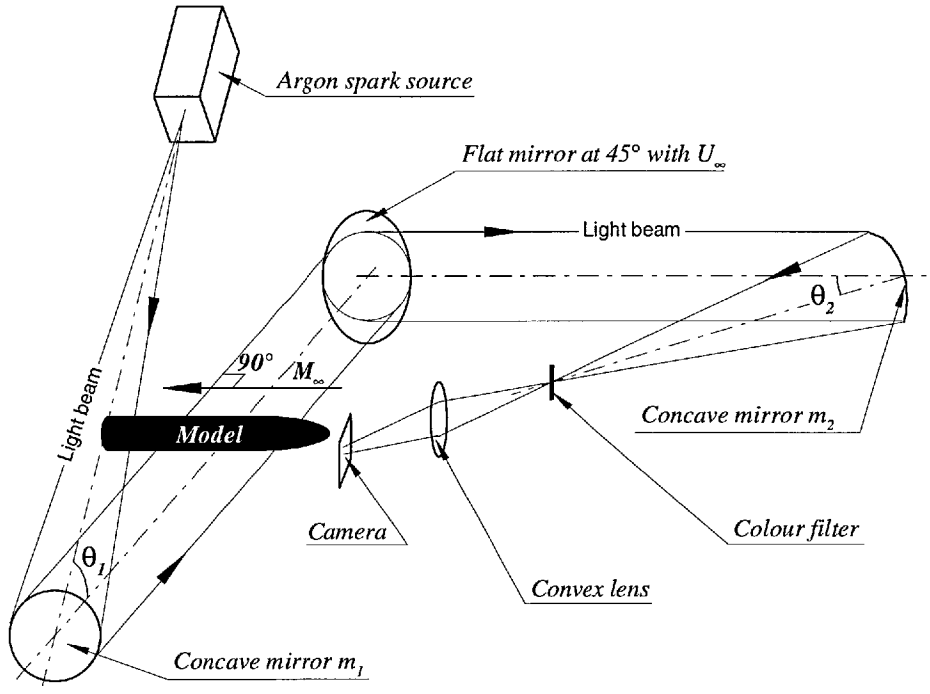

Figure 2.4: Illustration of the schlieren system set-up in the gun tunnel facility; Exaggerated scale of the focal angles θ_1 and θ_2.

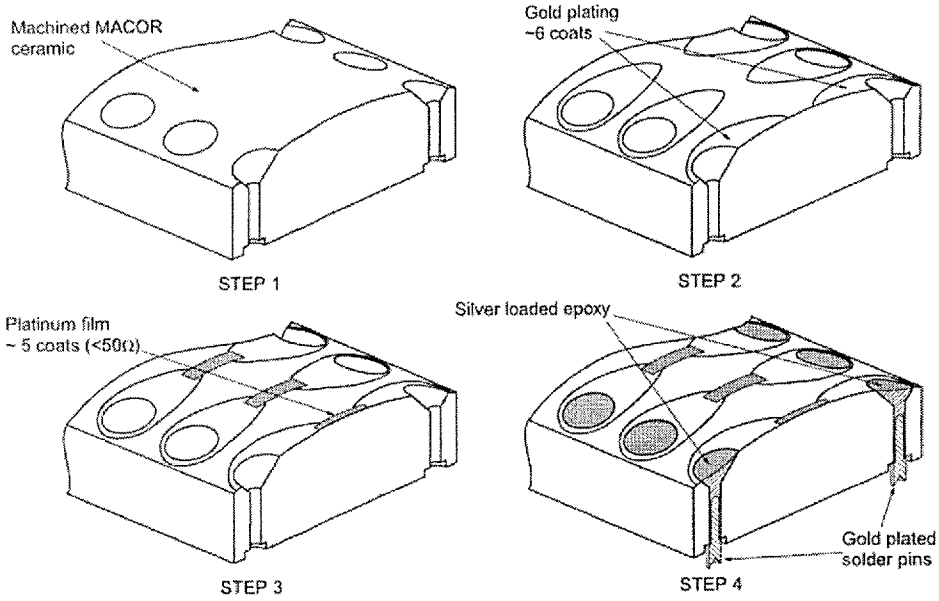

Figure 2.5: Overview of the four stages of manufacture of the thin-film heat transfer resistance gauge (Williams[105]).

2.2.2 Heat transfer measurement

Description of instrumentation

Heat transfer is the main property being investigated in the present study as it represents a critical design parameter for hypersonic vehicles and, in particular, an excellent boundary layer transition detector. For this reason, considerable care was taken in the design, manufacture, and calibration of the heat transfer modules used for measurement. These modules incorporate a multiple array of *thin-film* resistance gauges, hand-painted onto an insulating substrate which is made of a machinable glass ceramic known as MACOR. The substrate is machined integral to the model to ensure good surface continuity, very critical for transition. The thin-film is made of platinum which adheres very well to the MACOR ceramic and provides small temperature sensitivity and a good *figure of merit*[87] $\alpha_R\sqrt{\rho_R}$ (α_R being the temperature coefficient and ρ_R the resistivity). The process of manufacture of a typical thin-film heat transfer gauge is summarised schematically in figure 2.5.

The thin-film gauge is particularly suitable for short duration experiments and has been studied in detail by several researchers (e.g., Vidal[100] and Schultz and Jones[87]). It has been extensively used since its original development by Vidal[100] forty years ago, in particular for hypersonic experiments in the Imperial College gun tunnel such as the work of Sell,[89] Zanchetta,[112] and most recently Creighton[20] and Williams.[105] The considerable expertise of the laboratory workshop has resulted in significant improvement in gauge quality and resolution.

Data reduction

The platinum thin film is used to monitor the instantaneous variation of surface temperature and, using the thermal properties of the substrate, heat transfer is extracted following the expression given by Schultz and Jones:[87]

$$q_w(t) = \sqrt{\frac{\rho c k}{\pi}}\left[\frac{T(t)}{\sqrt{t}} + \frac{1}{2}\int_0^t \frac{T(t)-T(\tau)}{(t-\tau)^{3/2}}d\tau\right] \;;\; T(0)=0 \qquad (2.1)$$

where q_w is the required heat transfer; ρ, c and k are the substrate density, specific heat and thermal conductivity respectively; T is the measured temperature function of time t. For the MACOR ceramic substrate, $\sqrt{\rho ck}$ is equal to 0.2 J cm^{-2} K^{-1} s$^{-1/2}$.

The time histories for temperature are derived from the voltage imbalance, $\Delta V(t)$, measured across a Wheatstone bridge connected to the gauge, which captures the change in sensor resistance caused by surface temperature variation during a run. The formula for this is given as:

$$T(t) = \frac{4}{\alpha_r}\frac{\Delta V(t)}{V_b}\left(1 - 2\frac{\Delta V(t)}{V_b}\right)^{-1} \tag{2.2}$$

where V_b is the supply voltage and α_r is the thermo-resistivity of the film determined from gauge calibration. This is achieved my submerging the gauge into a thermostatic water bath, maintained at a series of temperatures in the range of the expected experimental data, and recording the corresponding resistance. The result yields a resistance-temperature curve, $R = f(T)$, that allows us to extract α_r from equation 2.3.

$$\alpha_r = \frac{1}{R}\frac{\partial R}{\partial T} \tag{2.3}$$

After digitisation of the temperature signal through the *Microlink* data logger (discussed in the following section), the heat transfer rate is obtained using the algorithm due to Cook and Felderman,[19] which is based on the assumption that the temperature distribution in time is piecewise linear (equation 2.4). This assumption, although it leads to acceptable result, introduces a certain amount of noise into the data which is of great significance when it comes to the detection of small scale turbulent spots (detailed discussion will be given in chapter 4).

$$T(\tau) = T(t_{i-1}) + \frac{T(t_i) - T(t_{i-1})}{t_i - t_{i-1}}(\tau - t_{i-1}) \;\; ; \;\; \tau \in [t_{i-1}, t_i] \tag{2.4}$$

substituting the above equation into equation 2.1, the following expression for

heat flux is obtained:

$$q_w(t_n) = \sqrt{\frac{\rho c k}{\pi}} \sum_{i=1}^{n} \frac{T(t_i) - T(t_{i-1})}{(t_n - t_i)^{1/2} + (t_n - t_{i-1})^{1/2}} \tag{2.5}$$

Measurement uncertainties

The expected experimental uncertainties associated with using the heat transfer gauges are summarised in table 2.2.

Substrate thermal properties	±5%
Thin-film thermo-resistive properties	±1%
Signal amplification	±1%
Gauge calibration	±2%
Spatial	±1%
Runs repeatability	±3%
Total uncertainty	±13%

Table 2.2: Breakdown of heat transfer measurement uncertainties.

2.2.3 Data acquisition system

The data acquisition system (figure 2.6-top) is composed of a signal amplifier unit, a 12-bit analogue-to-digital converter (the *Microlink* unit), a time-delay unit and a personal computer. The system includes 30 channels for signal record, of which one is used for the total pressure signal and the remaining 29 are connected to the tunnel test section (figure 2.6-bottom). The system is triggered by the rise in total pressure, output from the *Kistler* piezo-electric transducer which is mounted at the nozzle inlet, when the tunnel fires. This also sets off the schlieren argon spark with a controlled time delay. The analogue outputs from the Kistler transducer and heat transfer gauges are amplified and low-pass filtered, using the Microlink modules, at a frequency of 50 kHz in order to prevent anti-aliasing of the digitised signals. These are obtained at a sample rate of 125 kHz for each channel, providing 750 data points within the run steady time window. The digitised signals are then downloaded to a PC for post-processing.

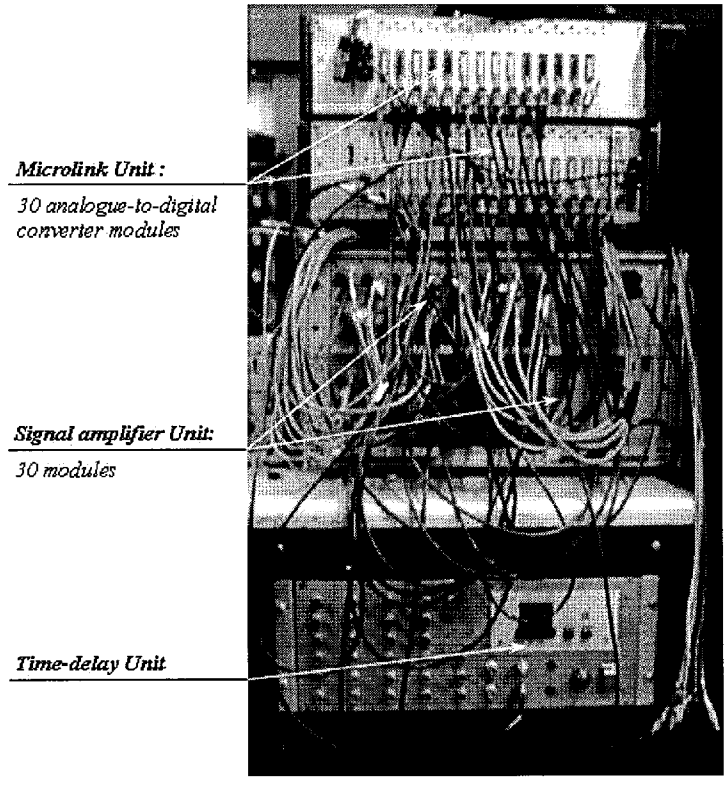

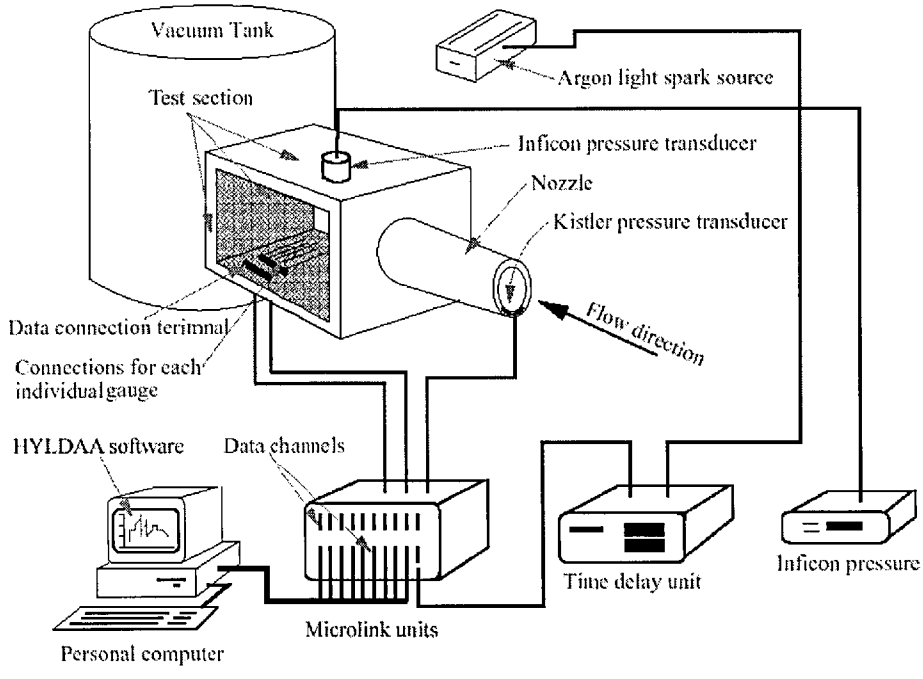

Figure 2.6: Data acquisition system. (a) Photograph of the Microlink, signal amplifier, and time delay units; (b) Schematic of the network between the tunnel test section, schlieren spark source and data acquisition system (Creighton[20]).

A new 'user-friendly' software, HYLDAA (the HYpersonics Laboratory Data Acquisition Application), has been developed during this study by Williams[105] to improve data acquisition accuracy. A detailed description of the software development and integration is found in his work. The source code implicitly comprises the temperature and pressure functions derived from the voltage signal outputs, so that they can be readily obtained through the software graphical user interface (figure 2.7). The latter allows full gauge calibration and data viewing and recording of all channels to be carried out automatically. It also enables straightforward selection of the number of operating channels, data type (either pressure, temperature or voltage), range and gain of the amplification procedure, and data labelling and saving. Work on integrating heat transfer data reduction into the source code has been initiated but remains to be achieved.

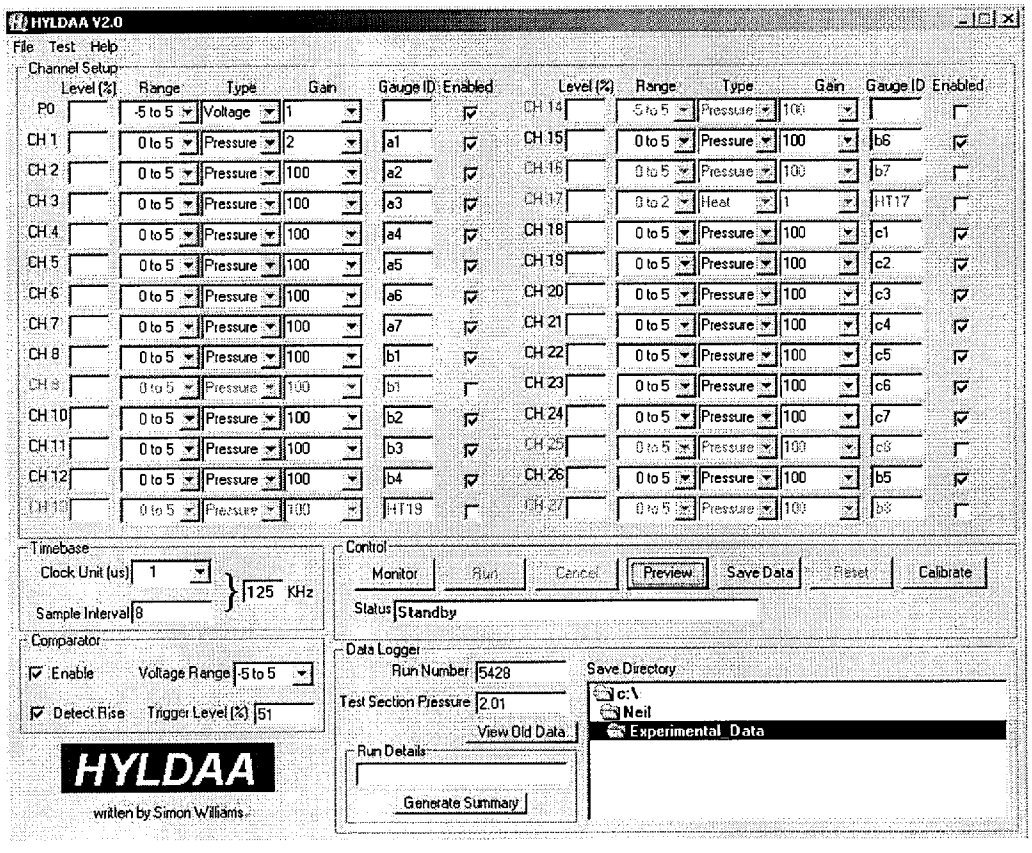

Figure 2.7: Data acquisition system software; GUI of HYLDAA (the HYpersonics Laboratory Data Acquisition Application).

2.3 Experimental models

2.3.1 Description

The model used in the experiments is a blunt-nosed cylinder with an afterbody diameter of 74.75 mm (figure 2.8). The model consists of; a forebody nosepiece of 25 mm radius spherical nose (figure 2.9); a range of non-instrumented interchangeable cylindrical afterbody segments of 66 mm, 132 mm, 187 mm, and 200 mm length; and two instrumented afterbody cylinders with an axial array and circumferential array of heat transfer gauges respectively (figures 2.10 and 2.11). The 25 mm radius nose and cylindrical afterbody are blended with a 273 mm radius arc.

The axial heat transfer module (figure 2.10) consists of 31 thin-film gauges (which have been described earlier) spaced at 3.4 mm pitch. Only the downstream 23 consecutive gauges were used for experiments as the remaining ones were damaged. The circumferential module (figure 2.11) comprises 18 'V'-shaped gauges spaced at 4 mm (or 6.1 degrees) pitch around the circumference. The spatial resolution of the gauges is approximately 2.5 mm and the frequency response is 100 kHz. The gauge-to-gauge spacing, whether axial or circumferential, was deliberately designed to allow simultaneous sampling of all sensors over a measurement interval which would cover the expected turbulent spot size entirely. The objective of the two different sets of gauge arrays was to capture as much data as possible on the streamwise and spanwise scales of turbulent events as detected by their thermal footprint.

2.3.2 Configuration

Various model configurations were designed for three main experimental categories; streamwise measurement of turbulent spots, spanwise measurement of turbulent spots, and finally spanwise measurement of turbulent wedges. Although the basic model geometry (as illustrated in figure 2.8) was the same in all cases, various types of model surfaces and instrumentation arrangements were used.

Turbulent spot streamwise measurement

For this case, two model configurations were employed:

Smooth nose. In this case, the entire model surface is polished and measurements are made between $x = 446.2$ mm and $x = 521.0$ mm distance from the model apex using the axial heat transfer module.

Rough nose. In this case, distributed surface roughness is applied to the nose by means of *silicon carbide* paper and the rest of the model is polished. The roughness size is estimated at about 1.6 μm (2% of the local CFD laminar boundary layer thickness). Measurements are made between $x = 406.2$ mm and $x = 481.0$ mm using the axial module.

Turbulent spot spanwise measurement

For this case, the whole model surface is polished and measurements are made at 3 different axial positions, $x = 213$ mm, 279 mm, and 334 mm, using the circumferential heat transfer module.

Turbulent wedge spanwise measurement

For this case, the entire model surface is polished and measurements are made at 4 different axial positions, $x = 147$ mm, 213 mm, 279 mm, and 334 mm, using the circumferential module. The turbulent wedge is generated with a diamond-shaped roughness-trip laid at a nominal axial position, x_k, of 37.75 mm. The roughness-trip size varies for different runs and will be described later in chapter 7.

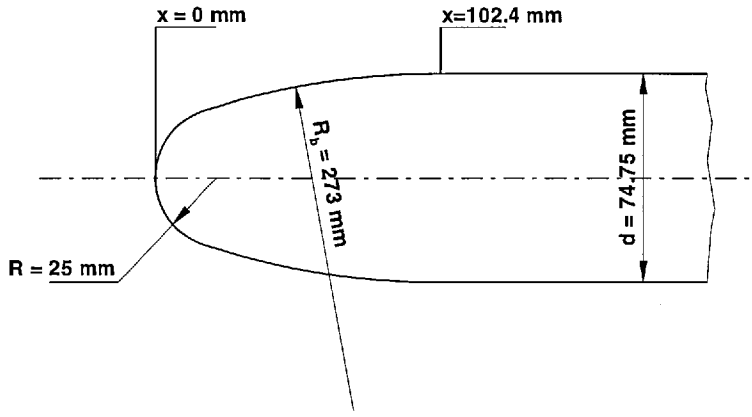

Figure 2.8: Schematic of the overall model, comprising a spherical nose with radius, R, of 25 mm, a cylindrical afterbody with diameter, d, of 74.75 mm, and a blending section with a constant arc radius, R_b, of 273 mm. The afterbody parallel section starts at $x = 102.4$ mm.

Figure 2.9: Photograph of the assembled non-instrumented model; Nosepiece and various interchangeable cylindrical afterbody segments.

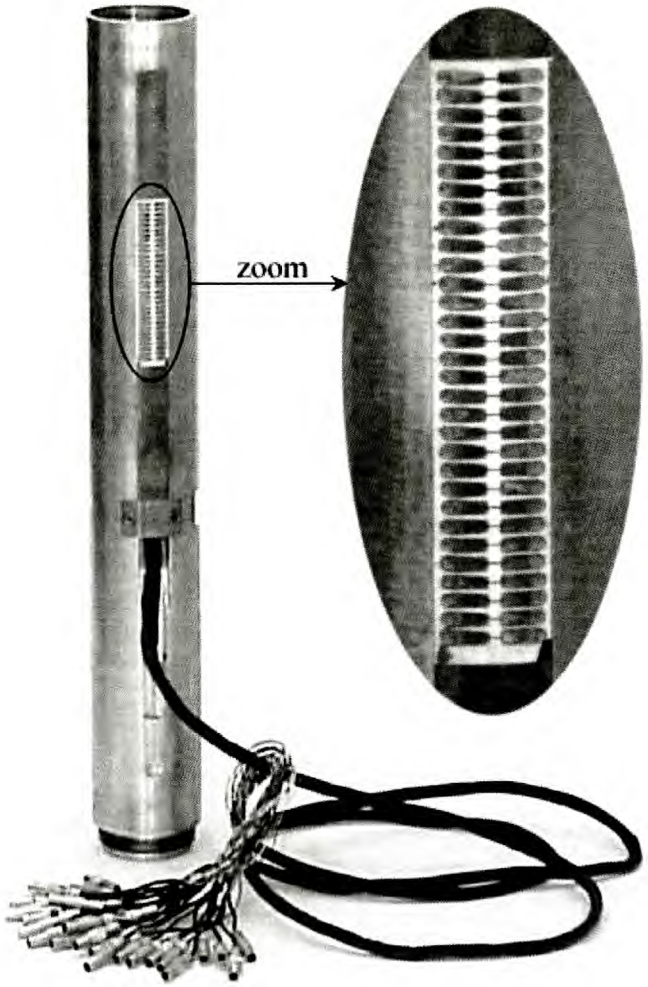

Figure 2.10: Photograph of the afterbody cylinder with the axial heat transfer module; Includes 31 gauges spaced at 3.4 mm.

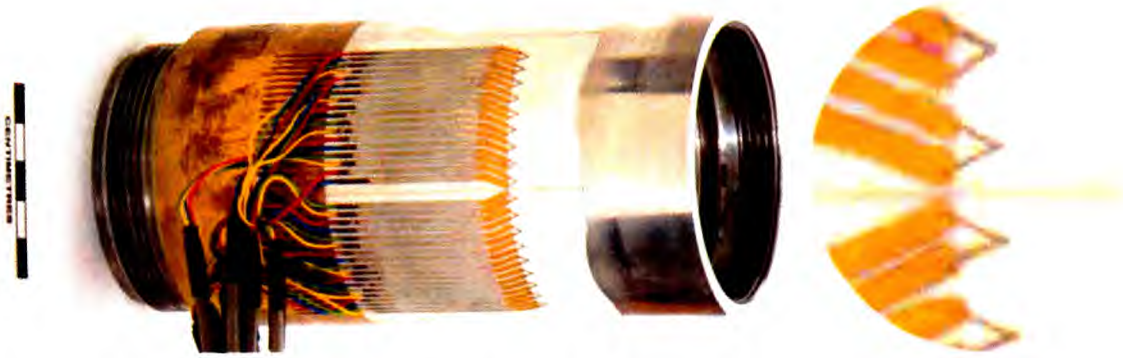

Figure 2.11: Photograph of the afterbody cylinder with the circumferential heat transfer module; Includes 18 'V'-shaped gauges spaced at 4 mm (or 6.1 degrees) around the circumference.

Chapter 3

Computational Methodology and Simulation

The computational procedure assisted the design of the nosepiece geometry as well as the determination of the necessary laminar and turbulent flowfield characteristics which support the analysis of the heat transfer data.

3.1 Methodology

The computational simulations used an in-house code which has been documented in the work of Sell[89] and Hillier et al.[33] The computational method is based upon 'convection-diffusion' splitting used on a structured mesh, whereby the convective (i.e., Euler) terms use an explicit second-order upwind *Godunov-type* method and the diffusive (viscous) terms are expressed with centred differencing and implicit time integration for the *thin shear-layer* Navier Stokes formulation. The overall solver is second order accurate in space and time. The turbulent calculation uses the one-equation Menter's variant of the two-equation $k - \epsilon$ model.[65]

3.1.1 Governing equations

The general conservative formulation of the Navier-Stokes equations for a three-dimensional compressible flow, derived from the conservation laws of mass, momen-

tum, and energy, is as follows:

$$\mathbf{Q}_t + \mathbf{F}(\mathbf{Q})_x + \mathbf{G}(\mathbf{Q})_y + \mathbf{H}(\mathbf{Q})_z = 0 \tag{3.1}$$

In equation (3.1), $\mathbf{Q}$ is the conserved vector containing the conserved variables and $\mathbf{F}(\mathbf{Q})$, $\mathbf{G}(\mathbf{Q})$, and $\mathbf{H}(\mathbf{Q})$ are the flux vectors, which are functions of the conserved vector $\mathbf{Q}$, in the x, y, and z directions respectively. The subscripts $_t$, $_x$, $_y$, and $_z$ represent the partial derivation with respect to these respective dimensions.

The flux vectors comprise both the convective (i.e., inviscid, indicated in superscript ^{c} in Eq. 3.2) and diffusive (i.e., viscous, indicated in superscript ^{d}) terms and thus equation (3.1) can be rewritten as:

$$\mathbf{Q}_t + \mathbf{F}^c_x + \mathbf{G}^c_y + \mathbf{H}^c_z = \mathbf{F}^d_x + \mathbf{G}^d_y + \mathbf{H}^d_z \tag{3.2}$$

where the conserved and flux vectors are given by:

$$\mathbf{Q} = \begin{bmatrix} \rho \\ \rho u \\ \rho v \\ \rho w \\ E \end{bmatrix} \tag{3.3}$$

$$\mathbf{F}^c = \begin{bmatrix} \rho u \\ \rho u^2 + p \\ \rho uv \\ \rho uw \\ u(E+p) \end{bmatrix}, \quad \mathbf{G}^c = \begin{bmatrix} \rho v \\ \rho uv \\ \rho v^2 + p \\ \rho vw \\ v(E+p) \end{bmatrix}, \quad \mathbf{H}^c = \begin{bmatrix} \rho w \\ \rho uw \\ \rho vw \\ \rho w^2 + p \\ w(E+p) \end{bmatrix} \tag{3.4}$$

$$\mathbf{F}^d = \begin{bmatrix} 0 \\ \tau^{xx} \\ \tau^{xy} \\ \tau^{xz} \\ u\tau^{xx} + v\tau^{xy} + w\tau^{xz} - q_1 \end{bmatrix} \tag{3.5}$$

$$\mathbf{G}^d = \begin{bmatrix} 0 \\ \tau^{yx} \\ \tau^{yy} \\ \tau^{yz} \\ u\tau^{yx} + v\tau^{yy} + w\tau^{yz} - q_2 \end{bmatrix} \tag{3.6}$$

$$\mathbf{H}^d = \begin{bmatrix} 0 \\ \tau^{zx} \\ \tau^{zy} \\ \tau^{zz} \\ u\tau^{zx} + v\tau^{zy} + w\tau^{zz} - q_3 \end{bmatrix} \tag{3.7}$$

where ρ is the density, u, v, and w are the velocity components in the x, y, and z directions respectively, p is the static pressure, E is the total energy per unit volume, q_1, q_2, and q_3 are the heat fluxes due to conduction in the x, y, and z directions respectively, and τ^{ij} are the viscous stresses.

For an axisymmetric flow, the Navier-Stokes equations are expressed in the cylindrical coordinates and are reduced to:

$$\frac{\partial \mathbf{Q}}{\partial t} + \frac{\partial \mathbf{F}^c}{\partial x} + \frac{\partial \mathbf{G}^c}{\partial r} - \mathbf{S}^c = \frac{\partial \mathbf{F}^d}{\partial x} + \frac{\partial \mathbf{G}^d}{\partial r} + \mathbf{S}^d \tag{3.8}$$

where $\mathbf{S}^c$ and $\mathbf{S}^d$ are source terms, algebraic functions of the flow variables.

The conserved, flux, and source vectors are given by:

$$\mathbf{Q} = \begin{bmatrix} \rho \\ \rho u \\ \rho v \\ E \end{bmatrix} \tag{3.9}$$

$$\mathbf{F}^c = \begin{bmatrix} \rho u \\ \rho u^2 + p \\ \rho uv \\ u(E+p) \end{bmatrix}, \quad \mathbf{G}^c = \begin{bmatrix} \rho v \\ \rho uv \\ \rho v^2 + p \\ v(E+p) \end{bmatrix}, \quad \mathbf{S}^c = -\frac{1}{r}\begin{bmatrix} \rho v \\ \rho uv \\ \rho v^2 \\ v(E+p) \end{bmatrix} \tag{3.10}$$

$$\mathbf{F}^d = \begin{bmatrix} 0 \\ \tau^{xx} \\ \tau^{xr} \\ u\tau^{xx} + v\tau^{xr} - q^x \end{bmatrix} \tag{3.11}$$

$$\mathbf{G}^d = \begin{bmatrix} 0 \\ \tau^{rx} \\ \tau^{rr} \\ u\tau^{rx} + v\tau^{rr} - q^r \end{bmatrix} \tag{3.12}$$

$$\mathbf{S}^d = \frac{1}{r}\begin{bmatrix} 0 \\ \tau^{rx} \\ \tau^{rr} - \tau^{\theta\theta} \\ u\tau^{rx} + v\tau^{rr} - q^r \end{bmatrix} \tag{3.13}$$

where u and v are the axial (x) and radial (r) components of velocity respectively. The total energy per unit volume, E, is the sum per unit volume of the kinetic and internal energies:

$$E = \frac{1}{2}\rho(u^2 + v^2) + e \tag{3.14}$$

The heat fluxes are defined as:

$$q^x = -k_L \frac{\partial T}{\partial x} \tag{3.15}$$

$$q^r = -k_L \frac{\partial T}{\partial r} \tag{3.16}$$

where k_L and T are the thermal conductivity and the static temperature of the fluid respectively.

Using the Stokes hypothesis, which postulates that the bulk viscosity of a Newtonian fluid is equal to zero, the viscous stresses can be expressed as:

$$\tau^{xx} = \mu\left(2\frac{\partial u}{\partial x} - \frac{2}{3}\,\mathrm{div}\,\vec{v}\right) \tag{3.17}$$

$$\tau^{rr} = \mu\left(2\frac{\partial v}{\partial r} - \frac{2}{3}\,\mathrm{div}\,\vec{v}\right) \tag{3.18}$$

$$\tau^{\theta\theta} = \mu\left(2\frac{v}{r} - \frac{2}{3}\,\mathrm{div}\,\vec{v}\right) \tag{3.19}$$

$$\tau^{xr} = \tau^{rx} = \mu\left(\frac{\partial u}{\partial r} + \frac{\partial v}{\partial x}\right) \tag{3.20}$$

where:

$$\mathrm{div}\,\vec{v} = \frac{\partial u}{\partial x} + \frac{\partial v}{\partial r} + \frac{v}{r} \tag{3.21}$$

It should be noted that the above system of equations must be closed by assuming an equation of state. In the present study, the fluid used is nitrogen (the experimental test gas) and considered to be thermally and calorically ideal, which means that c_p and c_v are constant and that:

$$p = \rho RT \tag{3.22}$$

$$e = \rho c_v T = \frac{p}{\gamma - 1} \tag{3.23}$$

The dynamic viscosity, μ, is given by Keyes law as a function of temperature:

$$\frac{\mu}{\mu_{ref}} = \frac{T^{0.5}}{1 + aT^{-1}10^{-b/T}} \tag{3.24}$$

where:

$$\mu_{ref} = 1.418.10^{-6}\ kg/ms\ ,\ a = 116.4\ ,\ b = 5$$

The conductivity of the gas, k_L, is extracted from the Prandtl number, Pr, which is considered constant over the temperature range of the computations carried out in the present study and is defined as:

$$Pr = \frac{c_p \mu}{k_L} = 0.72\ ;\ \text{for a laminar flow} \tag{3.25}$$

3.1.2 Flow solver

The flow solver is based upon the *convection-diffusion splitting* technique which treats the convective and diffusive parts independently, hence using different appropriate numerical schemes, in terms of both accuracy and efficiency, for the solution of each part. The end result is a highly efficient overall flow solver, which also offers prospects for improvement of both parts separately.

In this method, the evolution in time is divided into partial steps of convection and diffusion (Eq. 3.26). Indeed, the solution vector of equation (3.8) at the new time iteration $n + 1$, $\mathbf{Q}^{n+1}$, is obtained by applying to the solution vector at the

preceding time iteration n, $\mathbf{Q}^n$, first the diffusive operator, $\mathbf{O}_d$, over half a time step, then the convective operator, $\mathbf{O}_c$, over a full time step, and finally once more the operator $\mathbf{O}_d$ over half a time step. The procedure is applied in a symmetrical manner so that the second order accuracy of the overall numerical scheme is preserved.

$$\mathbf{Q}^{n+1} = \left[\mathbf{O}_d\left(\frac{\Delta t}{2}\right)\ \mathbf{O}_c\left(\Delta t\right)\ \mathbf{O}_d\left(\frac{\Delta t}{2}\right)\right]\mathbf{Q}^n \tag{3.26}$$

- $\mathbf{O}_c$ is the convective operator,
- $\mathbf{O}_d$ is the diffusive operator.

The above operators are formulated from the *convection-diffusion splitting* of equation (3.8) which results in the following two equations:

$$\frac{\partial \mathbf{Q}}{\partial t} + \frac{\partial \mathbf{F}^c}{\partial x} + \frac{\partial \mathbf{G}^c}{\partial r} = \mathbf{S}^c \tag{3.27}$$

$$\frac{\partial \mathbf{Q}}{\partial t} - \frac{\partial \mathbf{F}^d}{\partial x} - \frac{\partial \mathbf{G}^d}{\partial r} = \mathbf{S}^d \tag{3.28}$$

Euler solver

The convective equation (Eq. 3.27) is again solved by operator splitting into a sequence of 'one dimensional passes' in which the equation is solved in the two 'quasi-normal' directions of the mesh, ξ and η, the *body-tangent* and *body-normal* respectively. The procedure which allows the update of the solution vector, $\mathbf{Q}$, in both mesh directions, ξ and η, through one time step, Δt, is given by:

$$\mathbf{Q}^{n+1} = \left[\mathbf{O}_\eta\left(\frac{\Delta t}{2}\right)\ \mathbf{O}_\xi\left(\frac{\Delta t}{2}\right)\ \mathbf{O}_s\left(\Delta t\right)\ \mathbf{O}_\xi\left(\frac{\Delta t}{2}\right)\ \mathbf{O}_\eta\left(\frac{\Delta t}{2}\right)\right]\mathbf{Q}^n \tag{3.29}$$

- $\mathbf{O}_\eta$ is the operator which advances in the *body-normal* direction,
- $\mathbf{O}_\xi$ is the operator which advances in the *body-tangent* direction,
- $\mathbf{O}_s$ is the operator which advances the source term.

The above operators are determined using an explicit second order accurate method developed by Hillier[33] and based on the *Generalised Riemann Problem* proposed by Ben-Artzi.[8] This method uses a second order discretisation in space, which implies a piecewise-linear interpolation of flow variables across a cell using the fluxes at cell interfaces.

Viscous solver

In the diffusive equation (Eq. 3.28), the mass conservation equation is reduced to a constant density through the partial viscous time step, and thus the solution is required only for the momentum and energy equations. Using the *thin shear-layer* approximation, these two equations can be decoupled and solved separately. The resolution of the x and r-momentum equations generates the new velocities, which are then used to solve the energy equation. The equations are solved implicitly in time using a centred differencing discretisation in space.

Turbulence modelling

Although there has been no fully turbulent simulations carried out in the present study, in the chapters to come the experimental data have been compared to results obtained from the fully turbulent CFD computations performed by Hillier.[35] His calculations used the one-equation variant of the $k-\epsilon$ eddy-viscosity model proposed by Menter[65] to provide closure to the time-averaged Reynolds stress equations. In this case, the compressibility effects are taken into account using the compressibility corrections due to Wilcox.[104] In the eddy-viscosity approach, the terms of eddy viscosity, μ_T, and turbulent heat flux, q_{T_j}, are added directly to their laminar counterparts in the Navier-Stokes equations (Eqs. 3.9 to 3.13), which are then solved in the same manner as described previously.

Heat Flux:

$$q_j = q_{L_j} + q_{T_j} = -\left(\frac{\mu c_p}{Pr} + \frac{\mu_T c_p}{Pr_T}\right)\frac{\partial \bar{T}}{\partial x_j} \tag{3.30}$$

where the subscripts $_L$ and $_T$ refer to laminar and turbulent respectively, $\bar{T}$ is the Reynolds-averaged static temperature, and Pr_T is the turbulent Prandtl number which is set equal to 0.9 in the present study.

Viscous Stresses: The total viscosity coefficient, $\tilde{\mu}$, is expressed as the sum of molecular and eddy viscosities:

$$\tilde{\mu} = \mu + \mu_T \tag{3.31}$$

The transformation from a two-equation $k - \epsilon$ eddy-viscosity model to a one-equation model is based on Bradshaw's assumption that the turbulent shear stress is proportional to the specific (i.e., per unit mass) turbulence kinetic energy k. In the standard $k - \epsilon$ model, this is equivalent to:[65]

$$Production_k = Dissipation_k$$

The second assumption is that the diffusion coefficients in the turbulence kinetic energy and dissipation rate equations, σ_k and σ_ϵ, are the same:[65]

$$\sigma_k = \sigma_\epsilon = \sigma$$

3.1.3 Mesh generation

Initial mesh

A structured mesh is constructed around the body after specification of the number of grid points used in both *body-tangent* and *body-normal* directions, i and j, respectively. The mesh outer boundary is estimated from experiments in order to optimise the capture of the shock wave and minimise the number of j-cells used in the freestream. In the i direction, the cells are uniformly distributed around the hemi-spherical nose then constantly stretched downstream using a constant stretching factor. In the j direction however, the cells are clustered right from the wall boundary towards the outer domain. Several mesh configurations are used, in terms of cell number around the nose, stretching factors in both the i and j directions, and

the extent of the outer domain, in order to acquire the best possible computational solution.

Mesh reform

After a first converged solution is obtained, a new mesh is constructed with maximum clustering around the shock wave location and across the boundary layer near the wall. The number of cells in the j direction across the boundary and shock layers is kept constant along the body-tangent direction i, allowing better capture of the shock and boundary layer streamwise growth. The mesh reform procedure is performed for better resolution of the inviscid region (particularly around the nose region whereby high flow gradients take place across the shock) and the viscous region for improved flow property profiles at the wall.

3.1.4 Boundary and initial conditions

Boundary conditions

No-slip and *isothermal* wall conditions are set at the body surface (i.e., $u_w = v_w = 0$, $T_w = 298\ K$) and *symmetry* condition is set along the stagnation line (i.e., $\partial/\partial r = 0$). The remaining boundary conditions are set to *in-flow* and *out-flow* as appropriate.

Initial conditions

The flowfield is initiated with both *uniform* and real *tunnel-gradient* freestream conditions as follows:

- **Uniform freestream**

  This is summarised in table 3.1. $M_\infty = 8.8$ is taken as an approximate average of the actual value which varies along the axis of the tunnel test section.

M_∞	T_{0_∞} (K)	p_{0_∞} (Pa)	T_∞ (K)	p_∞ (Pa)	U_∞ (m/s)	ρ_∞ (kg/m^3)	e_∞ (J/m^3)
8.8	1150	60×10^6	69.75	3296.58	1491.03	0.16	8241.44

Table 3.1: Uniform freestream conditions implemented in the laminar CFD simulations.

- **Real tunnel-gradient freestream** This consists of a freestream with an axial gradient along the tunnel test section,[56] defined as a 2.7% per metre increase in Mach number and a 19% per metre decrease in static pressure.

3.1.5 Solution procedure and convergence process

As described in section 3.1.2, the flowfield is obtained by time marching the solution vector until the convergence condition is verified. The blunt-body hypersonic flow problem is of elliptic and hyperbolic nature at the same time. Elliptic in the subsonic region around the hemi-spherical nose and hyperbolic downstream in the supersonic region. In the former, the solution is dependent upon the whole computational domain as information propagate in all directions. In the latter however, there is a weak upstream influence only within the boundary layer and information is mainly propagated downstream. Therefore, the computation is first restricted to the block of cells containing mainly the subsonic region such that the downstream end of this block is supersonic. Once converged, the computation is continued in a new block, with a supersonic upstream end, with one or more cells overlap between the downstream end of the first block and the upstream end of the new block. The procedure is then repeated until the whole computational domain is converged. This technique is known as *block marching* and allows efficient resolution of the flow, not only because the computation is no longer performed in the already converged first block, but also due to the fact that the computation is marched at larger time steps controlled by the local minimum cell size in the block in question rather than the smallest cell size in the whole computational domain.

3.2 Laminar flow computational simulation

This section describes the laminar CFD results obtained using the methodology described previously. The results are presented in terms of contour plots, surface data, and boundary layer profiles and edge conditions. Three various levels of mesh resolution, namely coarse (250×60), fine (500×120), and ultra-fine (800×320) (the latter being provided by Hillier[35]) were used in the computations to demonstrate the mesh independency of the solution acquired. The results shown below are those obtained using the fine mesh, considered to be mesh-independent as will be discussed in more details in section 3.2.5 (i.e., grid dependency analysis).

3.2.1 Mesh configuration and flow properties contours

Figure 3.1(a) illustrates the mesh around the model using 500 and 120 cells in the i and j directions, the *body-tangent* and *body-normal* directions respectively. This mesh included 90 cells around the nose, uniform in the i-direction along with the subsequent 110 downstream cells. Downstream of $i > 200$, the cells are stretched continuously using a constant stretching factor ($\omega_n > 1$). This approach was used to make sure that the first block of computation, containing the subsonic region with a supersonic downstream end, uses the finest possible local mesh resolution. Figure 3.2(a) shows a close view of the mesh configuration in the nose region. In the j-direction however, the mesh is clustered across the boundary layer and around the bow shock wave location, both determined from a first converged solution using a 'good trial' mesh. The mesh is then reconstructed in a way that the shock wave and boundary layer edge are aligned with pre-set i-mesh lines across the entire wetted length of the body. The final computation is then performed using the interpolated flowfield distribution of the first converged solution as the new initial condition.

The most important feature of hypersonic blunt body flows is the existence of the vorticity or 'entropy' layer which spreads across a significant portion of the body length, in this case, the entire length. Figure 3.1(b) presents contours of

relative entropy increase with respect to the freestream. The drastic variation in flow properties across the 'high-angled' portion of the bow shock around the nose region flows downstream to form the entropy layer, which is of significant thickness as a result of the high freestream Mach number. At the furthest downstream distance, the entropy layer appears to remain much thicker than the boundary layer, shown in red in figure 3.1(b), thus far from being swallowed by it.

Figure 3.2 illustrates a close view of the flowfield within the nose region up to an axial distance $x = 2R$ (R being the nose radius). Figure 3.2(b) reveals smooth constant density lines around the stagnation point and further downstream demonstrating the efficiency of the solution obtained. The shock wave lies at a distance of 115 cells from the body surface. The sonic line ($M = 1$), limiting the subsonic region within the inviscid flow, is found to be located within the hemi-spherical nose region (figure 3.2(c)).

3.2.2 Flow properties surface distributions

One of the main reasons for using a blended blunt cylinder in transition experimentation is the presence of a continuous favourable pressure gradient along the whole body length as shown in figure 3.3. This figure shows the variation of density, static pressure, and heat transfer with wetted distance, S, along the surface of the body. The over expansion of the flow across the nose followed by the presence of an adverse pressure gradient, witnessed in blunt cone flows such as the work of Zanchetta,[112] are disposed of by incorporating the blending region. The respective values of density, static pressure, and heat transfer are highest at the stagnation point then decrease with wetted distance as a result of flow expansion over the curved surfaces of the model forebody (figure 3.3(a), (b), and (c)). The rate of decrease is strongest across the nose, reduces along the blending zone, then asymptotically approaches zero in the afterbody region.

3.2.3 Shock and boundary layers profiles

Figures 3.4 to 3.7 present shock layer and boundary layer profiles in the direction normal to the body surface at $x = 500\ mm$, a location around the downstream end of the heat transfer measurement interval. The abscissa represents various flow properties normalised by their freestream values, whereas the ordinate, y_w/R, represents the normal distance from the wall, y_w, normalised by the nose radius R. The shock is located at a distance, y_s, of approximately $5.1R$ at this axial position, right outside the domain shown in figures 3.4 and 3.5.

Because of the curved bow shock wave and boundary layer, flow properties such as the total pressure vary continuously from the body surface to the shock wave. Figures 3.4 to 3.7 (for the location of $x = 500$ mm) show a very rapid variation from the body surface ($y_w = 0$) to the position of approximately $y_w = 0.15R$; this is the boundary layer. Outboard of this the properties continue to change, though at a reduced rate. This is pure entropy layer effect, and inviscid effect associated with the curvature of the bow shock. Although the entropy layer is referred to as a 'layer', it really occupies the complete space from the boundary layer up to the shock wave. Due to the presence of this entropy layer therefore, flow properties do not recover to uniform values at the edge of the boundary layer (figures 3.4 and 3.5) and thus the common definition of total velocity recovery can no longer hold. Instead, since the total temperature must recover to the freestream value outside the viscous layer (as demonstrated in figures 3.4 and 3.6), the edge is defined as the location, y_e, where $(T_0 - T_w)$ is recovered to 99.5% of $(T_{0_\infty} - T_w)$.

3.2.4 Boundary layer edge conditions

Using the definition of total temperature recovery described above, boundary layer edge conditions were determined and are presented in figures 3.8 and 3.9. The boundary layer displacement and momentum thicknesses, δ_1 and δ_2 respectively, are determined as follows:[110]

$$\delta_1 + \frac{{\delta_1}^2}{d} = \int_0^{\delta} \left(1 - \frac{\rho u}{\rho_e U_e}\right)\left(1 + \frac{2y_w}{d}\right) dy_w \tag{3.32}$$

$$\delta_2 + \frac{{\delta_2}^2}{d} = \int_0^{\delta} \frac{\rho u}{\rho_e U_e}\left(1 - \frac{u}{U_e}\right)\left(1 + \frac{2y_w}{d}\right) dy_w \tag{3.33}$$

The result is shown in figure 3.8(a) along with boundary layer thickness, δ, as a function of wetted distance, S, along the body surface. The 'adjustment' for axisymmetry in equations 3.32 and 3.33, represented by the extra terms $({\delta_1}^2/d)$, $({\delta_2}^2/d)$, and $(1 + 2y_w/d)$ compared with the 2D case, is very small considering the values of displacement and momentum thicknesses obtained. The latter are estimated at about 1.25 mm and 0.33 mm respectively at $x = 500\ mm$ compared to the model afterbody diameter, d, of 74.75 mm. At $x = 500\ mm$, the boundary layer edge-to-freestream ratio of unit Reynolds number, Mach number, velocity, and total pressure are estimated at 5.58% ($Re_e = 2.73\ million/metre$), 42.4% ($M_e = 3.73$), 88.3%, and 0.58% respectively. The latter hardly changes across the entire length of the model (figure 3.9(c)), demonstrating that the boundary layer edge conditions are essentially governed by the streamlines passing through the normal portion of the bow shock around the stagnation line. It also indicates that the total pressure is far from recovering to the sharp-body value, thus the entropy layer is far from being swallowed by the boundary layer at these axial locations.

3.2.5 Mesh dependency analysis

The laminar CFD solution was obtained on three different mesh resolutions; coarse (250×60), fine (500), and ultra-fine[35] (800×320) (figure 3.10). This section discusses the dependency of the computational result, as presented in sections 3.2.1 to 3.2.4, on the resolution of the mesh used.

The discrepancy in surface heat transfer—a sensitive indicator of mesh independency and the crucial flow property as far as the experimental results are concerned—

is estimated at about 0.6% variation in the coarse-to-fine refinement and about 0.2% in the fine-to-ultra-fine refinement at the most downstream measurement location $x = 521\ mm$ (figure 3.11). Clearly, at this level of discrepancies, the CFD solution in general and the heat transfer solution in particular are regarded as mesh independent.

The examination of shock layer profiles and boundary layer profiles and edge conditions, shown in figures 3.12 to 3.14 for the three different mesh resolutions, confirms the mesh independency of the solution obtained. Indeed, the maximum discrepancy in flow properties presented in these figures, which display property distributions virtually identical on the 3 mesh configurations, is found to be less than 1% between the coarse and the ultra-fine mesh.

3.2.6 Uniform versus real tunnel freestream

The laminar CFD simulations were carried out using the uniform freestream and the real tunnel freestream with axial gradient. The result in terms of boundary layer edge conditions and surface heat transfer distribution is presented in figures 3.15 and 3.16 respectively. The consideration of the axial flow gradient (2.7% per metre in M_∞) resulted in approximately 5% increase in boundary layer thicknesses, δ, δ_1, and δ_2, at the most downstream measurement location, x, of 521 mm (figure 3.15(a)). It also introduced less than 2% increase in boundary layer edge velocity and Mach number (figure 3.15(b)), and about 5% decrease in unit Reynolds number. Of most importance to the analysis of the experimental heat transfer in the later chapters, the effect of tunnel axial gradient on the computational laminar heat flux was to reduce it by approximately 8% at $x = 521\ mm$ compared with the uniform freestream simulation (figure 3.16).

3.3 Comparison of laminar CFD versus schlieren

Figure 3.17 presents, in exactly the same scale, the laminar CFD density contours in the top half and the experimental schlieren image in the bottom half. The direct comparison of the bow shock wave location obtained from the laminar CFD and experiment shows an excellent agreement with less than 5% discrepancy in terms of normal distance to the wall of the shock wave location. This is verified at a number of stations along the length of the model.

Schlieren was also used for the visualisation of the boundary layer whether it be laminar, fully turbulent (or existence of turbulent wedges), or transitional (existence of individual turbulent spots). Unfortunately, this was not successful, primarily due to the axisymmetric nature of the model—that significantly reduces the schlieren contrast of the *wall/flow* edge compared with a planar configuration—in combination with the very modest thickness of the boundary layer, the negligible difference between the wall and boundary layer edge density values as a result of the entropy layer effect (as seen in section 3.2.3), and the low flowfield density (particularly within turbulent spots and wedges) which decreases the optical sensitivity. Furthermore, the high level of background noise and freestream turbulence (figure 3.17), produced random patterns of pressure change which made the detection of more regular pressure waves that would be generated from the interaction of turbulent spots and wedges with the surrounding laminar flow—as reported by Schneider[83] from the work of Reda[71,72]—virtually impossible.

3.4 Figures

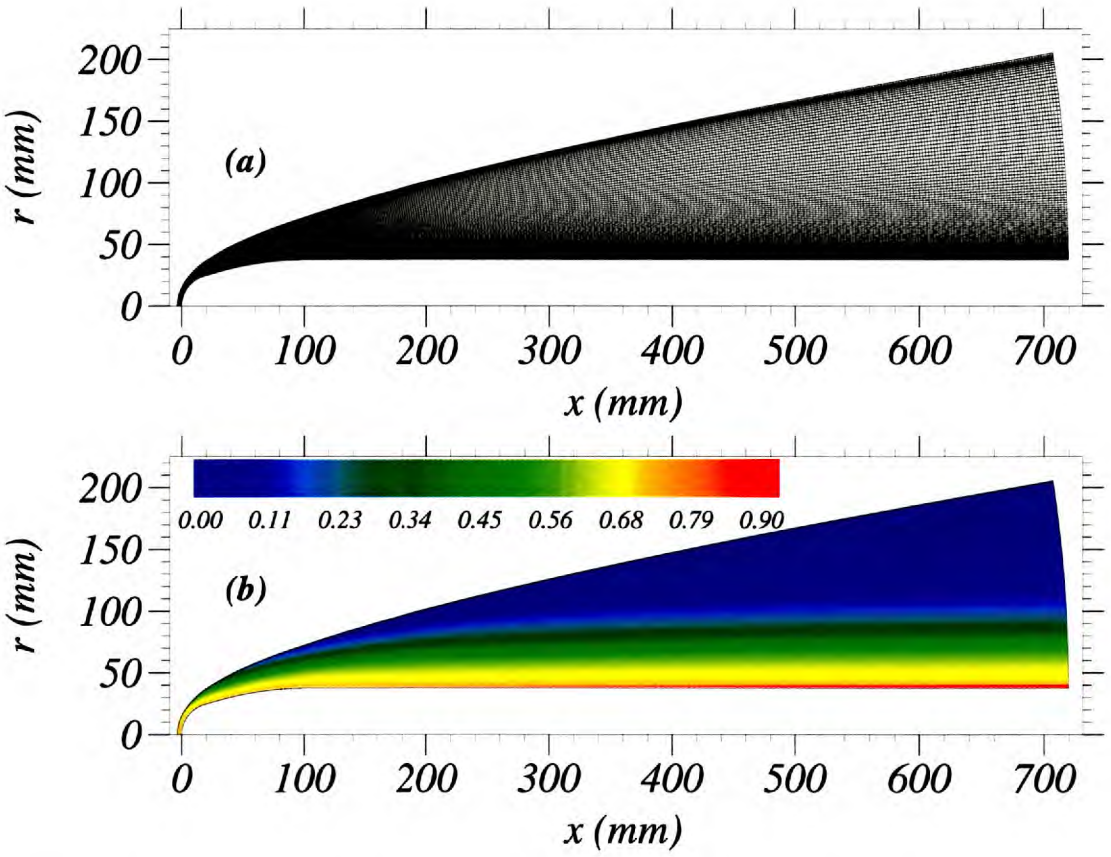

Figure 3.1: (a) mesh configuration, (b) contours of entropy increase $(s - s_\infty)/s_\infty$.

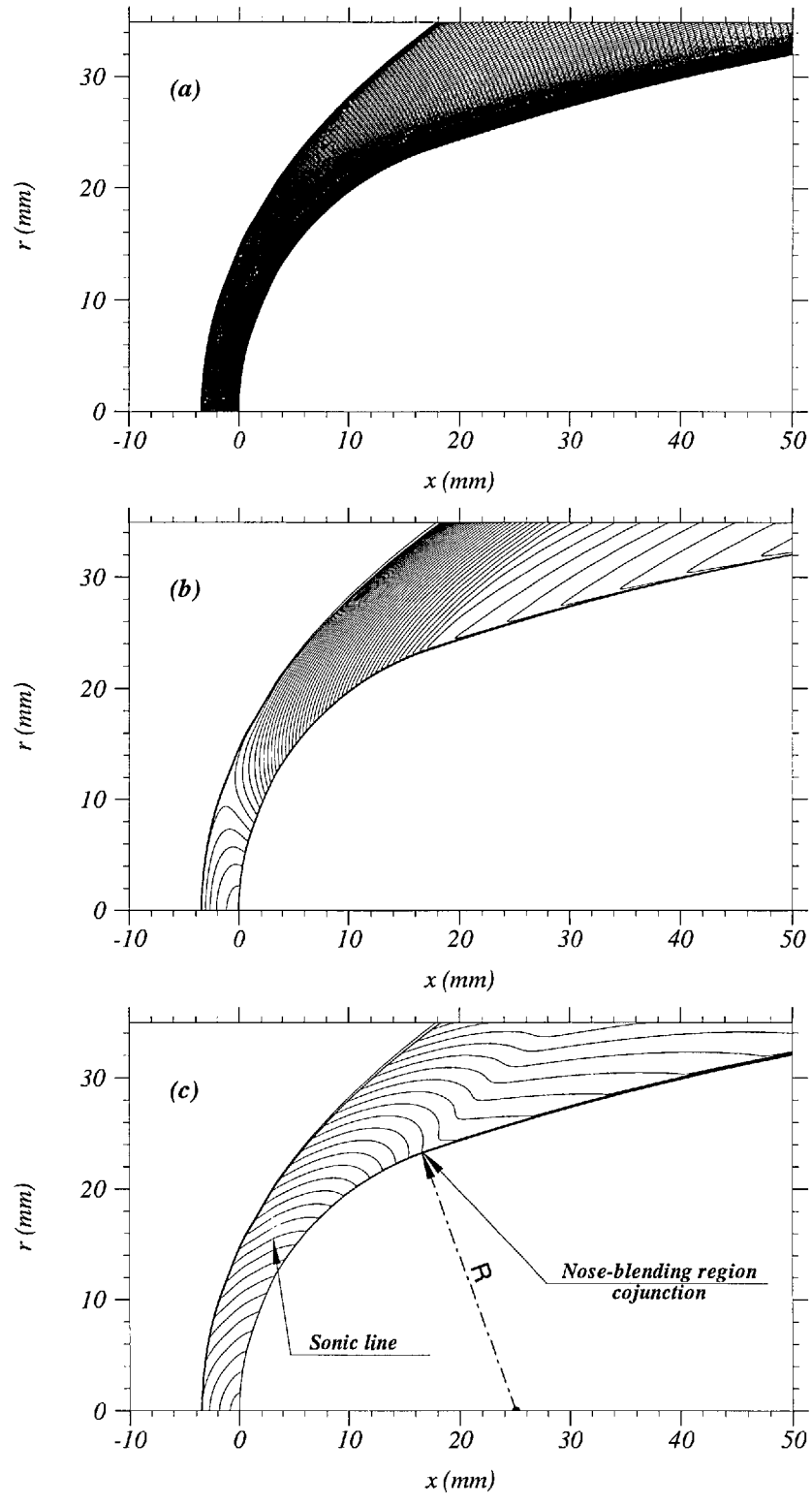

Figure 3.2: Zoom into the nose region; (a) mesh configuration, (b) density contours, (c) Mach number contours.

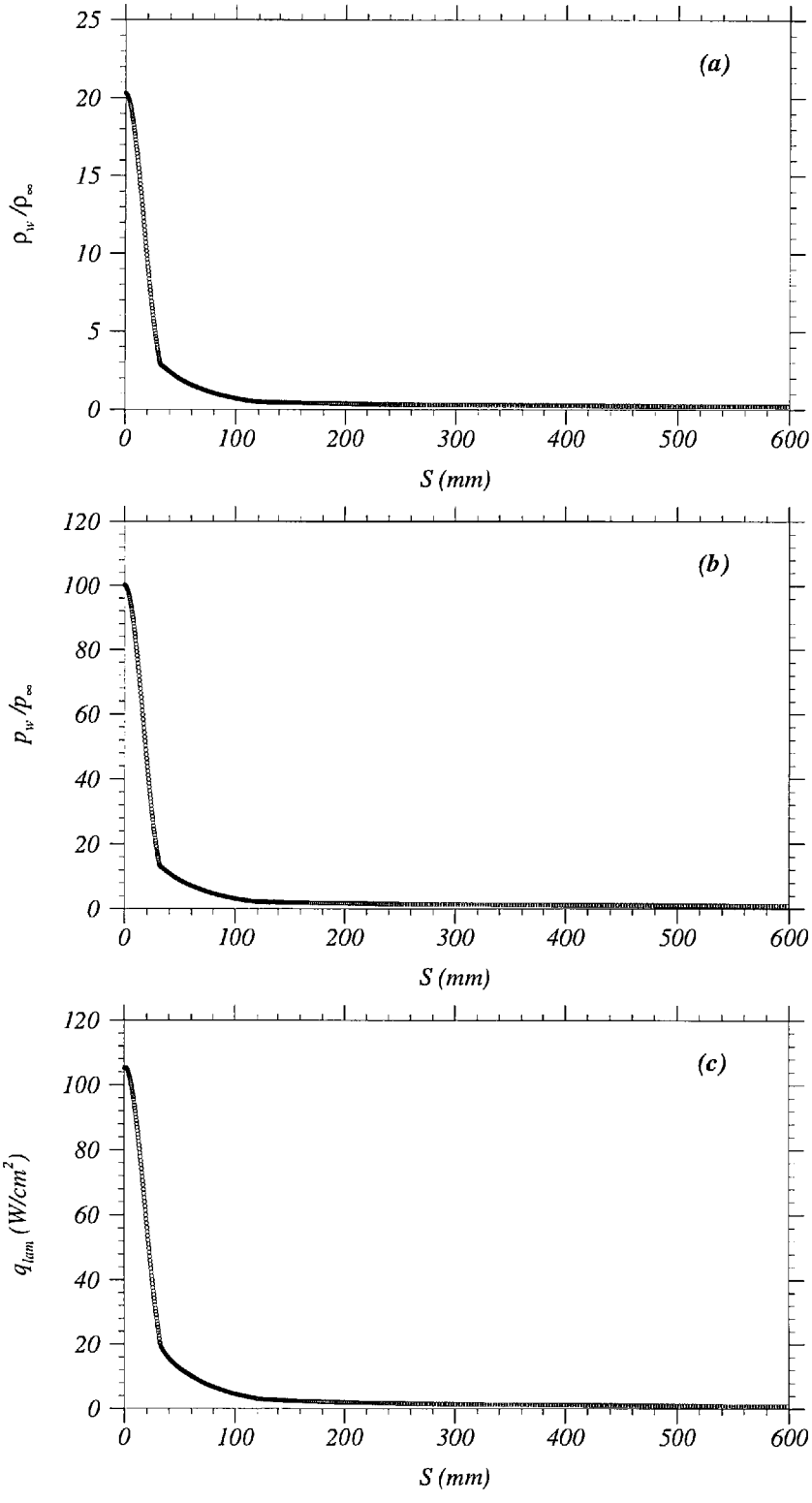

Figure 3.3: Variation of flow properties with wetted distance, S, along the model surface; (a) density, (b) static pressure, (c) heat transfer.

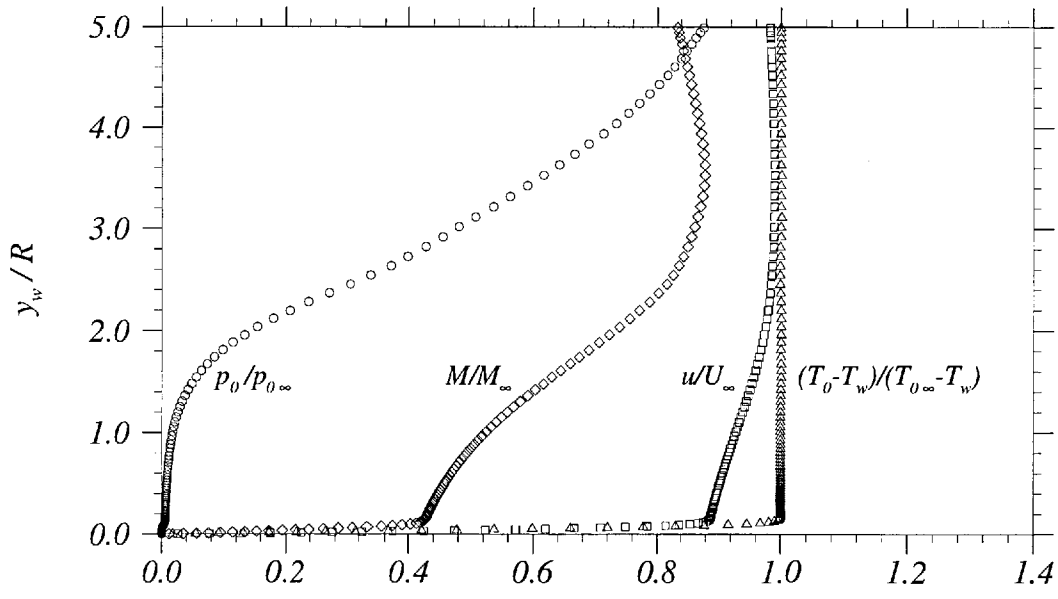

Figure 3.4: Shock layer flow properties profiles in the direction normal to the model surface at $x = 500\ mm$; y_w is the normal distance from the wall and R is the nose radius. ○, $p_0/p_{0\infty}$; ◇, M/M_∞; □, u/U_∞; △, $(T_0 - T_w)/(T_{0\infty} - T_w)$.

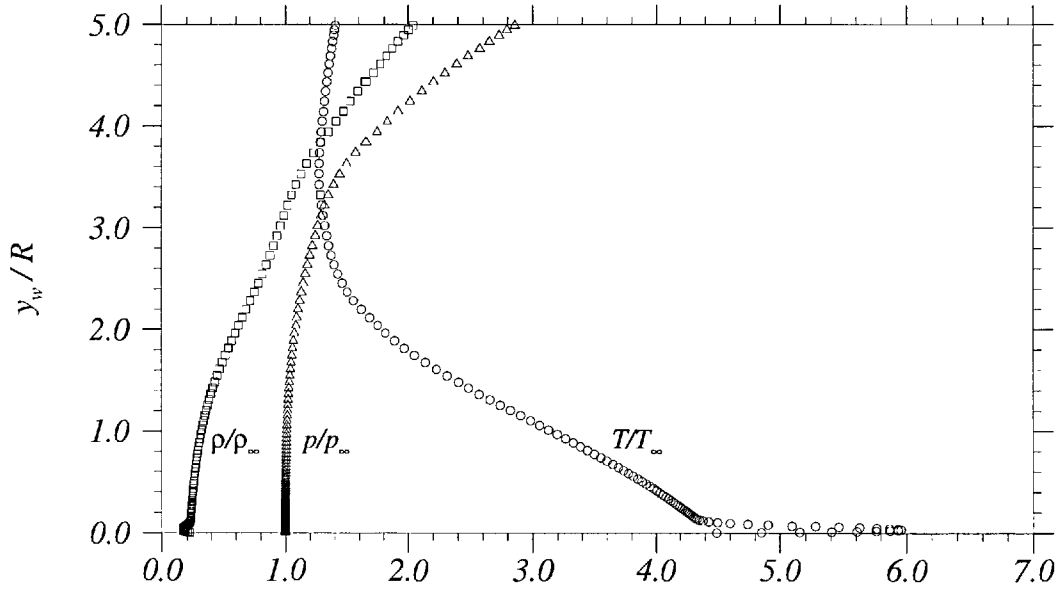

Figure 3.5: Shock layer flow properties profiles in the direction normal to the model surface at $x = 500\ mm$; y_w is the normal distance from the wall and R is the nose radius. ○, T/T_∞; □, ρ/ρ_∞; △, p/p_∞.

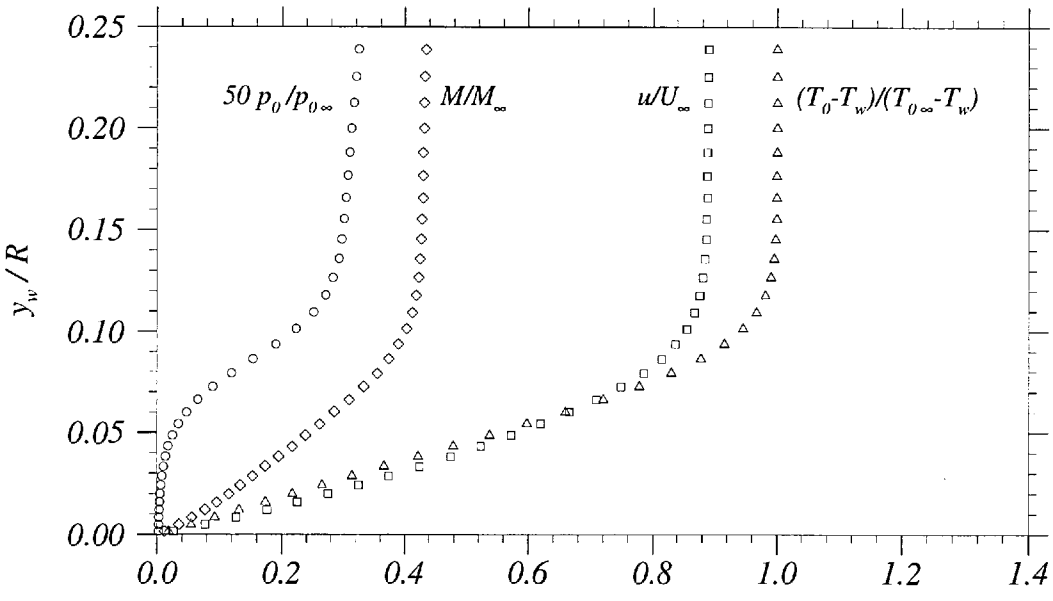

Figure 3.6: Boundary layer flow properties profiles in the direction normal to the model surface at $x = 500\ mm$; y_w is the normal distance from the wall and R is the nose radius. ○, $p_0/p_{0\infty}$; ◇, M/M_∞; □, u/U_∞; △, $(T_0 - T_w)/(T_{0\infty} - T_w)$.

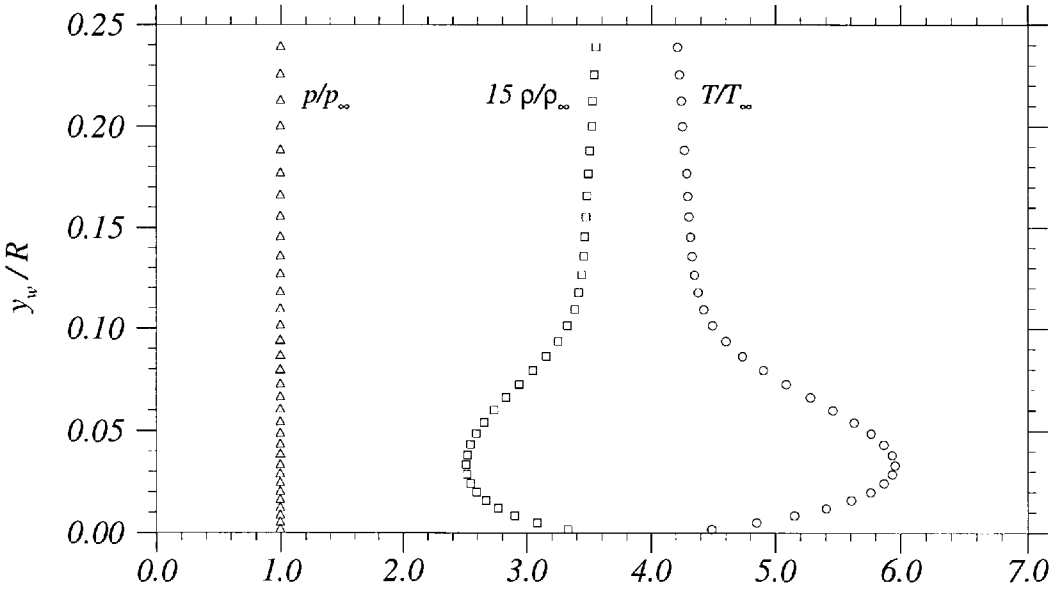

Figure 3.7: Boundary layer flow properties profiles in the direction normal to the model surface at $x = 500\ mm$; y_w is the normal distance from the wall and R is the nose radius. ○, T/T_∞; □, ρ/ρ_∞; △, p/p_∞.

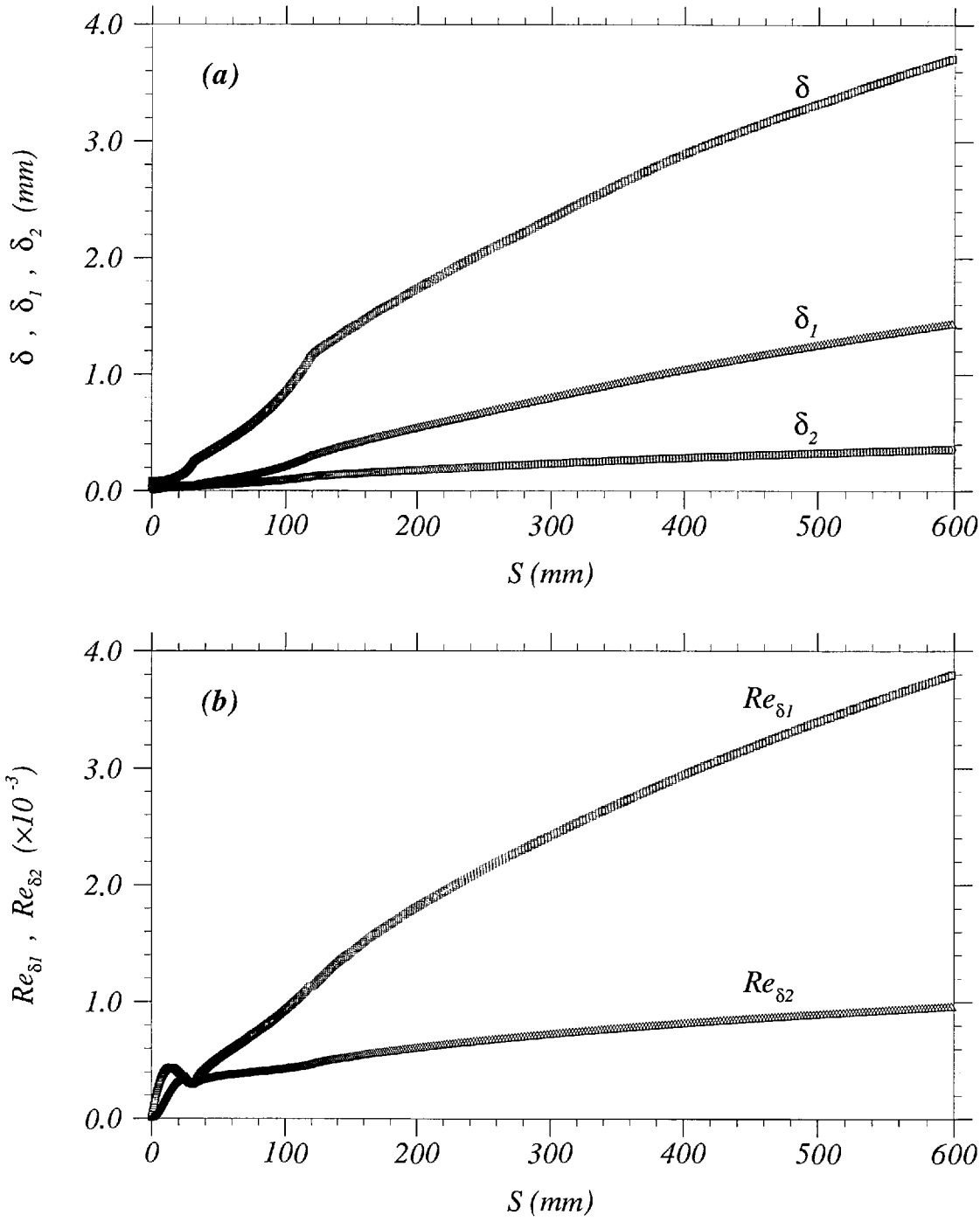

Figure 3.8: Variation of boundary layer edge conditions with wetted distance, S, along the body surface. (a) boundary layer thickness δ, displacement thickness δ_1, and momentum thickness δ_2; (b) Reynolds number based on boundary layer displacement and momentum thicknesses, Re_{δ_1} and Re_{δ_2}, respectively.

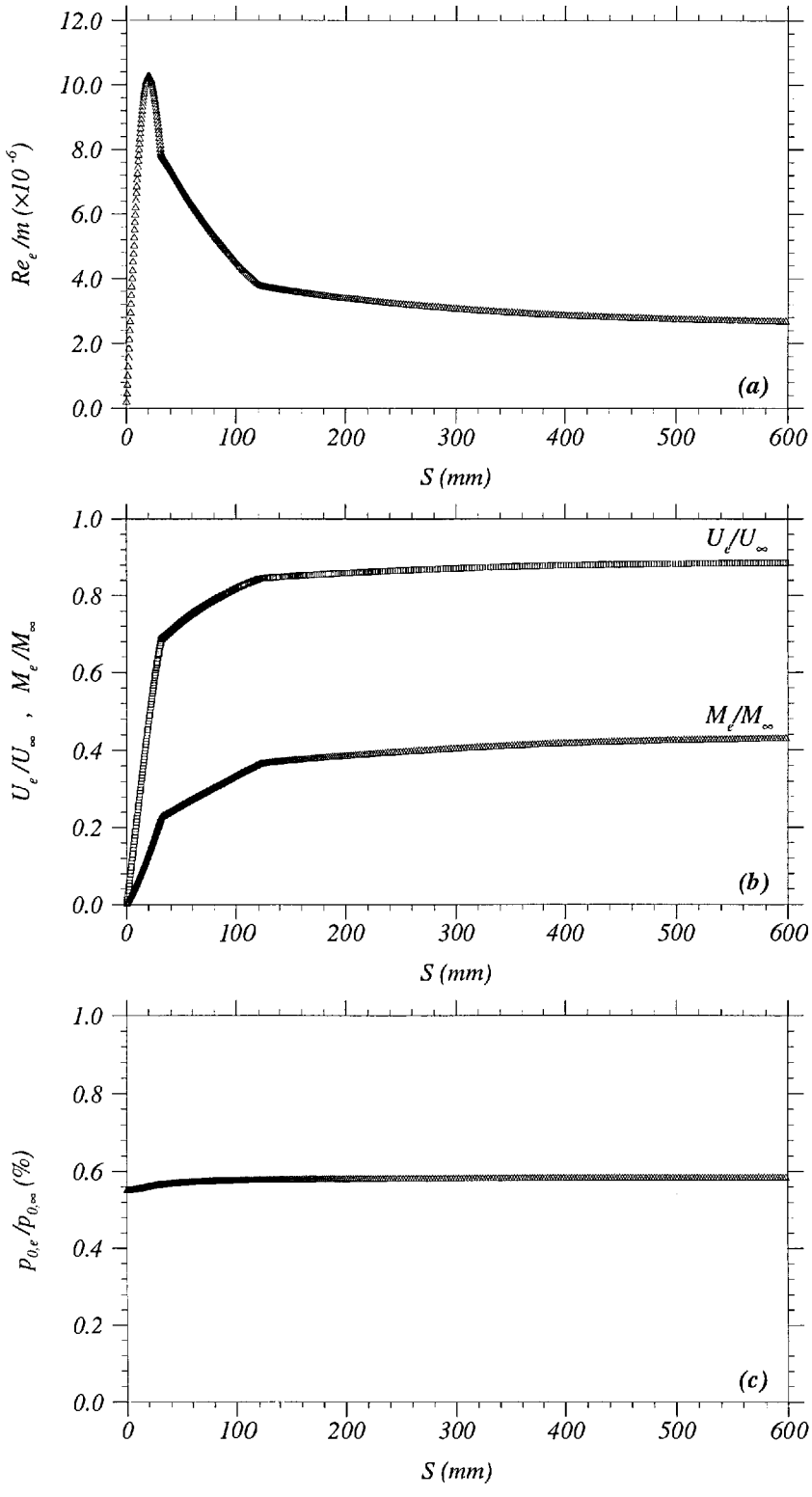

Figure 3.9: Variation of boundary layer edge conditions with wetted distance, S, along the body surface. (a) unit Reynolds number Re_e/m; (b) velocity and Mach number, U_e/U_∞ and M_e/M_∞, respectively; (c) total pressure p_{0_e}/p_{0_∞}.

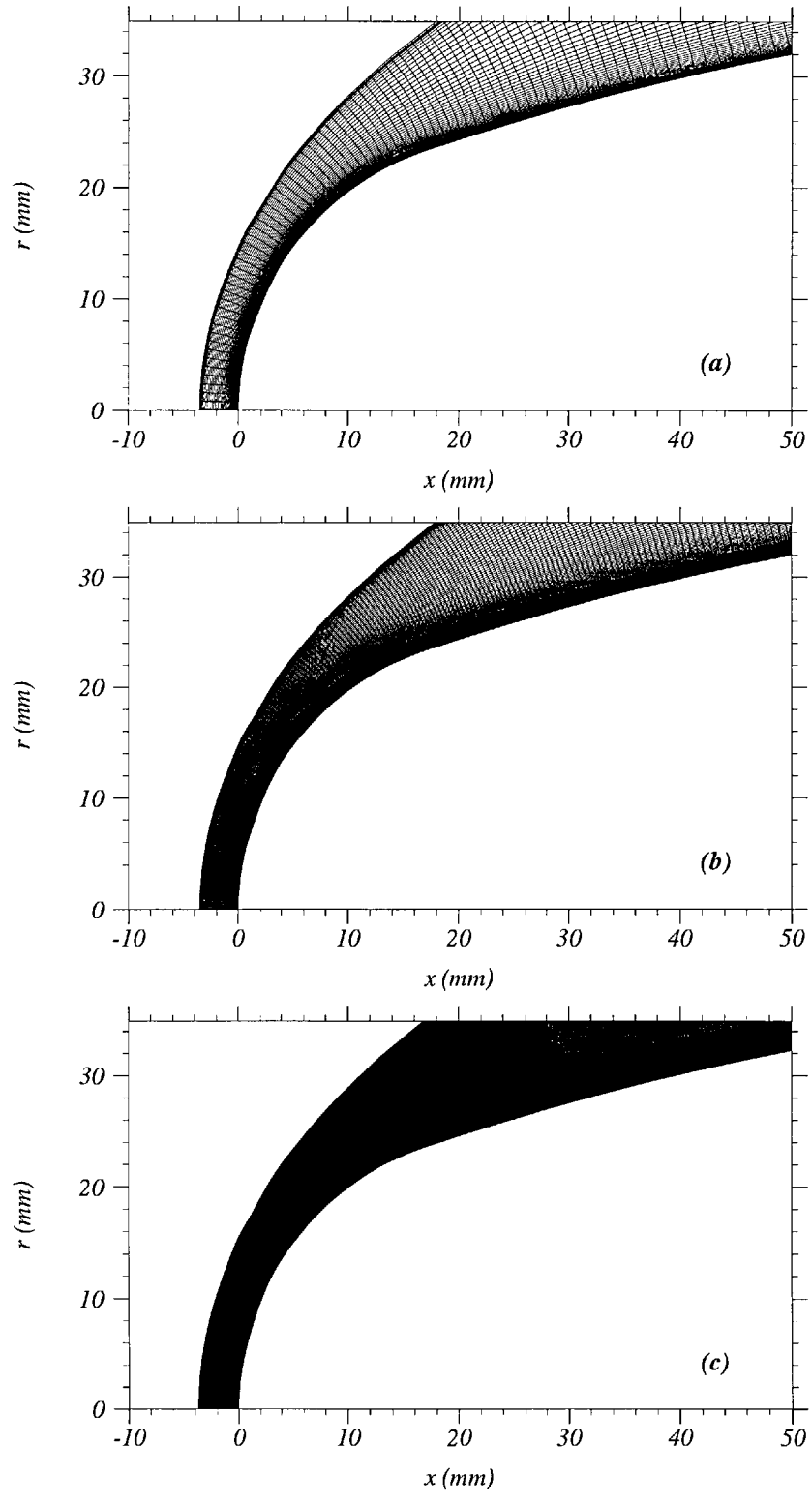

Figure 3.10: Mesh configuration; zoom into the nose region. (a) 250×60, (b) 500×120, (c) 800×320.

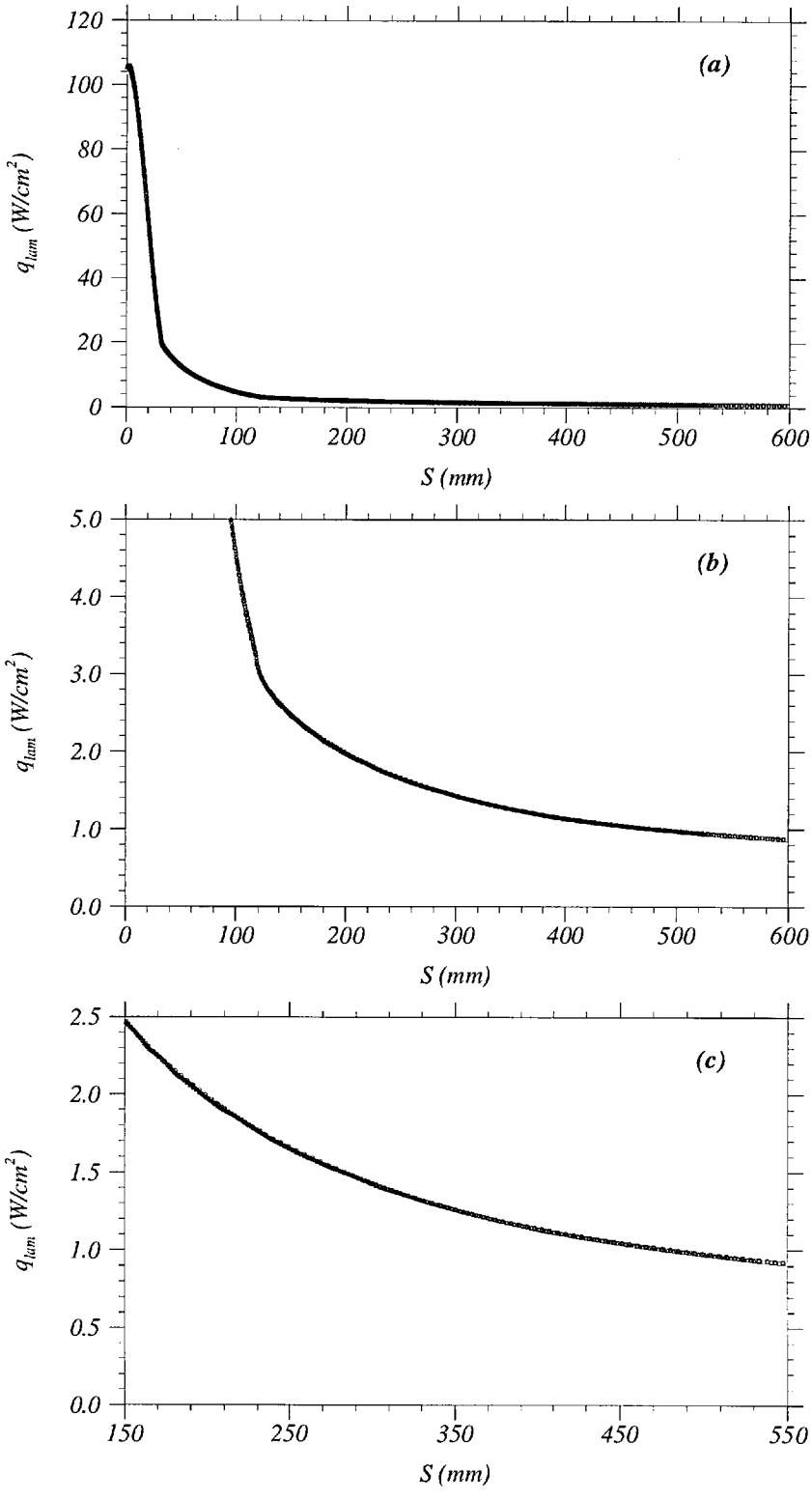

Figure 3.11: Variation of heat transfer with wetted distance, S, along the model surface. ○, 250×60; □, 500×120; △, 800×320.

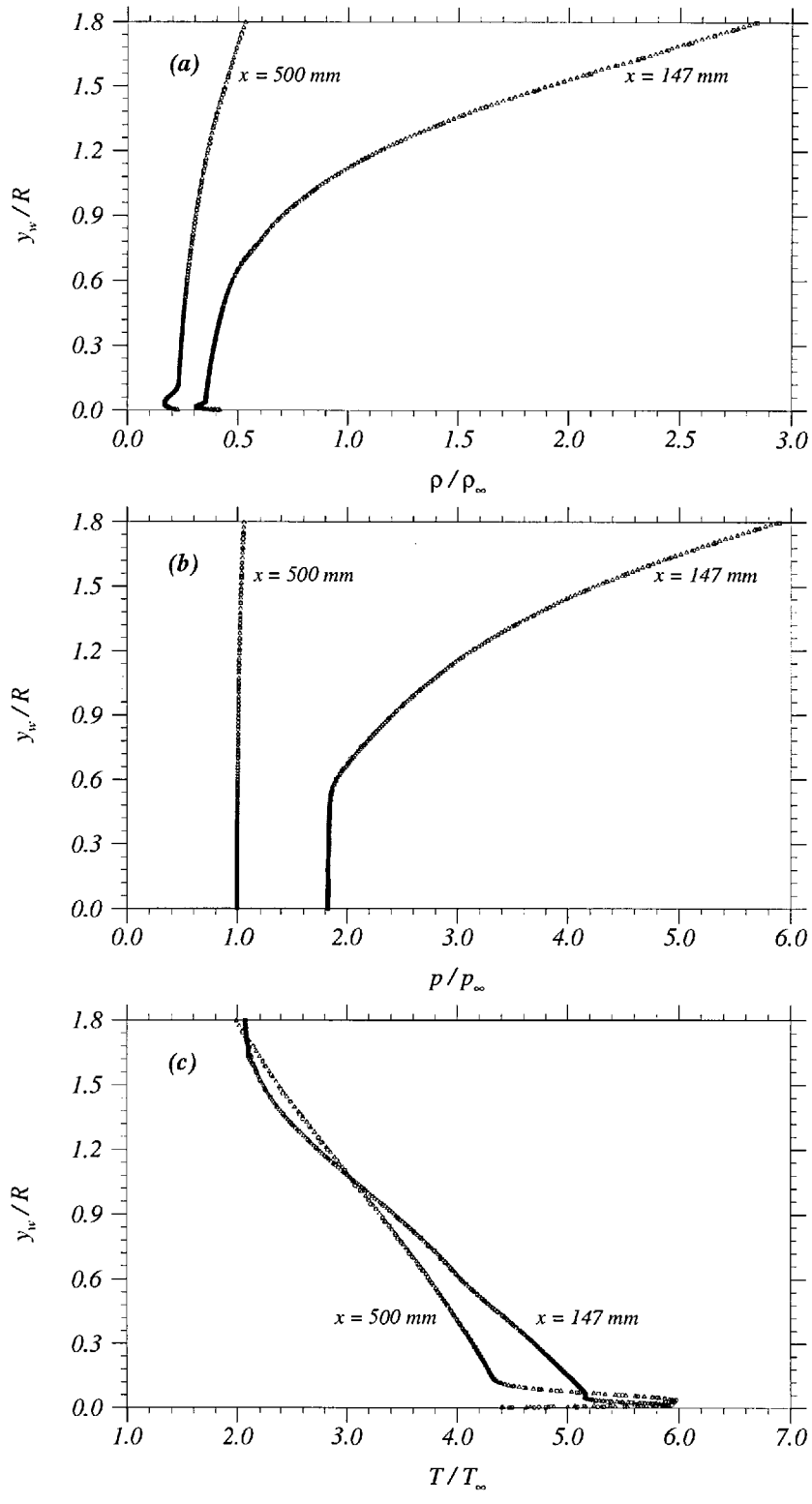

Figure 3.12: Data profiles in the direction normal to the model surface at $x = 147\ mm$ and $x = 500\ mm$; y_w is the normal distance from the wall and R is the nose radius. (a) density, (b) static pressure, (c) static temperature. ○, 250×60; □, 500×120; △, 800×320.

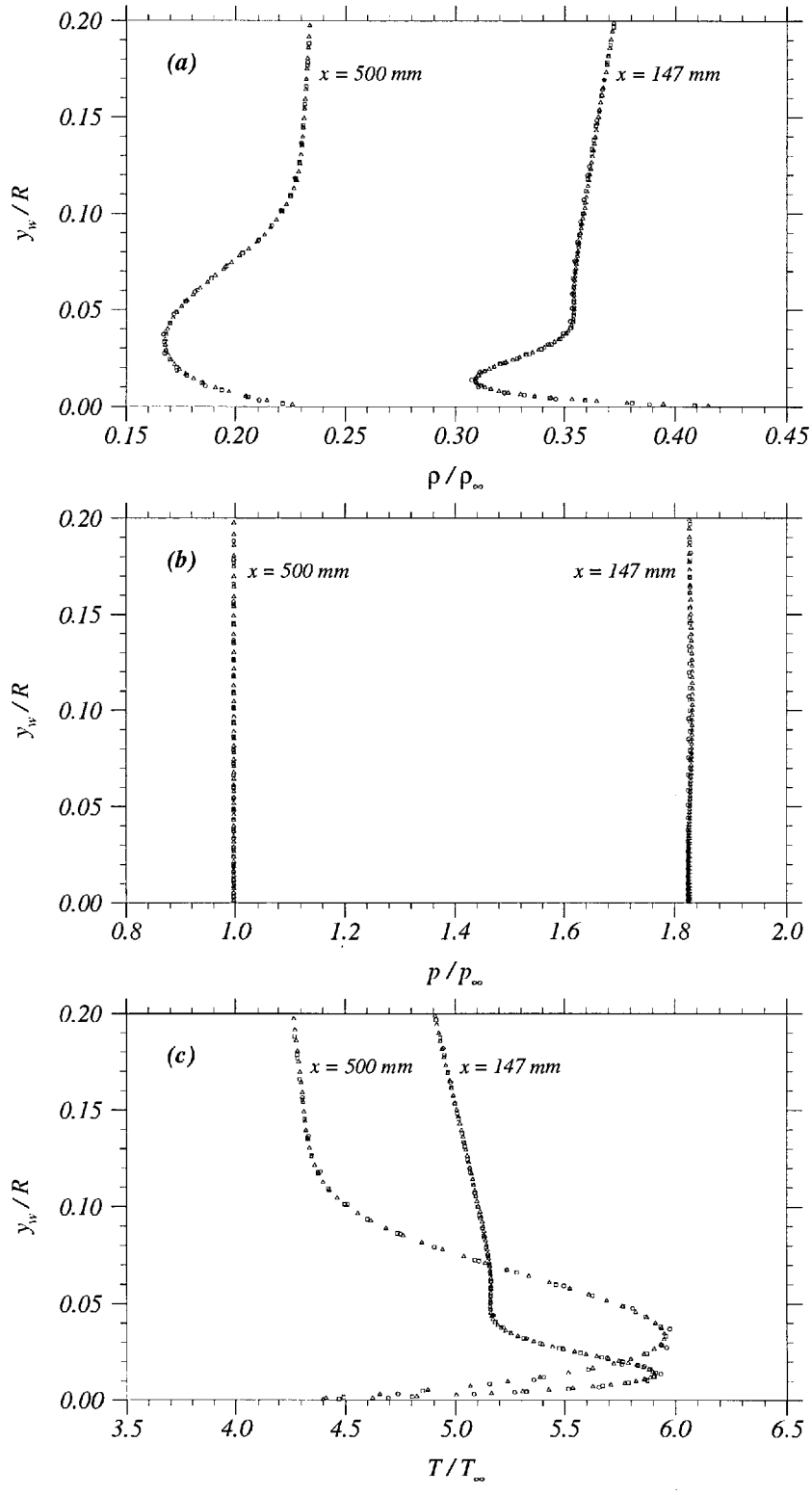

Figure 3.13: Boundary layer profiles in the direction normal to the model surface at $x = 147\ mm$ and $x = 500\ mm$; y_w is the normal distance from the wall and R is the nose radius. (a) density, (b) static pressure, (c) static temperature. ○, 250×60; □, 500×120; △, 800×320.

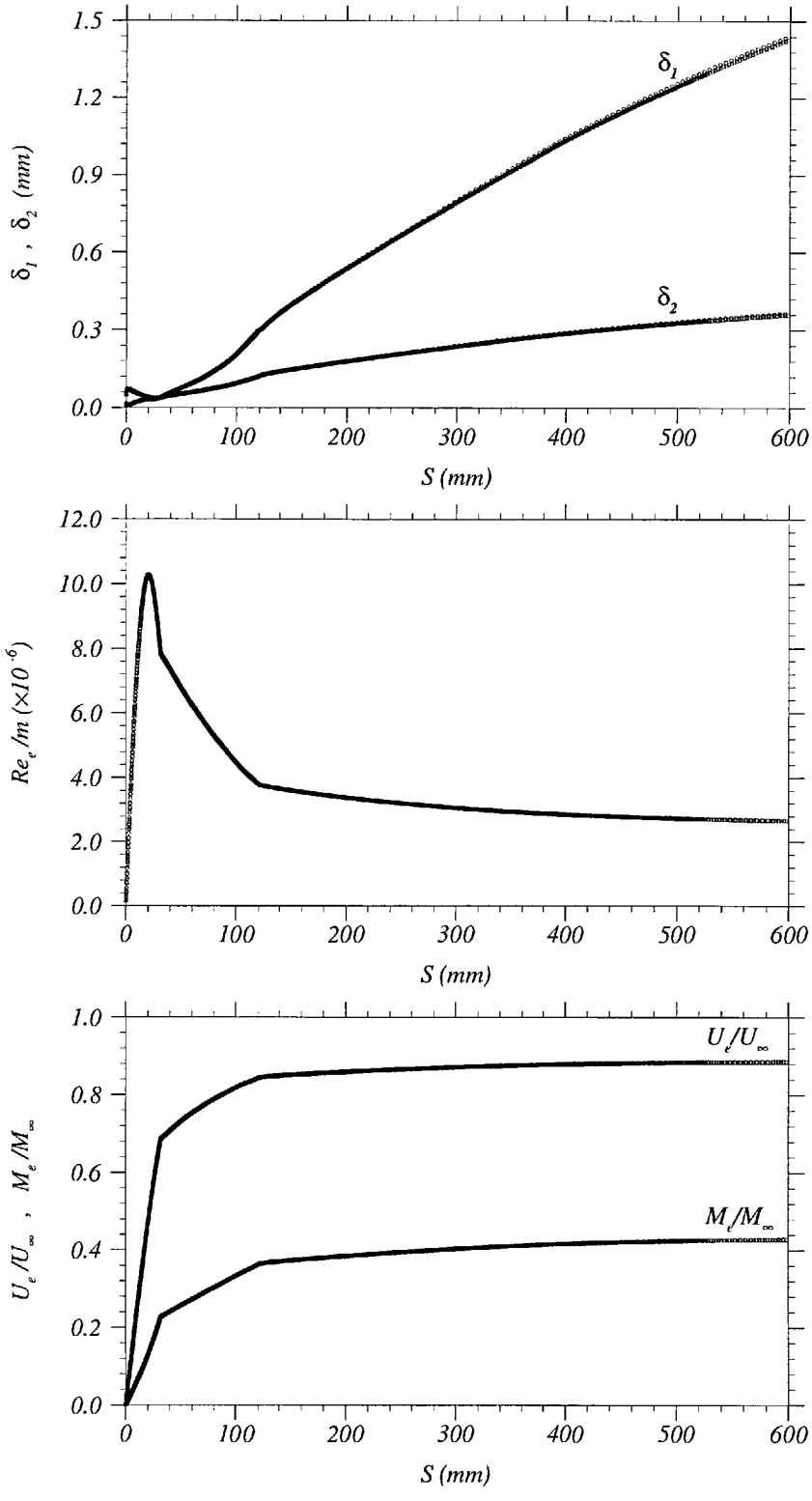

Figure 3.14: Variation of boundary layer edge conditions with wetted distance, S, along the body surface. (a) boundary layer thickness δ, displacement thickness δ_1, and momentum thickness δ_2; (b) unit Reynolds number Re_e/m; (c) velocity and Mach number, U_e/U_∞ and M_e/M_∞, respectively. ○, 250×60; □, 500×120; △, 800×320.

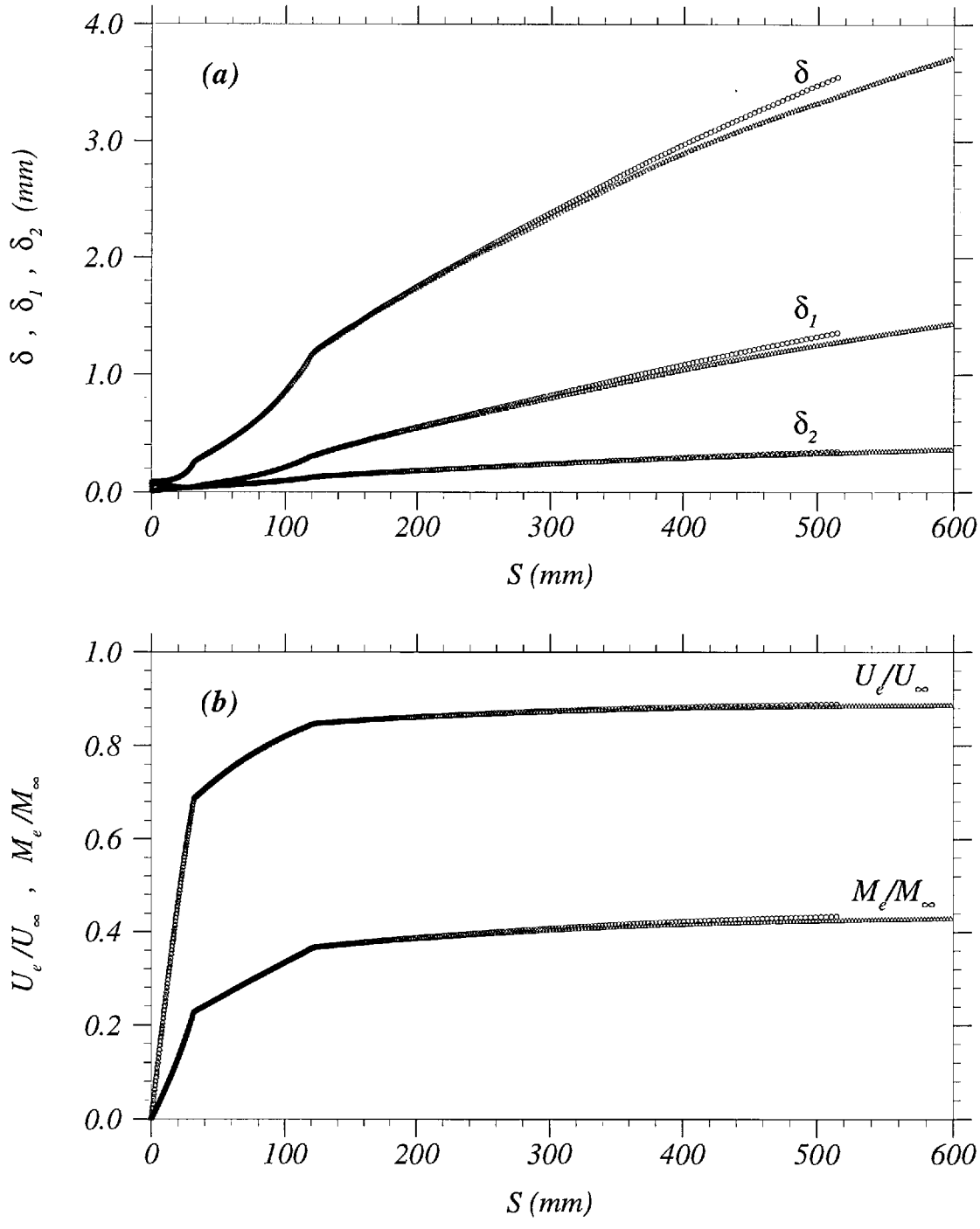

Figure 3.15: Variation of boundary layer edge conditions with wetted distance, S, using the uniform and real tunnel freestreams. (a) boundary layer thickness δ, displacement thickness δ_1, and momentum thickness δ_2; (b) velocity and Mach number, U_e/U_∞ and M_e/M_∞, respectively. $\triangle$, uniform freestream; $\circ$, real tunnel freestream.

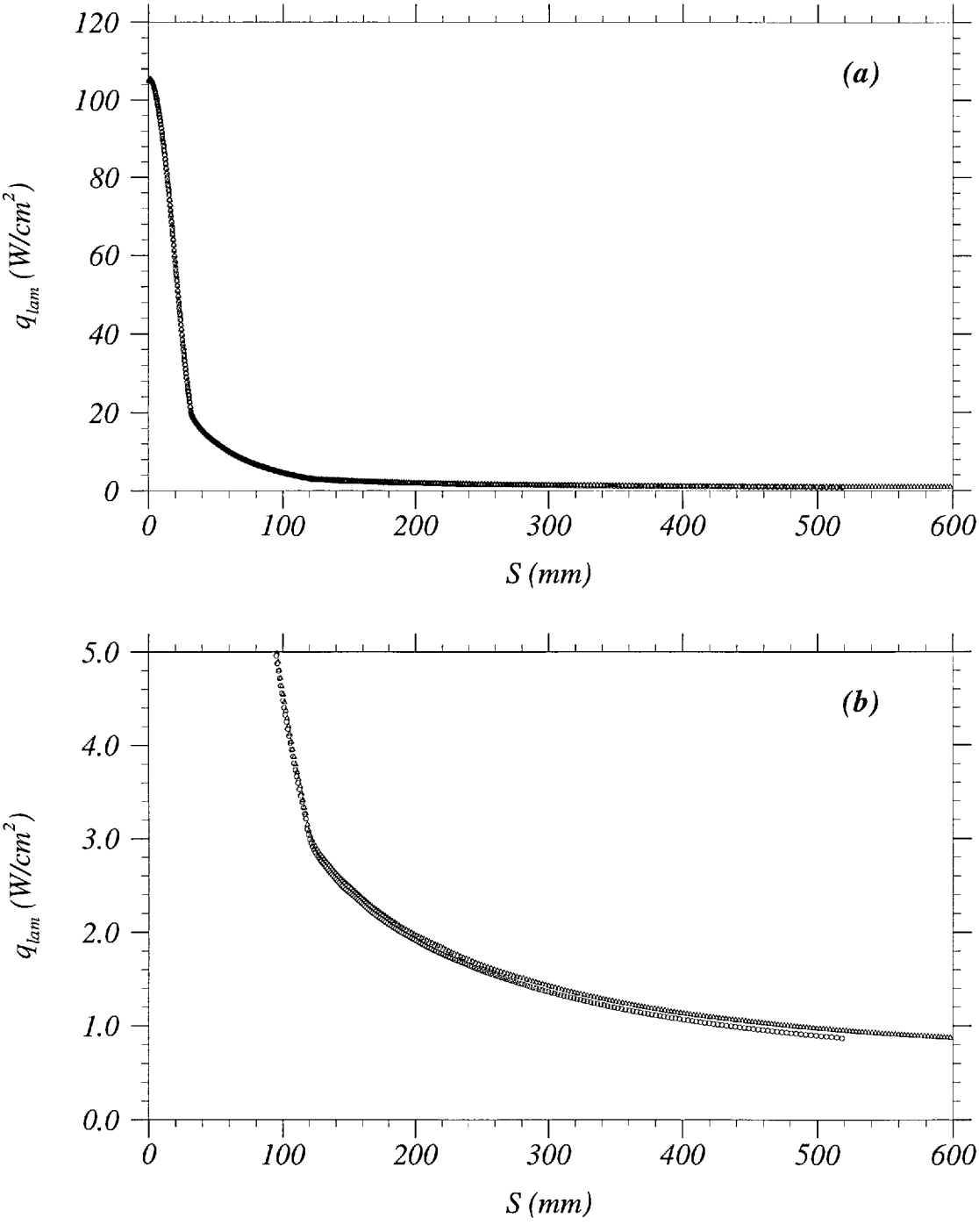

Figure 3.16: Variation of heat transfer with wetted distance, S, along the model surface, using the uniform and real tunnel freestreams. Δ, uniform freestream; $\circ$, real tunnel freestream.

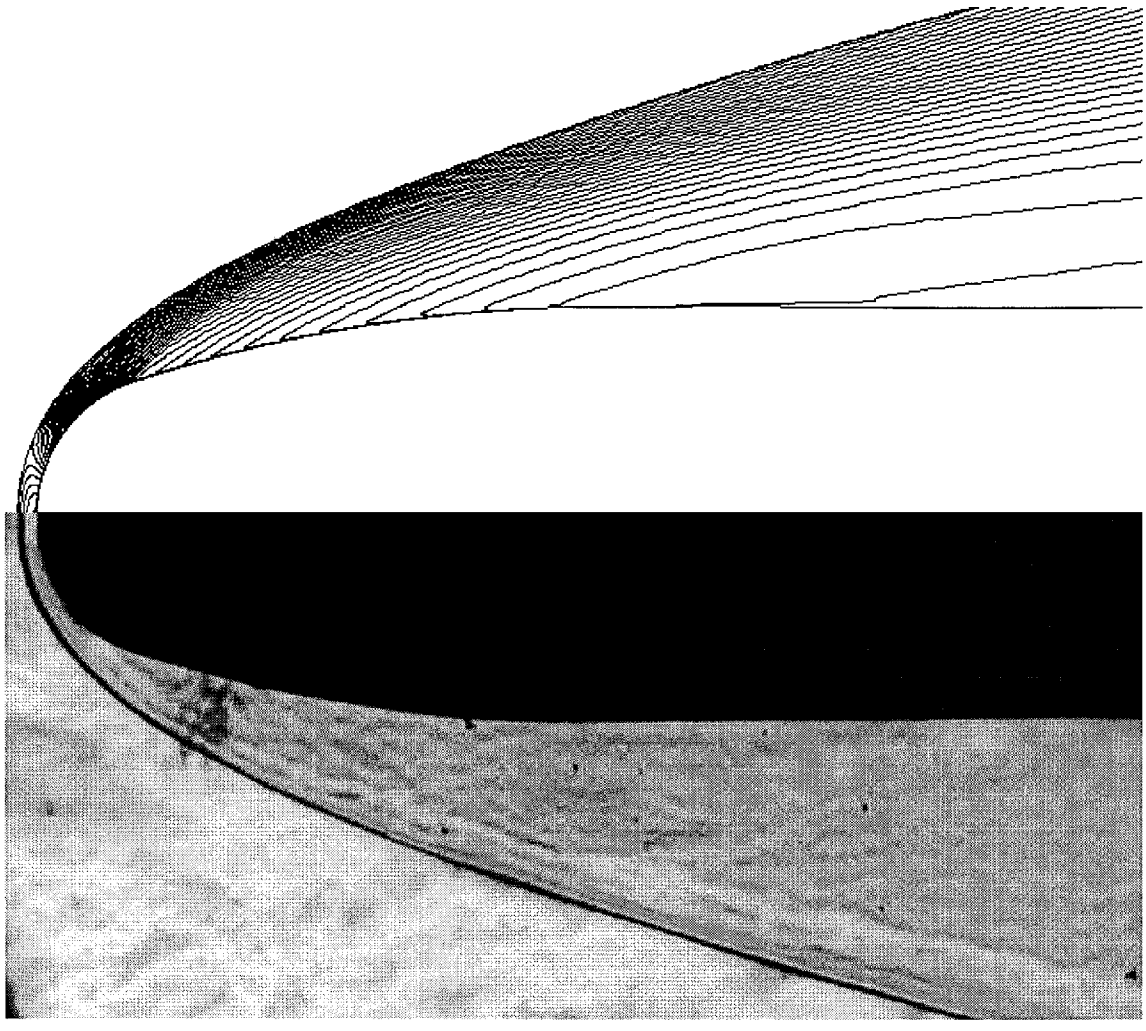

Figure 3.17: Direct comparison of the detached bow shock location obtained from the laminar CFD density contours (top) versus schlieren image (bottom).

Chapter 4

Streamwise Time-Dependent Heat Transfer Database

As described in chapter 2, the axial module allowed heat transfer measurements in the streamwise direction to be made. The emphasis was upon measuring the instantaneous surface heat transfer fluctuations at each gauge location. This was considered as a good method for detecting laminar-turbulent transition, including in particular intermittency variations. Furthermore, it enabled the streamwise description of heat transfer profiles of turbulent events as well as their dynamic characteristics.

4.1 Basic time-dependent data

The data obtained from each experiment is illustrated in terms of temperature rise time-histories of the resistance gauges. The heat transfer is then derived following the algorithm which was described in detail in chapter 2. The signals spread over approximately 20 ms of tunnel running-time, of which only a 6 millisecond window is taken as a steady state freestream. Figure 4.1 illustrates the total pressure, p_{0_∞}, time-history of a typical tunnel run. The steady state interval is located between approximately 9.9 ms and 15.9 ms from the start of the run (t=0 ms).

The steady flow window of 6 ms, obtained from each experiment, is only long enough to provide a 'stationary' data record sample for time-averaged heat transfer

if the flow is fully laminar or fully turbulent. In effect, the 6 ms interval covers flow convection distances of several thousand times the local laminar (or turbulent) boundary layer thicknesses. With intermittent-transitional flows however, the single 6 ms window is not sufficiently long to provide 'stationary' data record sample due to the low turbulent event formation rates, which categorised this set of experiments as attractive in the first place. These low production rates, in particular, allow data acquisition of individual events from single runs which, in turn, provide information on turbulent spot characteristics. Although the 6 ms window represents steady flow, it yet shows some oscillations in the total pressure signal (figure 4.1). These have been found to have no effect as far as the spot formation rate is concerned, as will be discussed in detail later in this chapter.

Typical temperature signals obtained from one experiment (e.g., run 4840) at two different 'x' axial locations ($x = 446.2$ mm and $x = 521.0$ mm distance from the model apex) are shown in figure 4.2 for purpose of illustration. A delay of approximately 1 ms was applied to the temperature rise signals in order to synchronise them with the steady flow window of the total pressure signal. This is the time that the flow takes to travel between the nozzle throat, where the p_{0_∞} transducer is located, and the positions where the heat transfer measurements are made. Two distinct trends in terms of temperature level are revealed. The first trend represents an increase in the average temperature of the resistance gauges across the 6 ms time window due to the aerodynamic heating effect (figure 4.2). The second trend shows local temperature rises which represent turbulent events, as will be discussed in more detail in the next section.

In the following sections, the data is presented in two parts as follows:

Set A; Smooth nose. In this series, the entire model surface is polished and measurements are made between $x = 446.2$ mm and $x = 521.0$ mm distance from the model apex (covering a length of 74.8 mm) using the axial heat transfer module. This set contains 21 repeated runs;

Set B; Rough nose. In this series, distributed surface roughness is applied to the nose by means of *silicon carbide* paper and the rest of the model is polished. The roughness size is estimated at about 1.6 μm (2% of the local CFD laminar boundary layer thickness). Measurements are made between x = 406.2 mm and x = 481.0 mm (covering a length of 74.8 mm) using the axial module. This set contains 21 repeated runs.

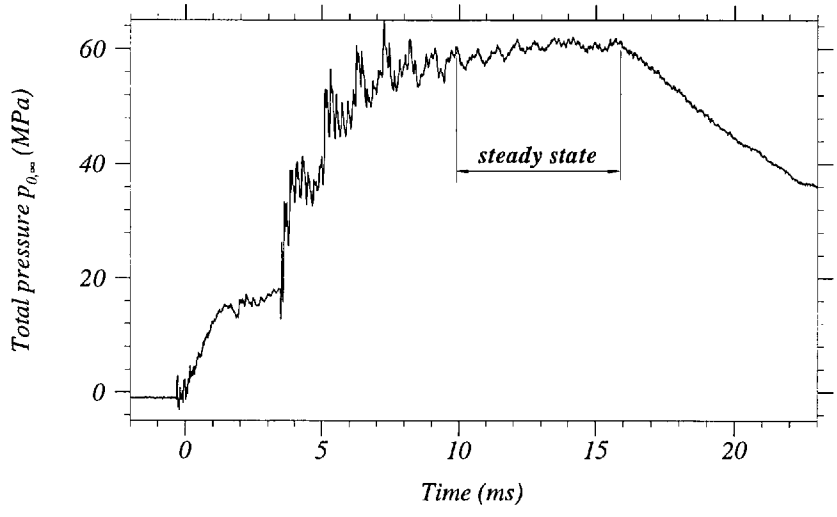

Figure 4.1: A typical total pressure, p_{0_∞}, time-dependent signal, indicating the 6 ms steady flow window (from run 4840).

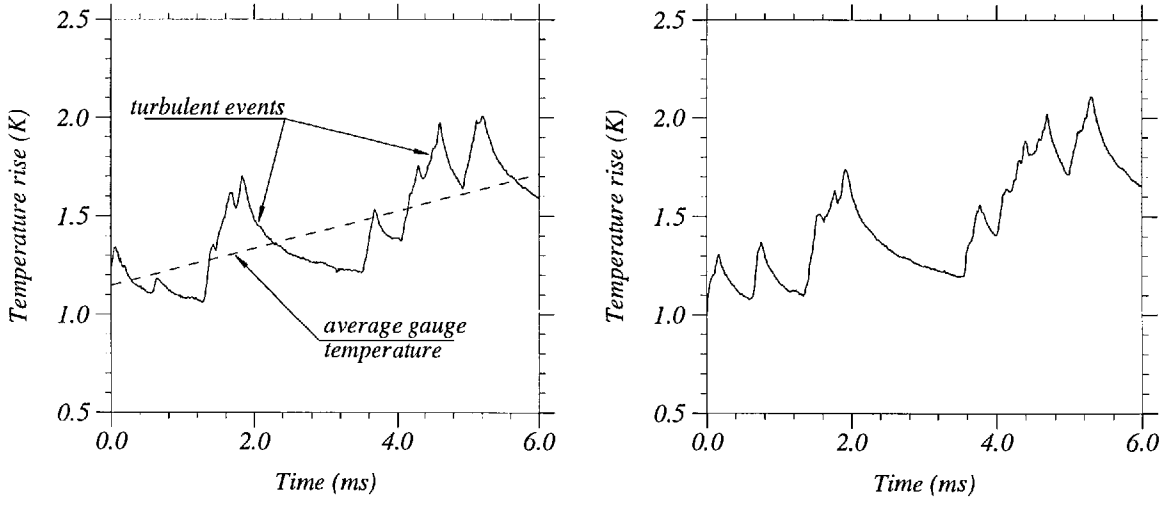

Figure 4.2: Typical time-dependent signals of the heat transfer gauge temperature rise (run 4840). (left) x = 446.2 mm; (right) x = 521.0 mm, distance from the model apex.

4.2 Real-time heat transfer signal

The time-dependent heat transfer signals are acquired by integrating the basic temperature histories using the algorithm due to Cook and Felderman,[19] described in detail in chapter 2. In all the analysis presented in this chapter and the next, gauge 06 data was in effect excluded because of damage.

4.2.1 Set A (smooth nose) heat transfer time-histories

Figure 4.3 presents time-histories for heat transfer at 12 of the 22 measurement locations (covering a length of 74.8 mm) obtained from a typical tunnel run (in this case, run 4840). The signals are clearly intermittent and show two distinct heat transfer levels which characterise the laminar flow (low level) and the turbulent flow (high level).

The 'turbulent events' (or turbulent spots) are characterised by a sharp increase in heat transfer up to a maximum value, followed by a plateau-like region, depending on the event size, then a sharp decrease which becomes more gradual through the spot wake region as it again approaches the laminar level.

It is possible to 'match' the turbulent events, labelled *(a)* to *(e)*, across the measurement length (figure 4.3). Careful inspection of these 'matching events' reveals a time delay and growth with axial distance, demonstrating the downstream propagation and the spatial-temporal growth of the spots. A possible classification of these turbulent events can be made according to their magnitude and time scale as labelled in figure 4.3-(top). Event *(a)* is an 'emerging-type' event, suggesting either a 'newly' born spot crossing the gauge array at it centreline (case (B) in figure 4.4), or an already 'developed' spot sweeping alongside the heat transfer module and gradually, via its lateral growth, covering it (case (A) in figure 4.4 which illustrates the dynamics of an 'emerging-type' event with respect to the heat transfer module spanwise position). No possible distinction can be made between these two situations using 1D-type measurements. Event *(b)* consists of three amalgamating

spots (as distinguished with the two minima inside the event) with increasing interaction as they propagate downstream, to form a large turbulent event. Event *(c)* illustrates an emerging event coalescing with an already grown spot. Event *(d)* represents two amalgamated spots with a merging third spot, either newly formed or sweeping alongside the sensor array. Finally, the large scale event *(e)* reveals either a grown spot generated, or two different spots combined, further upstream of the measurement region.

Figure 4.3 also reveals some level of fluctuations in the laminar fraction of the signals. This is attributed to several factors namely:

Data acquisition and reduction. These introduce noise from three different sources; the analogue-to-digital conversion of the low frequency-filtered analogue electrical signal at 50 kHz to the high 125 kHz frequency digital signal; the thin-film resistance gauge response; and the extraction of heat transfer from gauge temperature-rise (the assumption of piecewise linear gauge temperature distribution in time, as described in detail in chapter 2);

Laminar flow instabilities. These represent the unstable disturbances growing within the laminar boundary layer after reception of the external (to the boundary layer) disturbances. These include temperature spottiness, pressure and vorticity fluctuations, freestream turbulence, particulate, and acoustic noise generated from the turbulent boundary layer of the tunnel nozzle wall;

High vorticity medium. This identifies the region of high rate turbulence diffusion between the laminar flow and turbulent spots. The presence of the latter causes a continuous destabilisation and entrainment of the surrounding laminar flow;

'Emerging' turbulent events. These are characterised by a low heat transfer level, similar to that of the noise maximum peaks mostly predominant in the laminar regions (e.g., event (a) at $x = 446.2$ mm in figure 4.3).

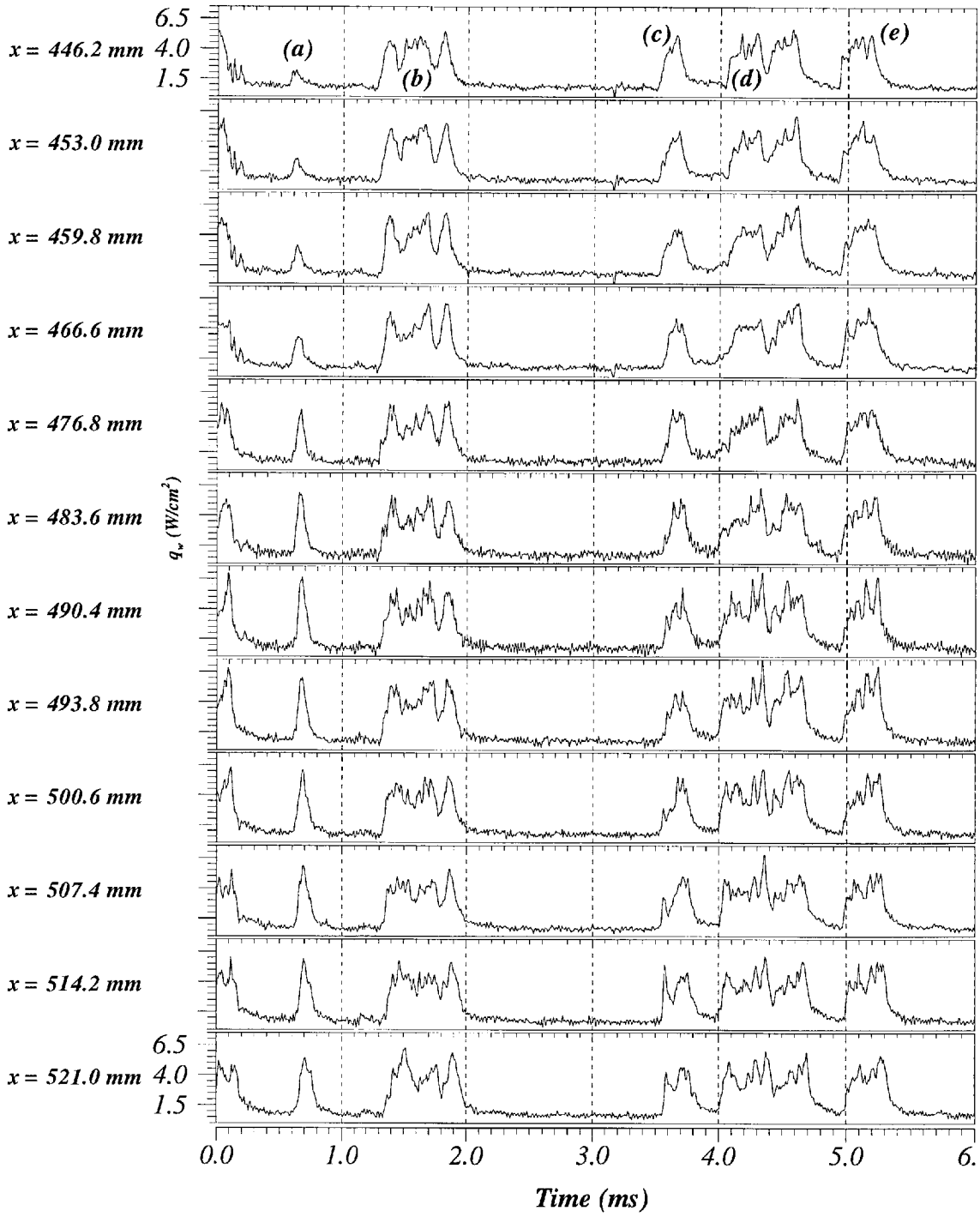

Figure 4.3: Time-dependent heat transfer distributions inside the 6 ms window at 12 of the 22 measurement locations, obtained from run 4840 (smooth nose case). The different interesting regions are labelled; (*a*) emerging event (either a centered newly born spot or a grown spot edge sweeping sideways), (*b*) three amalgamating spots, (*c*) emerging event coalescing with an already grown spot, (*d*) two amalgamated spots with a merging third spot, and (*e*) a grown spot generated, or two different spots combined, further upstream.

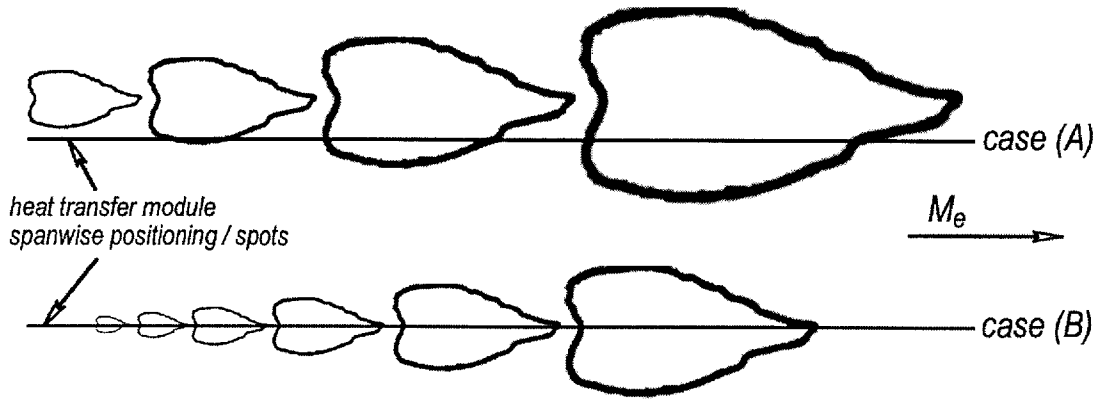

Figure 4.4: Illustration of the propagation of an 'emerging-type' event with respect to the heat transfer module position. (top) case (A), a grown spot sweeping sideways of the heat transfer module; (bottom) case (B), a newly born spot propagating at its centreline along the heat transfer module.

In order to better analyse the data and extract sufficiently accurate information on turbulent events, the level of noise is reduced. This is achieved using three-point data averaging which consists in replacing each heat transfer value, Q_w^i, at a time, t^i, with a new averaged value $q_w^i = (Q_w^{i-1} + Q_w^i + Q_w^{i+1})/3$. The result is shown in figures 4.5 and 4.6 which present time-histories for heat transfer and intermittency signals obtained from two different runs, at axial locations of $x = 446.2$ mm and $x = 521.0$ mm, the most upstream and most downstream measurement locations respectively. The runs of concern here are 4840 (figure 4.5) and 4849 (figure 4.6) which reveal different rates of turbulent events. The intermittency signal is defined as a square function, I, which is equal to 0 for the laminar fraction of the flow and 1 for the turbulent fraction of the flow. The average intermittency, I_{avg}, is defined as:

$$I_{avg} = \frac{1}{T}\int_0^T I(t)\,dt = \frac{1}{n_{max}}\sum_{i=1}^{n_{max}} I(t_i) \tag{4.1}$$

where T is the 6 ms run window and n_{max} is the number of data points included in this time window.

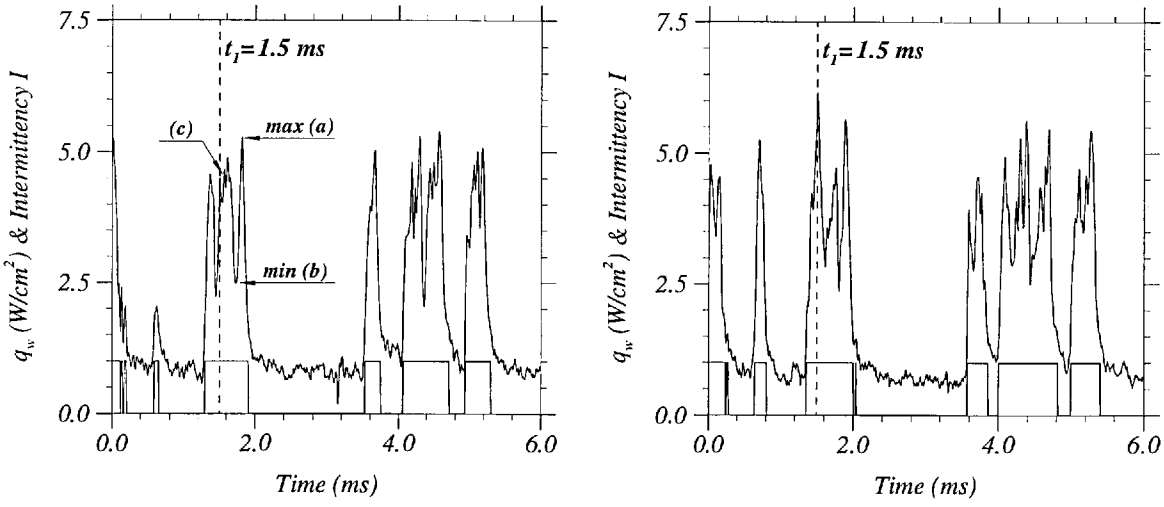

Figure 4.5: Time-dependent heat transfer and intermittency signals from run 4840; (left) $x = 446.2$ mm, the first gauge location; (right) $x = 521.0$ mm, the last gauge location.

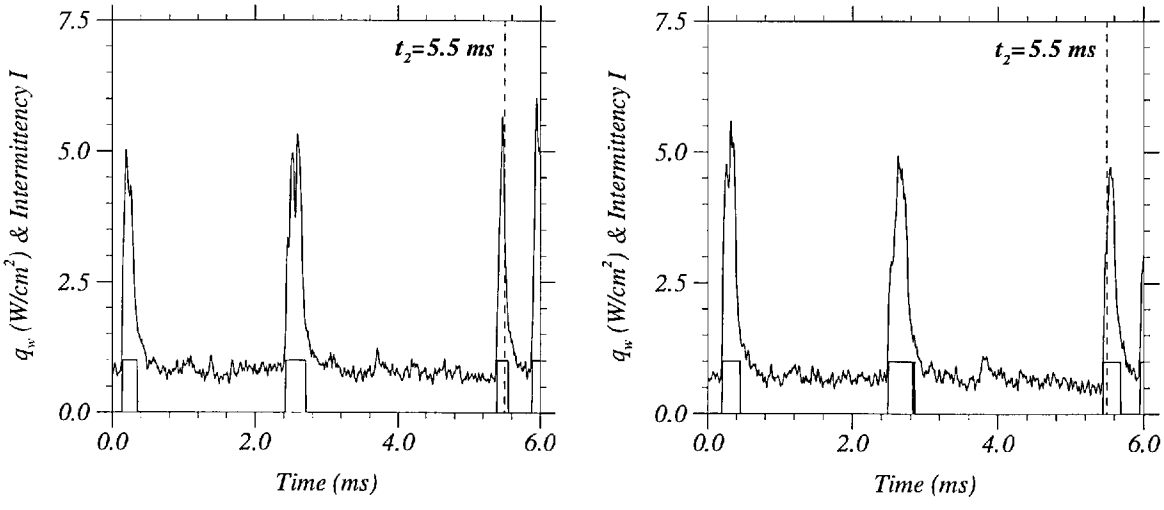

Figure 4.6: Time-dependent heat transfer and intermittency signals from run 4849; (left) $x = 446.2$ mm, (right) $x = 521.0$ mm.

Figures 4.5 and 4.6 allow the evaluation of the laminar heat transfer level as approximately 0.85 W/cm^2 at $x = 446.2$ mm dropping to 0.75 W/cm^2 at $x = 521.0$ mm. The turbulent value however is more difficult to estimate due to the associated high level fluctuations. The latter is evaluated ($\pm 15\%$ fluctuations) at approximately 5 W/cm^2 at $x = 446.2$ mm decreasing to 4.5 W/cm^2 at $x = 521.0$ mm. These experimental values agree within $\pm 10\%$ (laminar) to $\pm 15\%$ (turbulent) of the CFD predictions discussed in chapter 3.

It is important to emphasise that the definition of the intermittency function (i.e., $I = 0$ for laminar and $I = 1$ for turbulent) can only be applied if a distinct boundary and assessment criterion between the laminar and turbulent levels is available. Therefore, the effect of the remaining noise (after three-point averaging, figures 4.5 and 4.6) is disposed of by using conditional data sampling, in which a pre-specified threshold of $\epsilon = 1.7$ times the predicted steady laminar CFD value is considered as the frontier between the laminar and turbulent flows. This results in an intermittency function I defined as (where q_{lam} is the predicted laminar CFD value):

$$I = 0, \text{ if } q_w < \epsilon\, q_{lam}$$

$$I = 1, \text{ if } q_w \geq \epsilon\, q_{lam}$$

The value of $\epsilon = 1.7$ is chosen only for convenience to dispose of any noise of amplitudes below the corresponding value of heat transfer. The optimum value would be just above 1 where the signal would present no fluctuations at all. Although the value of $\epsilon = 1.7$ partially conceals the detection of 'emerging' events (presented as type (a) in figure 4.3 and illustrated in figure 4.4), that have lower heat transfer than the threshold value, the data acquired after threshold sampling is considered better for analysis, particularly for the determination of spots fronts and backs. These are defined in the way that the change in intermittency from 0 to 1 identifies the front of the spot, whereas the change back from 1 to 0 identifies the back of the spot. Indeed, in this respect, the choice of the threshold value has no tangible effect due to the dramatic jump in heat transfer level across the spot front. Moreover, the spot

back lies somewhere ahead of the wake region, which presents large uncertainties due to the gradual decrease in heat transfer level, and hence a change in the threshold value has hardly any contribution to these uncertainties.

The use of the laminar CFD value as a reference is merely to unify the analysis of the data with respect to a 'steady' solution instead of the experimental value, which varies particularly in the vicinity of the turbulent events where the laminar 'unsteadiness' can be significant.

The inspection of the 'matching events' (in figure 4.5 for run 4840 and in figure 4.6 for run 4849) yet again reveals a time delay and growth between the two gauge locations for each separate run. Although the turbulent events describe thermal footprints of different spots convecting downstream, there is no way of determining the spanwise position of a spot as it crosses the heat transfer module. That is, a short duration turbulent event could either represent a spot with short axial scale centred with the gauge or a larger spot which is offset laterally from the gauge (as depicted in figure 4.4). This, in fact, suggests that discrepancies will be associated with the determination of spot streamwise geometrical and dynamic characteristics.

The high level fluctuations in heat transfer present in the large turbulent events (such as events (*b*) and (*d*) in figure 4.3) suggest the existence of turbulent fluctuations (labelled (*c*) in figure 4.5) and possible spot internal structures (more details are presented in chapter 6). However, the significant variation between the maxima and minima of the fluctuations within these large events (such as those labelled (*a*) and (*b*) in figure 4.5) indicates the presence of several amalgamated spots which evolve with distance into a larger spot.

4.2.2 Set B (rough nose) heat transfer time-histories

Figure 4.7 presents time-histories for heat transfer at 12 of the 22 measurement locations (covering a length of 74.8 mm) obtained from a typical tunnel run (in this case, run 4861). The signals are clearly intermittent and show two distinct heat

transfer levels which characterise the laminar flow (low level at approximately 0.875 to 0.775 W/cm^2 between the first and last gauges) and the turbulent flow (high level at approximately 6.5 to 5.0 W/cm^2 ±25% fluctuations between the first and last gauges). Similarly to set A data, it is possible to match turbulent events between each 2 successive stations and demonstrate the time delay and growth from one location to another of these matching events.

The rough nose data shown in figure 4.7 present similar types of events as classified previously for set A (the smooth nose case shown in figure 4.3). The first striking difference however, is the number of turbulent events captured in the 6 ms time window between the most upstream and most downstream stations (x = 406.2 mm and x = 481.0 mm respectively) in this case compared with the previous experimental set. Although the average intermittency level, I_{avg} (as defined in equation 4.1), obtained from the two different runs selected here (run 4840 in figure 4.3 and run 4861 in figure 4.7) is within 20% difference, the structure of the intermittent signal is clearly dissimilar. Type (a) events (as illustrated in figure 4.4) are more predominant in this case, suggesting the effect of surface roughness in the nose region (k/δ = 2%; k being the roughness height and δ the local laminar boundary layer thickness) on this 20% increase in intermittency level. This is translated as a higher rate of spot formation either immediately downstream of the nose, in which case the spikes in the heat transfer signal represents already evolved spots crossing the sensor array off their centrelines, or within the measurement location, in which case the turbulent spikes represent newly born spots crossing the gauge array on their centrelines. Clearly the roughness height of $k = 0.02\delta$ appears to be sufficient to dramatically hasten the transition process. Further discussion regarding surface roughness effect is given in section 4.4 and in chapter 5.

Figures 4.8 and 4.9 present time-histories for heat transfer and intermittency signals obtained from two different runs (run 4869 in figure 4.8 and run 4861 in figure 4.9). In each case, data are shown at two axial positions, x = 406.2 mm and x = 481.0 mm, the first and last measurement locations respectively.

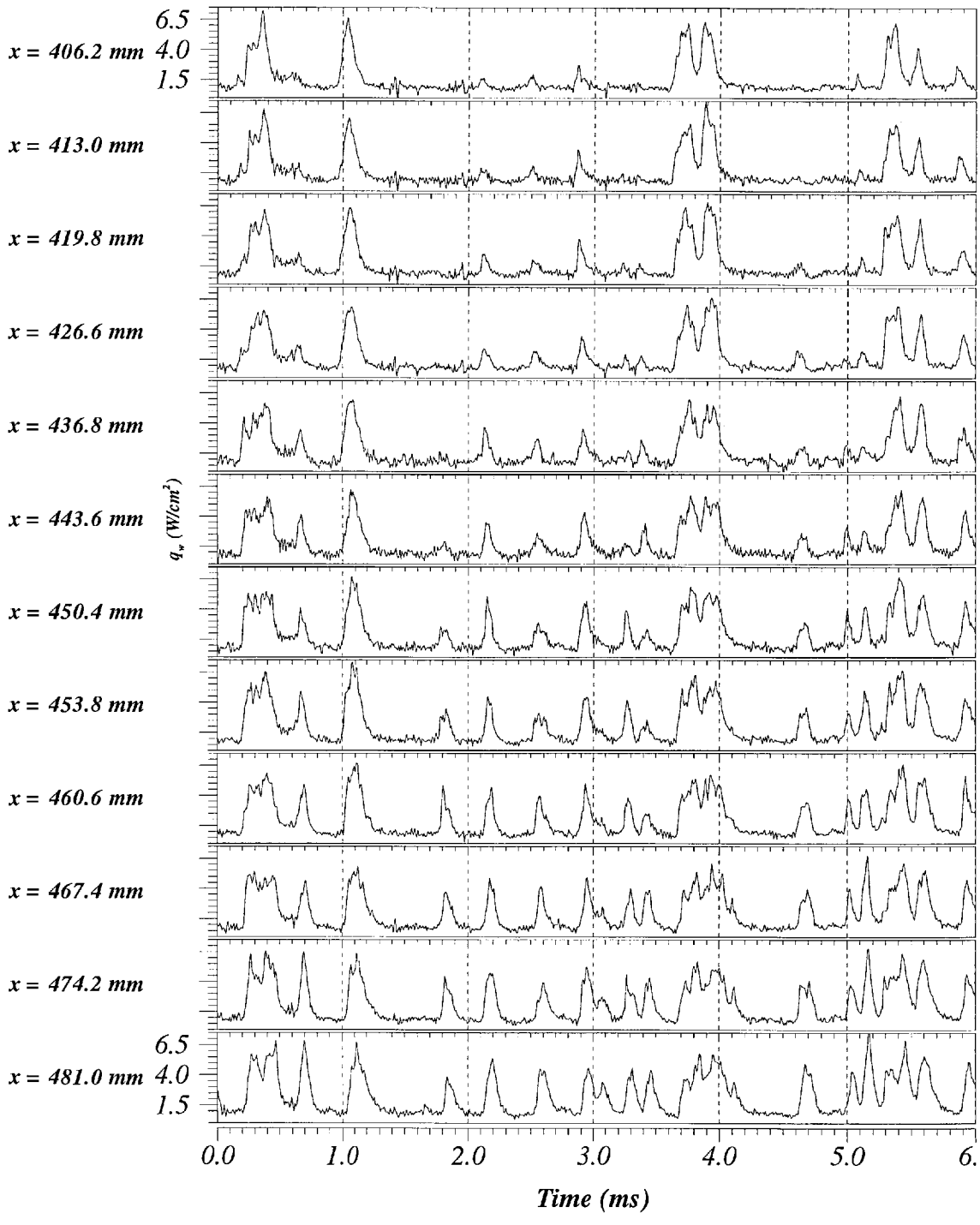

Figure 4.7: Time-dependent heat transfer distributions inside the 6 ms window at 12 of the 22 measurement locations, obtained from run 4861 (rough nose case, $k/\delta = 0.02$; k being the roughness height and δ the local laminar boundary layer thickness).

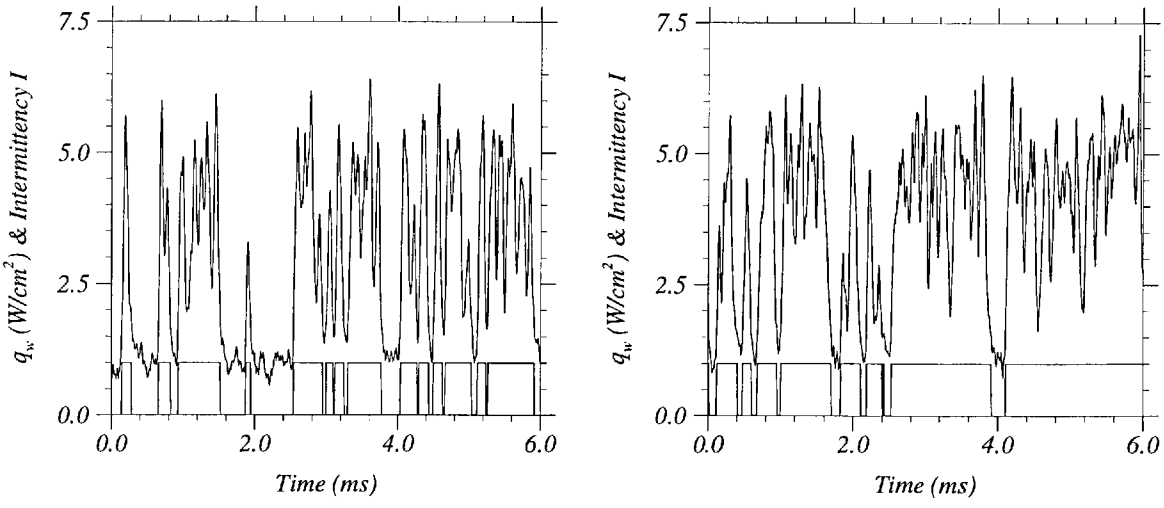

Figure 4.8: Time-dependent heat transfer and intermittency signals from run 4869; (left) $x = 406.2$ mm, the first measurement location; (right) $x = 481.0$ mm, the last measurement location.

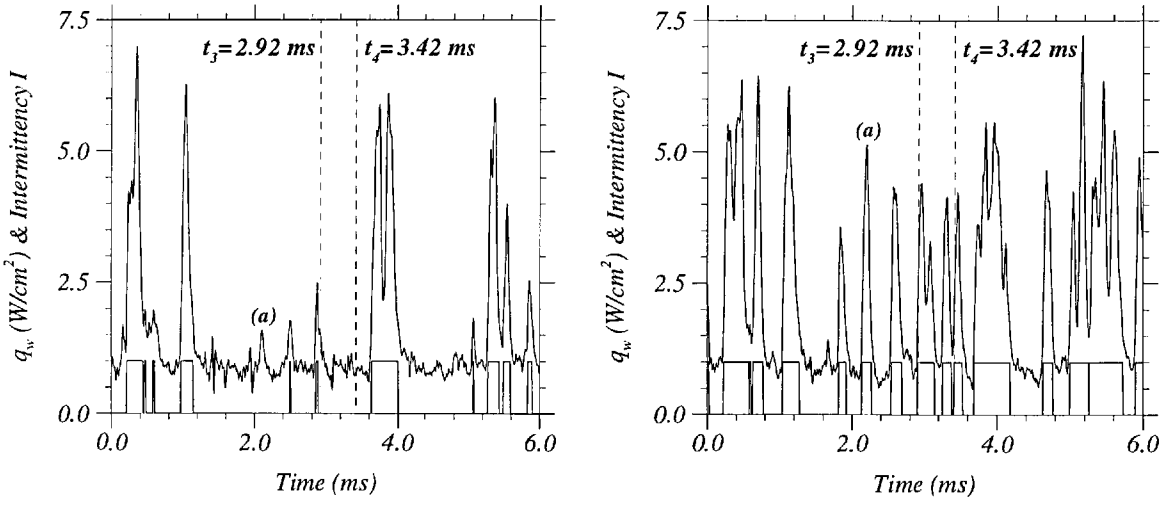

Figure 4.9: Time-dependent heat transfer and intermittency signals from run 4861; (left) $x = 406.2$ mm, (right) $x = 481.0$ mm.

The figures demonstrate the large difference in the average intermittency level, I_{avg}, obtained at the same location x from each run (in the same manner to figures 4.5 and 4.6 for the smooth nose case). Figure 4.8 shows a high intermittency flow at the front gauge (x = 406.2 mm), with I_{avg} = 0.62, developing into an almost fully turbulent flow, with I_{avg} = 0.86, over a distance of 74.8 mm, that is the distance between the first and last measuring gauges. Over the same distance on the other hand, figure 4.9 reveals a lower value of average intermittency, I_{avg} = 0.20, at the first gauge rising to I_{avg} = 0.51 at the last gauge.

4.3 Streamwise heat transfer distribution

The time-dependent data allow the extraction of instantaneous axial heat transfer distributions at fixed times, thus the capture of instantaneous spot streamwise profiles as illustrated in figures 4.10 and 4.11. The figures show axial distributions obtained from 3 different runs (runs 4840 and 4849 for the smooth nose case, set A, and run 4861 for the rough nose case, set B; the same runs discussed in section 4.2) and around different times, that in turn, describe different scales of turbulent events. These distributions are given at 3 times with a time interval Δt of 0.04 ms, however, are not necessarily obtained along the centreline of the spot.

Figure 4.10-left presents heat transfer evolution along the heat transfer module length (x = 446.2 mm to 521.0 mm) at three different times surrounding t_1 = 1.5 ms—i.e., 1.46 ms, 1.50 ms, and 1.54 ms—of run 4840 (t_1 is indicated in figure 4.5). The profile shows no significant change with time, suggesting the presence of a large scale (time and length scales) turbulent event. The event has a time scale larger than 0.08 ms ($2\Delta t$), as demonstrated in figure 4.5, and a length scale larger than the measurement length of 74.8 mm. On the other hand, figure 4.10-right—presenting heat transfer evolution along the heat transfer module length (x = 446.2 mm to 521.0 mm) at three different times surrounding t_2 = 5.5 ms (i.e., 5.46 ms, 5.50 ms, and 5.54 ms) of run 4849 (t_2 is indicated in figure 4.6)—reveals a change in heat

transfer axial distribution from a decreasing trend at $t = 5.46$ ms to an increasing trend at $t = 5.54$ ms. This demonstrates, in effect, the downstream propagation of the turbulent event, which in this case is partially captured, along the heat transfer module.

Figure 4.11 presents heat transfer axial evolutions of two different events—one, shown on the left, at three times surrounding $t_3 = 2.92$ ms (i.e., 2.88 ms, 2.92 ms and 2.96 ms) and the other, shown on the right, at three times surrounding $t_4 = 3.42$ ms (i.e., 3.38 ms, 3.42 ms and 3.46 ms), as indicated in figure 4.9 obtained from run 4861 (experimental set B; rough nose case). In addition to their downstream propagation, there is an evident growth, both in scale and magnitude, of the turbulent events, identifying their type as 'emerging' events (type (a)). The event shown in figure 4.11-right emerges within the measurement length and shows significant growth in scale and magnitude with distance.

It is clear from figures 4.10 and 4.11 that the instantaneous axial scale of a turbulent event is longer than the 74.8 mm measurement length. In future experiments, it would be desirable to lengthen this if possible.

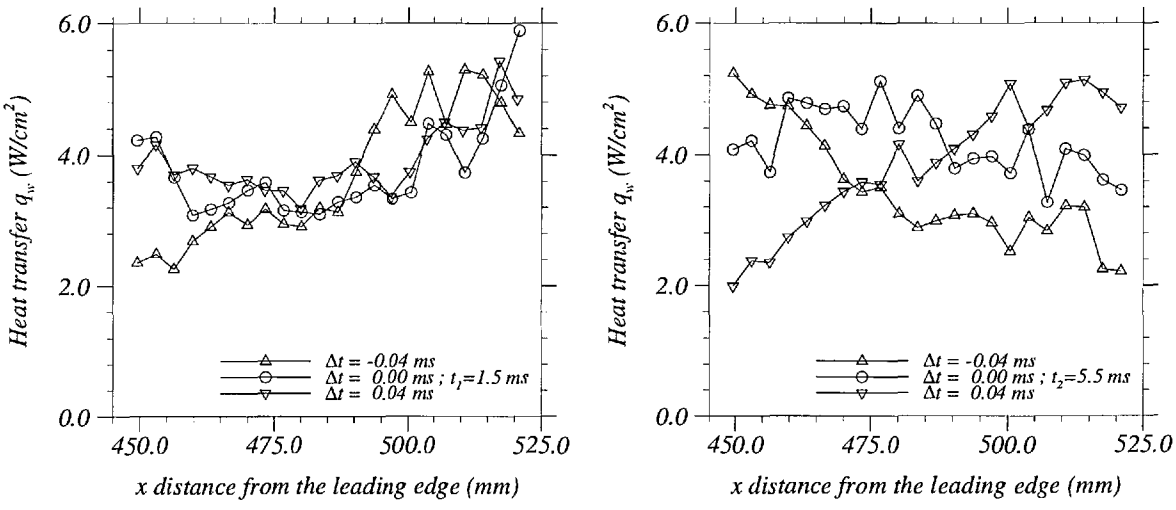

Figure 4.10: Streamwise heat transfer distributions across a turbulent event at various times $t + \Delta t$; (left) run 4840, $t = t_1 = 1.5$ ms (as indicated in figure 4.5); (right) run 4849, $t = t_2 = 5.5$ ms (as indicated in figure 4.6); Experimental set A.

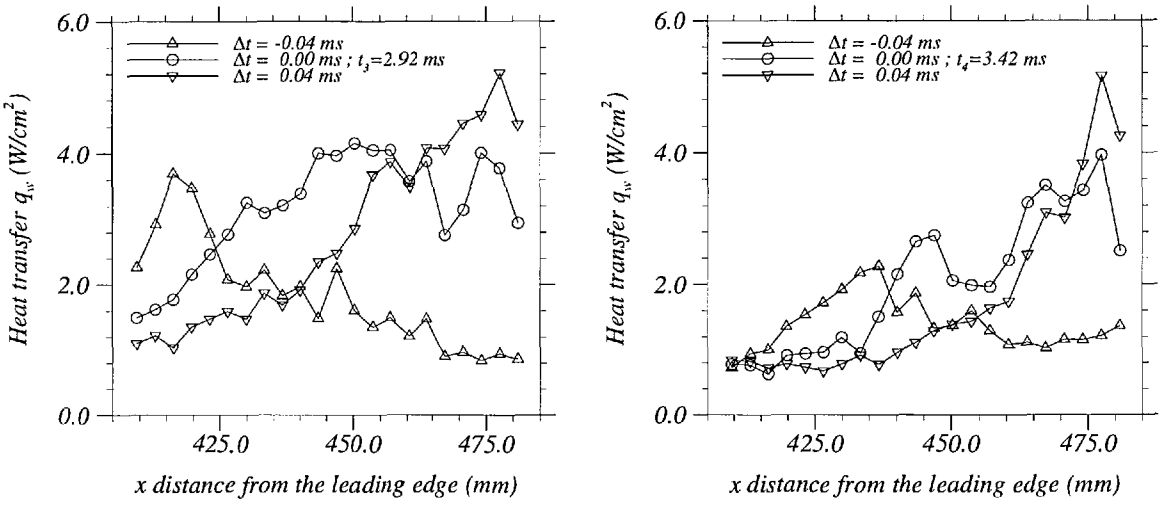

Figure 4.11: Streamwise heat transfer distributions across a turbulent event at various times $t + \Delta t$ obtained from run 4861 (as indicated in figure 4.9); (left) $t = t_3 = 2.92$ ms; (right) $t = t_4 = 3.42$ ms; Experimental set B.

4.4 Turbulent spot average speed

4.4.1 Space-time heat transfer contours

The axial distribution of the instantaneous heat transfer signals obtained from the 43 runs (e.g., figures 4.3 and 4.7) are converted into spatial-temporal contour plots of heat transfer. This allows a better visualisation of the convective characteristics of turbulent events as well as their fronts and backs according to the threshold criterion defined earlier. An example of the result obtained is shown in figures 4.12 to 4.15 which present 'x-t' contour plots of the three-point average time-dependent heat transfer data (shown as a function of time in figures 4.5, 4.6, 4.8, and 4.9).

The darker regions in the plots represent the turbulent high heating levels surrounded by the lighter low heating level laminar flow. The figures most importantly reveal a positive slope (dx/dt) of the edges between the laminar and turbulent regions, which once again demonstrates the downstream propagation of the spots. The figures also demonstrate the slight but apparent growth in time and space of the already existing turbulent regions but rather more significant growth in scale of 'emerging' events (e.g., events (a) and (b) in figure 4.15-top). The difference in the intermittency level obtained from each set of runs is better highlighted, particularly demonstrating the effect of nose roughness on the rate of production of turbulent spots and the fast subsequent coalescence. As a result, the intermittent region lengths appear to be much less substantial compared to smooth nose data.

The effect of the threshold selection, discussed in section 4.2.1, can be better seen in figure 4.12. Two different threshold levels are shown, namely 1.7 q_{lam}, used for data sampling in the present work, and 1.0 q_{lam}, which would define the boundary between the laminar and turbulent flows in a more realistic manner. A number of interesting flow features, labelled (a') to (e'), are illustrated in the bottom plot of figure 4.12 ($\epsilon = 1.0$). (a') represents an individual spot growing with distance and time; (b') illustrates an emerging event (either a newly born spot traversing the gauge arrays at its centreline, or an already developed spot leading edge sweeping

sideways upon the heat transfer module) as the contours become increasingly darker with distance; (c') corresponds to a bulk of several amalgamated spots, shown in figure 4.3 as event (d); (d') reveals the wake region behind the turbulent event (event (e) in figure 4.3); and finally (e') which characterises either high level noise or an emerging event (as it appears with a similar slope compared to the main events). Clearly, the dark regions are virtually identical in both plots. In effect, the increase in the threshold value results in the exclusion of the emerging events (b'), the event wake zone (d'), and the uncertain nature of region (e'), which is the reason for using this sampling technique in the first place.

The variation in threshold value also underscores, at least qualitatively, the variation in the resulting average intermittency level (i.e., I_{avg}). The latter has no big significance as far as experimental set A is concerned (see figures 4.12 and 4.13) because of the associated low spot formation rates. In set B however, this variation becomes more important as higher number of spots is produced (figures 4.14 and 4.15). This is a direct consequence of the increase in turbulent fractions of the flow produced by reducing threshold values. Indeed, figure 4.14 illustrates a large variation in intermittency of approximately 30% as a result of 0.7 q_{lam} difference in threshold. This would have a significant effect if intermittency functions for the intermittent-transition region are to be determined (further discussion regarding this issue is given in chapter 5). However, for the purpose of this study, the threshold technique is merely used to facilitate the definition of the spot streamwise extent, including fronts and backs, and spot convective properties as described in the following section.

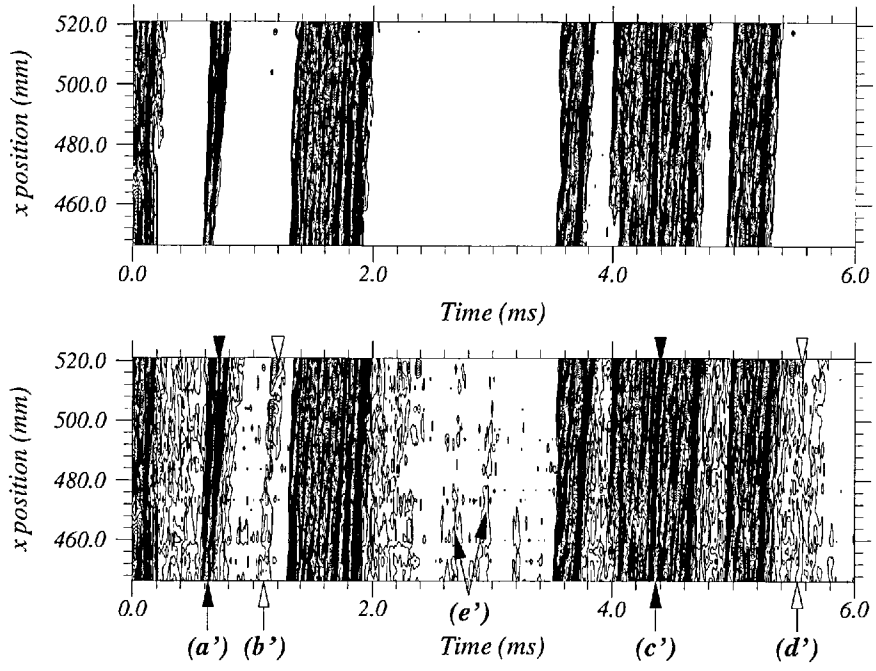

Figure 4.12: x-t plot of heat transfer (run 4840 from set A; smooth nose); (top) ϵ = 1.7; (bottom) ϵ = 1.0. (a') individual spot, (b') emerging event, (c') bulk of several amalgamated spots, (d') spot wake extent, and (e') discrete noise or emerging event.

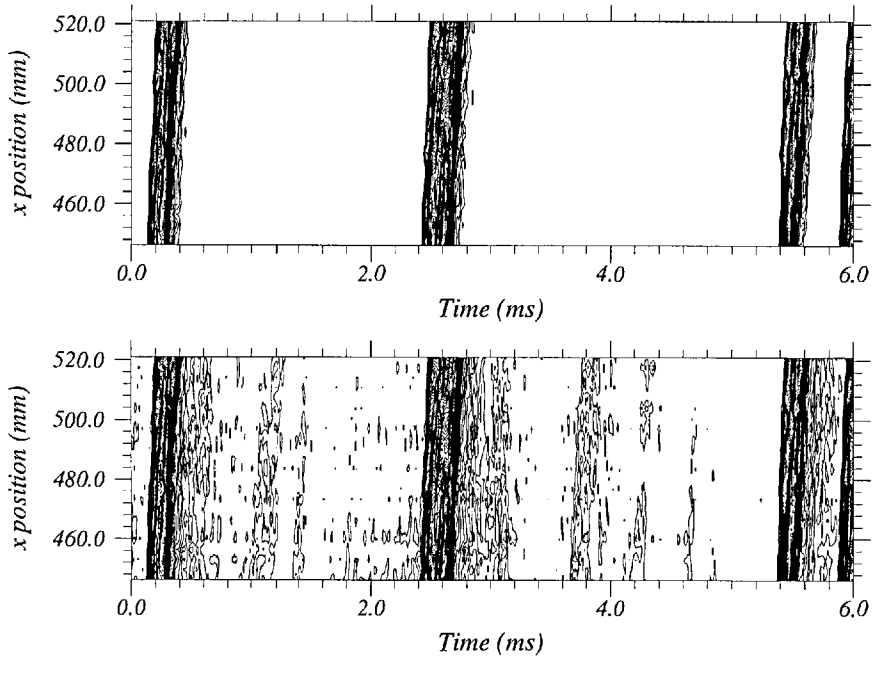

Figure 4.13: x-t plot of heat transfer (run 4849 from set A; smooth nose); (top) ϵ = 1.7; (bottom) ϵ = 1.0.

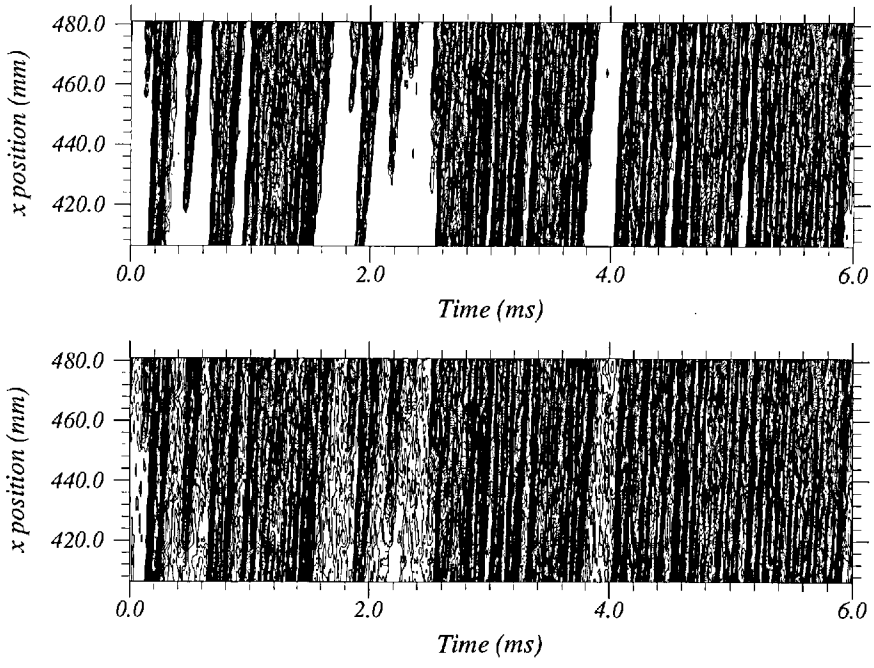

Figure 4.14: x-t plot of heat transfer (run 4869 from set B; rough nose); (top) $\epsilon = 1.7$; (bottom) $\epsilon = 1.0$.

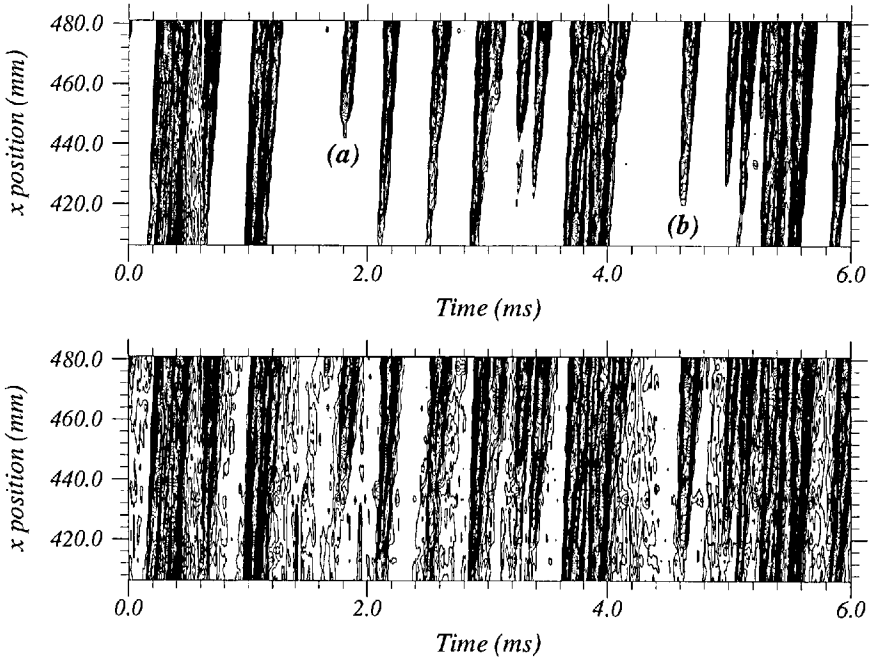

Figure 4.15: x-t plot of heat transfer (run 4861 from set B; rough nose); (top) $\epsilon = 1.7$; (bottom) $\epsilon = 1.0$.

4.4.2 Spot front and back propagation speeds

After demonstrating the downstream convection of turbulent spots, it is necessary to determine the convection velocity. To achieve this, the fronts and backs of each and every turbulent event encountered in the heat transfer and, consequently, intermittency signals are determined. The fronts and backs are defined using the variation of the square intermittency function through time from 0 to 1 for the fronts and from 1 to 0 for the backs respectively.

The data acquired from both experimental sets, A and B, provide a large number of turbulent spots, which varies in each run. Since the change in intermittency from 0 to 1 and vice-versa takes place at exactly 1.7 q_{lam}, that can be situated between any two successive data points defining a finite lapse of time—i.e., for a spot front, $t_i < t_{front} < t_{i+1}$ corresponding to $q_i < 1.7\ q_{lam} < q_{i+1}$—the actual temporal location of fronts and backs, t_{front} and t_{back}, are determined by interpolation between the surrounding points (i.e., t_i and t_{i+1}). Consequently, the end result greatly depends upon the local heat transfer gradient $\partial q_w/\partial t$, which, in turn, is affected by noise.

Figures 4.16 to 4.19 present spot front and back trajectories respectively in the x-t plane, obtained at various locations in time and from different runs from both experimental sets, A and B. The plots are acquired assuming a reference time t=0 for a spot passing through the most upstream gauge (gauge 01 at $x = 446.2$ mm for set A and $x = 406.2$ mm for set B) of the axial heat transfer module. A large number of events (over 200 from both experimental sets) were studied separately in order to minimise undesirable effects and achieve sufficiently accurate event dynamic characteristics. The final result (which is presented in figures 4.16 to 4.19) takes into consideration a limited number of events (about 30 events from set A and 45 events from set B) that spread over a large fraction of the measurement distance (over 50%) and suffice acceptable uncertainties. The process of determining the spot front and back propagation speeds and the related issues is discussed in detail in this section.

The average spot front and spot back speeds are determined using the least-squares fit technique applied to the set of data points gathered in the x-t plane. This assumes that there is no variation of spot leading and trailing edge speeds with axial distance. Indeed, the streamwise measurements only cover a distance of 74.8 mm at a time, which is insufficient in defining the trend of spot speeds. Ideally, the longer the measurements interval, the better the chance to properly establish the nature of spot propagation speed. Nevertheless, the analysis presented in section 4.4.1 predominantly demonstrated the linear nature of the spots leading and trailing edges identified by their x-t plots.

For the smooth nose case (i.e., experimental set A), the spot front and back average speeds, U_{f_1} and U_{b_1}, are estimated at 1050.4 m/s and 536.4 m/s (±2%) respectively, which correspond to approximately 0.80 and 0.41 of the boundary layer edge velocity, U_e, obtained from the laminar CFD prediction. For the rough nose case (i.e., experimental set B), the average front and back speeds, U_{f_2} and U_{b_2}, are estimated at 1000.0 m/s and 528.4 m/s (±1%) respectively, which correspond to approximately 0.76 and 0.40 of U_e. The difference between the front and back speeds (by a factor of 2) confirms the growth of the spot as it moves downstream. The mean spot convection speeds, U_{c_1} and U_{c_2}, are considered as the arithmetic mean of the front and back values and are estimated at approximately 793.4 (±2%) m/s and 764.2 (±2%) m/s for set A and set B respectively, equivalent to 0.60 U_e and 0.58 U_e.

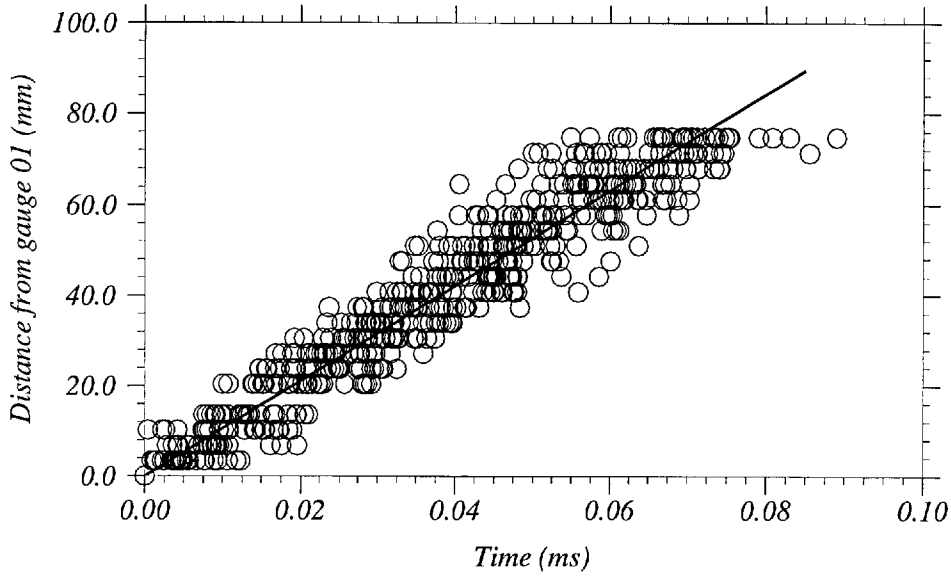

Figure 4.16: x-t plot of the fronts of turbulent spots determined from experimental set A. Average spot front speed estimated at $U_{f_1} = 1050.4$ m/s $= 0.80\ U_e$ ($\pm 2\%$).

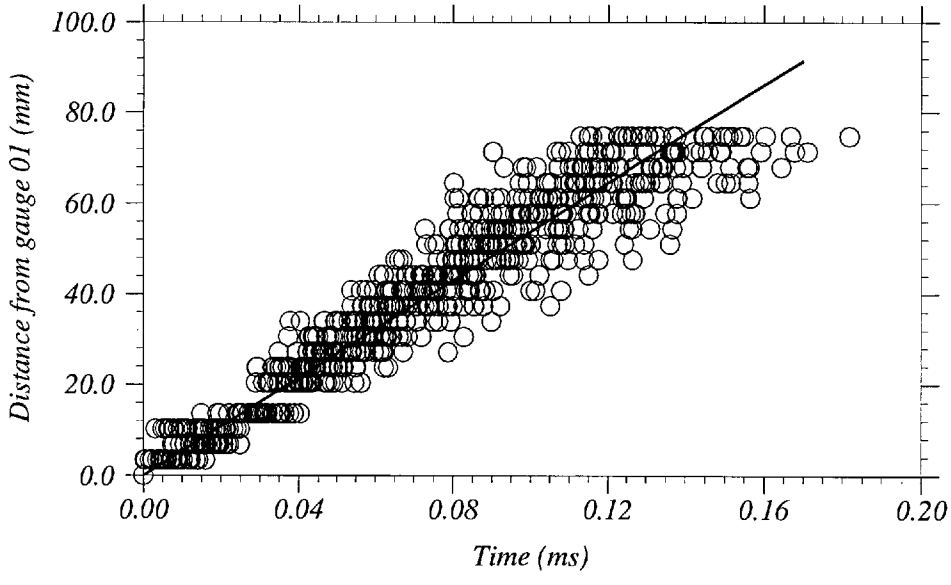

Figure 4.17: x-t plot of the backs of turbulent spots determined from experimental set A. Average spot back speed estimated at $U_{b_1} = 536.4$ m/s $= 0.41\ U_e$ ($\pm 2\%$).

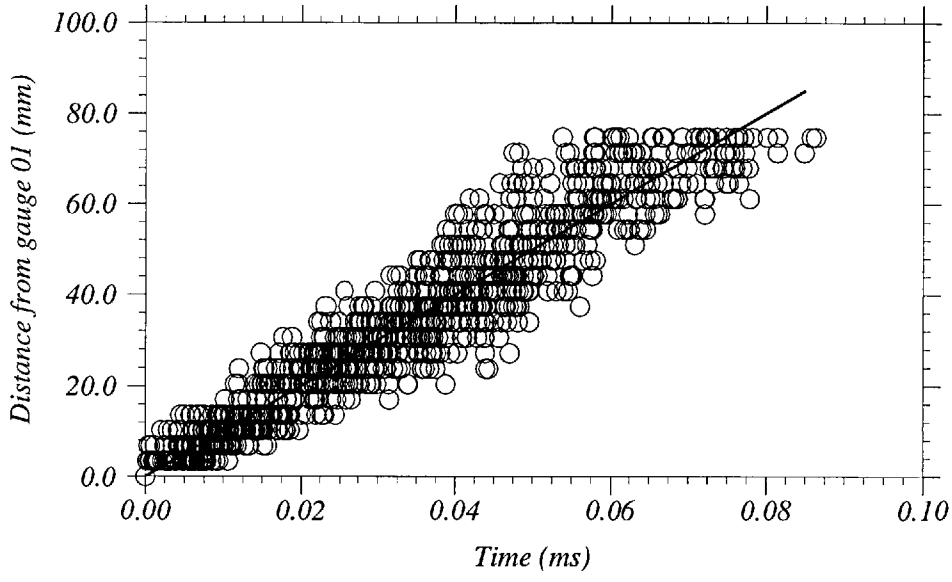

Figure 4.18: x-t plot of the fronts of turbulent spots determined from experimental set B. Average spot front speed estimated at $U_{f_2} = 1000.0$ m/s $= 0.76\ U_e$ ($\pm 1\%$).

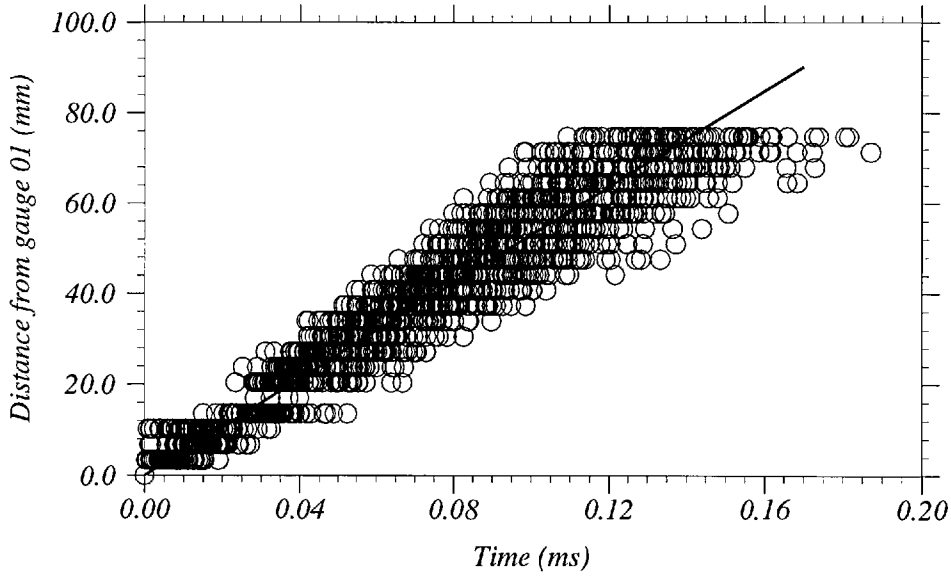

Figure 4.19: x-t plot of the backs of turbulent spots determined from experimental set B. Average spot back speed estimated at $U_{b_2} = 528.4$ m/s $= 0.40\ U_e$ ($\pm 1\%$).

The results obtained from the two different sets of experiments (set A and set B) show a good agreement with a 3.4% discrepancy in terms of spot average convection speed. This is barely greater than the experimental uncertainties (which are about 2%). The discrepancy is attributed to larger errors in defining fronts and backs in the 'near-amalgamated' spots regions which occurred at a larger scale in set B compared with set A. The discrepancy obtained is small enough to suggest the independency of spot average propagation speed of small distributed roughness ($k/\delta \approx 0.02$).

Despite this similarity in events dynamics, it is crucial to point out that the average spot speeds included all sorts of events in terms of scale, onset location, transverse location with respect to the heat transfer gauges, and local interaction between different events. All these parameters affect individual event analysis and the resulting individual and average dynamic characteristics obtained from the two different experimental sets. Furthermore, they partly affect scatter clearly present in the data plotted in the x-t reference frame.

The scatter in the spot front data is partly attributed to measurement uncertainties and noise, but most importantly to the fact that spots are most likely to cross the gauges at different transverse stations, hence capturing different spanwise locations of the actual spot front. The true value of the front speed would vary around the average as a function of the spanwise position across the spot—as discovered by several investigators on their work on spot dynamics at incompressible speeds (e.g., Wygnanski et al.[106]). The scatter is also associated with the spot-to-spot interaction, in the way that spots that are situated right behind others tend to travel faster due to less flow resistance associated with the wake region of the proceeding spot—that is particularly the case in experimental set B where large spot formation rates take place. The presence of this data scatter is partly behind the discrepancy in spot average speed (about 3.4%) acquired from the two different experimental sets, A and B. The scatter in the spot back data is in part associated with large uncertainties across the spot wake region, which is characterised by small heat transfer gradients and large fluctuations.

4.5 Cross-correlations

4.5.1 Cross-correlation functions

The cross-correlations of the time-dependent signals are obtained at pairs of gauges. This is carried out in order to determine the spot average convection speed from the heat transfer and intermittency time-dependent signals, $q_w(t)$ and $I(t)$, respectively. This is achieved by determining the shift in time, τ, at which the maximum correlation between the signals of each pair of gauges takes place.

The cross-correlation function, $R_{ij}(\tau)$, of a time-dependent signal, such as heat transfer $q_i(t)$, between two i and j gauge locations, is defined as:

$$R_{ij}(\tau) = \frac{1}{\overline{q_i'}\,\overline{q_j'}} \frac{1}{T} \int_0^T q_i'(t) q_j'(t+\tau) dt \tag{4.2}$$

$q_i'(t)$ is the fluctuation defined by (where $\bar{q}_i$ is the signal mean):

$$q_i'(t) = q_i(t) - \bar{q}_i \tag{4.3}$$

The root mean square is defined as:

$$\overline{q_i'} = \left[\frac{1}{T} \int_0^T \left(q_i'(t)\right)^2 dt \right]^{1/2} \tag{4.4}$$

T is a time period chosen long enough so that the result obtained could be regarded as statistically average. However, the data record sample of individual runs—6.144 ms which corresponds to approximately 768 sampling points at 125 kHz—is not sufficiently long to provide a statistically average set of data for an individual run with low intermittency. To overcome this, the correlations are calculated for 21 separated runs, and then averaged.

The final cross-correlation plots of heat transfer and intermittency data are achieved for both experimental sets, A and B, by averaging the outcome from each run (figures 4.20 to 4.23). The correlation function takes the maximum value of

1 (i.e., auto-correlation of the gauge-pair (1,1)) since the two signals are perfectly identical. It then gradually decreases between gauge-pair (1,1) and (1,23) demonstrating the gradual change with axial distance in the signal, more specifically, in the scale and magnitude of the turbulent events. Lower correlations are witnessed in the intermittency data, compared to those of heat transfer, due to the square-function property of the intermittency signal—that is, at each position in time there is either full correlation (i.e., $I(t) = I(t+\tau) = 0$ or 1) or no correlation at all (i.e., $I(t) \neq I(t+\tau)$; $I(t) = 0$ and $I(t+\tau) = 1$, or vice-versa), in contrast to heat transfer signal where intermediate values exist between full correlation and no correlation.

Inspection of the correlations plots (figures 4.20 to 4.23) shows that the rate at which the maximum correlation, $R_{1j_{max}}$, decreases with increasing distance from gauge 01 is higher in set B than in set A—by comparison of both heat transfer correlations (figure 4.20 versus 4.22) and intermittency correlations (figure 4.21 versus 4.23). This is associated with the higher rate of small scale emerging events (type (a), as illustrated in figure 4.4) captured in set B compared with that in set A, which are also characterised by higher growth rates in scale and magnitude.

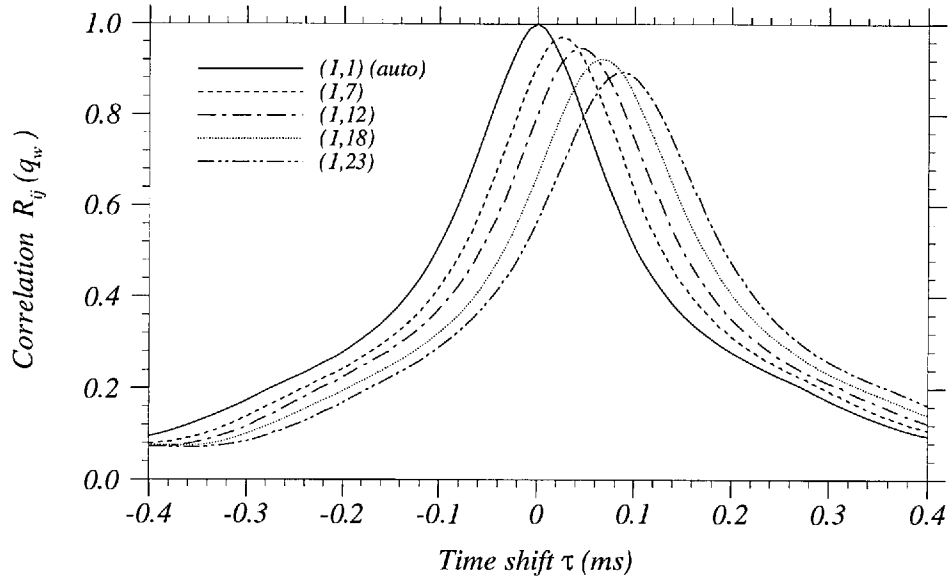

Figure 4.20: Cross-correlation of heat transfer signal q_w (experimental set A; smooth nose).

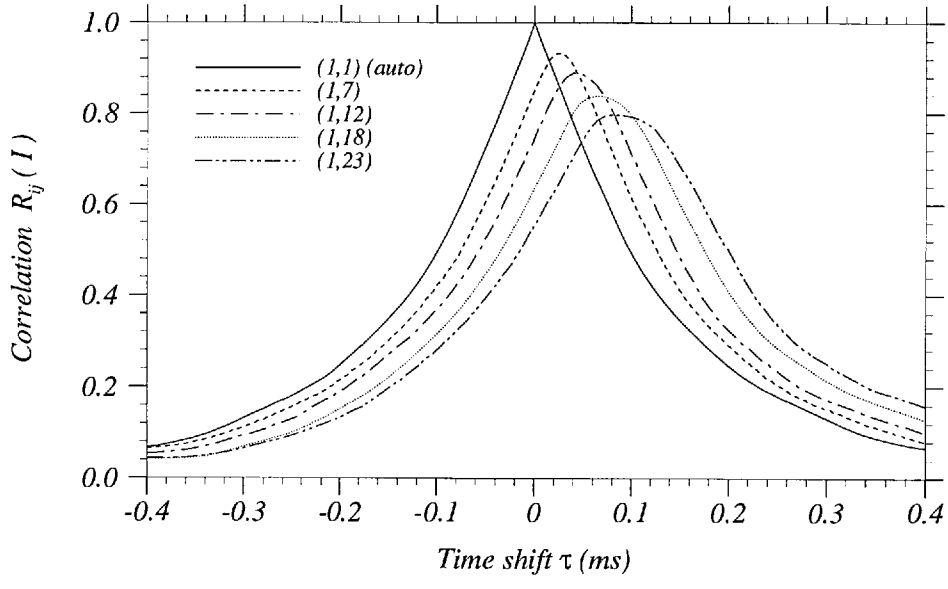

Figure 4.21: Cross-correlation of intermittency signal I (experimental set A; smooth nose).

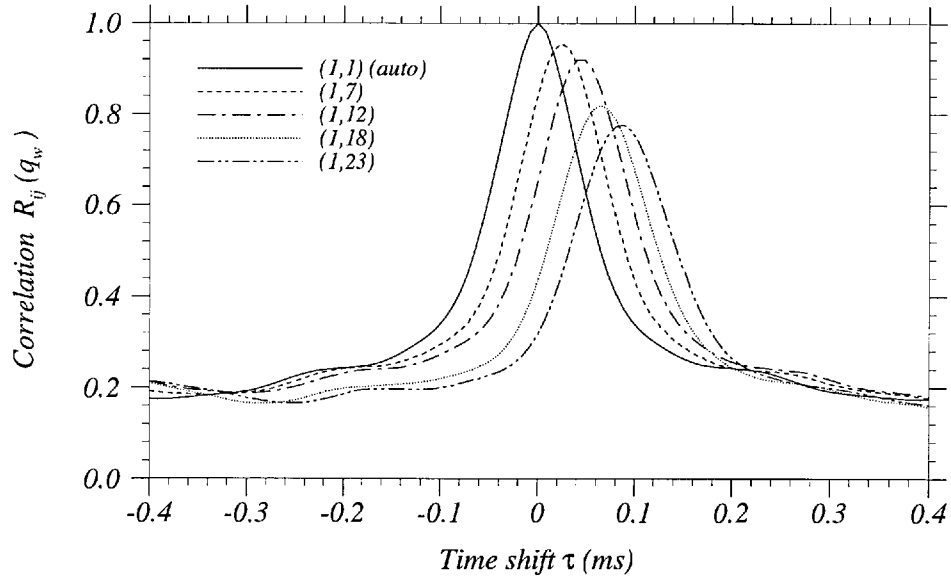

Figure 4.22: Cross-correlation of heat transfer signal q_w (experimental set B; rough nose).

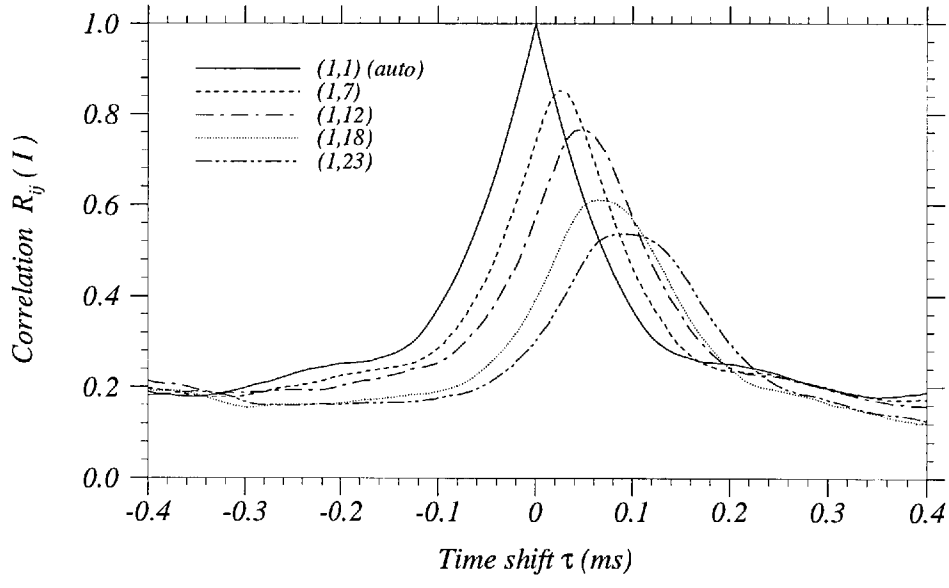

Figure 4.23: Cross-correlation of intermittency signal I (experimental set B; rough nose).

4.5.2 Spot average convection speed

The time shift and the corresponding distance between the maximum correlation values at each pair of heat transfer gauges, (1,1) to (1,23), provides the basis for the spot average speed to be obtained. The result derived from cross-correlation performed on heat transfer and intermittency signals is different due to the difference in nature of the basic time-dependent signal. The x-t plot of the maximum correlations obtained from heat transfer and intermittency data of sets A and B is shown in figures 4.24 to 4.27. The average spot speed is estimated from the graphs and summarised in table 4.1.

	Set A Intermittency I	Set A Heat transfer q_w	Set B Intermittency I	Set B Heat transfer q_w
U_c (m/s)	909.2	870.5	844.0	874.1
U_c/U_e	0.691	0.661	0.643	0.666

Table 4.1: Spot average speed determined from signal cross-correlation analysis.

There is an excellent consistency in the average speed determined from heat transfer cross-correlations in both sets A and B, which is estimated at approximately 0.66 U_e. This result demonstrates, once again, the independency of spot dynamics of roughness. The value of 0.66 U_e is still somewhat higher than those determined by 'geometrical means' in section 4.4.2., estimated at approximately 0.60 U_e and 0.58 U_e in set A and set B respectively. This difference is attributed to the fact that a well selected set of turbulent events (fully developed distinct individual spots) were considered in the first approach, whereas, in the cross-correlation approach, all sorts of turbulent events, including newly formed, fully developed, and amalgamated spots, as well as noise, are taken into account. In spite of the consistency in the spot average speed obtained from heat transfer correlations between set A and set B, the intermittency figures reveal two distinct values namely 0.69 U_e and 0.64 U_e in set A and set B respectively. As mentioned in the previous section, there is less signal correlation in set B associated with high spot formation rates, and as a result, a lower average speed.

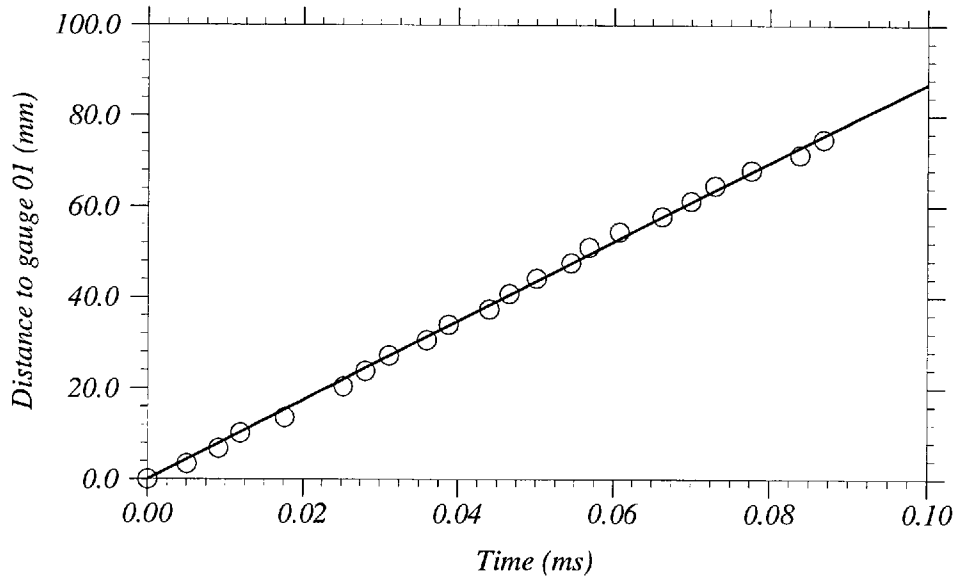

Figure 4.24: Average spot speed obtained from cross-correlations of heat transfer signal q_w (experimental set A)

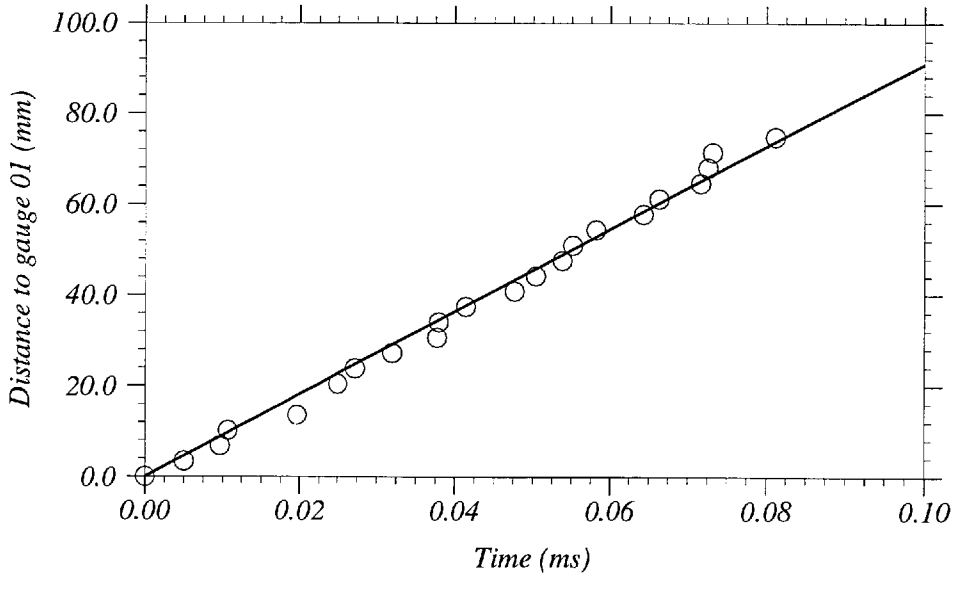

Figure 4.25: Average spot speed obtained from cross-correlations of intermittency signal I (experimental set A)

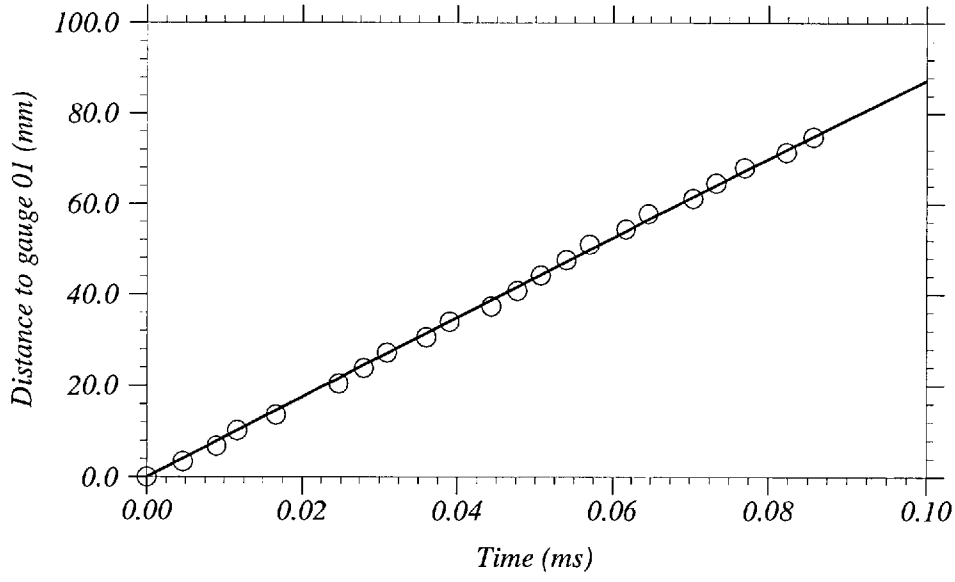

Figure 4.26: Average spot speed obtained from cross-correlations of heat transfer signal q_w (experimental set B)

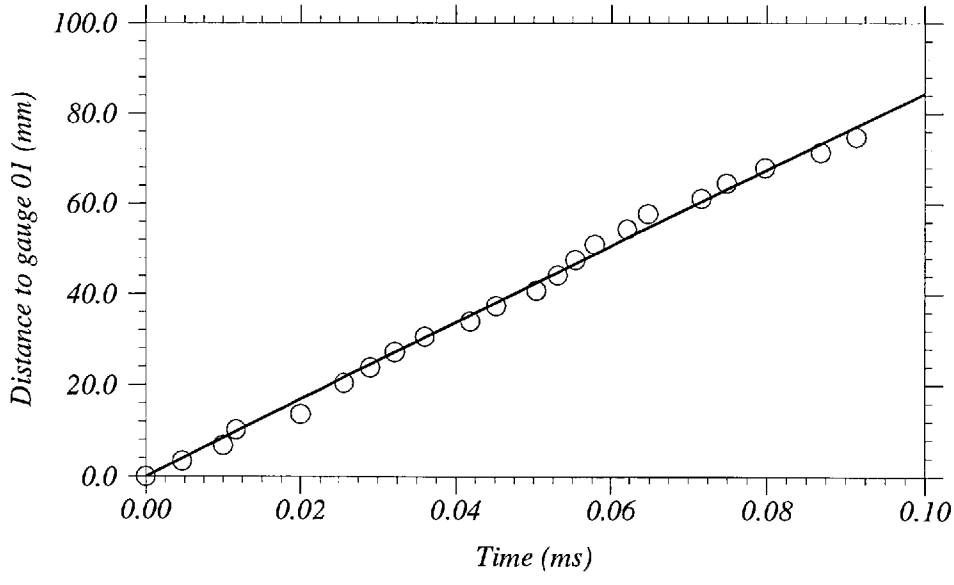

Figure 4.27: Average spot speed obtained from cross-correlations of intermittency signal I (experimental set B)

The variation in the spot average speed determined using the two different approaches (i.e, geometrical and cross-correlation techniques), is estimated at approximately 9.7% in set A and 13.8% in set B. Although these figures are somewhat acceptable, the analysis of individual well selected spots is necessary if accurate representation of spots dynamics is required. Clearly, the cross-correlation method provides a quick and good approximation of events dynamics, however, with a certain level of uncertainty particularly with regard to the associated roughness effects.

4.5.3 Comparison of spot convection speed for present and previous studies

The spot front and back average propagation speeds determined in the present study compare extremely well with their counterparts at incompressible, low subsonic and supersonic speeds obtained by other investigators. Table 4.2 summarises some of the findings.

study	spot type	M_e	Re_e ($\times 10^{-5}\mathrm{m}^{-1}$)	U_f/U_e	U_b/U_e	U_c/U_e
Schubauer et al.[86]	artificial	0.03	6	0.88	0.50	0.69
Wygnanski et al.[106]	artificial	0.03	6	0.89	0.50	0.70
Mautner et al.[59]	artificial	0.03	5.9	0.83	0.55	0.69
Ching et al.[14]	natural	0.11	24	0.81	0.50	0.68
Ching et al.[14]	natural	0.19	42	0.86	0.48	0.63
Clark et al.	natural	0.24	—	—	—	0.71
Clark et al.	natural	0.55	—	—	—	0.69
Clark et al.	natural	1.32	—	—	—	0.70
Clark et al.	natural	1.86	—	—	—	0.68
present	natural	3.70	27.7	0.76 – 0.80	0.41	0.58 – 0.69

Table 4.2: Comparison of spot propagation speed for present and previous studies at a range of boundary layer edge Mach and unit Reynolds numbers, M_e and Re_e, respectively.

Chapter 5

Streamwise Time-Averaged Heat Transfer Database

The time-averaged heat transfer data allows the quantification of heat transfer and intermittency increase with axial distance through the intermittent-transition region. It also enables the prediction of transition onset using extrapolation methods. This chapter presents time-averaged heat transfer and intermittency axial distributions from both experimental sets, A and B. The averaging process was performed for the 6 ms steady flow window provided by the gun tunnel. As discussed in detail in chapter 4, this window is considered short for run-to-run stationary averages to be acquired due to the low frequency and physical scale of the turbulent events obtained. Several repeated runs, as a result, were performed in order to extend the data record sample and improve the statistics of the total averaged data set.

5.1 Time-averaged heat transfer distribution

The streamwise heat transfer distributions are obtained by averaging the instantaneous data, presented in chapter 4, over the steady flow window of 6 ms. This is obtained from equation 5.1 which is given by:

$$\bar{q}_w = \frac{1}{T}\int_0^T q_w(t)dt = \frac{1}{n_{max}}\sum_{i=1}^{n_{max}} q_{w_i} \tag{5.1}$$

where T is the 6 ms window that includes n_{max} data points and q_{w_i} is the measured heat transfer.

The result is shown in figures 5.1 and 5.2 for experimental sets A and B respectively (set A; smooth nose and set B; rough nose). 21 different repeated runs for each set are illustrated alongside the fully laminar and fully turbulent CFD predictions (presented in chapter 3). The data cover an axial distance of 74.8 mm extending between 446.2 mm to 521.0 mm in set A and between 406.2 mm to 481.0 mm in set B. The data are located between the laminar and turbulent CFD predictions as they represent an intermittent flow.

There is a large run-to-run variation as a consequence of low intermittent frequencies. The smooth nose data (i.e., set A) reveal a heat transfer level variation from a near-laminar value to approximately 40% of the expected fully turbulent value. The rough nose data (i.e., set B) however, show higher heat transfer levels of up to 70% of the expected fully turbulent value. Again, as discussed in chapter 4, this increase is a direct consequence of nose roughness which hastened the susceptibility of the boundary layer to transition.

The scatter in the data is partly due to manufacturing imperfections of the heat transfer gauges and related errors generated from the calibration and data acquisition, and partly due to the noise (temperature spottiness, pressure and vorticity fluctuations) generated from the shock compression process taken place ahead of the tunnel nozzle inlet, as well as the turbulent boundary layer formed at the nozzle wall (as pointed out in chapter 4).

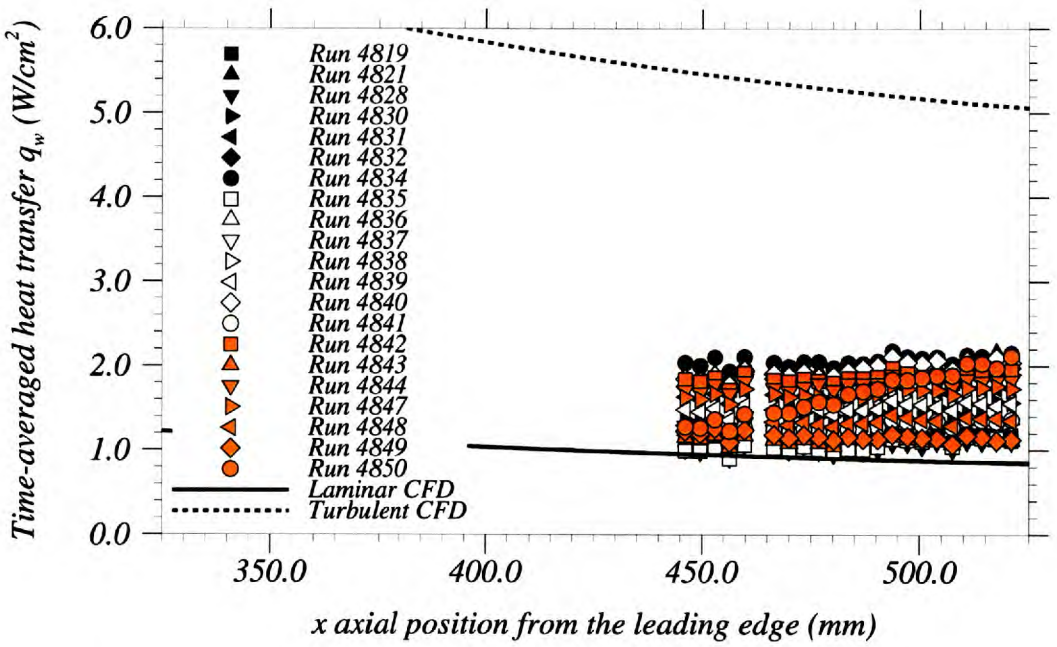

Figure 5.1: Time-averaged heat transfer axial distribution together with the fully laminar and fully turbulent CFD predictions (21 repeated runs in experimental set A).

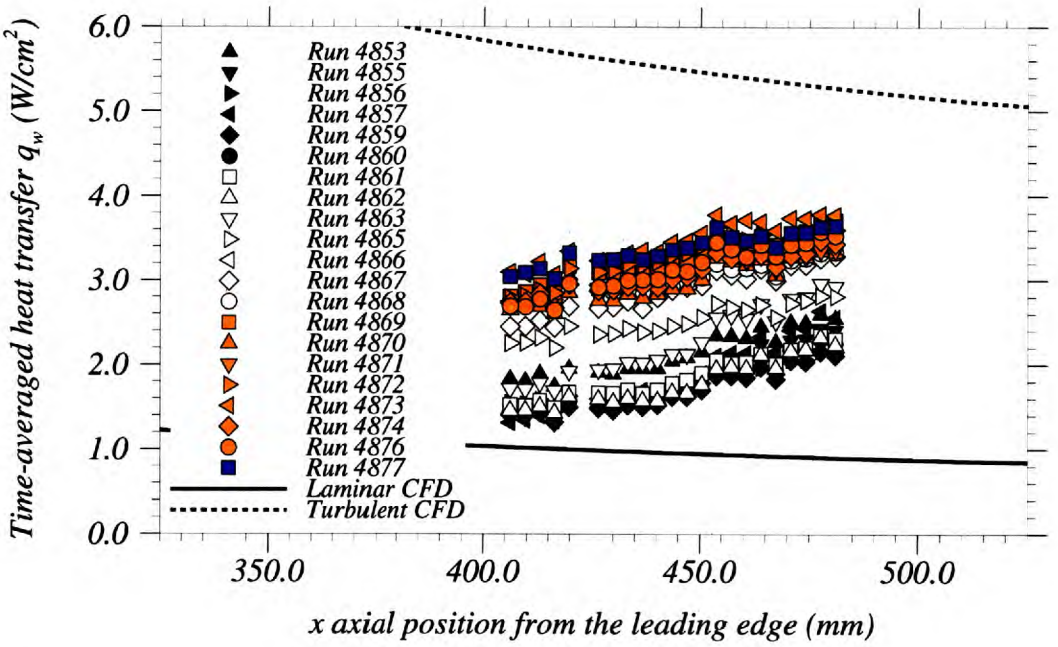

Figure 5.2: Time-averaged heat transfer axial distribution together with the fully laminar and fully turbulent CFD predictions (21 repeated runs in experimental set B).

5.2 Intermittency distribution

In order to better visualise what takes place in the mean sense in terms of intermittent events, the intermittency factor γ is introduced. It is defined here as:

$$\gamma = \frac{\bar{q}_w - q_{lam}}{q_{tur} - q_{lam}} \tag{5.2}$$

where $\bar{q}_w$ is the time-averaged measured heat flux and q_{lam} and q_{tub} are the predicted fully laminar and fully turbulent CFD heat fluxes respectively (as illustrated in figures 5.1 and 5.2). This function is different from the average intermittency function, I_{avg}, described in chapter 4 for three principal reasons associated with the characteristics of I_{avg}, namely:

- Due to 'noise', the assumed change from laminar to turbulent in the calculation of $I(t)$ in the time-dependent signals takes place at a threshold value, 1.7 q_{lam};
- For the unsteady flow in the vicinity of a spot, the 'non-turbulent' value is probably different from the predicted mean laminar value;
- The variation in heat transfer in the turbulent (or 'non-laminar') flow is not taken into account in the calculation of I_{avg} but does affect γ.

Therefore,

$$\gamma \neq I_{avg} \; ; \quad I_{avg} = \frac{1}{T}\int_0^T I(t)dt$$

Figures 5.3 and 5.4 present the axial distributions of intermittency γ obtained from each individual run of set A and set B respectively, as well as the runs-averaged distribution $\overline{\gamma}$ in each set. The runs-averaged data could potentially represent a single experiment with a record sample window of about 126 ms for each set.

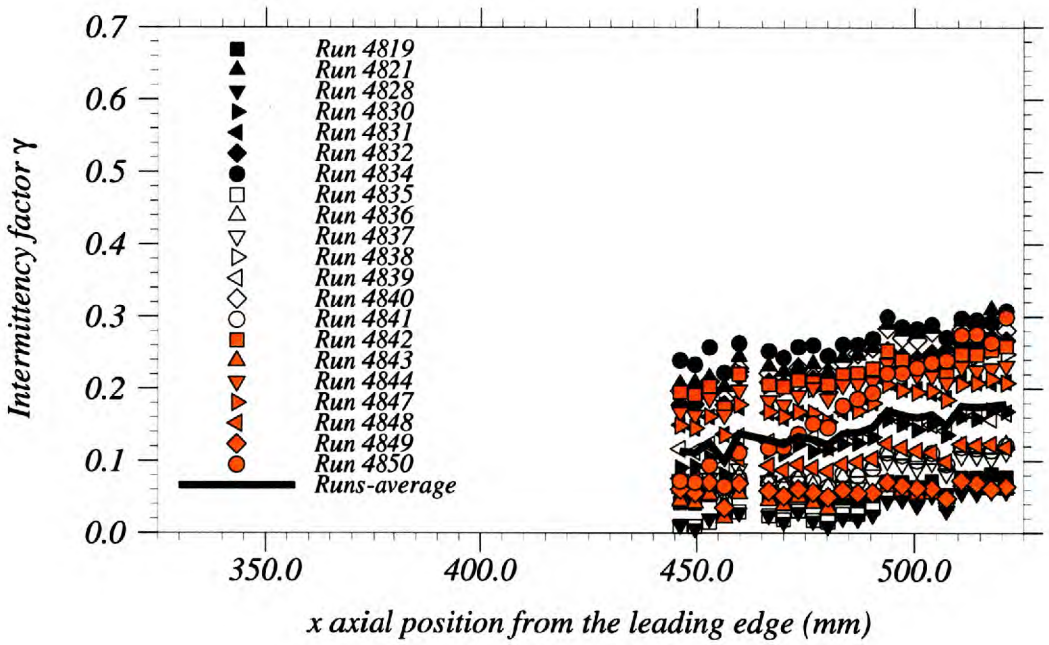

Figure 5.3: Intermittency (γ) axial distribution (experimental set A).

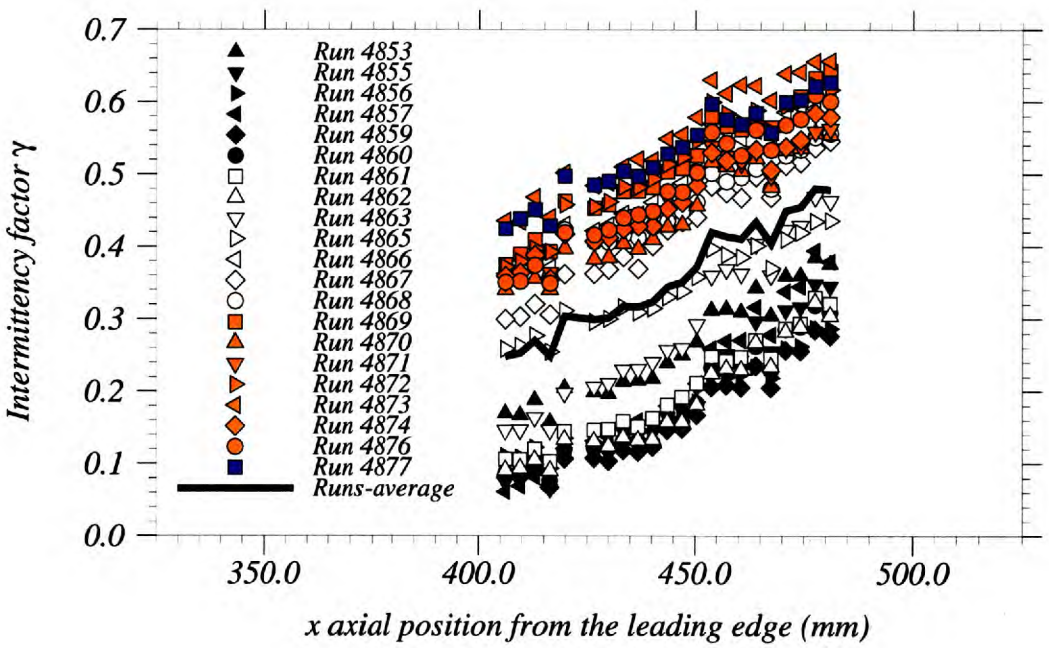

Figure 5.4: Intermittency (γ) axial distribution (experimental set B).

The clear increase in γ with distance demonstrates the spatial-temporal growth of the turbulent events. The intermittency, γ, varies from a minimum of approximately 1% to a maximum of approximately 31% in set A. This variation is even higher in the data of set B varying from a minimum of about 6% to a maximum of about 66%. The resulting runs-averaged intermittency function $\overline{\gamma}$ is found to vary between 10% to 18% in the smooth nose case (i.e., set A) compared with 25% to 48% in the rough nose case (i.e., set B). These figures yield a rate of increase ($\partial\overline{\gamma}/\partial x$) of approximately 0.11%/mm and 0.31%/mm in set A and set B respectively. Table 5.1 summarises critical intermittency values.

	γ_{min}	γ_{max}	$\overline{\gamma}_{min}$	$\overline{\gamma}_{max}$	$\partial\overline{\gamma}/\partial x$ (/m)
Set A (smooth nose)	0.01	0.31	0.10	0.18	1.1
Set B (rough nose)	0.06	0.66	0.25	0.48	3.1

Table 5.1: Critical intermittency values (experimental sets A and B).

5.3 Experiment-intermittency relationship

The large variations in intermittency level between different runs might suggest that it is associated with continuous damage of the model. However, the plots of space-averaged intermittency (averaged over the 74.8 mm measurement length) distribution against chronological order of runs (figures 5.5 and 5.6 for set A and set B respectively), show no evident rise in run-to-run intermittency level, particularly true in the smooth nose case. In the rough nose case, two relatively distinct regions are present (figure 5.6) due to some incurred damage that was witnessed during experimentation. Yet, the remaining data of each region reveal no apparent trend throughout the run-window of this experimental set (see figure 5.6). This random run-to-run variation demonstrates the randomness of the transition process and the possible variation in the triggering events in this specific set of experiments. It also highlights the significance of the data record sample time length used in the averaging process, specifically in this type of study where large variations in turbulent event physical scales and frequency of occurrence are involved.

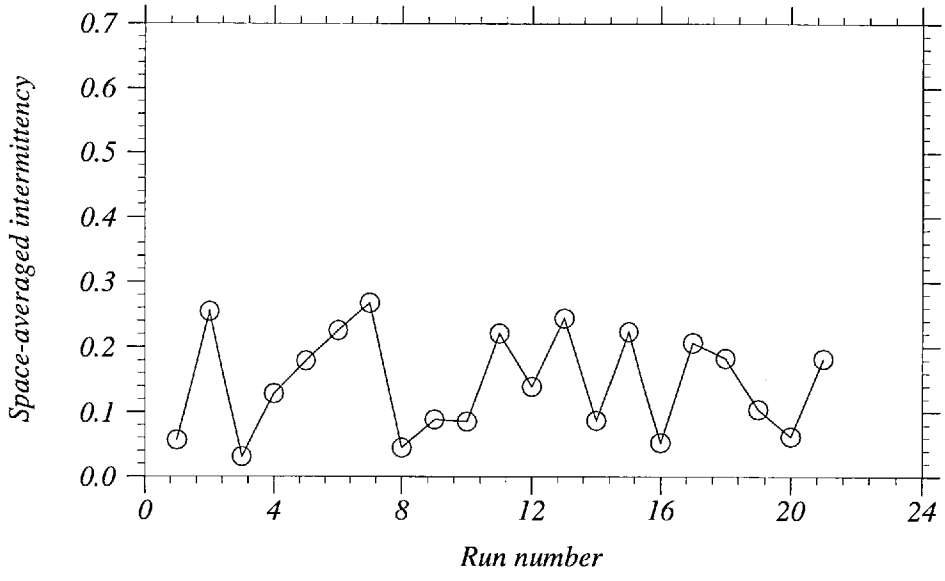

Figure 5.5: Space-averaged (over the 74.8 mm measurement length) intermittency variation with run number (experimental set A).

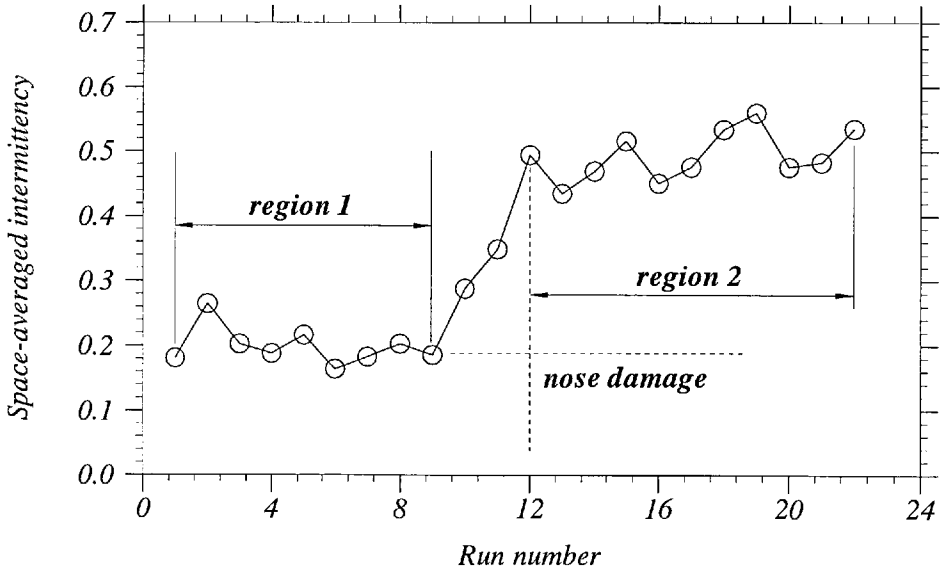

Figure 5.6: Space-averaged (over the 74.8 mm measurement length) intermittency variation with run number (experimental set B).

5.4 Surface roughness effects

The two experimental sets A and B enabled the achievement of two distinct intermittent behaviours. As shown in chapter 4, there is an increase in spot production rate with increased surface roughness not only in the nose region but also downstream along the length of the model up to the locations where the measurements were made. In spite of the fact that roughness was only present in the nose section, its effect is apparently encountered across the whole length of the boundary layer. The significant similarity in terms of spot average speeds determined from both sets A and B (see section 4.4.2 of chapter 4) indicates consistency in the rate of event streamwise spatial-temporal growth. Consequently, the difference in the rate of increase in intermittency ($\partial\overline{\gamma}/\partial x$), obtained from sets A and B, must be associated with the high production rate of turbulent events in set B, along the total length up to the measurement location (figures 5.3 and 5.4). The attempt to predict the onset of transition in this case (i.e., rough nose) using simple extrapolation methods is virtually impossible due to the short spatial interval within which the measurements were made. A simple linear upstream extrapolation of the data yields onset locations in set B downstream of those obtained in set A (figures 5.7 to 5.10), which is of course unacceptable with the argument of roughness effect so far put forward. It is, therefore, more probable that ($\partial\overline{\gamma}/\partial x$) takes smaller values at upstream locations for the earlier stages of the transition process. This is illustrated by a suggested schematic in figure 5.11, where the intermittency distribution obtained from set A (smooth nose case) adopts *slope 1*, whereas that obtained from set B (rough nose case) adopts *slope 2*.

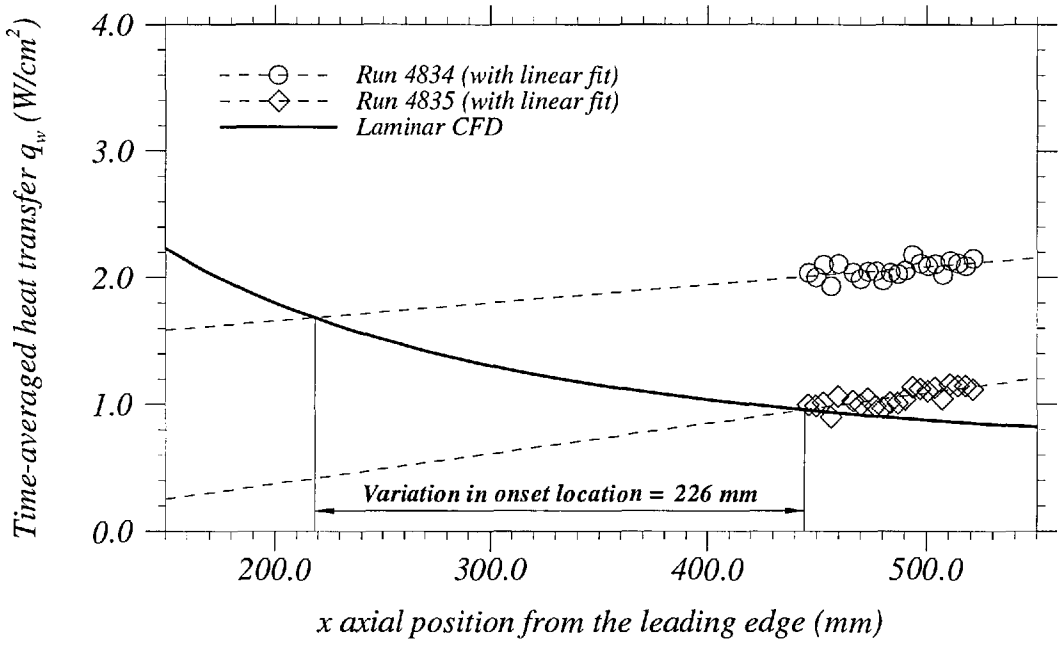

Figure 5.7: Time-averaged heat transfer axial distribution together with the laminar CFD prediction; linear extrapolation for onset prediction (experimental set A). Run 4835, low intermittency; run 4834, high intermittency.

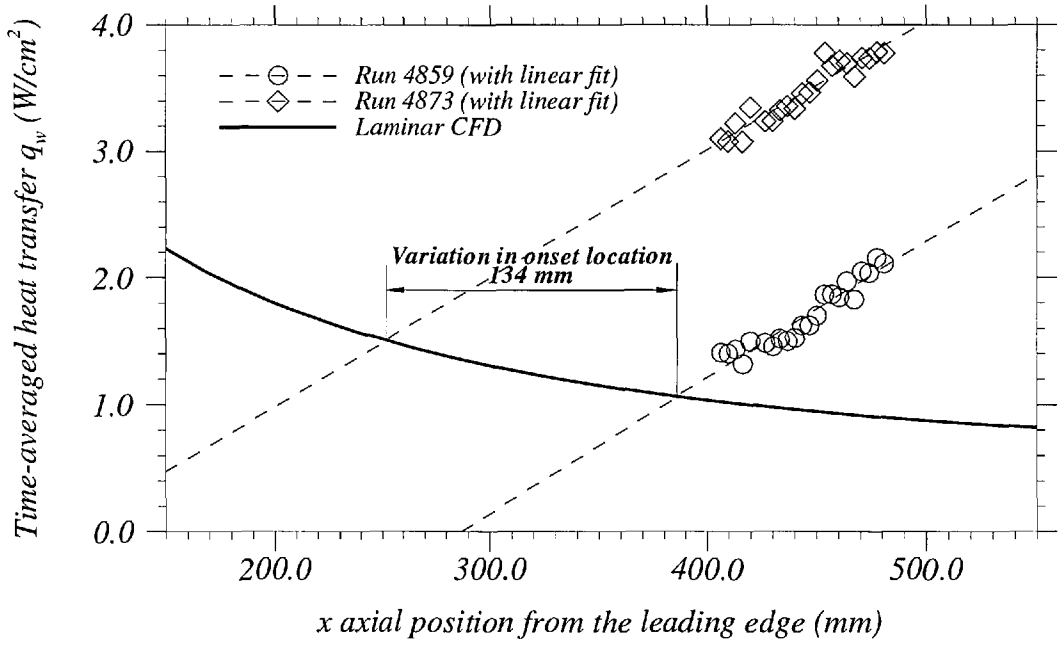

Figure 5.8: Time-averaged heat transfer axial distribution together with the laminar CFD prediction; linear extrapolation for onset prediction (experimental set B). Run 4859, low intermittency; run 4873, high intermittency.

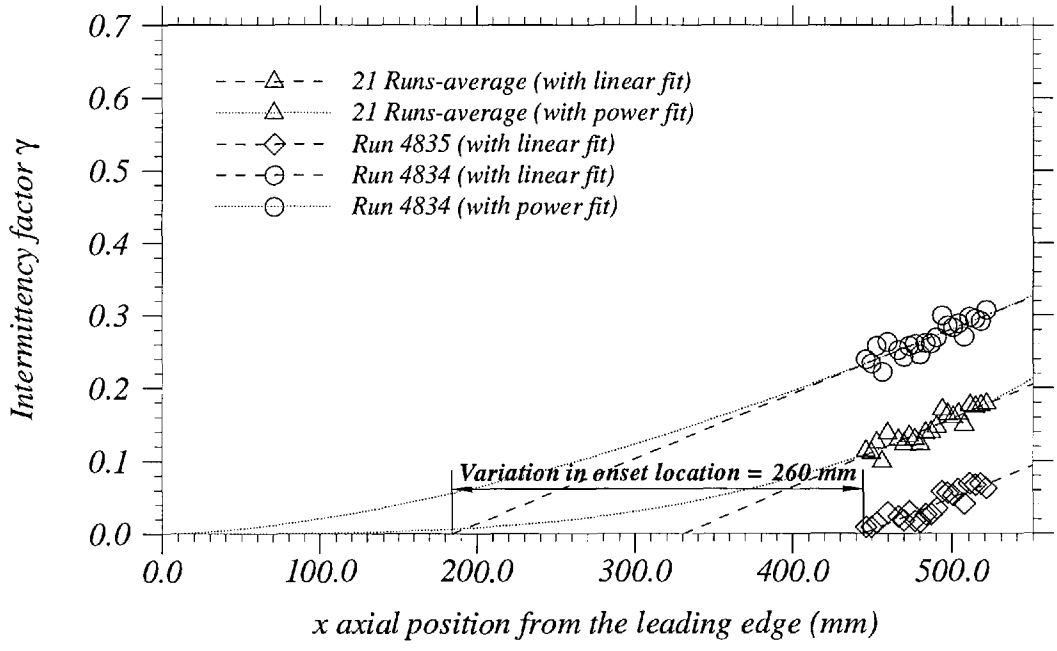

Figure 5.9: Intermittency axial distribution; linear extrapolation for onset prediction (experimental set A). Run 4835, low intermittency; run 4834, high intermittency.

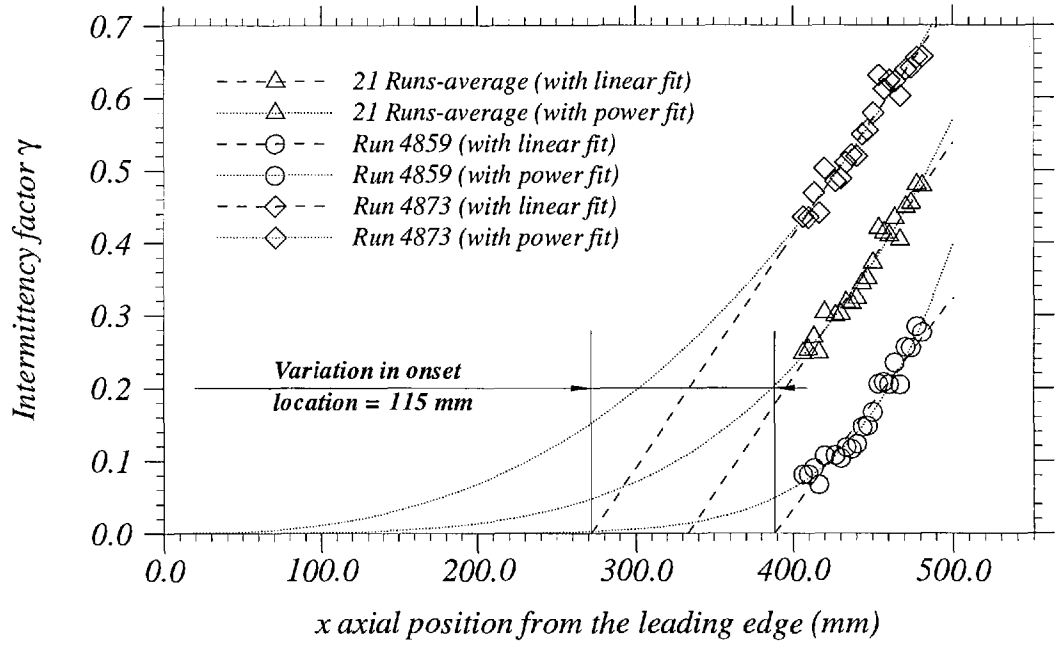

Figure 5.10: Intermittency axial distribution; linear extrapolation for onset prediction (experimental set B). Run 4859, low intermittency; run 4873, high intermittency.

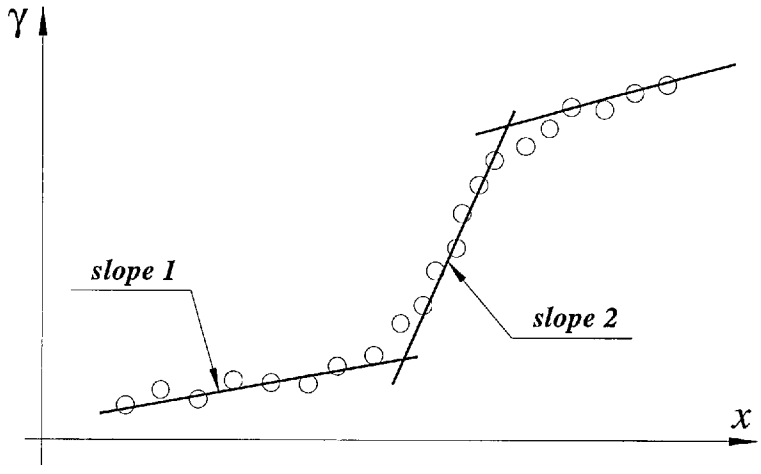

Figure 5.11: Schematic of intermittency distribution with streamwise distance.

It emerges from the above analysis that the receptivity mechanisms in the presence of distributed roughness ($k/\delta = 0.02$) are different from those in the presence of smooth nose surface. It appears that two separate signatures of the disturbance environment (roughness) on the boundary layer arise; one mode involves the immediate breakdown to turbulence right behind the nose region and a second mode consists of growing instabilities and late generation of turbulent events. The former hastens the latter through extended regions of disturbed laminar flow in the event vicinity.

5.5 Transition onset and region extent

Although the heat transfer measurements could successfully capture the dynamics of individual spots, the instrumented distance in each set of experiments is not sufficient for a detailed time-averaged analysis to be made of the transition onset location and the extent of the intermittent-transition region. Nevertheless, some qualitative and approximate estimations are extracted from the data. In effect, the data clearly reveal small axial slopes of the intermittency rise, suggesting substantial lengths of transition flow. The measurements only permitted the detection of the

early to middle stages of the transition process. The smooth nose data predict intermittent distances of order of 600 mm, whereas the rough nose data give a lesser value of order of 300 mm, a consequence of the higher spot formation rates. These elongated intermittent distances are a direct consequence of nose bluntness and the associated entropy layer effects in significantly reducing the boundary layer edge conditions as demonstrated in chapter 3.

The prediction of the onset locations with acceptable accuracy is not possible. Nonetheless, very approximate estimations can be made if simple linear extrapolations are used (figures 5.7 to 5.10). Clearly, the discrepancy in such an approach is larger in the rough nose data (set B) as higher intermittency levels are encountered. These describe the mid-zone of the intermittent-transition region which is defined with a different intermittency equation—described by *slope 2* in figure 5.11—compared with that defining the lower intermittency levels (set A)—described by *slope 1* in figure 5.11. The actual onset locations lie somewhere upstream of the predicted values due to the nonlinearity of the intermittent curve at the beginning of the process. Using the intermittency distributions (figures 5.9 and 5.10), the onset location is found to lie between approximately $x = 180$ mm and $x = 440$ mm in set A and between 270 mm and $x = 390$ mm in set B (a difference in onset location between the low and high intermittency runs for each set). This extrapolation approach is clearly not adequate for the data obtained in set B experiments for the reasons mentioned above. However, it illustrates the variation in onset location between the low and high intermittency runs (runs 4835 and 4834 respectively in set A and runs 4859 and 4873 respectively in set B). The runs-averaged distributions suggest an onset location of approximately $x = 330$ mm in both cases (i.e., sets A and B). However, since the intermittency equation slope is different in both sets (with *slope 2*>*slope 1*), the onset location moves upstream with surface roughness.

Chapter 6

Circumferential Heat Transfer Database

This chapter presents spot planform geometrical characteristics, streamwise and transverse spatial development, and spot internal structures obtained at the model surface. This was achieved using the circumferential heat transfer module (described in chapter 2) positioned at three different axial locations, namely $x = 213$ mm, $x = 279$ mm, an $x = 334$ mm distance from the model apex. The measurement covered a distance of 68 mm around the model circumference using 18 'V'-shaped heat transfer gauges which provide a gauge-to-gauge spatial resolution of 4 mm. The experiments aimed to gather as much individual turbulent spots as possible in order to acquire statistically average spot characteristics at each axial location. A significant number of tunnel runs were performed for each measurement location (around 160 runs in total). A fraction of these runs resulted in heat transfer histories which did not exhibit individual spots. The analysis presented in this chapter only includes the data which produced individual spots well contained within the spanwise measurement distance of 68 mm.

6.1 Time-dependent heat transfer signal

Figure 6.1 presents time-histories for heat transfer signals through the 6 ms steady-run time window of the tunnel run, for all the spanwise gauges at $x = 334$ mm for one sample run. There is a finite number of captured travelling turbulent events at each spanwise location labelled (a) to (f). A number of these events spread over the whole spanwise distance (e.g., events (b), (d), and (f)), whereas others are restricted only to a finite number of gauges (e.g., events (a), (c), and (e)). The latter are interpreted as the spots that only partially cover the spanwise array. The events represent either discrete individual turbulent spots (e.g., event (f)) or an amalgam of spots (e.g., events (b) and (d)). The 'matching' of these events across the spanwise measurement length shows no time delay from one spanwise location to another. Indeed the variation rather occurs in terms of event time-scale and magnitude, indicating different streamwise profiles at each transverse location.

6.2 'w-t' heat transfer contours

To have a better visualisation of the turbulent events shown in the time-dependent data (figure 6.1), heat transfer contour plots are obtained in the 'w-t' plane, where w is the spanwise distance, and are shown in figure 6.2. The heat transfer rate increases from blue to red, a convention which is used in all heat transfer contour plots presented in this study. The data are acquired from two different tunnel runs (runs 5139 and 5140), which exhibit different intermittency levels. The figure displays individual turbulent events of different sizes (e.g., events (f), (g), and (h)), fractions of discrete events (e.g., events (a), (c), and (e)), amalgamated events contained within the measurement distance (e.g., event (i)), and amalgamated events which spread outside the measurement window (e.g., events (b) and (d)). The events labelled (a) to (f) in figure 6.2-bottom correspond to the events previously indicated in figure 6.1 (obtained from the same run; run 5140).

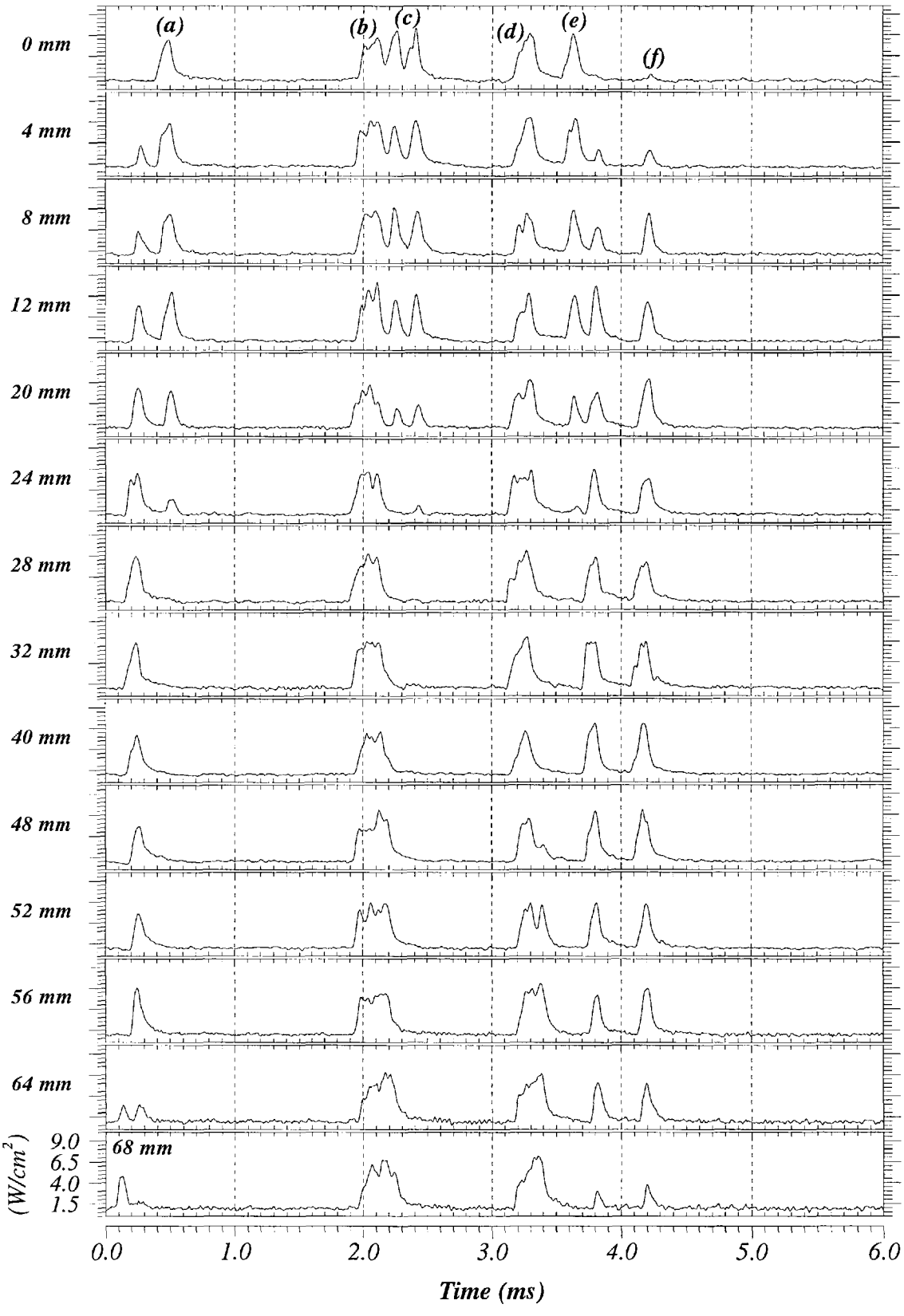

Figure 6.1: Time-dependent heat transfer signals across the circumferential gauges (68 mm distance) at $x = 334$ mm (Run 5140).

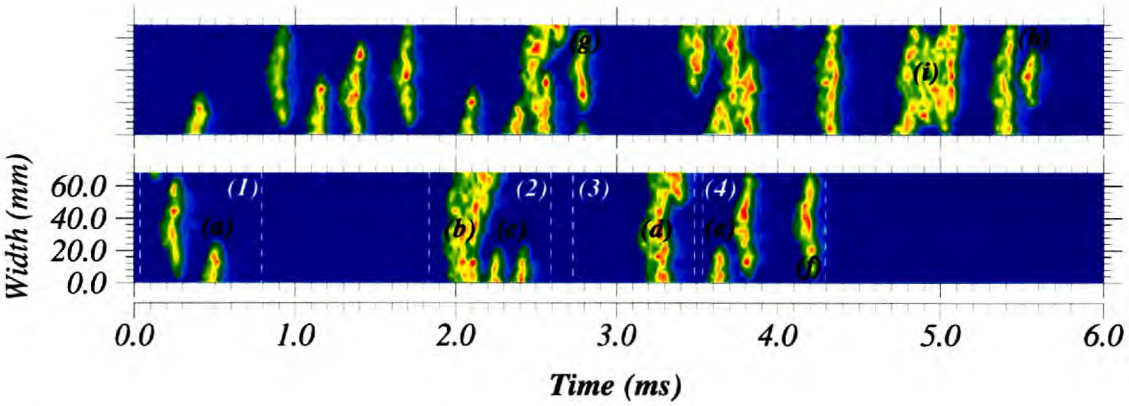

Figure 6.2: w-t plot of heat transfer contours at $x = 334$ mm. (top), Run 5139; (bottom), Run 5140 which is shown as heat transfer time histories in figure 6.1. Blue corresponds to the lowest heat transfer rate and red corresponds to the highest, a convention used in all heat transfer contour plots.

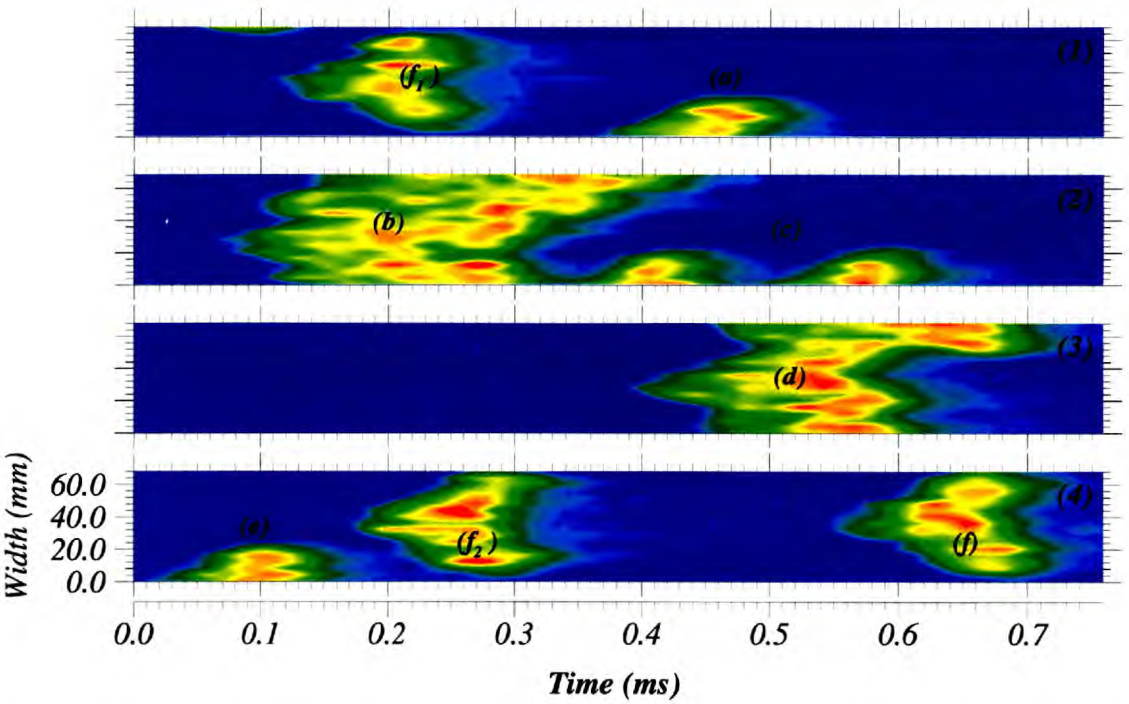

Figure 6.3: w-t plot of heat transfer contours at $x = 334$ mm (Run 5140). Zoom into the 0.75 ms windows, (1), (2), (3), and (4), indicated in figure 6.2 (bottom).

The discrete events represent individual turbulent spots as demonstrated in figure 6.3, which represents a zoom into the four different 0.75 ms time windows (1 to 4) indicated in figure 6.2-bottom (run 5140). The time scale is scaled in such a way that it can be interpreted approximately as a physical length scale. Once again, the events labelled (a) to (f) correspond to the same events shown in the two previous figures (i.e., figures 6.1 and 6.2). Events (f), (f_1), and (f_2) represent full individual turbulent spots; events (a), (c), and (e) illustrate fractions of discrete spots; whereas events (b) and (d) depict amalgamation of turbulence.

6.2.1 Turbulent spot thermal footprint

The data from the 160 tunnel runs, obtained using the circumferential heat transfer module positioned at the three various axial locations (i.e., x = 213 mm, 279 mm, and 334 mm), was treated in the same manner as above. As a result, a large number of isolated spots was obtained, some of which are shown in figures 6.4 to 6.9. These figures illustrate thermal footprints (heat transfer contours) of 12 different individual spots for each axial measurement location, x = 213 mm (figures 6.4 and 6.5), x = 279 mm (figures 6.6 and 6.7), and x = 334 mm (figures 6.8 and 6.9).

The plots are presented in a 'w-L' (i.e., spanwise-streamwise) reference frame, with a point of origin (w=0 and L=0) arbitrarily taken as the approximate location of the 'centre' of the turbulent spot. The streamwise length scale, L, is obtained from multiplication of the time-scale by the spot average convection speed, U_c, obtained in chapter 4—that is $L = -U_c t$. This represents a convenient non-dimensional scaling (when divided by δ_1; the laminar displacement thickness) of time. The length scale, L, would only represent the true streamwise scale if the spot convection speed was constant (i.e., the spot convects as a frozen structure). In fact, it not only varies (slightly) from one spot to the next, but more importantly from spot apex (leading edge) to spot trailing edge. Therefore, the spot planforms shown in figures 6.4 to 6.9 do not represent the exact spatial geometry.

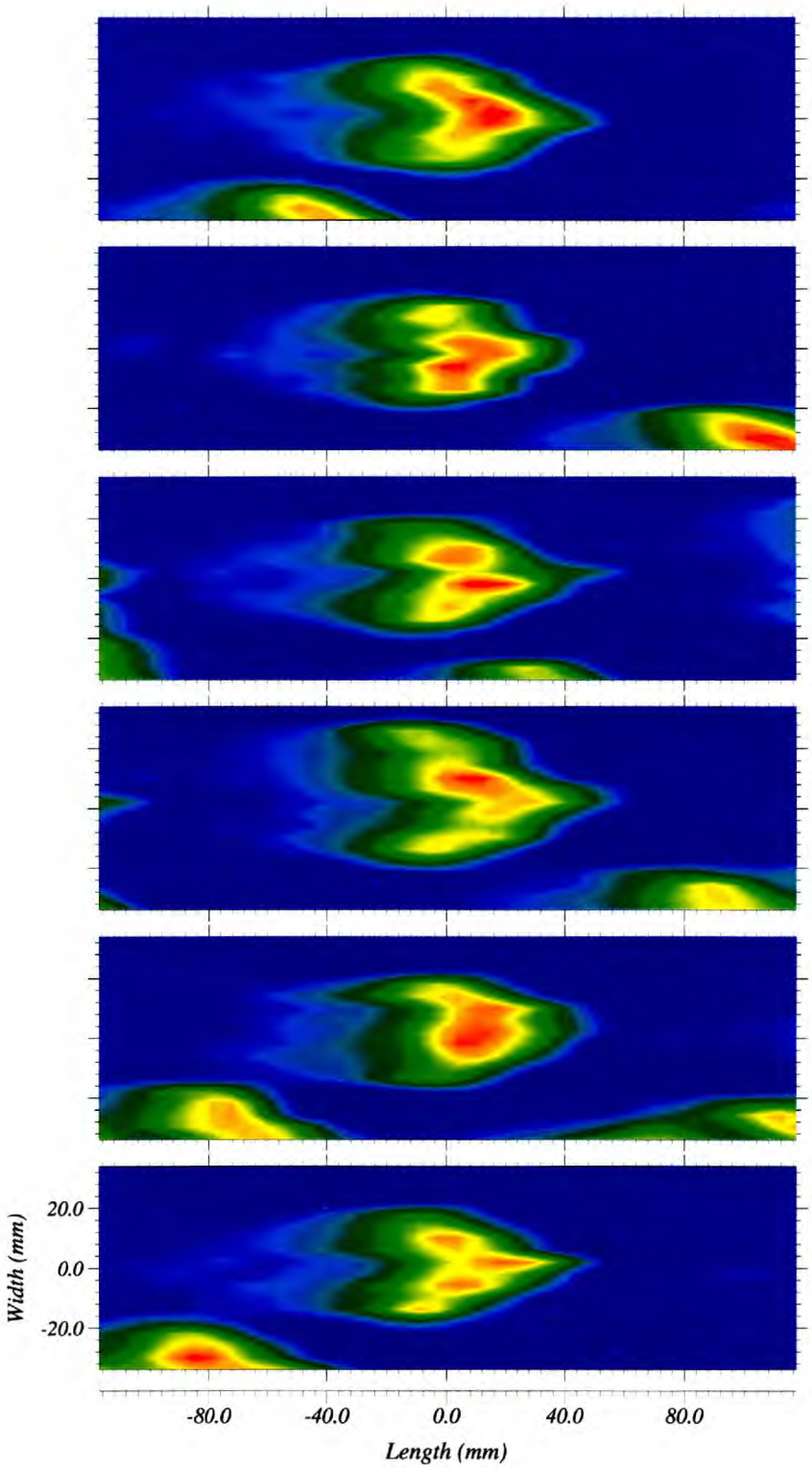

Figure 6.4: Typical thermal footprints of turbulent spots obtained from heat transfer contour plots at $x = 213$ mm. The length scale $L = -tU_c$ is achieved assuming a frozen spot average convection speed $U_c = 0.6U_e = 793.4$ m/s.

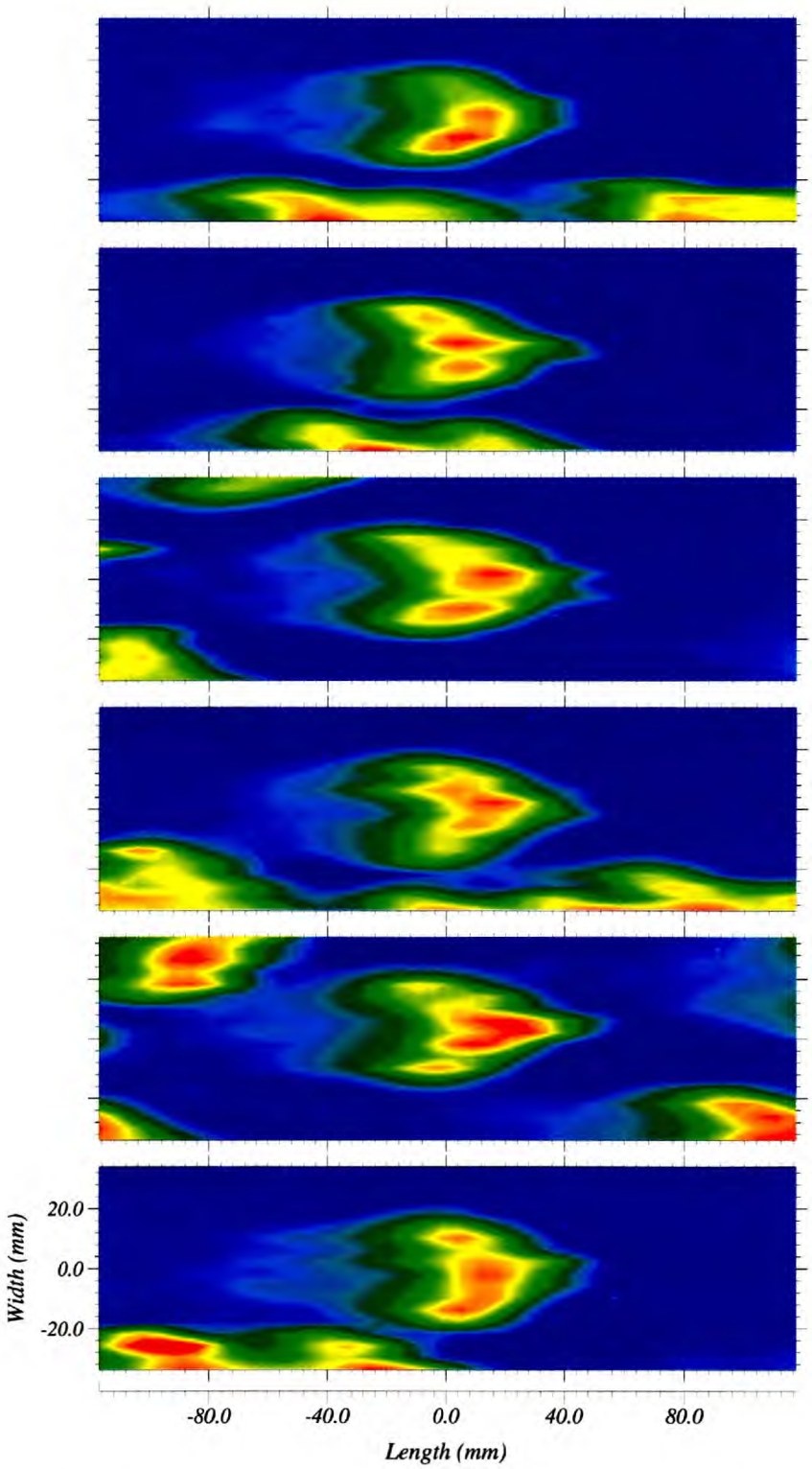

Figure 6.5: Typical thermal footprints of turbulent spots obtained from heat transfer contour plots at $x = 213$ mm. The length scale $L = -tU_c$ is achieved assuming a frozen spot average convection speed $U_c = 0.6U_e = 793.4$ m/s.

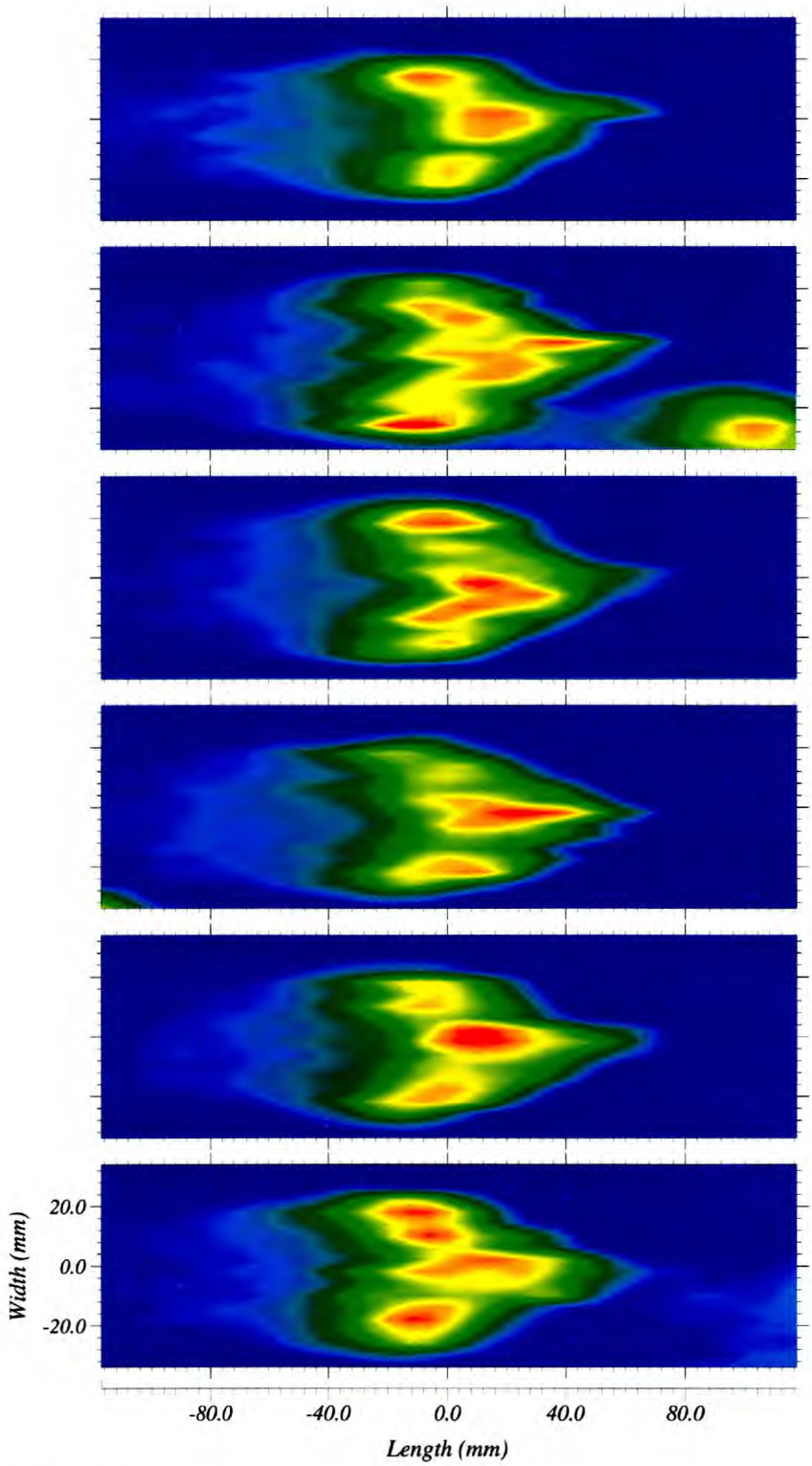

Figure 6.6: Typical thermal footprints of turbulent spots obtained from heat transfer contour plots at $x = 279$ mm. The length scale $L = -tU_c$ is achieved assuming a frozen spot average convection speed $U_c = 0.6U_e = 793.4$ m/s.

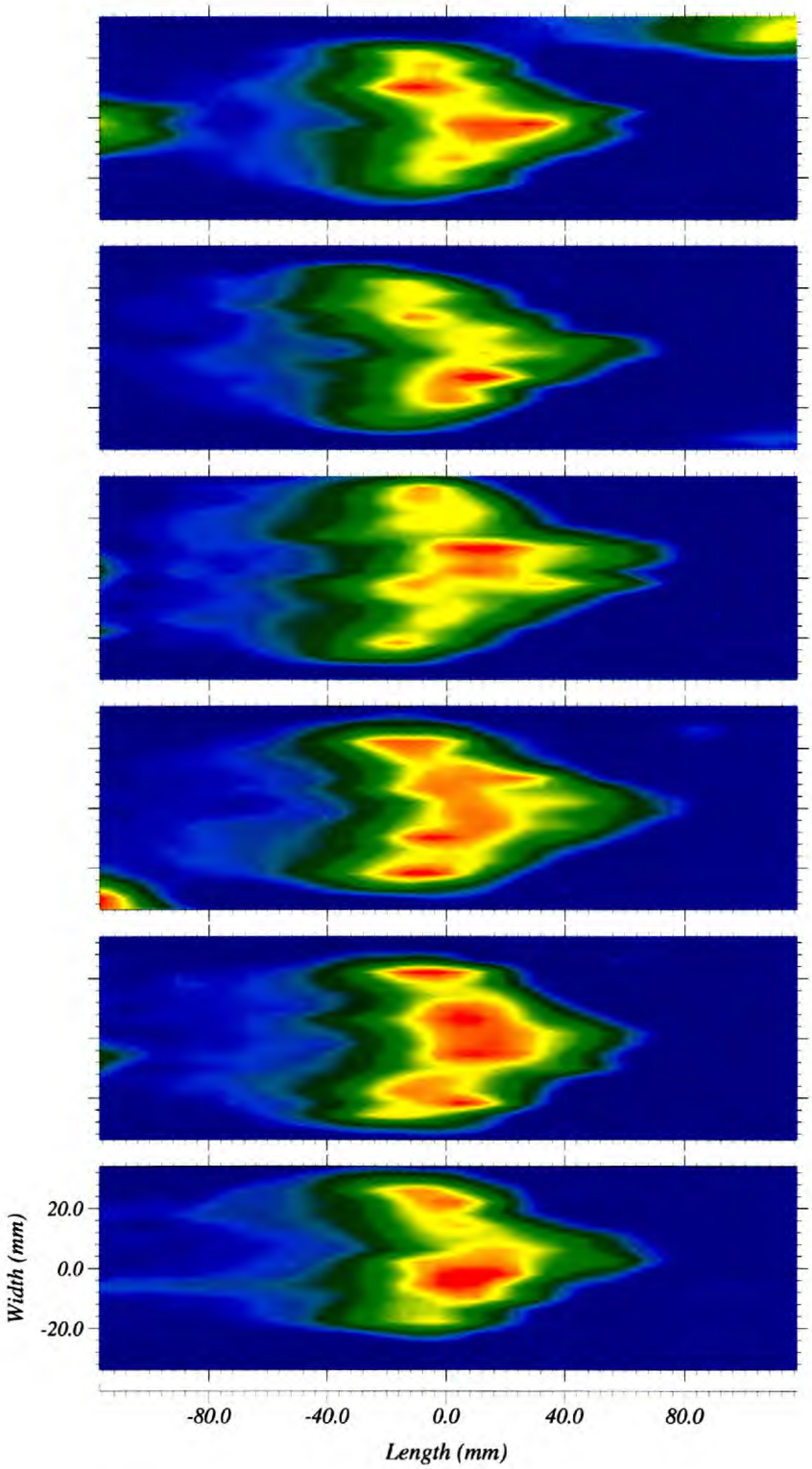

Figure 6.7: Typical thermal footprints of turbulent spots obtained from heat transfer contour plots at $x = 279$ mm. The length scale $L = -tU_c$ is achieved assuming a frozen spot average convection speed $U_c = 0.6U_e = 793.4$ m/s.

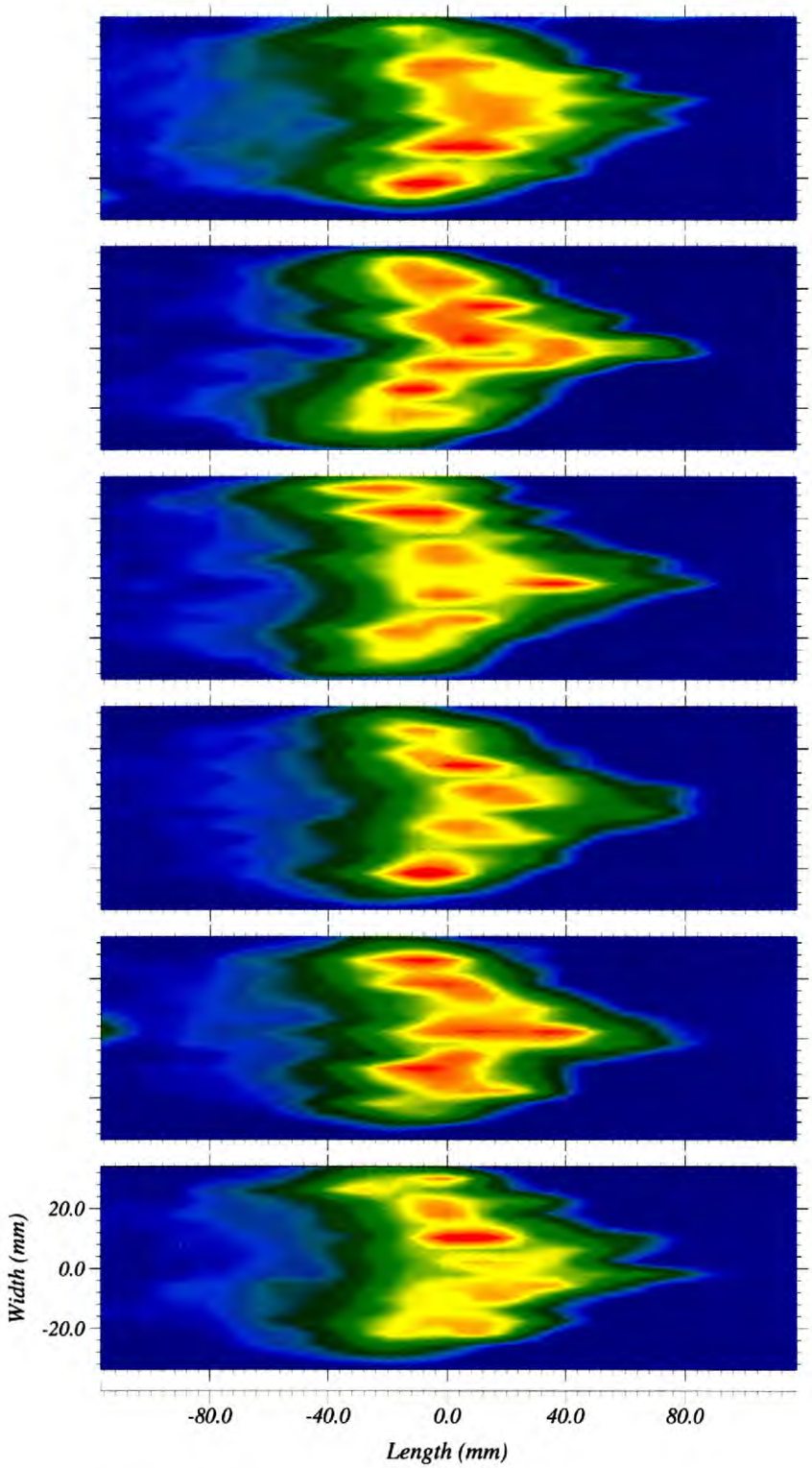

Figure 6.8: Typical thermal footprints of turbulent spots obtained from heat transfer contour plots at $x = 334$ mm. The length scale $L = -tU_c$ is achieved assuming a frozen spot average convection speed $U_c = 0.6U_e = 793.4$ m/s.

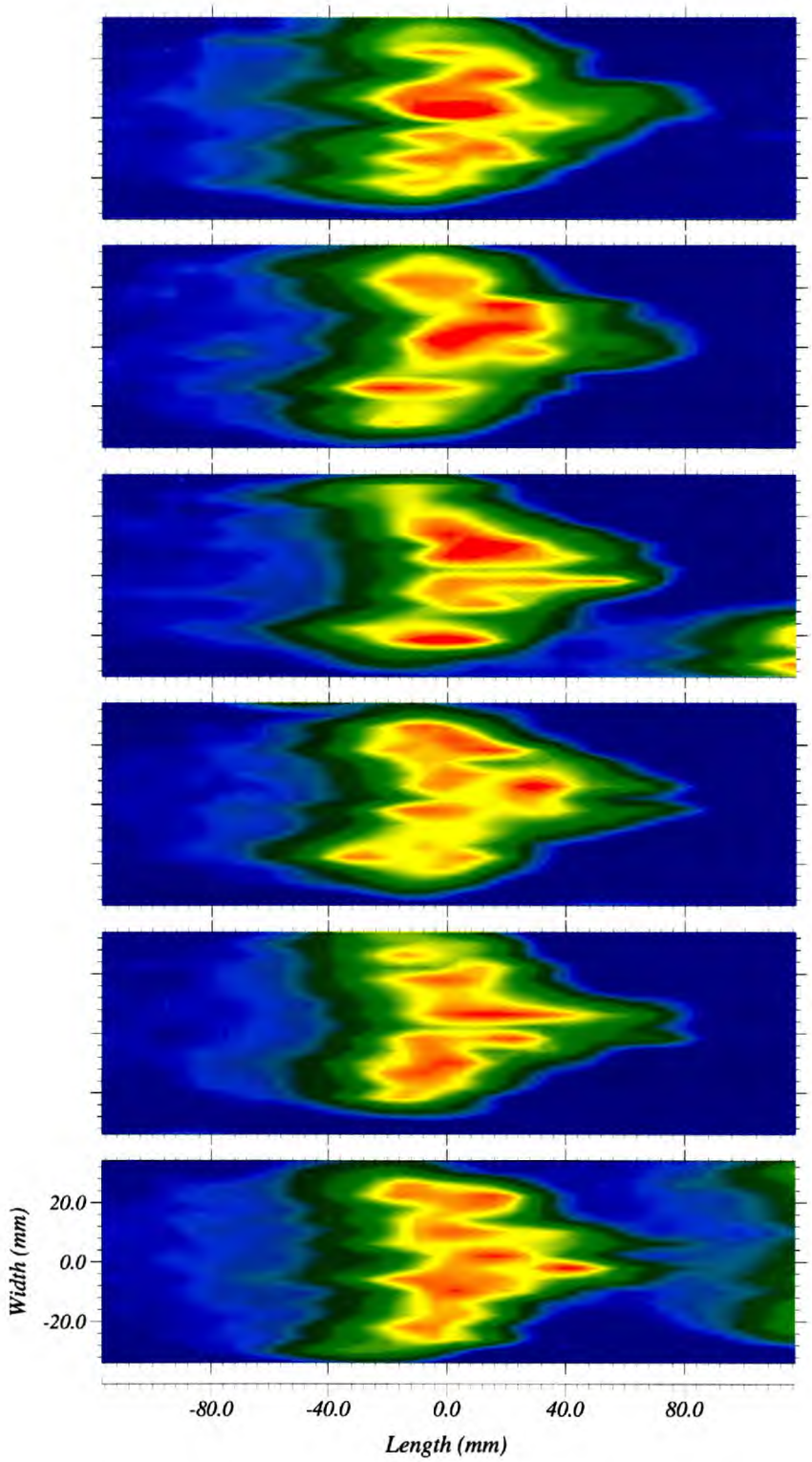

Figure 6.9: Typical thermal footprints of turbulent spots obtained from heat transfer contour plots at $x = 334$ mm. The length scale $L = -tU_c$ is achieved assuming a frozen spot average convection speed $U_c = 0.6U_e = 793.4$ m/s.

The first and most important observation to make is the considerable similarity of the turbulent spot general shape obtained in these flow conditions ($M_e \approx 3.5$) compared to those reported at incompressible speeds (see for example Falco's work[26] reported by Schlichting[81] and shown in figure 1.5). The spot shape also compares well with that obtained by James[42] in similar flow conditions (shown in figure 1.10). The spot depicts an 'elongated heart-like' or 'arrowhead' geometry which includes 'wedge-like' leading edges, a maximum width region, and a wake region. These three different parts of the spot grow with axial propagation, resulting in the growth of the entire turbulent spot. The heat transfer level is highest within the interior of the spot and decreases in all directions towards the surrounding laminar flow. The hot interior displays a 'cellular' pattern which represents internal spot structures (further discussion will be presented later in this chapter). The boundaries of the spot exhibit irregular lines which grow in scale as the spot grows with axial distance.

6.2.2 Spot geometrical parameters

The thermal footprint (heat transfer contour plot) of a typical spot is shown in figure 6.10, which also indicates the definition of the spot geometrical parameters, namely width, w_s, length, l_s, and apex half-angle, θ_s. The spot planform geometry shown in the figure does not represent the true spatial geometry (as discussed in the previous section). However, provided that the spot physical scale is assessed at the mid-point of its time history (midway between the spot apex and base reaching the sensor location), the length l_s is in fact close to the actual physical length of a spot at a fixed instant (figure 6.11). If T_s is the time elapsed between the spot apex (convecting at a velocity U_f) first attaining a gauge location—at a time t_f—and the spot trailing edge (convecting at a velocity U_b) just passing it—at a time t_b, then:

$$T_s = t_b - t_f \tag{6.1}$$

$$X_f = 0.5 T_s U_f \tag{6.2}$$

$$X_b = 0.5T_sU_b \tag{6.3}$$

Thus,

$$l_s = X_f + X_b = 0.5T_s(U_f + U_b) = [0.5(U_f + U_b)]T_s = U_cT_s \tag{6.4}$$

Therefore, multiplying time by mean convection speed, as carried out in figure 6.10, provides a close estimate of the spot length provided, as stated above, that the estimate is made at the mid-point of the spot time history. It is useful to note that if the spot length is estimated at the instant that the spot apex or spot base, respectively, reach the sensor, the equivalent spot lengths would be given by the scalings $l_f = U_bT_s$ and $l_b = U_fT_s$ (figure 6.11).

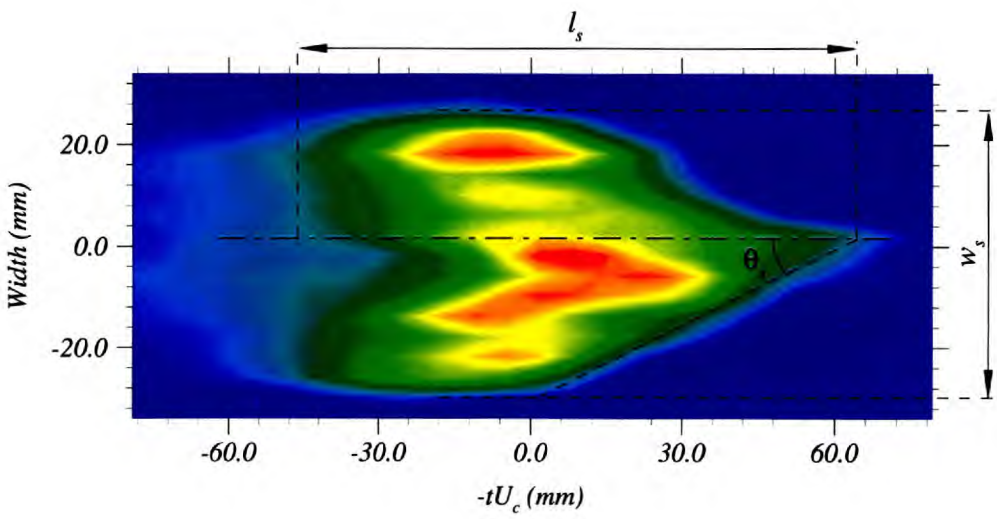

Figure 6.10: Thermal footprint (heat transfer contours) of a typical turbulent spot, indicating the spot length, l_s, width, w_s, and apex half-angle, θ_s.

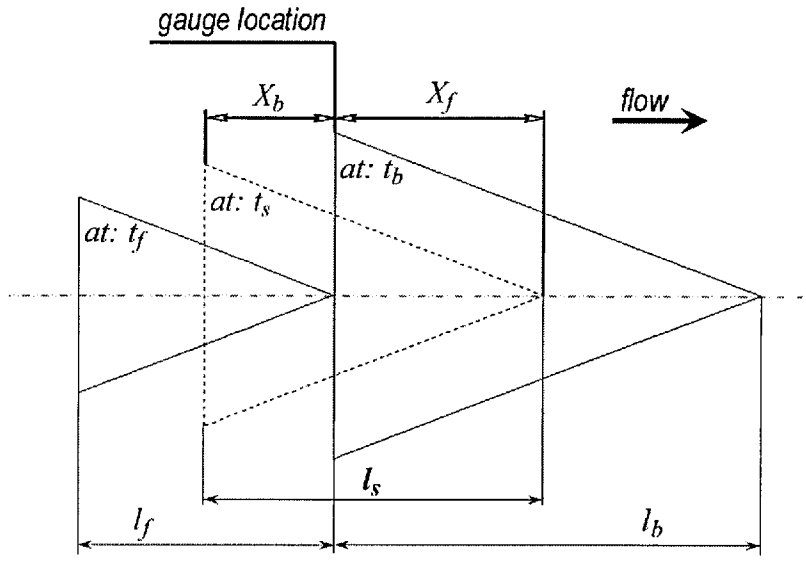

Figure 6.11: Schematic of a spot convecting across a gauge location including the various spot lengths, l_f, l_b and l_s.

The experimental uncertainties associated with the spot parameters are evaluated as ± 4 mm in terms of w_s (4 mm being the spacing between two neighbouring gauges), ± 6.35 mm in terms of l_s (125 kHz frequency of measurement × U_c = 793.4 m/s) in addition to ± 5% uncertainty associated with the determination of the spot back due to the presence of the wake region, and approximately ± 4.0 to 5.5 degrees in terms of θ_s (combination of all the errors described above).

The examination of the large number of spot thermal footprints, similar to those of figures 6.4 to 6.9, determined from the accumulated circumferential heat transfer data obtained at the three measurement locations, x = 213 mm, x = 279 mm, and x = 334 mm, allowed the extraction of the associated geometrical characteristics. The average spot geometrical parameters together with the fully laminar and fully turbulent CFD predictions of the boundary layer thicknesses are summarised in table 6.1.

parameter	$x = 213\ mm$	$x = 279\ mm$	$x = 334\ mm$
$\delta\ (mm)$	1.984	2.379	2.712
$\delta_1\ (mm)$	0.613	0.780	0.917
$\delta_2\ (mm)$	0.196	0.233	0.262
$\delta_{1,T}\ (mm)$	1.121	1.573	1.957
$\delta_{2,T}\ (mm)$	0.379	0.499	0.593
$w_s\ (mm)$	39.9 (±10.9%)	54.9 (±7.8%)	66.0 (±6.6%)
$l_s\ (mm)$	88.6 (±13.1%)	117.3 (±11.1%)	136.2 (±10.3%)
$\theta_s\ (deg)$	23.1 (±24.0%)	23.4 (±18.9%)	23.9 (±16.8%)
w_s/l_s	0.450 (±24.0%)	0.468 (±18.9%)	0.484 (±16.8%)
w_s/δ	20.10 (±10.9%)	23.06 (±7.8%)	24.33 (±6.6%)
l_s/δ	44.67 (±13.1%)	49.31 (±11.1%)	50.23 (±10.3%)
w_s/δ_1	65.06 (±10.9%)	70.34 (±7.8%)	71.96 (±6.6%)
l_s/δ_1	144.56 (±13.1%)	150.40 (±11.1%)	148.54 (±10.3%)
w_s/δ_2	203.47 (±10.9%)	235.49 (±7.8%)	251.87 (±6.6%)
l_s/δ_2	452.13 (±13.1%)	503.49 (±11.1%)	519.89 (±10.3%)
w_s^+	6144 (±10.9%)	7302 (±7.8%)	7956 (±6.6%)
l_s^+	13652 (±13.1%)	15611 (±11.1%)	16423 (±10.3%)

Table 6.1: Average spot geometrical parameters, width w_s, length l_s, and apex half-angle θ_s. δ, δ_1, and δ_2 are the laminar boundary layer thickness, displacement thickness, and momentum thickness respectively. $\delta_{1,T}$ and $\delta_{2,T}$ are the fully turbulent displacement and momentum thicknesses respectively. w_s^+ and l_s^+ are the average spot width and length in wall scale units as predicted by the turbulent CFD simulation.

6.3 Spot spatial development

6.3.1 Spot width and length

The variation of the spot width, w_s, and length, l_s, with axial distance are plotted in figures 6.12 and 6.13. The data include both fully captured spots, i.e., located well within the spanwise measurement window such as those presented in figures 6.4 to 6.9, and partially captured spots where over half of the spot width is detected. In the latter case, the total width is equivalent to twice the transverse distance between the edge and the 'centreline' of the spot. The scatter in the data illustrates the difference in spot size obtained at each axial location, not only emphasising the level of measurement uncertainties, but also the difference in the location where each individual spot forms and the manner it subsequently evolves.

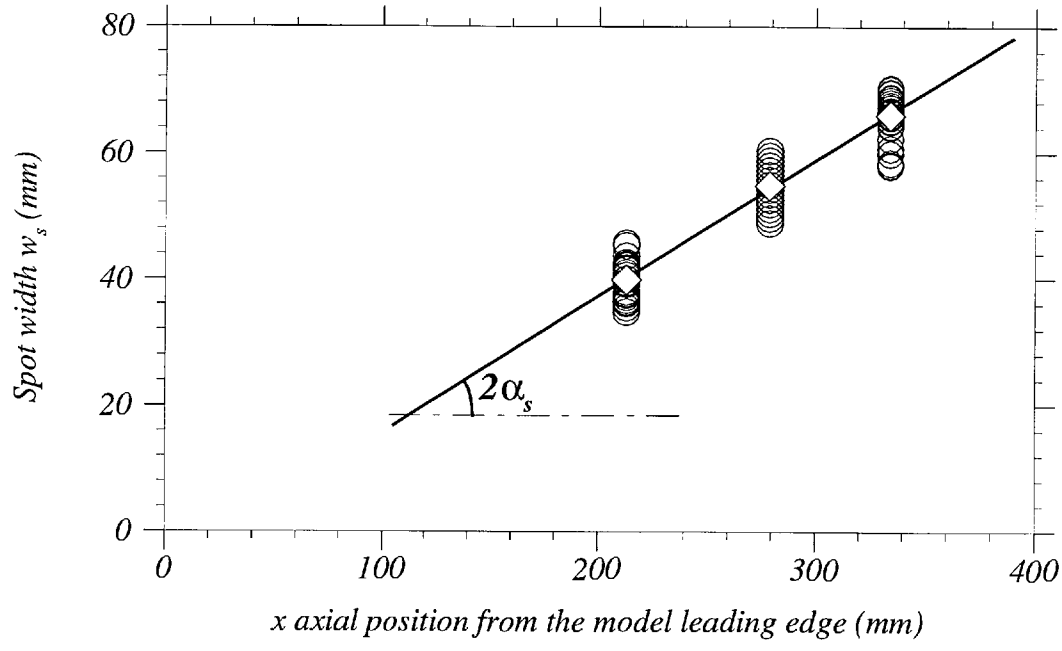

Figure 6.12: Variation of spot width, w_s, with axial distance. Open symbols, individual spot width estimates; solid symbols, spot average width estimates. α_s is the spot lateral spreading half-angle.

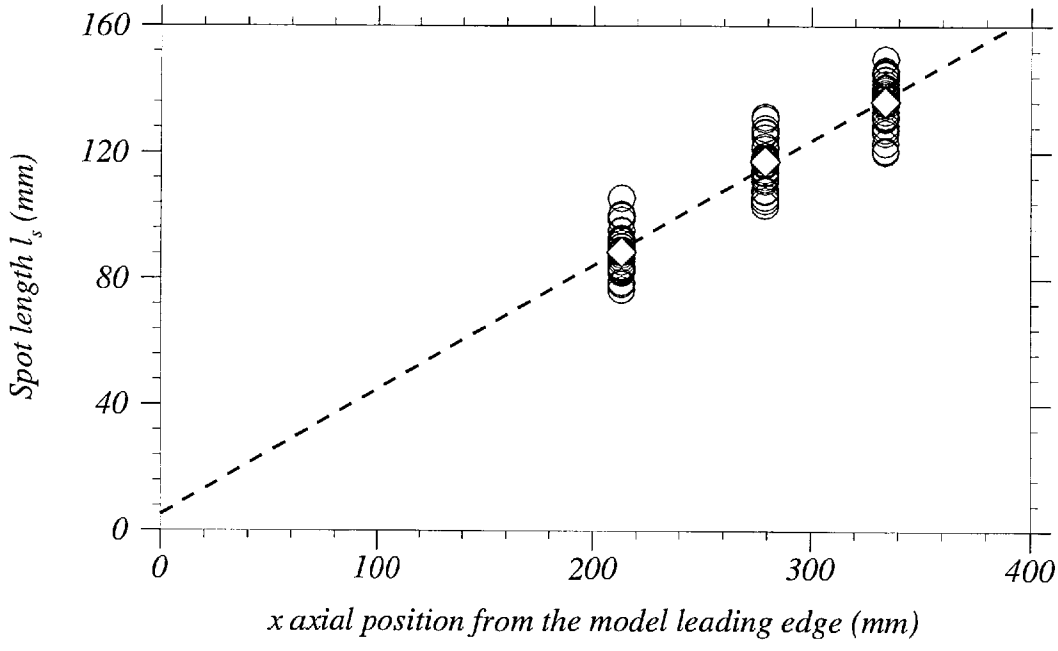

Figure 6.13: Variation of spot length l_s with axial distance. Open symbols, individual spot length estimates; solid symbols, spot average length estimates.

Despite the measurement uncertainties involved with the determination of the spot parameters, the figures show a clear growth with distance in the average spot length and width, confirming the general growth of the spot. The discrete points show an overlap in width and length estimates from one location to another. This means that some of the spots obtained at $x = 213$ mm are bigger than those obtained at $x = 279$ mm and, in the same way, the ones at 279 mm compared to those at 334 mm. Consequently, as all the spots are assumed to evolve within the same flow and model conditions in each individual run (i.e., good repeatability of the experiments), the bigger spots captured at $x = 213$ mm are produced at axial locations further upstream of the smaller spots captured at $x = 279$ mm.

Figure 6.12 allows the estimation of the spot half-angle lateral spreading rate, α_s, at approximately 6.2 ± 1.45 degrees, assuming a linear growth with distance. This trend also indicates a main spot production region near the model apex, extending from $x = 0$ to approximately $x = 60$ mm. The linear growth assumption is a good approximation since the variation in boundary layer edge conditions across the measurement length (i.e., between $x = 213$ mm and $x = 334$ mm) is not very significant. The latter is estimated from the laminar CFD predictions at approximately 6% increase in terms of boundary layer edge Mach number, M_e, and about 25% decrease in terms of boundary layer edge static pressure p_e (presence of a streamwise favourable pressure gradient, $\partial p/\partial x < 0$). In the author's knowledge, no study of streamwise pressure gradient effects on turbulent spot growth has been performed in the hypersonic regime. Therefore, no formulation exists in the literature which relates spot lateral spreading rate half-angle, α, to the amount of streamwise pressure gradient $\partial p/\partial x$. On the other hand, studies at incompressible speeds, such as Narasimha[69] and Zhong,[116] reported a reduction in spot and wedge lateral growth rates in the presence of a favourable pressure gradient, compared with their counterparts at zero pressure gradient. This reduction becomes more significant as the gradient level intensifies. Furthermore, Clark et al.[16,17] and Seifert et al.[88] reported increased spot spreading rates in the presence of an adverse pressure gradient in

both incompressible and compressible boundary layers.

With regards to the effect of boundary layer edge Mach number, M_e, the theoretical work of Fischer[28] and Doorly et al.[23] suggest a slight reduction with distance in the lateral spreading rate associated with the increase in the boundary layer edge Mach number.

The spot spreading half-angle, α_s, estimated from figure 6.12, is somewhat higher than that suggested, at the corresponding boundary layer edge Mach number range ($3.43 < M_e < 3.61$), by Fischer[28] of between 3.3 to 5.5 degrees and Doorly et al.[23] predictions—$\alpha_s = tan^{-1}(3^{-3/2}2^{1/2}M_e^{-1})$—of approximately 4.4 degrees. It is unclear whether this difference is of significance since Fischer's tabulated data took into account both individual spot and wedge growth rates, which have been found to be different in low speed (e.g., Schubauer[86]). While the lower band of the experimental value obtained (taken into account measurement uncertainties, $4.7 < \alpha_s < 7.6$ degrees) is still located within Fischer's interval, it is most likely that this difference is related to the presence of a streamwise pressure gradient, weak in the region of measurements but stronger in the spot production zone near the model apex. The difference might also be attributed to the intricacy in defining an exact boundary of a spot, which is bounded by the resolution of the measurements made.

The evolution of the spot length, l_s, with axial distance appears to follow the same trend as the spot width, w_s, along the measurement region (figure 6.13). On the forebody zone however, the growth trend is not known, but clearly the effects of large flow gradients, in terms of both streamwise pressure and Mach number, are significant.

6.3.2 Dimensionless spot width and length

Figures 6.14 and 6.15 represent the same data illustrated in figures 6.12 and 6.13, but this time, in wall scale units obtained from the fully turbulent CFD simulation. The figures highlight the large physical scale of the measured spots at large distances

from the model apex. This is further emphasised in figures 6.16 and 6.17, which illustrates the average values of the spot width and length normalised by the local laminar boundary layer thickness, displacement thickness, and momentum thickness, δ, δ_1, and δ_2 respectively. The large physical scale of the spots, in addition to the good comparison of the heat transfer distribution obtained from the fully CFD prediction with that across the turbulent spots (the peak heating rates in the time-dependent signals; e.g., figure 6.1), implies some similarities in structure between fully developed turbulent flows and sufficiently grown turbulent spots.

Given the associated experimental uncertainties, the spot average width and length, expressed in terms of the displacement thickness, δ_1, seem to barely vary with axial distance (figures 6.16 and 6.17), at least at these distances from the model apex where the spots are sufficiently developed. Indeed, the spot thermal footprints shown in figure 6.18 appear to have similar widths and lengths, w_s and l_s respectively, at all three measurement locations. This result translates itself as *self-similar* or 'near' *self-similar* streamwise and spanwise growths of a turbulent spot. It concludes that for sufficiently developed spots far downstream of their inception point, the spot maximum streamwise and spanwise scales and growth directly scale with the local laminar displacement thickness; that is:

$$\frac{w_s}{\delta_1} = C_1 \tag{6.5}$$

$$\frac{l_s}{\delta_1} = C_2 \tag{6.6}$$

$$2\tan\alpha_s = \frac{w_s}{x} = C_1\frac{\delta_1}{x} \tag{6.7}$$

$$\frac{l_s}{x} = C_2\frac{\delta_1}{x} \tag{6.8}$$

where C_1 and C_2 are constants which depend on flow conditions. This result illustrates the reduction in spot growth rates with increasing model nose radii.

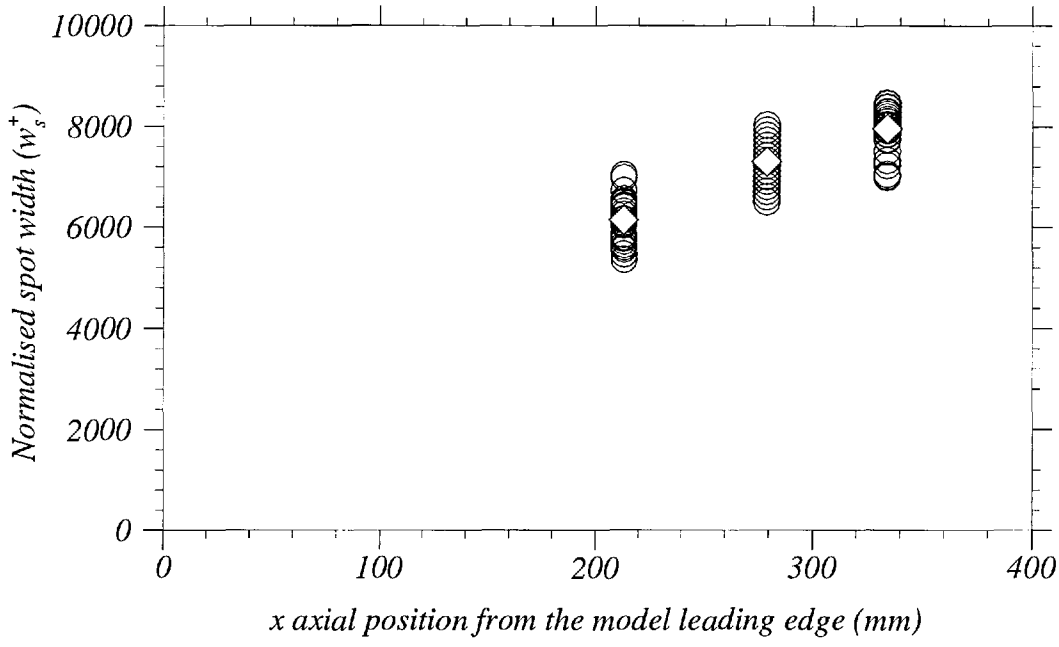

Figure 6.14: Variation of spot width in turbulent wall scale units, w_s^+, with axial distance. Open symbols, individual spot estimates; solid symbols, average estimates.

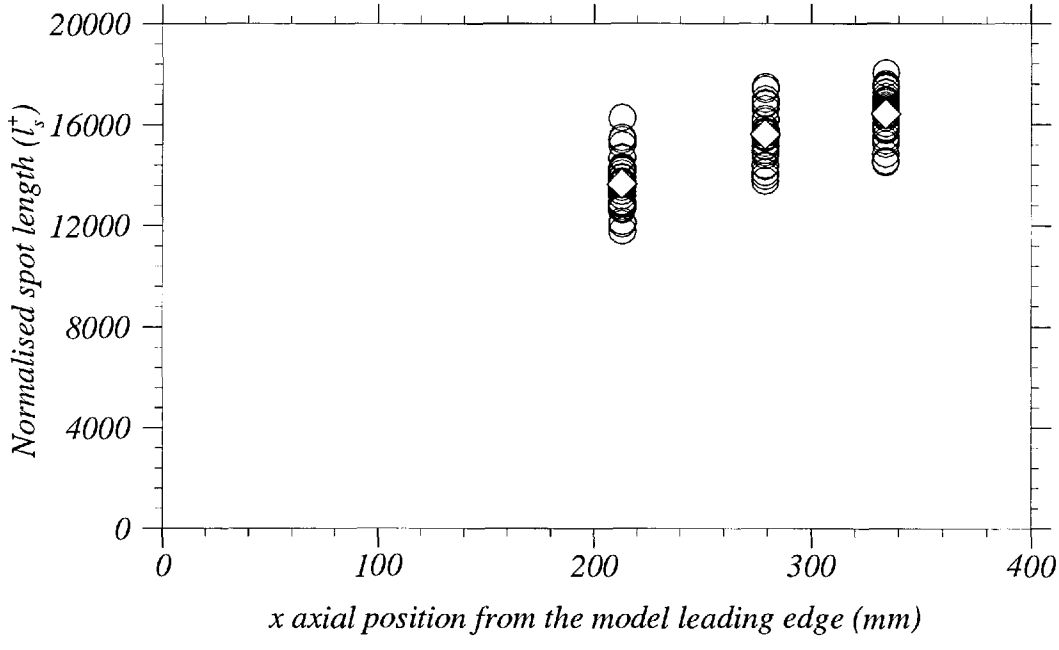

Figure 6.15: Variation of spot length in turbulent wall scale units, l_s^+, with axial distance. Open symbols, individual spot estimates; solid symbols, average estimates.

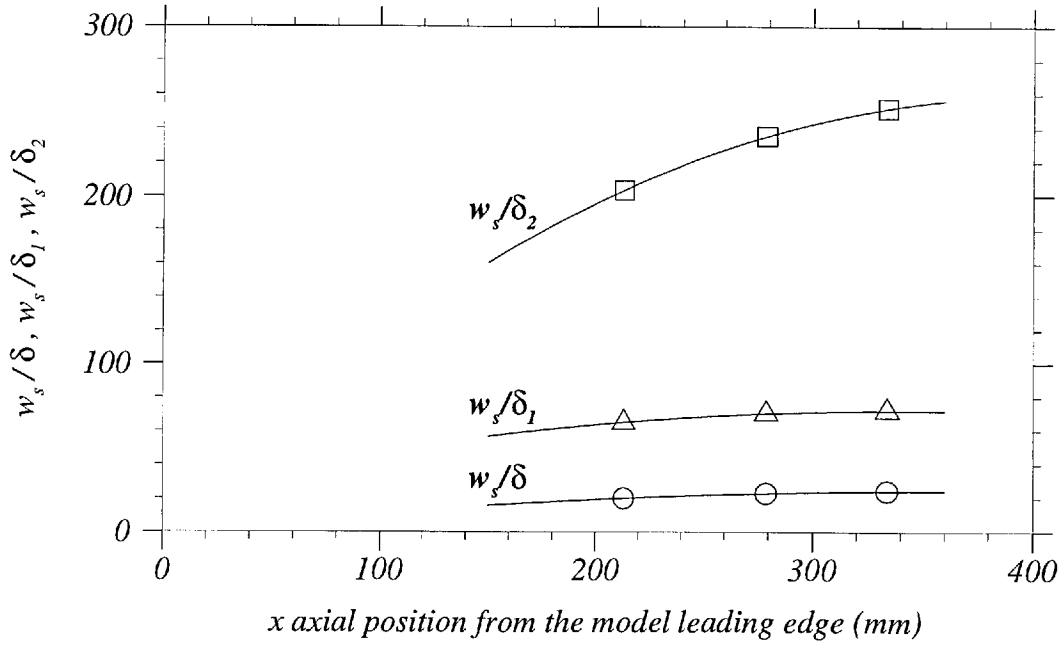

Figure 6.16: Variation of spot width normalised by the laminar boundary layer thicknesses, w_s/δ, w_s/δ_1 and w_s/δ_2, with axial distance.

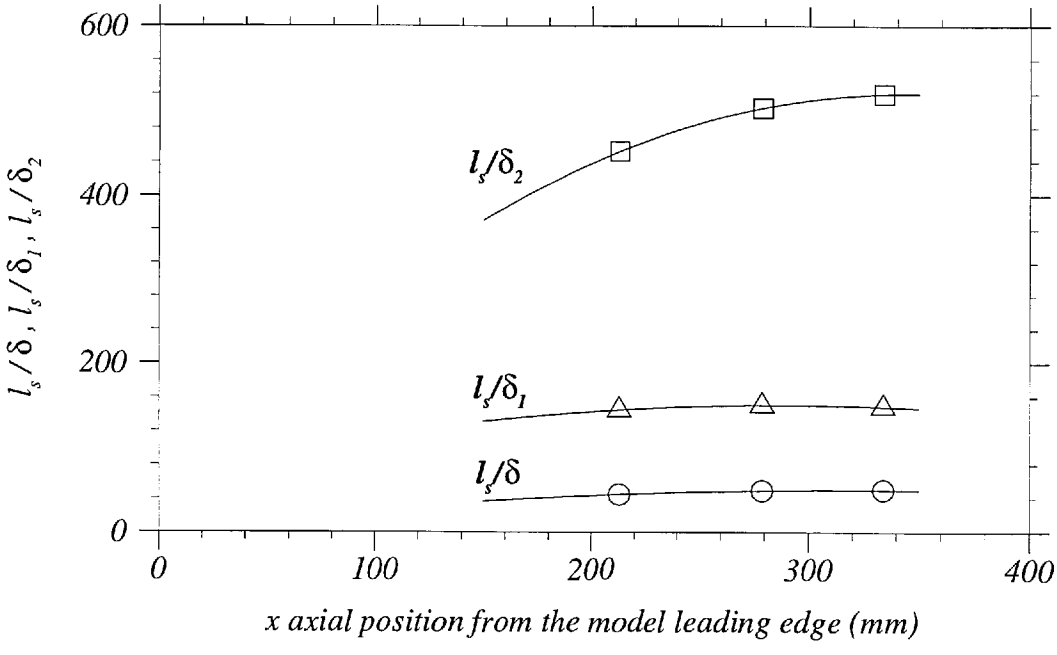

Figure 6.17: Variation of spot length normalised by the laminar boundary layer thicknesses, l_s/δ, l_s/δ_1 and l_s/δ_2, with axial distance.

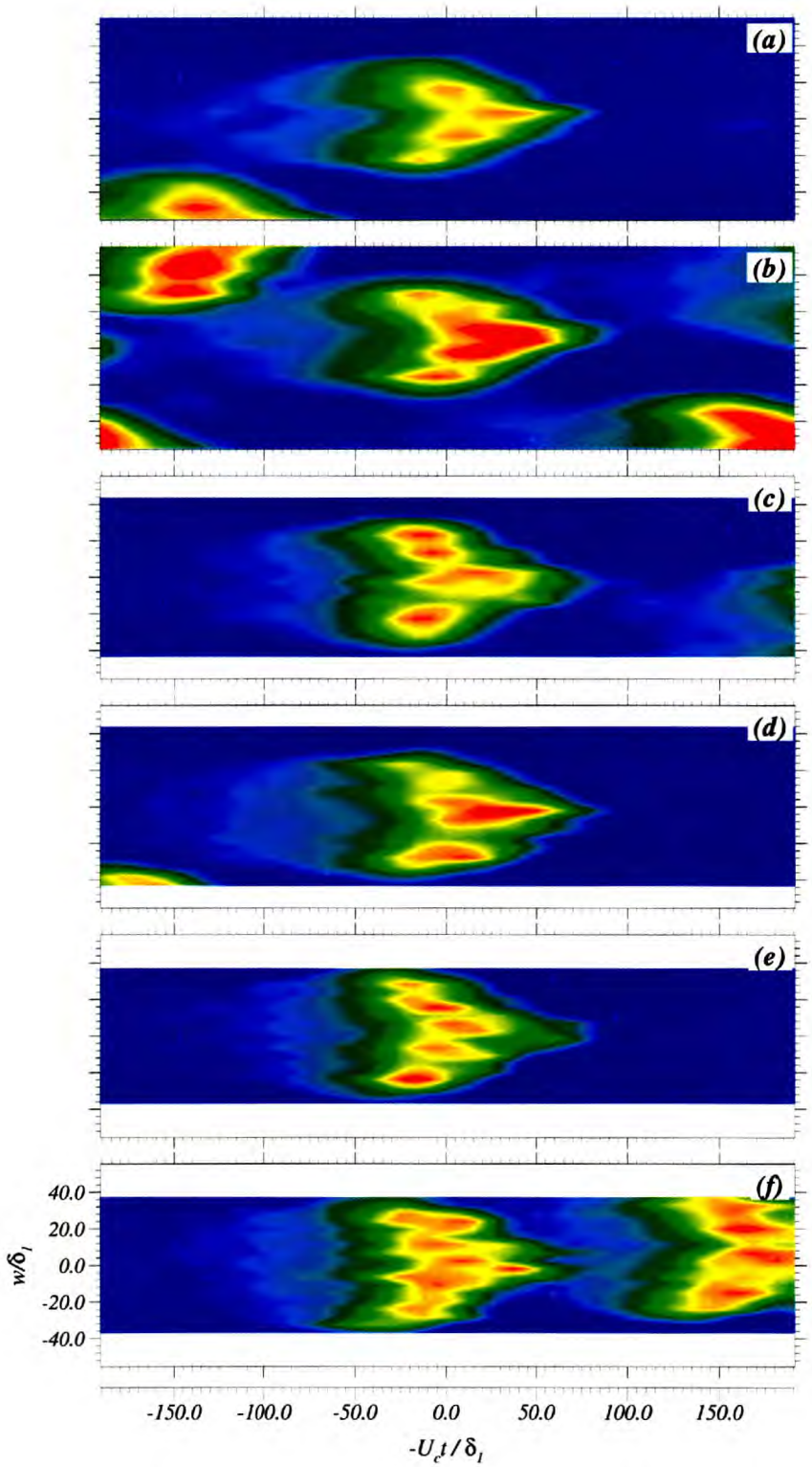

Figure 6.18: Heat transfer contour plots at; (a) and (b) $x = 213$ mm; (c) and (d) $x = 279$ mm; (e) and (f) $x = 334$ mm. The ordinate is w/δ_1, the spanwise distance normalised by the local boundary layer displacement thickness δ_1. The abscissa is $L = -tU_c/\delta_1$, where t is time and U_c is the spot average convection speed.

6.3.3 Spot apex half-angle

The evolution of the spot average apex half-angle, θ_s, displays a very small increase with axial distance (figure 6.19). The variation of the spot width to length ratio, w_s/l_s, depicts similar trend but at a slightly higher growth rate. This suggests that the spanwise growth rate of the spot is greater than its streamwise counterpart. The direct comparison of the two slopes of figure 6.19 (i.e. $d(tan\theta_s)/dx$ versus $d(w_s/l_s)/dx$) suggests that the fraction of the spot that contains the triangular front grows in length with axial distance, an observation which is further supported by examination of spot planforms presented in figure 6.18. It is important however, to emphasise that these trends are observed in the presence of experimental uncertainties which are larger than the actual amount of change in these parameters over the measurement length (see figure 6.19 and table 6.1) and therefore their occurrence cannot be conclusively established.

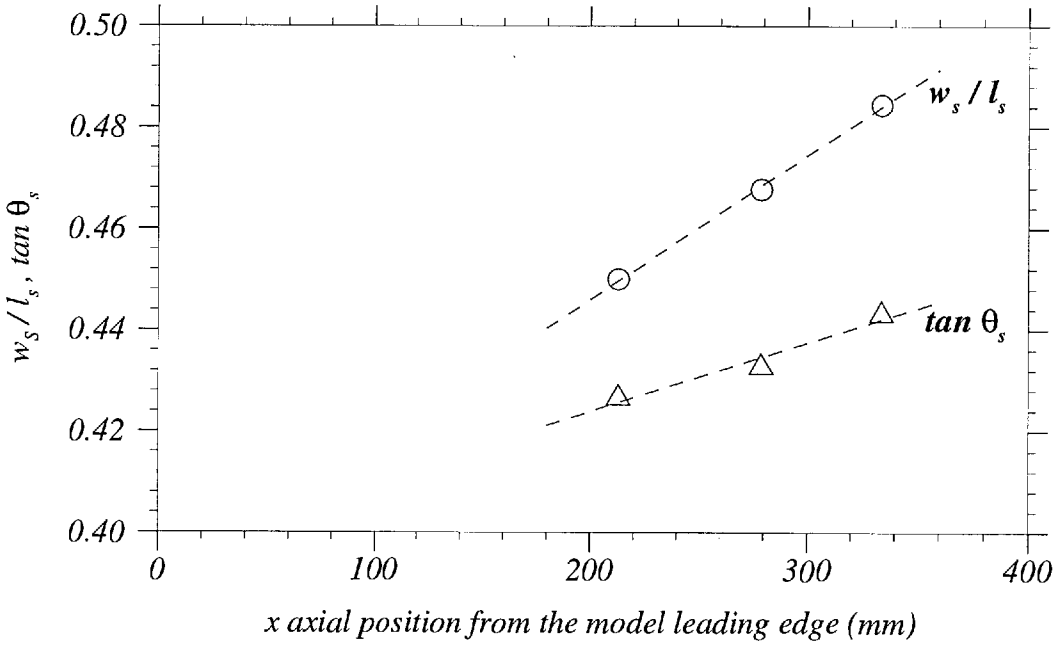

Figure 6.19: Variation of spot width-to-length ratio, w_s/l_s, and spot apex half-angle, θ_s, with axial distance.

6.4 Spot inception

Figure 6.12 suggests a spot production region near the model apex, extending from the hemi-spherical nose up to approximately $x = 60$ mm. The transition trigger can be related to either surface roughness, freestream disturbance environment or both. The latter comprises freestream noise (i.e., temperature, pressure, and vorticity fluctuations), particulates, and turbulence intensity. These factors define and shape the disturbance environment which the laminar flow has to accommodate leading eventually to its breakdown to an intermittent flow.

The formation of turbulent spots within the model apex region suggests high receptivity of the boundary layer to disturbances (both freestream and surface roughness). The boundary layer thickness in this region, obtained from the laminar CFD predictions, is estimated to vary between approximately 0.08 mm at the stagnation point to about 0.4 mm at $x = 60$ mm. It is clear that discrete surface roughness resulting from particulates hitting the model during experimentation can be considered as the transition trigger. As mentioned in chapter 5, there is no apparent correlation between the accumulated damage of the model after each run and the run-to-run variation in intermittency level. This implies that the presence of random sizes and shapes of roughness has a different effect on the transition onset location, either immediately behind the roughness location or further downstream, thus on the resulting physical scale of the spots measured downstream.

The external disturbances mentioned earlier no doubt contribute to the instability of the laminar boundary layer. However, it is important to emphasize that the noise generated from the nozzle wall in particular is most likely to occupy the whole circumference surrounding the model. In this case the turbulence would manifest itself as a large amalgam of various spots, which covers the entire model circumference, rather than discrete events. In effect, some experiments demonstrated the presence of these amalgams of spots, which were disposed of by changing the location of the model in the test section.

The discussion given above relied upon observations made from experimental data that were obtained at distances well downstream of the spot inception region. This did not allow the resolution of the actual process of spot formation, but at these measurement distances, spots are well developed and thus they are expected to be independent of the mechanisms by which they were produced.

6.5 Spot substructure

Despite the uncertainties associated with the experimental resolution, the spot thermal footprints presented in figures 6.4 to 6.9, revealed spatial variation in heat transfer level across the turbulent spots. This variation represents actual internal 'cellular' structure within the spots rather than possible gauge-to-gauge variation. To better reveal these structures, some of the spot thermal footprints presented in figures 6.4 to 6.9 are illustrated in figure 6.20, but now indicating the streamwise and spanwise locations where heat transfer profiles are taken and shown in figures 6.21 to 6.32. The spots are presented in a length scale normalised by the local computed laminar boundary displacement thickness δ_1. The number of these *hot* cells, the magnitude and scale of the spot leading edge irregularities, and the streamwise extent of the delta-like fraction and wake region of the spot increase with the increase in overall scale of the spot with axial distance (figures 6.4 to 6.9 and 6.20).

Figures 6.21 to 6.32 illustrate heat transfer profiles of spots obtained at the three various axial locations, $x = 213$ mm (figures 6.21 to 6.24), $x = 279$ mm (figures 6.25 to 6.28), and $x = 334$ mm (figures 6.29 to 6.32). There is an increase with axial distance in the overall heat transfer level across the spot with respect to the computed laminar value. Once again, this conforms to the trend of the laminar and fully turbulent CFD predictions presented in chapter 3. The streamwise distributions show a sharp increase in heat transfer level from the laminar value to the turbulent value which somewhat varies according to the corresponding spanwise location (figures 6.21, 6.23, 6.25, 6.27, 6.29, and 6.31). The heat transfer then

drops to a level higher than the laminar value at the spot trailing edge, which approximately corresponds to the start of the spot wake region. The heat transfer level continues to decrease gradually across the wake region until it reaches back to the laminar value.

The figures mentioned above generally display a larger slope in heat transfer in the spot forward region compared to its counterpart in the rearward region. The peak value in heat transfer varies from one 'hot' cell to another in the spanwise direction. The turbulent peak value appears to be around the spot centreline (figures 6.22, 6.24, 6.28, and 6.32), but occasionally takes place at other transverse locations (figures 6.26 and 6.30).

The 'cellular' structure inside the spots is further emphasised in figures 6.21, 6.23, 6.25, 6.27, 6.29, and 6.31. The transverse profiles demonstrate peak heating across the cells which increase in number from the spot leading edges towards the trailing edges. This number increase and the overall heat transfer spanwise distributions do not occur symmetrically across the spot. The plots, once more, show the increase in cell numbers as the spot grows with axial distance.

The important observations made regarding the spot 'cellular' internal structure, leading edge irregularities, and wake region extent, agree with the theory put forward by Perry et al.[70] In their experimental work on the internal structure of turbulent spots within an incompressible flat plate boundary layer, Perry et al.[70] discovered that a turbulent spot is composed of an array of Λ-shaped vortices which form initially as one undulated vortex filament developed right behind the disturbance location (figure 6.33-a). This filament stretches and laterally induces a new undulation on each side, which in turn evolve and induce new undulations (figure 6.33-b). This cascade nature of the process leads to the formation and development of the turbulent spot as shown in figure 6.33-c.

Although the boundary layer edge conditions in the present study and Perry's work are completely dissimilar (present study $M_e \approx 3.5$ and $Re_e \approx 3.1$ $million/m$, Perry et al. $M_e \approx 0$ and $Re_e \approx 53125/m$), it appears that the mechanisms which

drive the development of the turbulent spot once formed are independent of the flow regime. This conclusion is based merely upon the qualitative assessment performed on spot planforms, hence excluding the mechanisms contributing to the birth of the spots (i.e., instability and laminar breakdown).

To further support this conclusion, a quantitative assessment of the cellular structure of the measured spot planforms is made, allowing the estimation of the 'cell parameter', λ_s, which is defined in figure 6.33 (Perry et al. work[70]) and figure 6.34 (two examples of the present study). The estimates of the parameter λ_s together with the laminar and fully turbulent CFD boundary layer thicknesses are summarised in table 6.2. These estimates are given in absolute value, normalised value by the laminar CFD boundary layer thicknesses, and in wall scale units as predicted by the fully turbulent CFD simulations. The associated experimental errors include gauge-to-gauge spatial resolution, value-estimation (including anti-aliasing effects) and value-averaging errors.

parameter	$x = 213\ mm$	$x = 279\ mm$	$x = 334\ mm$
$\delta\ (mm)$	1.984	2.379	2.712
$\delta_1\ (mm)$	0.613	0.780	0.917
$\delta_2\ (mm)$	0.196	0.233	0.262
$\delta_{1,T}\ (mm)$	1.121	1.573	1.957
$\delta_{2,T}\ (mm)$	0.379	0.499	0.593
$\lambda_s\ (mm)$	16.0 (±38%)	21.1 (±32%)	23.4 (±30%)
λ_s/δ	8.0 (±38%)	8.9 (±32%)	8.6 (±30%)
λ_s/δ_1	26.0 (±38%)	27.0 (±32%)	25.5 (±30%)
λ_s/δ_2	81.4 (±38%)	90.4 (±32%)	89.4 (±30%)
λ_s^+	2458 (±38%)	2802 (±32%)	2823 (±30%)

Table 6.2: Average dimensions of the spot internal cells λ_s. δ, δ_1, and δ_2 are the computed laminar boundary layer thickness, displacement and momentum thicknesses respectively. $\delta_{1,T}$ and $\delta_{2,T}$ are the computed fully turbulent displacement and momentum thicknesses. λ_s^+ is the cell parameter expressed in computed fully turbulent wall scale units.

The evolution of λ_s with axial distance is presented in figure 6.35 and, in wall scale units as predicted by the fully turbulent CFD simulations, in figure 6.36. The average value of λ_s depicts a growth with axial distance in line with the growth in

overall scale of the spot. This growth however is not as apparent in λ_s/δ_1 estimates, which represent cell scales normalised by the computed laminar displacement thickness δ_1 (table 6.2), as they slightly vary with axial distance. Earlier in this chapter (section 6.3.2), the average spot scale was found to exhibit a self-similar or 'near' self-similar growth with axial distance. This, in addition to the fact that the spot internal cell numbers increase with axial distance, imply that the scale of the cells normalised by the laminar displacement thickness, λ_s/δ_1, has to decrease with axial distance. At incompressible speeds, Perry et al.[70] suggested a near-constant λ_s with axial distance, after sufficient downstream development of the spot, a fact which implies a decrease in λ_s/δ_1 with distance in line with the above proposition. On the other hand, the evolution with distance of the absolute scale of the spot internal structure, λ_s, appears to differ between the present case and Perry's findings.

The average values of the spot internal cells scale, λ_s, estimated from both the present study and Perry's work, are given in table 6.3. The latter includes normalised values by the local laminar displacement thickness, λ_s/δ_1, and values expressed in turbulent wall scale units, λ_s^+. The table also shows the corresponding Reynolds number based on the laminar displacement thickness.

parameter	λ_s/δ_1	λ_s^+	Re_{δ_1}	$Re_{\delta_1}/\lambda_s^+$	$Re_{\delta_1}/(\lambda_s/\delta_1)$
Perry et al.[70]	4.1	< 93	449	> 4.9	109
Present study ($\pm$33%)	26.2	2694	2360	0.9	90

Table 6.3: Average dimensions of the spot internal cells, normalised by the laminar displacement thickness, λ_s/δ_1, in turbulent wall scale units, λ_s^+, and normalised by the local Reynolds number based on the laminar displacement thickness, $Re_{\delta_1}/\lambda_s^+$ and $Re_{\delta_1}/(\lambda_s/\delta_1)$.

The normalised cell scale, λ_s/δ_1, is estimated at approximately 26.2, an average over the three axial positions. This value is substantially higher than that reported by Perry et al.,[70] estimated at approximately 4.1. This large difference is further emphasised in terms of turbulent wall scale units, presented in figure 6.36, which gives an average value, λ_s^+, of approximately 2694 compared to less than 93 in Perry's

case (table 6.3). This large scale of the internal structure is believed to be Reynolds number related ($Re_e \approx 3,100,000/m$ in the present study versus $\approx 53125/m$ in Perry's work). While the data show no correlation between the two studies in terms of turbulent wall scale units, $Re_{\delta_1}/\lambda_s^+$ (4.9 in Perry's case compared to 0.9 in the present case), the normalised scale by the laminar displacement thickness relative to the Reynolds number, $Re_{\delta_1}/(\lambda_s/\delta_1)$, correlates very well (90 in the present study versus 109 in Perry's case). In view of the measurements uncertainties, this result is very encouraging and supports a direct scaling between the internal structure of sufficiently developed turbulent spots and the properties of the surrounding laminar flow. It is fairly appropriate to put forward the following formulation:

$$\frac{\delta_1 Re_{\delta_1}}{\lambda_s} \approx constant \tag{6.9}$$

The implication of this finding is that, at sufficiently downstream positions of their inception point, the spot internal structure and the resulting overall spot belong rather to a surrounding laminar flow scaling, than to a fully turbulent wall sub-layer flow. Perry et al.[70] provide no fully turbulent data and hence no conclusion can be drawn regarding the scaling with respect to the turbulent 'outer flow'.

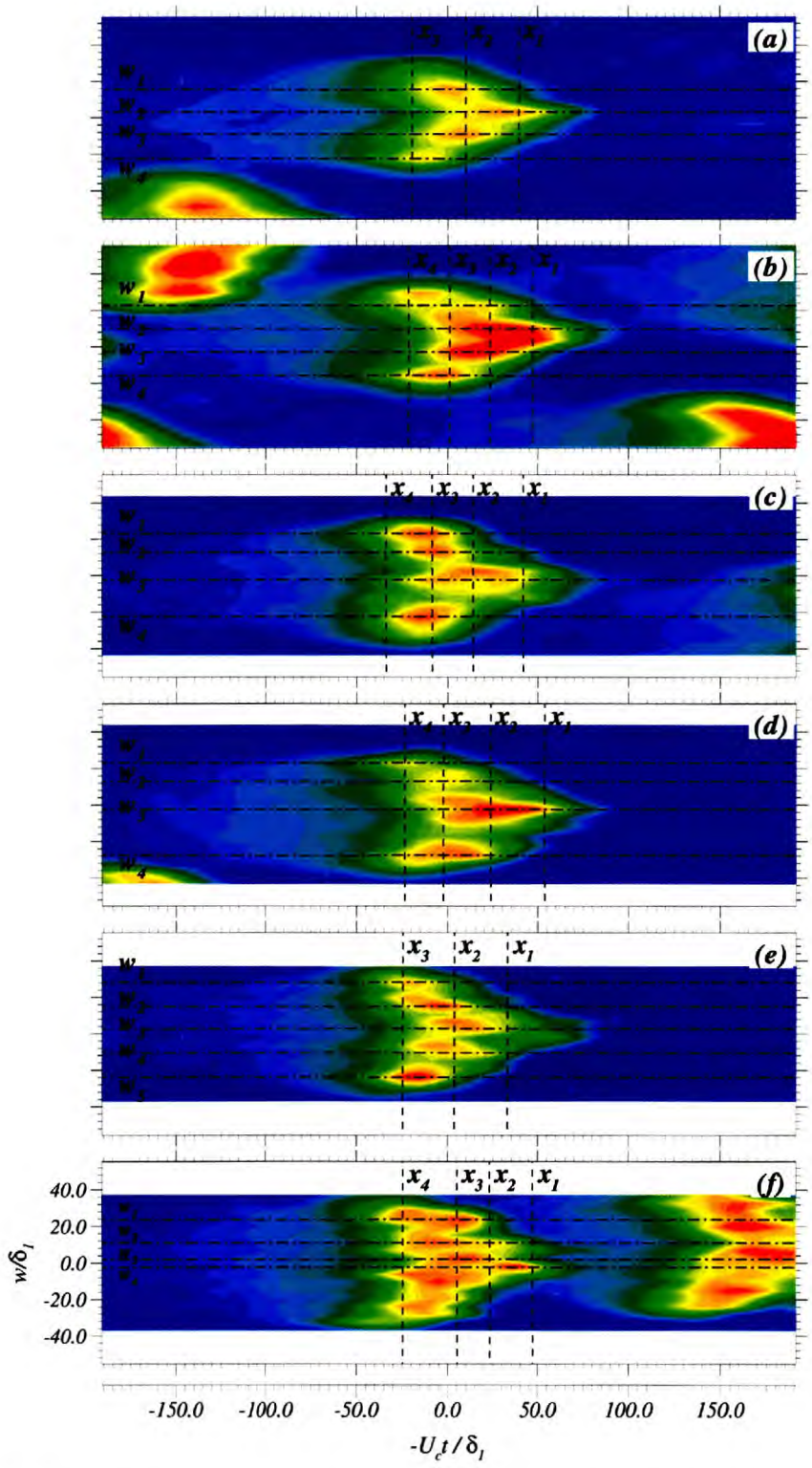

Figure 6.20: Heat transfer contour plots, at (a) and (b) $x = 213$ mm, (c) and (d) $x = 279$ mm, (e) and (f) $x = 334$ mm. The ordinate is w/δ_1, the spanwise distance normalised by the local boundary layer displacement thickness δ_1. The abscissa is $L = -tU_c/\delta_1$, where t is time and U_c is the spot average propagation speed.

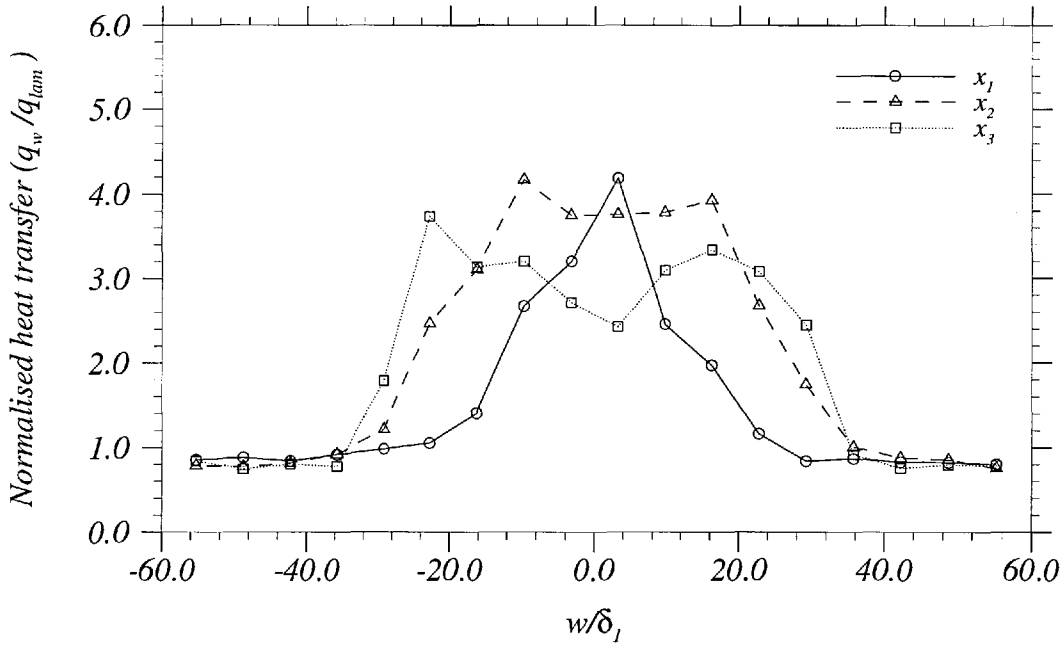

Figure 6.21: Heat transfer spanwise distribution at three various streamwise locations x_1, x_2, and x_3 as shown in figure 6.20 (a); $x = 213$ mm.

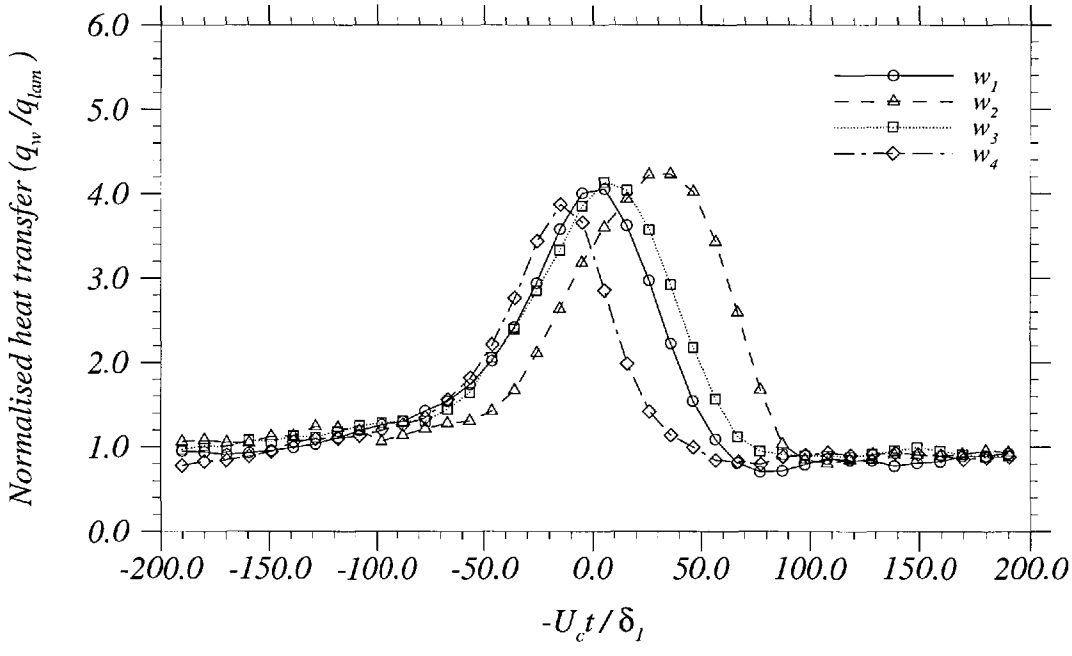

Figure 6.22: Heat transfer streamwise distribution at four various spanwise locations w_1, w_2, w_3, and w_4 as shown in figure 6.20 (a); $x = 213$ mm. w_2 is the spot centreline.

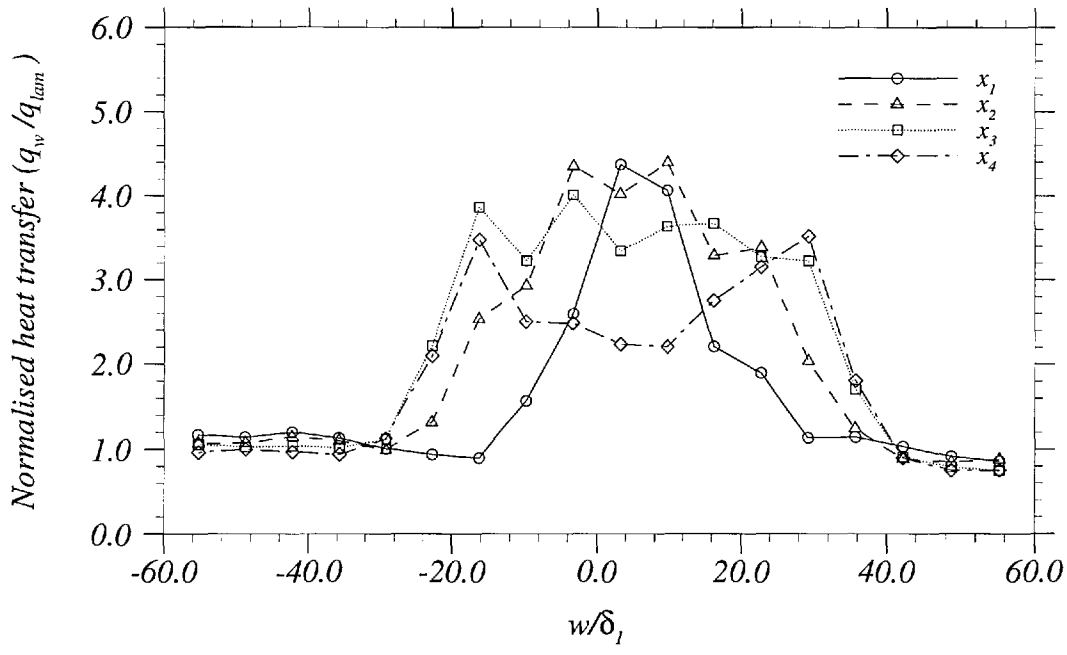

Figure 6.23: Heat transfer spanwise distribution at four various streamwise locations x_1, x_2, x_3, and x_4 as shown in figure 6.20 (b); $x = 213$ mm.

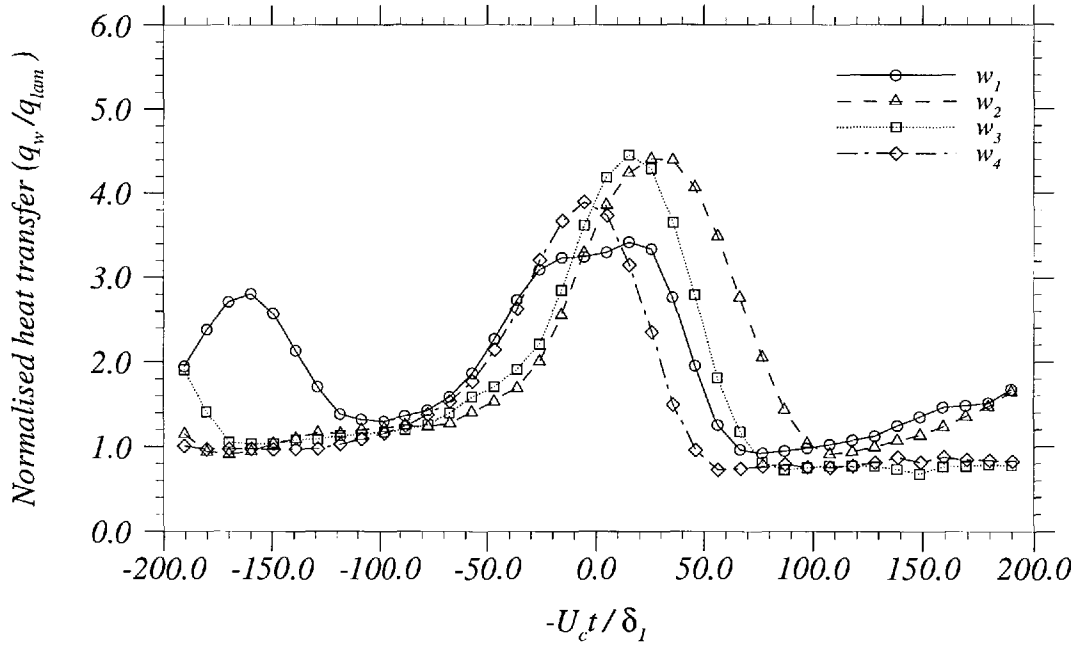

Figure 6.24: Heat transfer streamwise distribution at four various spanwise locations w_1, w_2, w_3, and w_4 as shown in figure 6.20 (b); $x = 213$ mm. w_2 is the spot centreline.

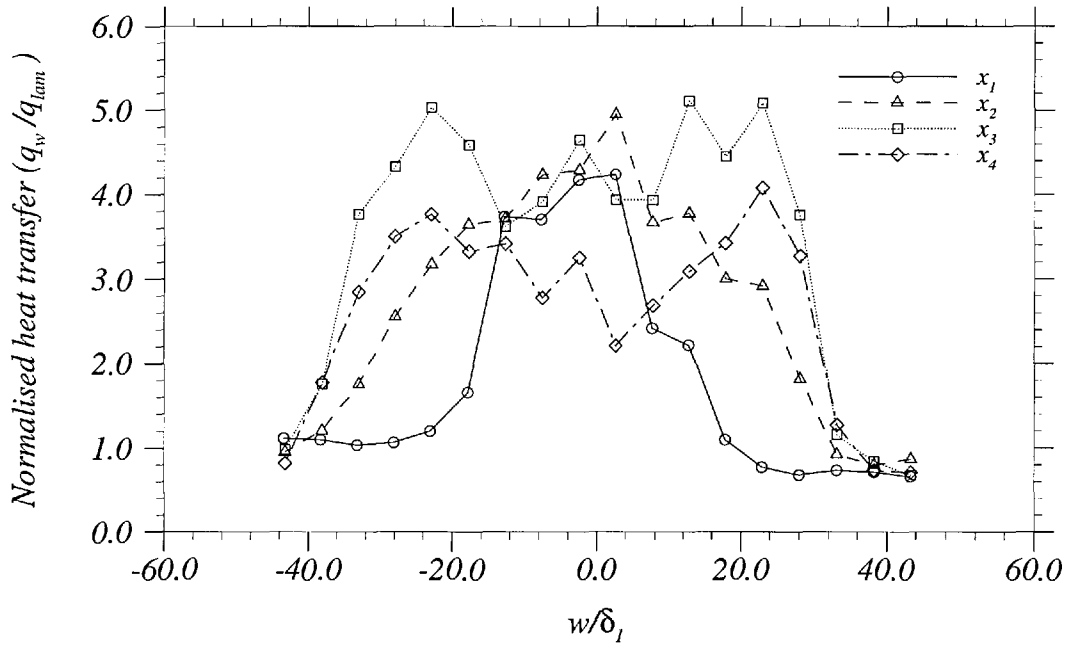

Figure 6.25: Heat transfer spanwise distribution at four various streamwise locations x_1, x_2, x_3, and x_4 as shown in figure 6.20 (c); $x = 279$ mm.

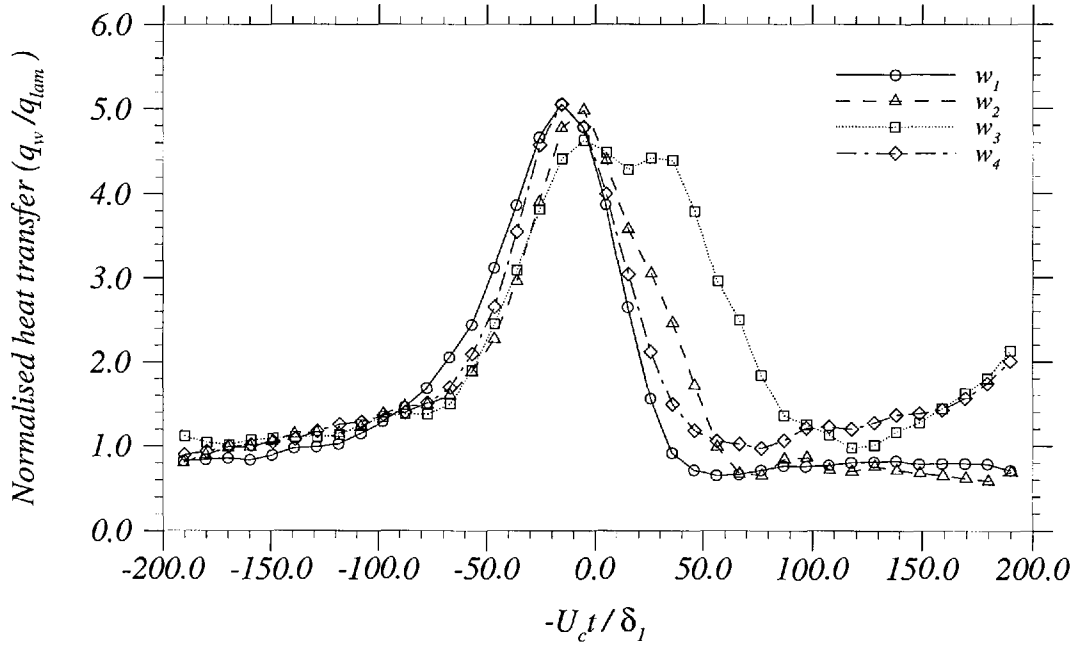

Figure 6.26: Heat transfer streamwise distribution at four various spanwise locations w_1, w_2, w_3, and w_4 as shown in figure 6.20 (c); $x = 279$ mm. w_3 is the spot centreline.

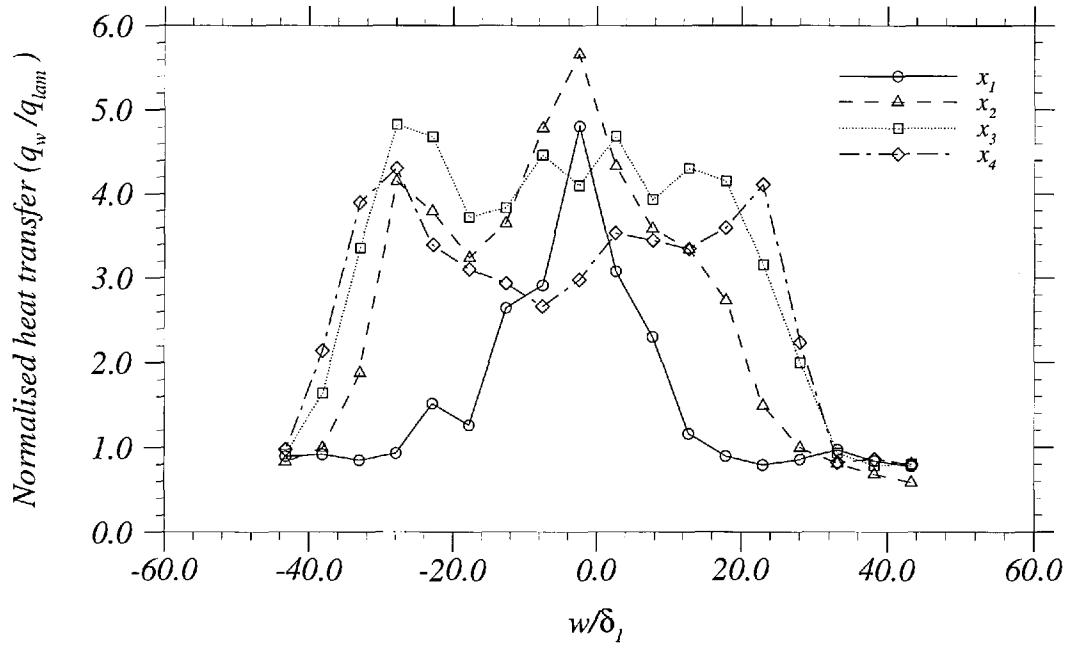

Figure 6.27: Heat transfer spanwise distribution at four various streamwise locations x_1, x_2, x_3, and x_4 as shown in figure 6.20 (d); $x = 279$ mm.

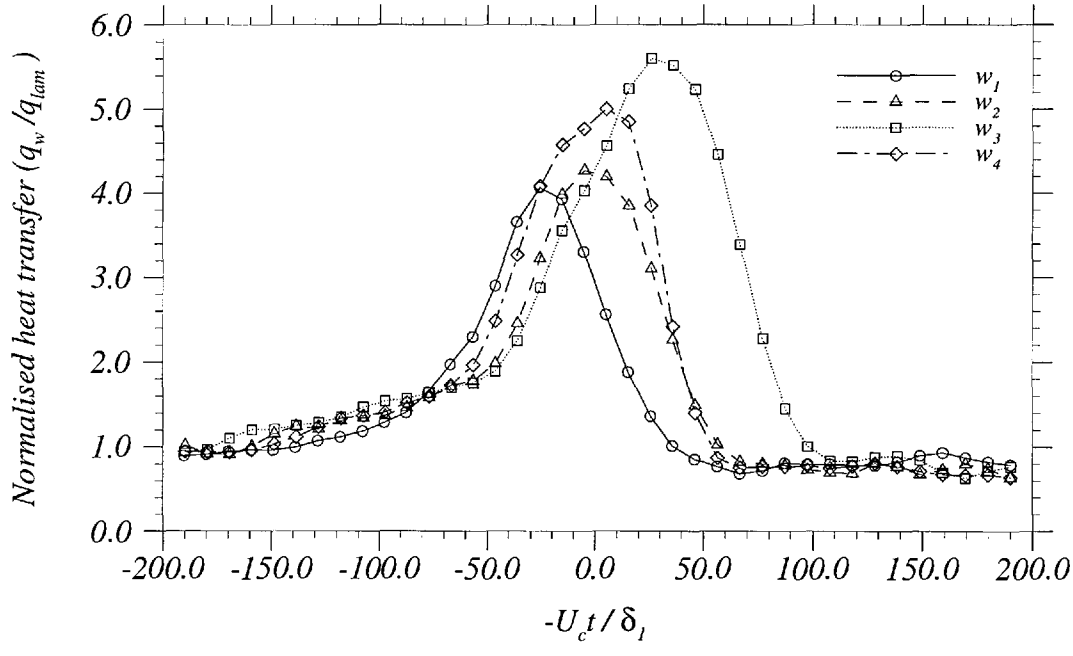

Figure 6.28: Heat transfer streamwise distribution at four various spanwise locations w_1, w_2, w_3, and w_4 as shown in figure 6.20 (d); $x = 279$ mm. w_3 is the spot centreline.

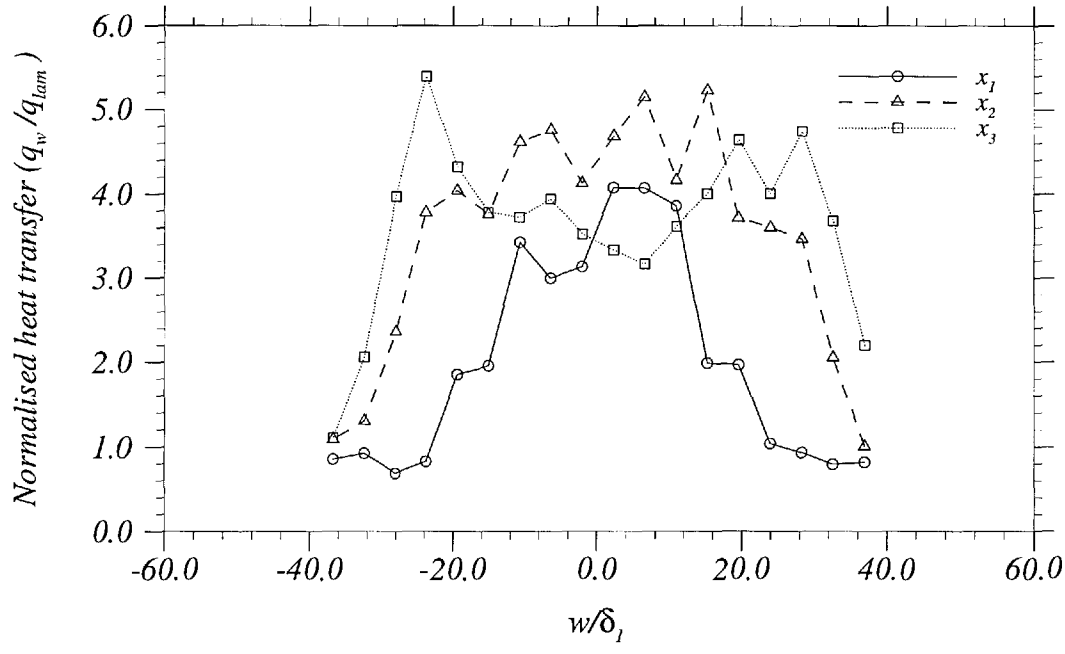

Figure 6.29: Heat transfer spanwise distribution at three various streamwise locations x_1, x_2, and x_3 as shown in figure 6.20 (e); $x = 334$ mm.

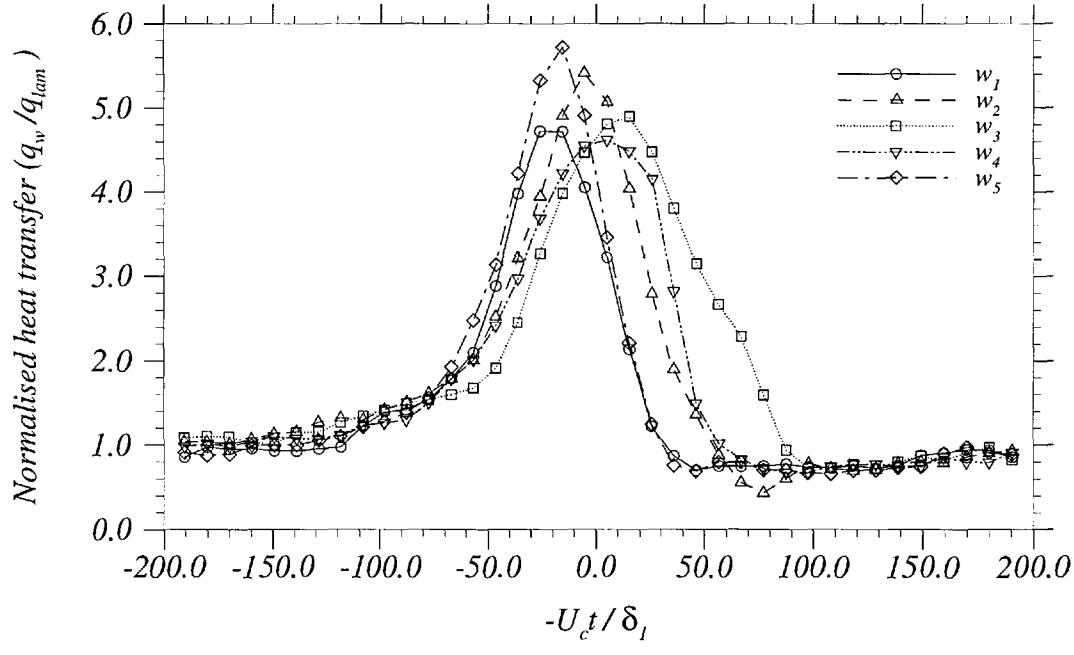

Figure 6.30: Heat transfer streamwise distribution at five various spanwise locations w_1, w_2, w_3, w_4, and w_5 as shown in figure 6.20 (e); $x = 334$ mm. w_3 is the spot centreline.

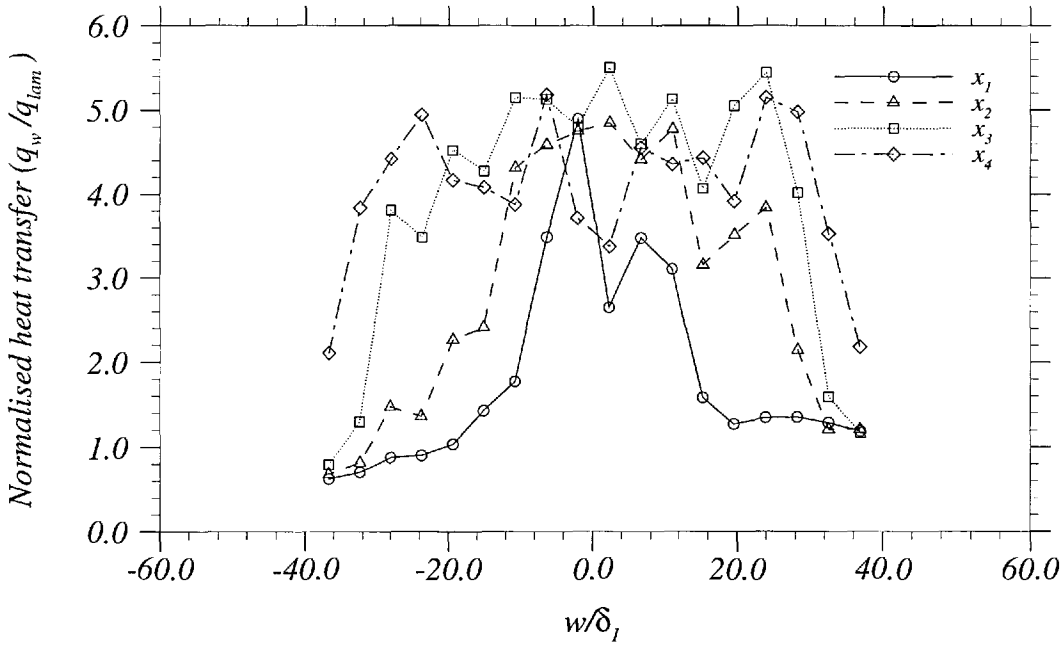

Figure 6.31: Heat transfer spanwise distribution at four various streamwise locations x_1, x_2, x_3, and x_4 as shown in figure 6.20 (f); $x = 334$ mm.

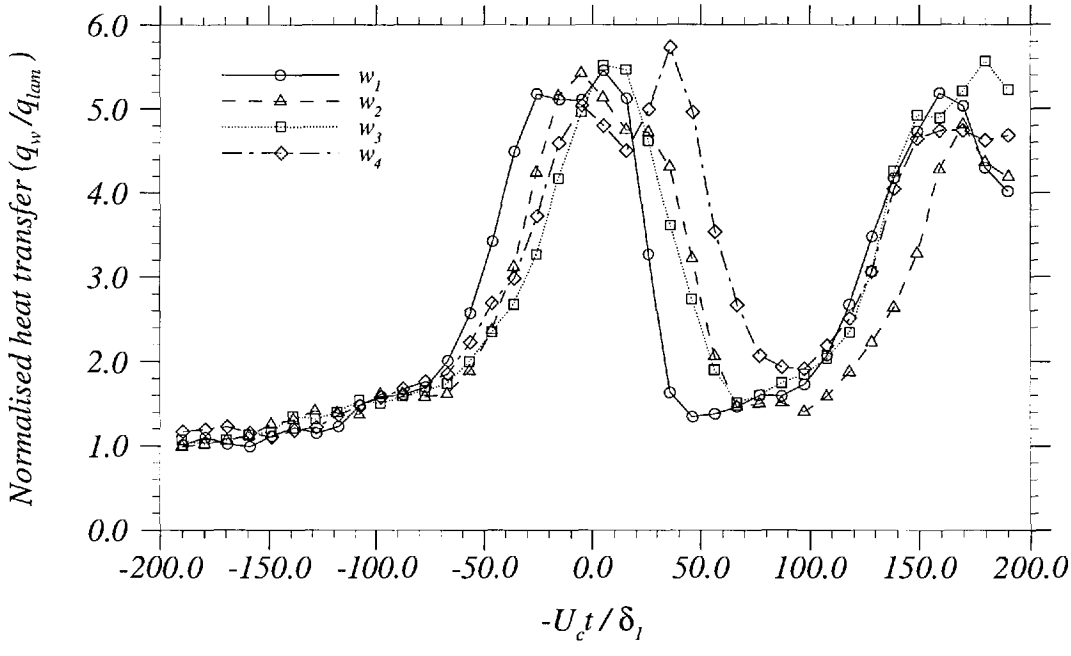

Figure 6.32: Heat transfer streamwise distribution at four various spanwise locations w_1, w_2, w_3, and w_4 as shown in figure 6.20 (f); $x = 334$ mm. w_3 is the spot centreline.

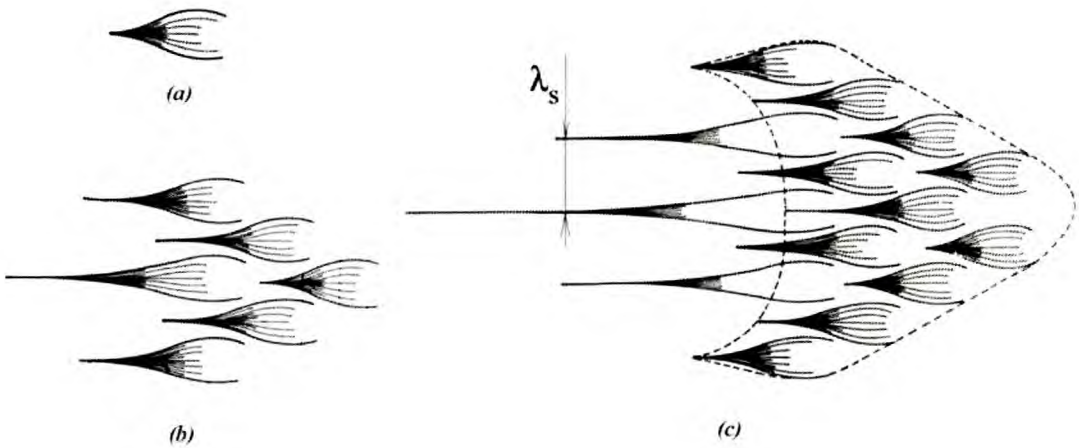

Figure 6.33: Turbulent spot internal structure according to Perry et al.[70] λ_s is the distance between the centres of two adjacent vortices.

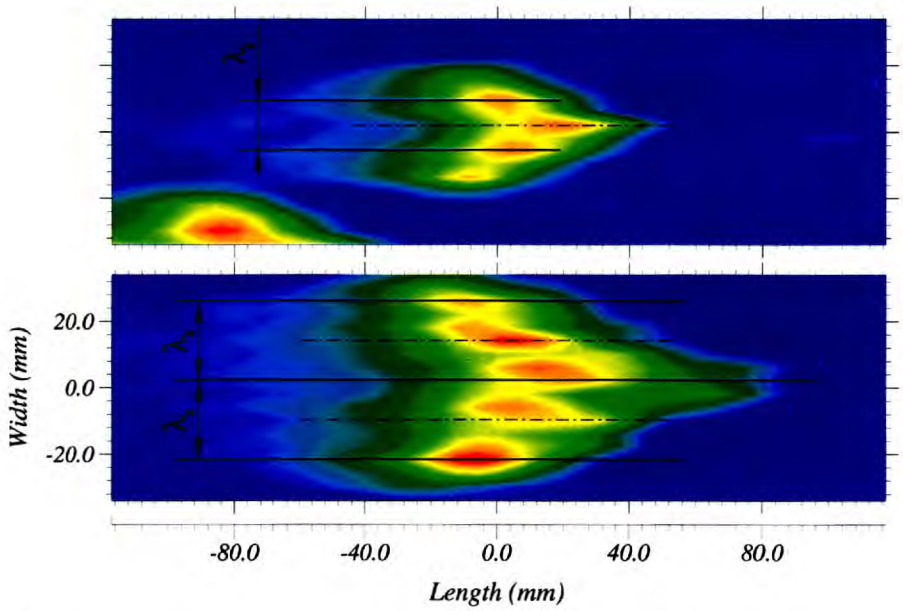

Figure 6.34: Thermal footprints of turbulent spots obtained at $x = 213$ mm and $x = 334$ mm. λ_s is the evaluated distance between the centres of two adjacent vortices, also referred to in the text as cell parameter or cell size.

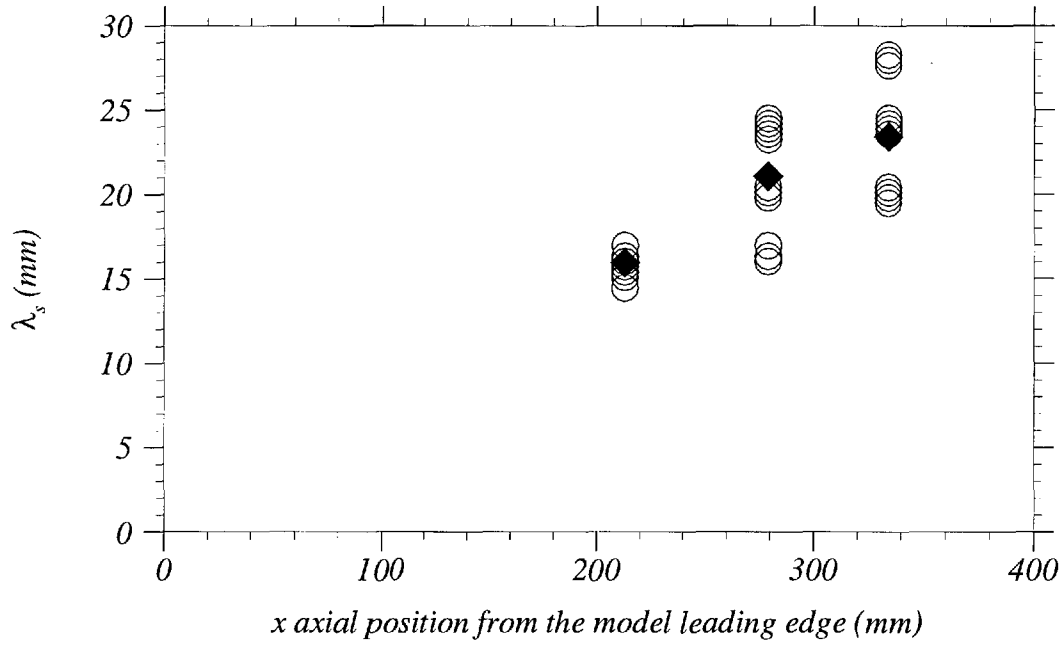

Figure 6.35: Variation of spot internal cell size, λ_s, with axial distance. Open symbols, individual spot values; solid symbols, spot average values.

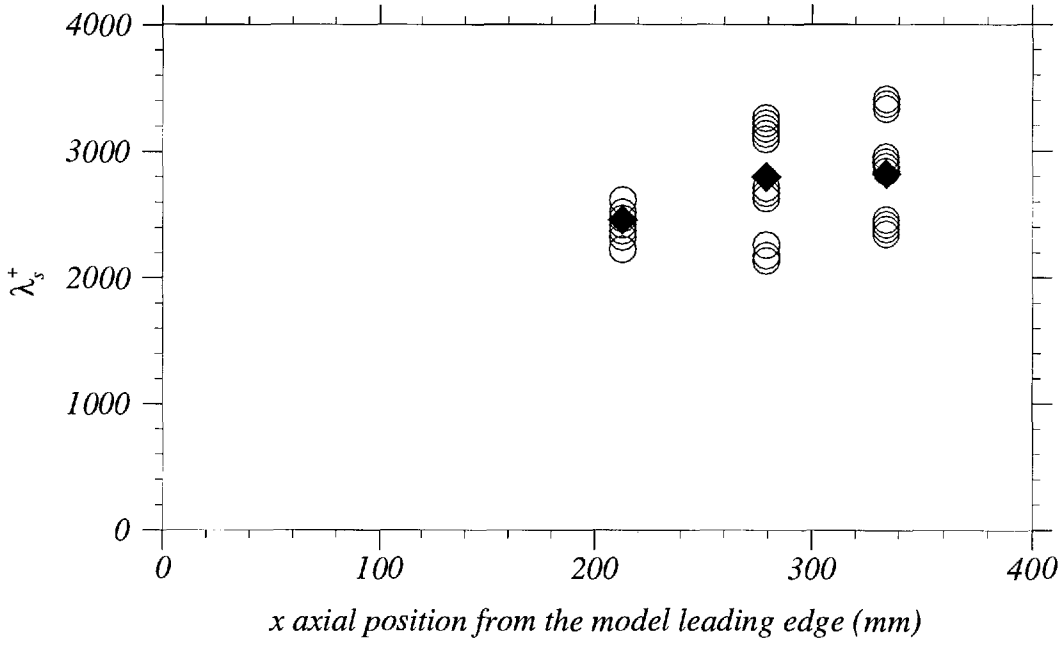

Figure 6.36: Variation of spot internal cell size expressed in turbulent wall scale units, λ_s^+, with axial distance. Open symbols, individual spot values; solid symbols, spot average values.

Chapter 7

Turbulent Wedge Analysis

The study of turbulent wedges was conducted as a result of two distinct outcomes of the individual spots analysis. Firstly, the lateral spreading rate (α_s) of the naturally-occurring spots (obtained in chapter 6) was higher than that documented by Fischer[28] and that predicted by Doorly et al.[23] Fischer tabulated data acquired from both naturally-occurring and roughness-induced individual spots, as well as turbulent wedges and unstable flows formed downstream of a roughness trip. The comparison of the wedge spreading rates, which would be obtained from the present study, with Fischer's and Doorly et al. work, was therefore seen to be valuable. Secondly, the heat transfer contours of the circumferential data occasionally revealed trains of near-amalgamating spots when large discrete damage was encountered in the nose region. Previous work by Zanchetta[112] showed the existence of a turbulent wedge downstream of a discrete roughness trip of adequate shape and size. The combination of these two results suggested a possible relationship between turbulent spots and the structure of fully developed turbulent wedges. Accordingly, turbulent wedge experiments were designed to investigate these effects.

The experiments were performed using a diamond-shape roughness trip at a nominal position, x_k, of 37.75 mm ±2% (figure 7.1). This location was chosen downstream of the nose where the boundary layer is sufficiently developed, in order to adequately contain the different sizes of the trip used without affecting the external inviscid flow (roughness parameter $(k/\delta)_{max} = 0.64$, where k is the roughness trip height and δ is the local laminar boundary layer thickness). The corresponding factor $(Re_{\delta_2}/M_e)_k$ is estimated at approximately 157 from the laminar CFD prediction (M_e is the boundary layer edge Mach number and $Re_{\delta_2} = \rho_e U_e \delta_2/\mu_e$ is the boundary layer edge Reynolds number based on the momentum thickness δ_2). The transverse location of the trip is approximately aligned with the centre of the circumferential measurements region that lies downstream. The trip is made of different types of tapes with various thicknesses, namely 0.12 mm, 0.06 mm, and 0.04 mm. The required trip height is achieved using multiple layers of appropriate thickness. The shape and width of the trip are obtained manually using a cutter and a high precision ruler (with 0.5 mm graduation).

Three different sets of experiments were carried out using various roughness trip sizes (variation in terms of trip width w_k and height k), as summarised in table 7.1. Set 1 was designed for effective tripping, thus generating a fully developed turbulent wedge. Sets 2 and 3, however, were designed, to gradually reduce the trip size (in terms of both width and height). The circumferential data covered a distance around the circumference of 68 mm at four various axial locations from the model leading edge, namely $x = 147$ mm, $x = 213$ mm, $x = 279$ mm, and $x = 334$ mm.

	x (mm)	w_k (mm)	k (mm) (± 10%)	k/δ (± 10%)
Set 1	147, 213, 279, 334	1.900 ± 9%	0.24	0.64
Set 2	279	1.950 ± 9%	0.24, 0.12, 0.08, 0.04	0.64, 0.32, 0.21, 0.11
Set 3	279	1.075 ±18%	0.12, 0.06	0.32, 0.16

Table 7.1: Turbulent wedge experimental setup. x is the measurement location, w_k and k are the roughness trip width and height respectively, k/δ is the relative trip height with respect to the local laminar boundary layer thickness δ.

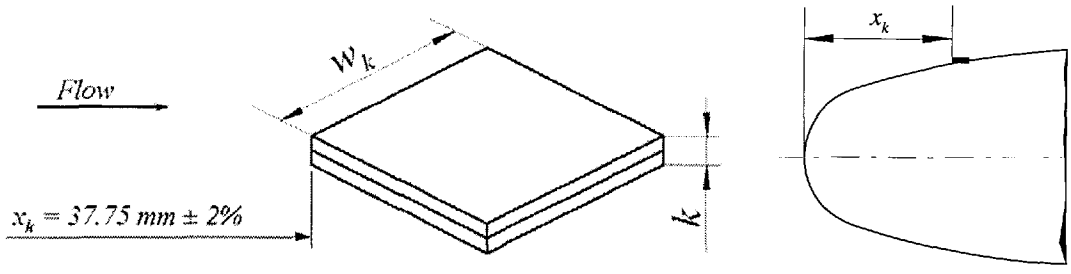

Figure 7.1: Roughness trip configuration. (Left) trip geometry; x_k is the axial distance between the model leading edge and the trip leading tip; k and w_k are the trip height and width respectively. (Right) positioning of the trip.

7.1 Effective roughness trip

The first experimental set was designed in order to enable the production of a fully developed turbulent wedge right behind the roughness trip (i.e., effective tripping). The choice of the trip size, in terms of (k/δ), was made by comparison to previous work[9,10,38,73,98] where effective tripping was achieved on blunt-body configurations using a trip height $(k/\delta)_{effective}$ of around 0.4 at the corresponding value $(Re_{\delta_2}/M_e)_k = 157$. Zanchetta[112] achieved effective tripping with a trip height of the order of the local boundary layer thickness. In the present study however, with the pre-fixed tape thicknesses provided, the effective trip height was set at $k = 0.24$ mm which corresponds to $k/\delta = 0.64$. This value was taken higher than that put forward by Berry[9,10] (to include a safety margin), but still lower than Zanchetta's value. Table 7.2 summarises the characteristics of the trip and the corresponding critical boundary layer parameters.

$x\ (mm)$	$w_k\ (mm)$	$k\ (mm)$	k/δ	k/δ_1	k/δ_2	Re_{kk}	M_k	Re_{kk}/M_k
147, 213, 279, 334	1.900	0.24	0.64	2.96	4.42	1620	2.24	724

Table 7.2: Experimental set 1 (effective trip). x is the measurement location. w_k and k are the roughness trip width and height respectively. δ, δ_1, and δ_2 are the local laminar boundary layer thickness, displacement thickness, and momentum thickness respectively. $Re_{kk} = \rho_k U_k k/\mu_k$ is the Reynolds number based on the roughness height k. M_k is the local Mach number at the trip height.

7.1.1 Time-dependent heat transfer

Figure 7.2 presents time-histories for heat transfer signals across the spanwise array of gauges at $x = 279$ mm obtained from a single run (run 5240, with $k/\delta = 0.64$ and $w_k = 1.9$ mm). The analysis also holds for the rest of the axial positions. The spanwise location, $z = 0$, approximately corresponds to the station which is immediately downstream of the roughness trip. Three flow regions at different heat transfer levels are witnessed, including laminar/near-laminar (as shown at $z = -34$ mm, -30 mm, $+30$ mm, and $+34$ mm), intermittent with fractions of laminar and turbulent (at $z = -26$ mm, -22 mm, $+22$ mm, and $+26$ mm), and fully turbulent (e.g., $z = -14$ mm, -6 mm, $+2$ mm, and $+14$ mm). The latter constitutes what will be referred to as the core of the turbulent wedge in the remainder of this chapter . The laminar region occasionally reveals turbulent events which are associated with individual turbulent spots generated from sources other than the roughness trip (further discussion will be presented subsequently). The intermittent flow region, which occupies a finite distance joining the core of the wedge and the fully laminar flow, displays a structure similar to that observed in individual spots heat transfer signals, however, with much higher intermittency levels. This suggests possible significant flow interactions between the highly vortical fluctuating turbulent core and the surrounding laminar flow. It might also depict individual spot-like internal structures within the intermittent zone or the turbulent core.

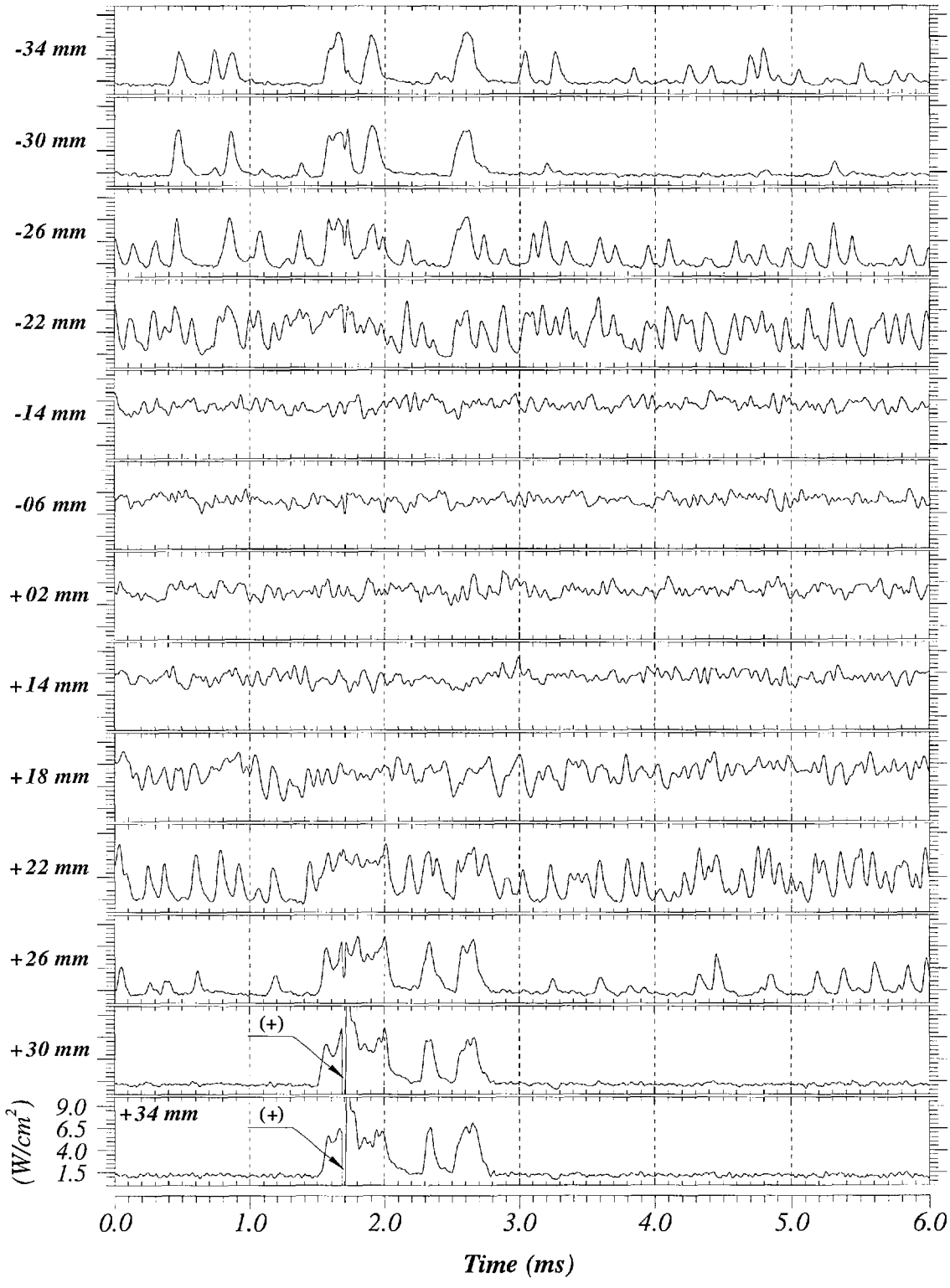

Figure 7.2: Typical time-dependent heat transfer signals across the circumferential gauges (68 mm distance) at $x = 279$ mm (Run 5240; effective tripping). $z = 0$ is the spanwise station immediately downstream of the trip. Note: (+) represents a spike associated with the schlieren spark taken simultaneously with the measurements.

7.1.2 Time-averaged heat transfer

Figure 7.3 illustrates the spanwise distribution of the time-averaged heat transfer data together with the laminar CFD predictions, q_{lam}, at the axial locations $x = 147$ mm, 213 mm, 279 mm, and 334 mm from the model leading edge. The data were averaged over the 6 ms steady time interval of the tunnel run. Two to three repeated runs were carried out for each measurement position in order to demonstrate the repeatability of the experiments and confirm the validity of the result obtained. There are two distinct levels of heat transfer; the low level laminar flow and the high level turbulent flow. The acquired experimental data compare within $\pm 10\%$ of the laminar computational value and within $\pm 15\%$ to $\pm 20\%$ of the fully turbulent CFD prediction. The edge of the turbulent wedge is defined by the location where the heat transfer level increases from the laminar to the turbulent level. This increase takes place over a finite space that represents a region of intermittent flow. The boundary between the fully laminar and intermittent zones is identified as the wedge *outer* boundary, whereas the boundary between the intermittent and fully turbulent zones is referred to as the wedge *core* or *inner* boundary.

The figure also shows a decrease in heat transfer level with axial distance, as predicted by the fully turbulent CFD calculation. This decrease is accompanied by a rise in width of the wedge core and intermittent zone. The latter is associated with the development of the turbulent core itself, hence larger flow interaction with the laminar surrounding, and/or the growth in scale of the wedge internal structures. The experimental laminar level is, in some cases (e.g., run 5244 at $x = 213$ mm and run 5240 at $x = 279$ mm), slightly higher than its CFD counterpart. This is due to the presence, at a low rate, of individual turbulent spots either naturally-occurring or generated from model damage around the nose (e.g., illustrated as individual turbulent events in figure 7.2 at $z = -34$ mm, -30 mm, $+30$ mm, and $+34$ mm). The heat transfer trend of the turbulent core reveals a concave-like distribution with spanwise distance, with a maximum value situated around the core boundaries and

a minimum value at the wedge centreline. These features are more likely to be associated with the internal structure of the wedge, which will be discussed in more detail in section 7.1.4.

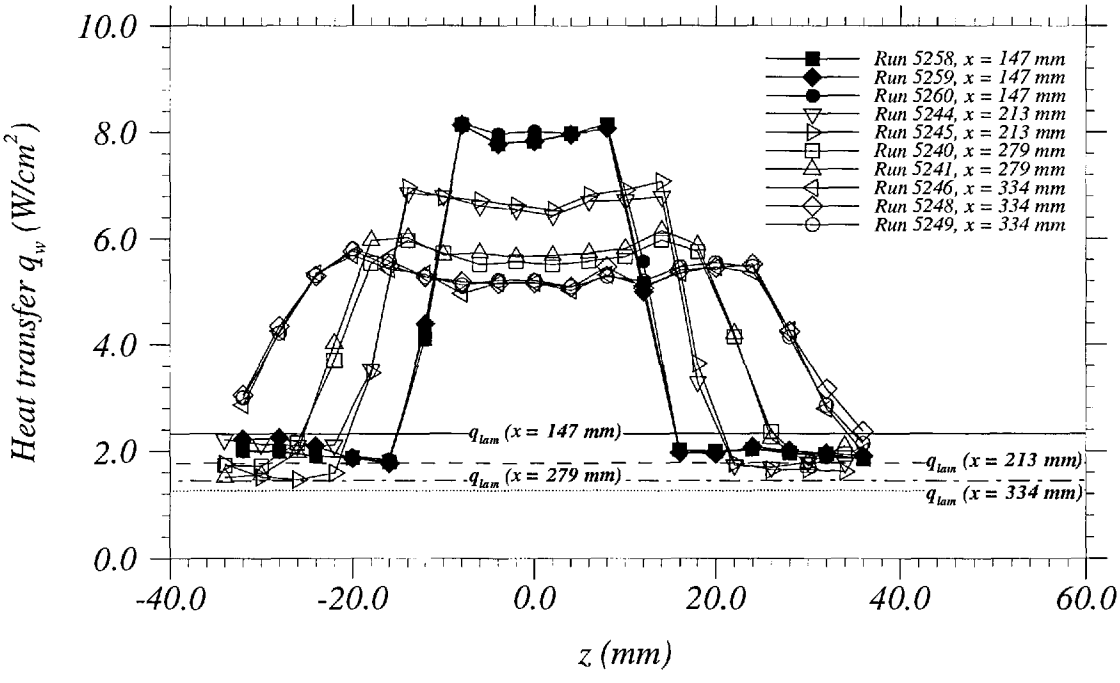

Figure 7.3: Spanwise time-averaged heat transfer distributions together with the laminar CFD values; x = 147 mm, 213 mm, 279 mm, and 334 mm. Experimental set 1 with w_k = 1.9 mm, k/δ = 0.64.

7.1.3 Wedge geometrical characteristics

The variation of the wedge outer and core spanwise extents with axial distance is presented in figure 7.4. The wedge outer boundary (i.e., the margin between the intermittent and fully laminar regions, described by the width w_e) and the wedge inner boundary (i.e., the margin between the intermittent zone and the wedge core, described by the width w_c) are defined in figure 7.5. The experimental errors associated with the definition of the wedge core and outer edges are constrained by the resolution of the heat transfer gauges, established as ±4 mm. The relative magnitudes of these errors with respect to the inner and outer wedge widths, w_e and w_c respectively, become less significant with axial distance as the spanwise size of the turbulent wedge increases. The maximum and minimum values of these errors are estimated at ±25% (at $x = 147$ mm) and ±5.1% (at $x = 334$ mm) respectively. The intersection point defining the wedge outer edge uses the laminar CFD value instead of its experimental counterpart—the latter being difficult to determine in the presence of discrete turbulent events within the laminar region, which are generated from sources other than the roughness trip (e.g., figure 7.2 at $z = -34$ mm and -30 mm). The consideration of this laminar value introduces a negligible additional error evaluated at approximately ±1% of the wedge outer width.

The evolution of the wedge width with axial distance is determined using the least squares fit method, which assumes a linear function (figure 7.4). Indeed, previous work on turbulent wedges[112,116] reported linear evolutions of wedge lateral growth with axial distance in the presence of a zero pressure gradient, which is relatively the case in the afterbody region. In any case, the number of measurement points achieved in the present study (4 axial locations) is not sufficiently large to prove otherwise. However, across the blending region, the wedge lateral growth is more likely to exhibit a non-linear trend due to the presence of axial flow gradients. The linear approximation function obtained results in a wedge onset location, x_{onset}, of between approximately 35 mm and 40 mm, very close to the actual location of the

roughness trip $x_k = 37.75$ mm. This result confirms the effectiveness of the trip with the height, k/δ, of 0.64, a value which corresponds to a Reynolds number based on the roughness height, Re_{kk} (where $Re_{kk} = \rho_k U_k k/\mu_k$), of 1620. The wedge lateral growth or *spreading rate* is expressed in terms of both core and outer half-angles α_c and α_e respectively. The wedge outer spreading half-angle α_e is estimated at 6.9 ± 0.95 degrees, whereas the wedge core spreading half-angle α_c is estimated at 4.3 ± 0.83 degrees. A schematic representation of the wedge is illustrated in figure 7.6.

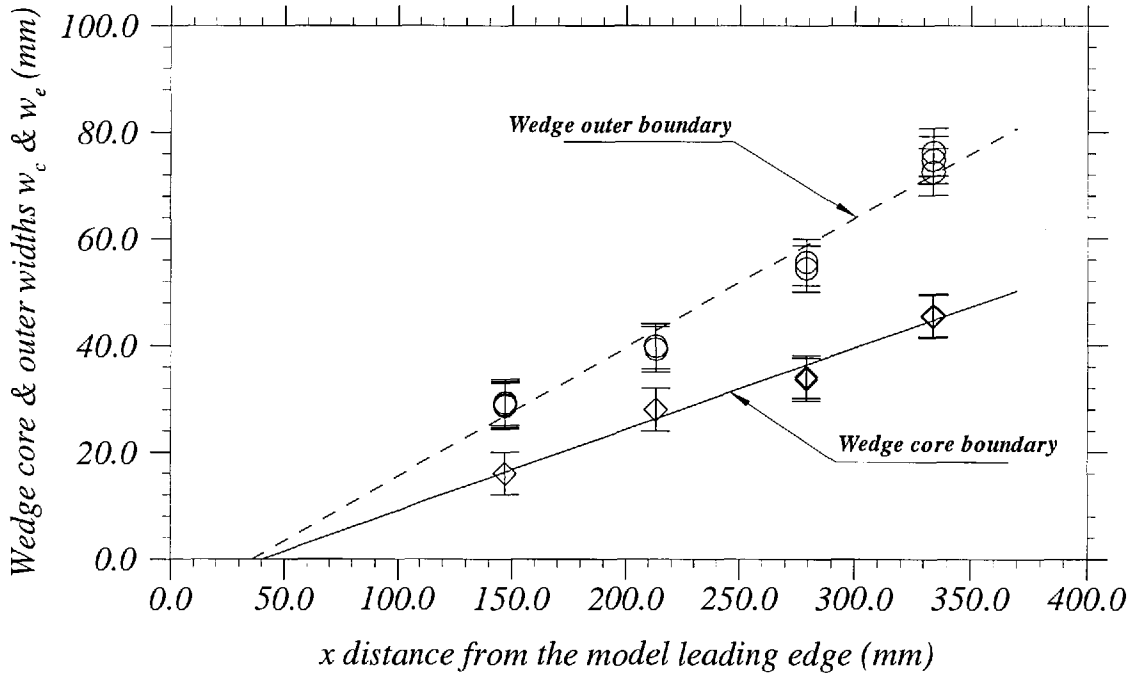

Figure 7.4: Variation of the wedge core (w_c) and outer (w_e) widths with axial distance.

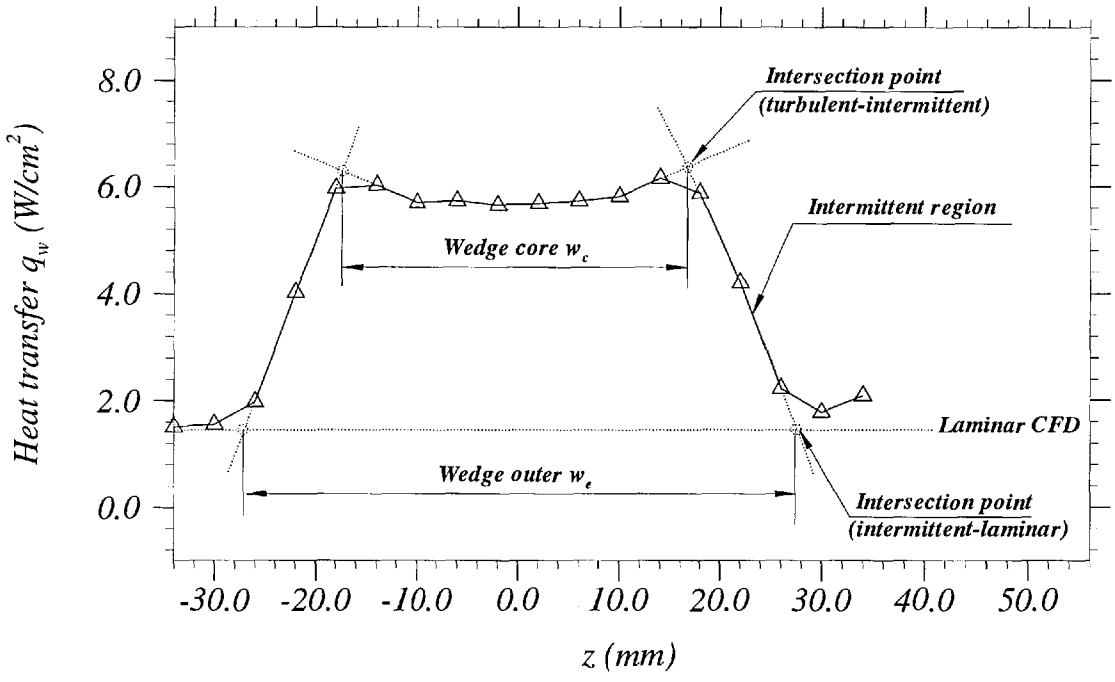

Figure 7.5: Definition of turbulent wedge core and outer boundaries.

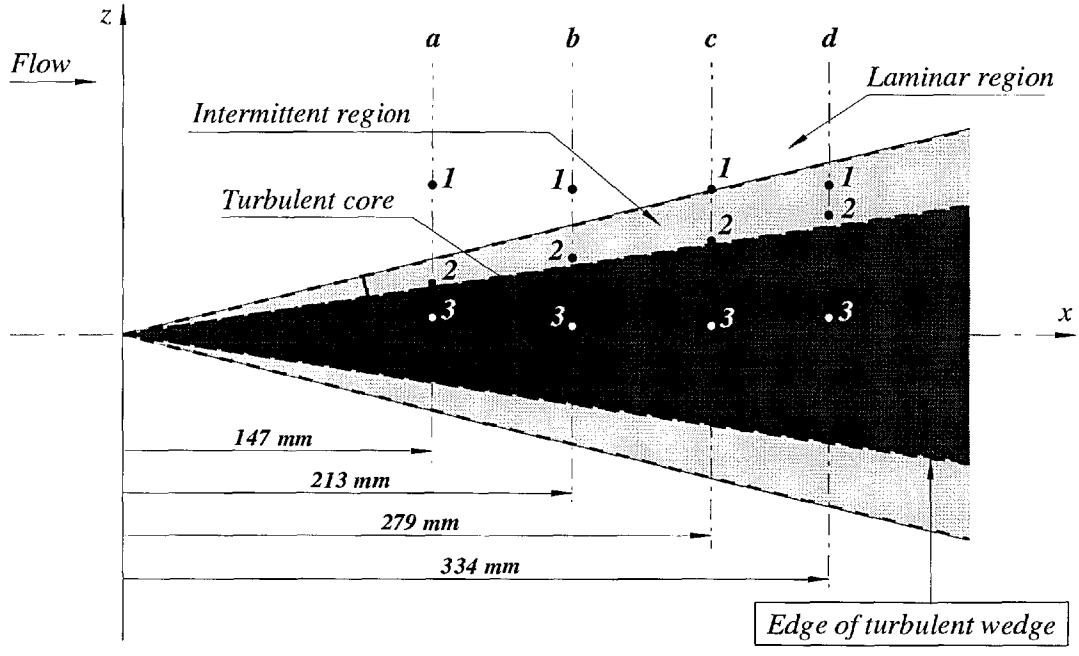

Figure 7.6: Schematic of the turbulent wedge footprint including the wedge core and outer spreading half-angles α_c and α_e respectively.

The direct comparison of the core and outer spanwise spreading rates of the turbulent wedge, $\alpha_c = 4.3 \pm 0.83$ degrees and $\alpha_e = 6.9 \pm 0.95$ degrees respectively, with that of a discrete turbulent spot, $\alpha_s = 6.2 \pm 1.45$ degrees (obtained in chapter 6), reveals that in the same flow conditions, a spot grows at a rate between that of the wedge core and outer edges (as sketched in figure 7.7). Schubauer et al.[86] also reported smaller spanwise growth rates for turbulent wedge cores compared with discrete turbulent spots in incompressible flows. The high α_e however, may be associated with the complex flow structure taking place around the roughness trip (such as flow separation, vortex generation and shock wave formation in the supersonic region of the boundary layer), which flows downstream along the measurement locations. Further discussion regarding the wedge formation process and internal structure will be presented in section 7.1.4..

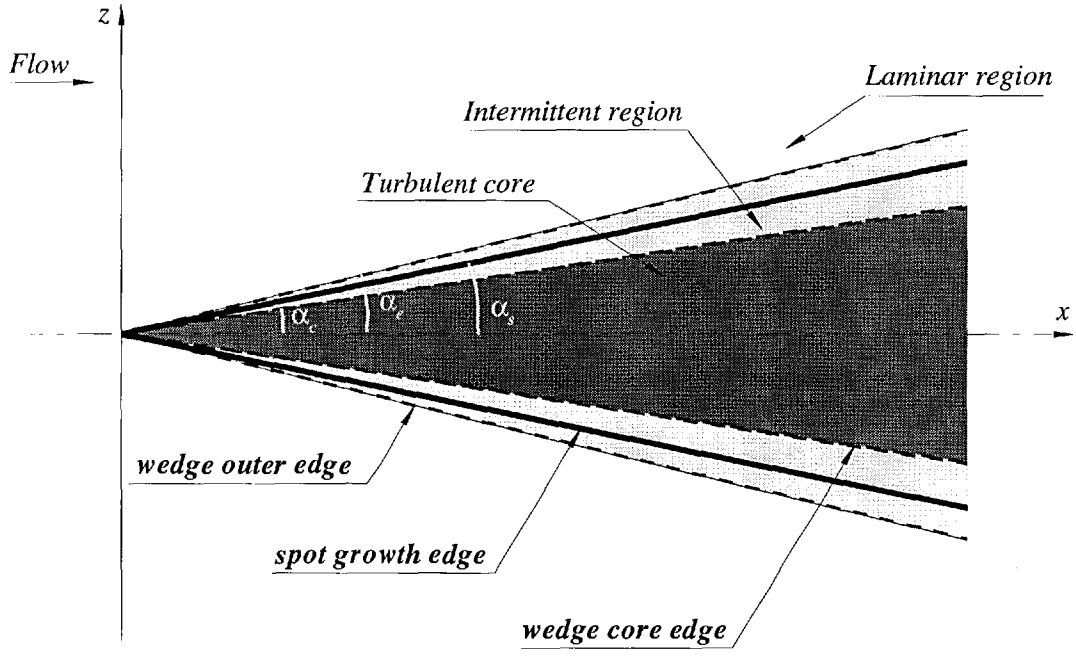

Figure 7.7: Schematic of the turbulent wedge and spot spanwise spreading rates α_c, α_e and α_s respectively.

The turbulent core spreading rate achieved is located well within the interval suggested by Fischer[28] of 3.3 to 5.5 degrees. Although he reported data which included both individual spot and wedge growth rates, it appears that his spots were probably roughness-induced. The result also agrees with the theoretical prediction of Doorly and Smith[23]—spanwise spreading rate angle $\alpha = tan^{-1}(3^{-3/2}2^{1/2}M_e^{-1})$—that yields a spreading half-angle of approximately 4.5 degrees over the measurement distance (i.e., between $x = 147$ mm and $x = 334$ mm with a corresponding M_e of between 3.6 and 3.3 respectively). On the other hand, the wedge outer spreading half-angle, α_e, lies outside the margins of Fischer's charted data. This is perhaps due to the difficulty in properly defining the outer boundary of the wedge (in his data), where the flow is no longer turbulent but increasingly low intermittent.

Figure 7.8 presents time histories for heat transfer signals at three spanwise locations (a_1, a_2, a_3), (b_1, b_2, b_3), (c_1, c_2, c_3), and (d_1, d_2, d_3) at the axial positions $x = 147$ mm, $x = 213$ mm, $x = 279$ mm, and $x = 334$ mm respectively (as indicated in figure 7.6, with $k/\delta = 0.64$ and $w_k = 1.9$ mm). Stations 1 describe a laminar flow with the presence of occasional discrete turbulent events; stations 2 illustrate a typical intermittent signal where fractions of laminar and turbulent flow coexist; and finally, stations 3 show a fully turbulent flow. Of importance here is the intermittent signals (a_2, b_2, c_2, and d_2), which reveal a structure similar to that observed in individual spot time-dependent heat transfer signals, however with much higher intermittency levels. This, in addition to the good comparison between the wedge and individual spot spreading rates, suggest a possible relationship between turbulent spots and the structure of fully developed turbulent wedges.

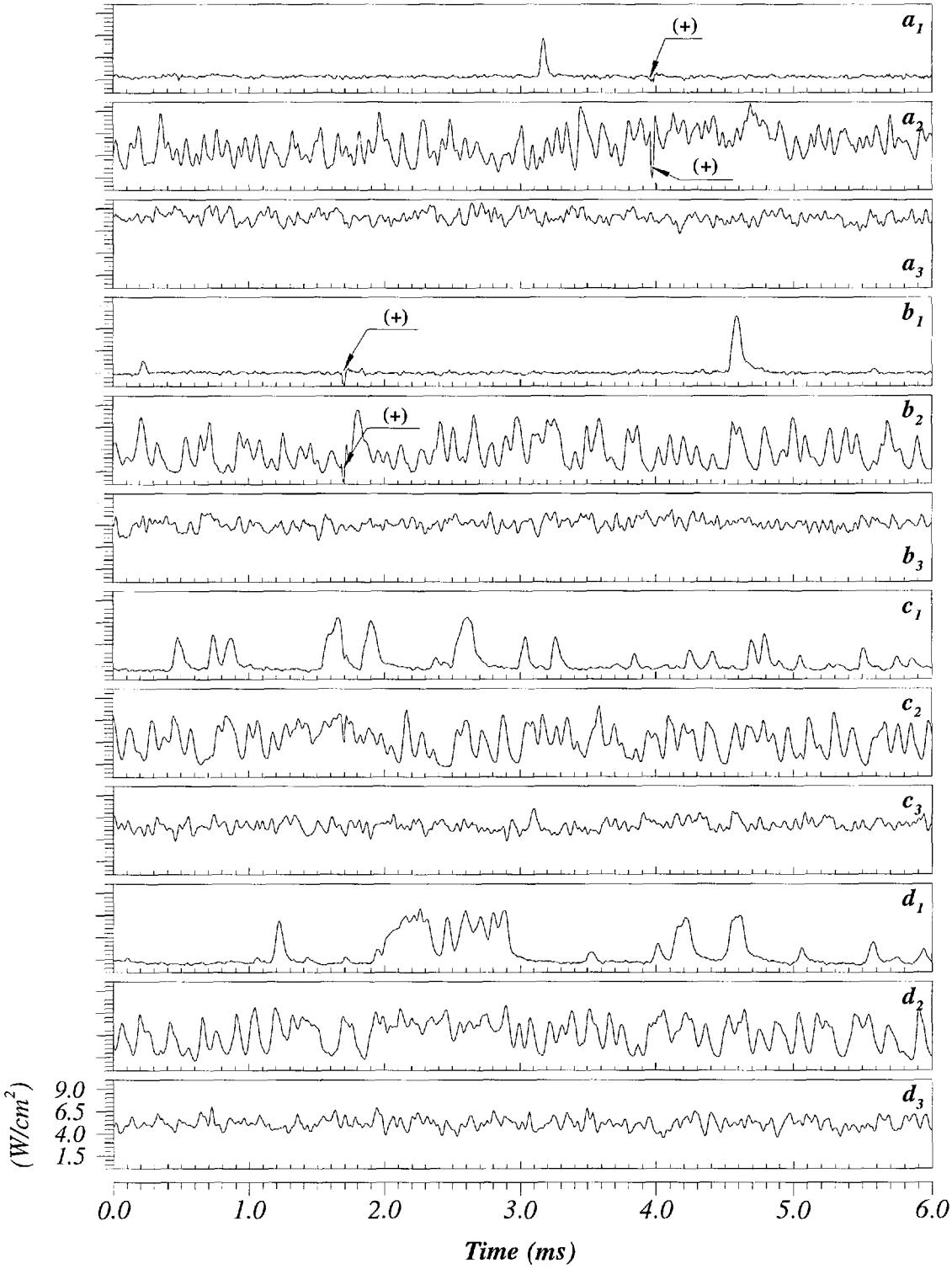

Figure 7.8: Time-dependent signals a_1, a_2, a_3 at $x = 147$ mm; b_1, b_2, b_3 at $x = 213$ mm; c_1, c_2, c_3 at $x = 279$ mm; d_1, d_2, d_3 at $x = 334$ mm (as shown in figure 7.6). Roughness-trip size; $k/\delta = 0.64$, $w_k = 1.9$ mm. Stations 1, laminar or near-laminar; stations 2, intermittent; stations 3, fully turbulent region. Note: (+) represents a spike associated with the schlieren spark taken simultaneously with the measurements.

7.1.4 Wedge internal structure

Figure 7.9 illustrates the 'z-t' plots of heat transfer contours at x = 147 mm, 213 mm, 279 mm, and 334 mm distance from the model leading edge (with $k/\delta = 0.64$ and $w_k = 1.9$ mm). There are three distinct flow regions, as was shown in figures 7.2 and 7.3, including fully laminar, intermittent, and fully turbulent. The laminar zone occasionally reveals discrete turbulent events which are either separated or coalesced with the turbulent wedge. These individual events are more apparent at x = 147 mm and x = 213 mm, where the laminar flow occupies a more significant fraction of the spanwise measurement window. The turbulent core extends over an increasing transverse space as it grows with distance. In effect, at x = 334 mm, the outer boundaries of the wedge are not fully captured, displaying a wedge outer width, w_e, greater than the actual 68 mm circumferential measurement length. The variation in heat transfer level throughout the wedge core suggests internal structures at the model surface. The intermittent zone is, in fact, a result of the temporal irregularities of the wedge boundaries, which are illustrated as intermittent turbulent events in the time-dependent data (figure 7.2) and a steady change in heat transfer level in the time-averaged data (figure 7.3).

A better visualisation of the wedge structure and the occasional individual spots is obtained from figure 7.10, which presents a zoom into the 0.75 ms indicated in each plot of figure 7.9. The time scale is chosen in such a way that it can be interpreted as a physical length scale by comparison with the actual length scale displayed in the spanwise axis. This is achieved by considering the individual spot average speed, determined in chapter 4, as the factor in scale of the two different axis. Once again, the idea behind this is only to obtain an approximate representation of the physical scale of the internal structures of interest rather than the global picture of the turbulent wedge itself. The discrete turbulent events (at x = 213 mm and 279 mm) take a shape similar to individual spots, including the delta-like leading edges, internal structure, and wake region.

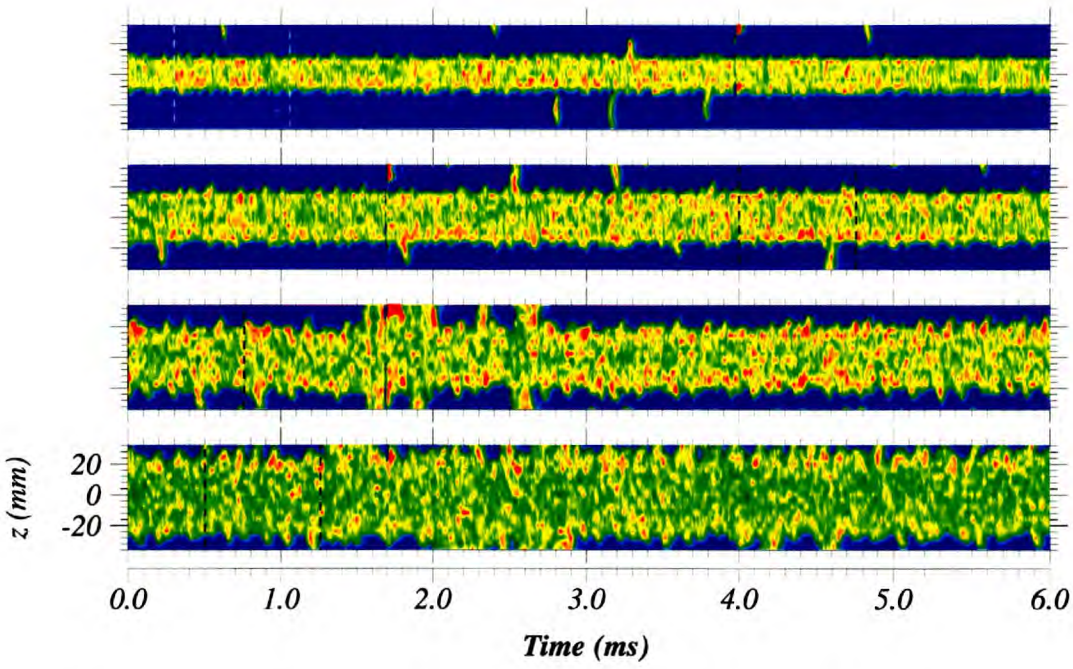

Figure 7.9: 'z-t' plot of heat transfer contours at $x = 147$ mm, 213 mm, 279 mm, and $x = 334$ mm (top to bottom). Roughness-trip size; $k/\delta = 0.64$, $w_k = 1.9$ mm.

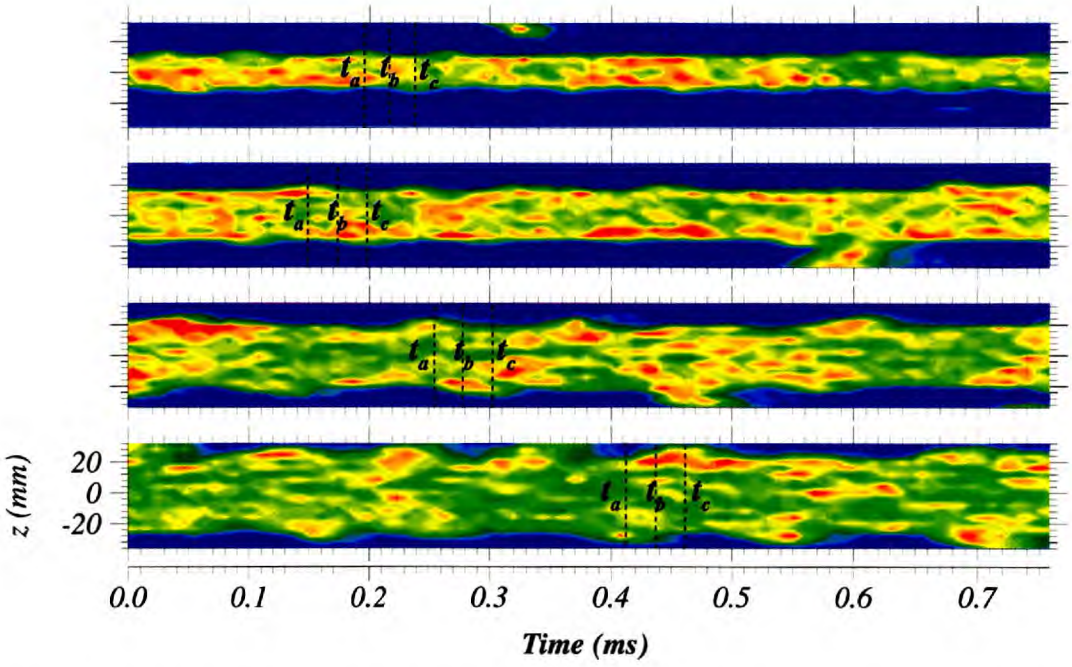

Figure 7.10: 'z-t' plot of heat transfer contours (zoom into the 0.75 ms window indicated in figure 7.9) at $x = 147$ mm, 213 mm, 279 mm, and $x = 334$ mm (top to bottom).

The irregularities observed in figure 7.9 take the form of rather irregular undulations (figure 7.10) and do not show a particularly clear periodic motion. At first sight, these undulations suggest characteristic shapes similar to those around the maximum width region of individual spots, as sketched in figure 7.11, where a possible scenario of the wedge flow is represented. Two 'trains' of amalgamated turbulent spots of different centrelines, each with a width w_s, are generated downstream of each side of the roughness trip (with a diagonal of $\sqrt{2}w_k \approx 2.7$ mm), with a possible third 'train' of the same centreline as the wedge, of width w_c, generated from the flow separation and reattachment behind the trip. The rate of spot production is so high that the spots of each 'train' coalesce immediately aft of the trip. The spanwise growth with axial distance eventually yields the amalgamation of the spot internal structures into one wedge structure at a certain distance downstream. During this process, parts of the spot boundaries are retained (figure 7.11) and depict the external shape of the resulting wedge edge.

The formation of two flow structures of different centrelines behind an isolated roughness element was also reported by Zanchetta.[112] He suggested that two *trailing vortices* form at the triangular trip rear corners. The two vortical structures underwent transition at a downstream distance 'x' (negligible in the case of effective tripping), which depended upon the trip size and local flow conditions. Transition first occurred in one structure, then by some contamination mechanism, spread to the other resulting in a larger spanwise growth with distance, which eventually led the two structures to merge into one turbulent wedge.

Figure 7.10 also shows that the maximum amplitude of the undulations increases with distance as demonstrated with the increase in the intermittent region extent shown in figure 7.3. An approximate physical length scale of these undulations can also be estimated directly from figure 7.10.

Figure 7.11 suggests a relationship between the various characteristic widths w_e, w_c, and w_s as being $w_s = (w_e + w_c)/2$, resulting in a lateral spreading half-angle $\alpha_s = (\alpha_e + \alpha_c)/2$. Using the spreading half-angles obtained in section 7.1.3, α_s is

estimated at 5.6 ± 0.89 degrees, a value slightly lower than that reported in chapter 6, yet within Fischer's interval.[28] This suggests that the spreading rate of spots varies initially according to the cause of their formation. The offset between the two spot-trains centrelines is evaluated as being $\Delta w_s = (w_e - w_c)/2$, which corresponds to a half angle $\Delta\alpha_s = (\alpha_e - \alpha_c)/2 = 1.3 \pm 0.89$ degrees.

Figure 7.12 shows a representation of the turbulent wedge shape which would be observed. Two distinct lines (continuous and dashed) are shown, representing the spatial location of the wedge boundaries at two different times t and $t + \Delta t$. The actual wedge edges would oscillate between the two spatial positions at a certain 'frequency' f_w. This frequency, and as a result the corresponding 'wave number', appear to decrease with distance as can be seen from the time and length scales of the undulations (figures 7.10 and 7.12). Due to the high irregularity of these undulations (as demonstrated in figure 7.9), no estimation of their frequencies was possible neither from the time-dependent heat transfer signals (e.g., figure 7.2), 'z-t' contour plots (e.g., figure 7.10), nor power spectral densities (PSD) of the time signals.

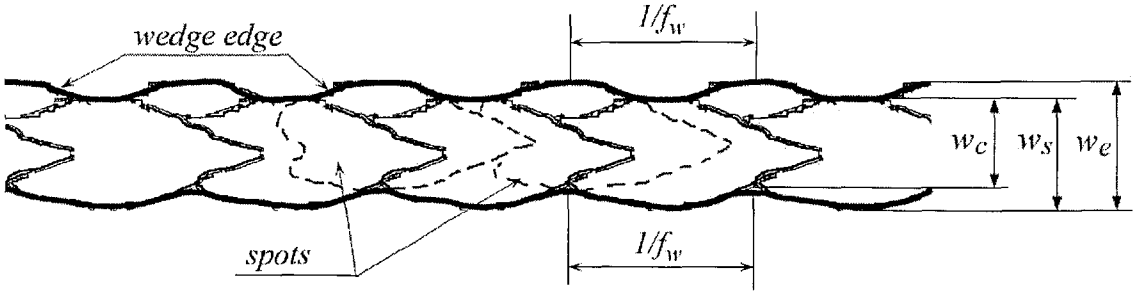

Figure 7.11: Schematic of a suggested internal structure of a turbulent wedge. w_e is the wedge outer width, w_c is the wedge core width, and w_s is the spot width.

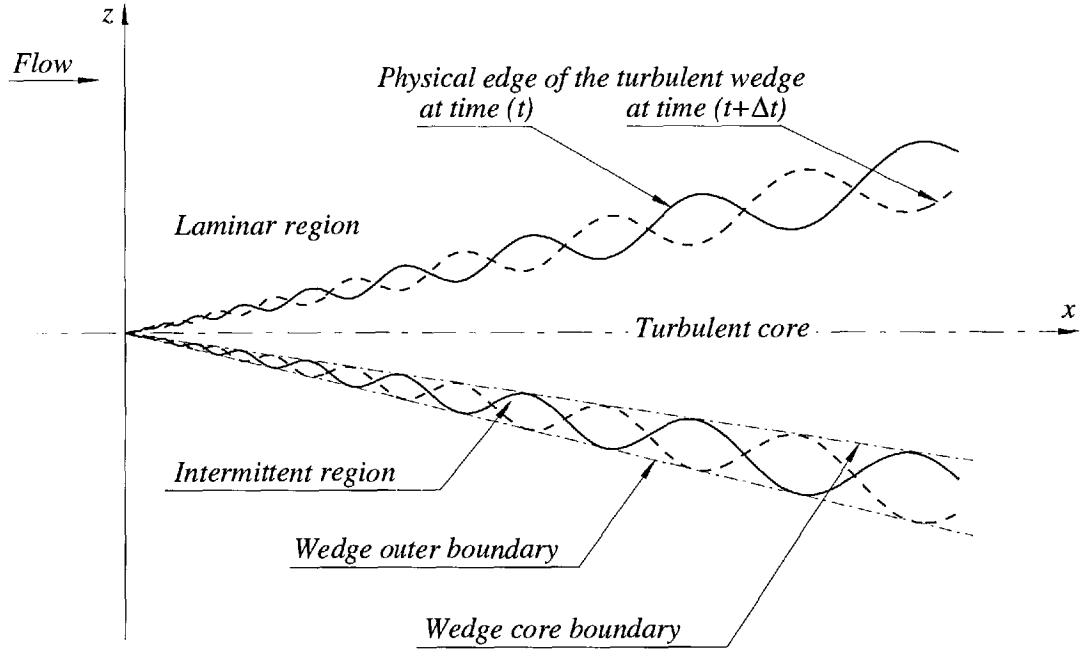

Figure 7.12: Schematic of the turbulent wedge footprint with a simplistic function of the wedge physical boundaries.

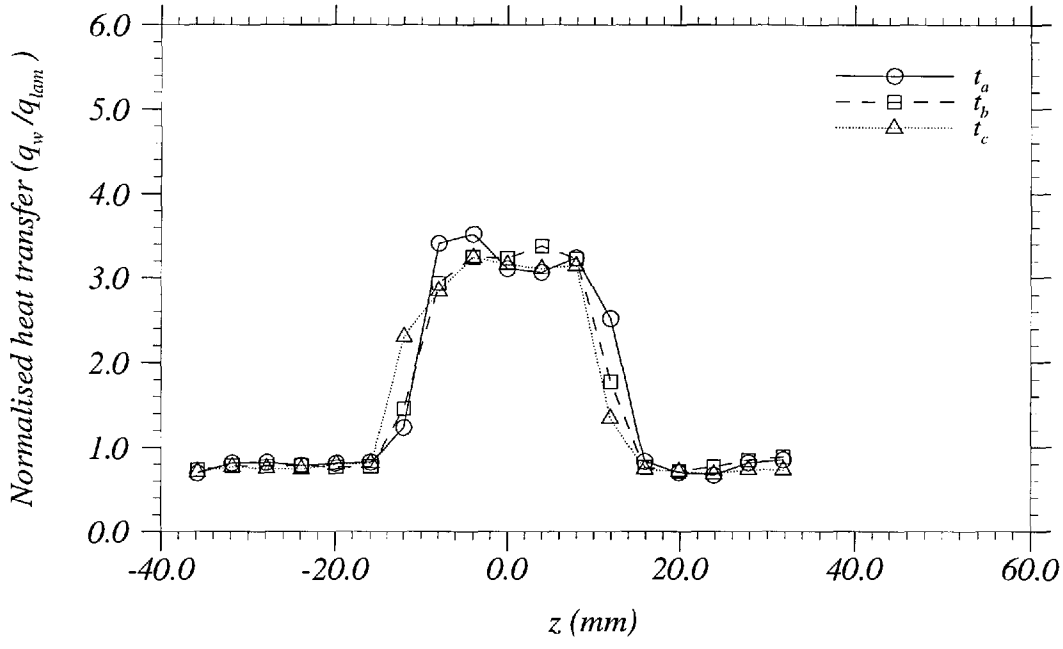

Figure 7.13: Heat transfer spanwise distribution at three various times t_a, t_b, and t_c (as shown in figure 7.10); $x = 147$ mm.

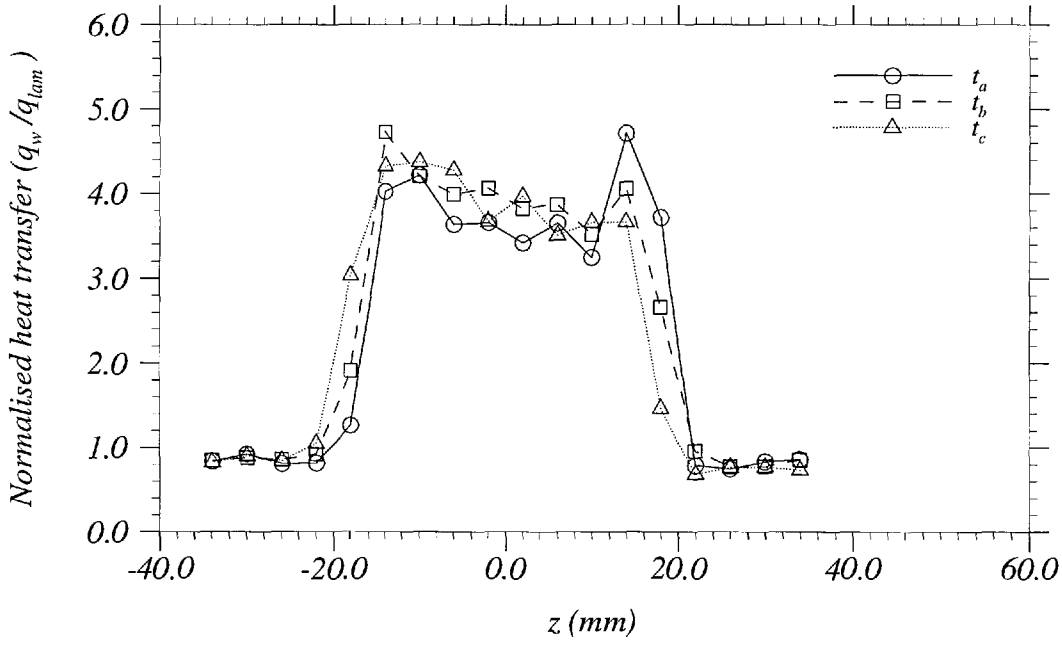

Figure 7.14: Heat transfer spanwise distribution at three various times t_a, t_b, and t_c (as shown in figure 7.10); $x = 213$ mm.

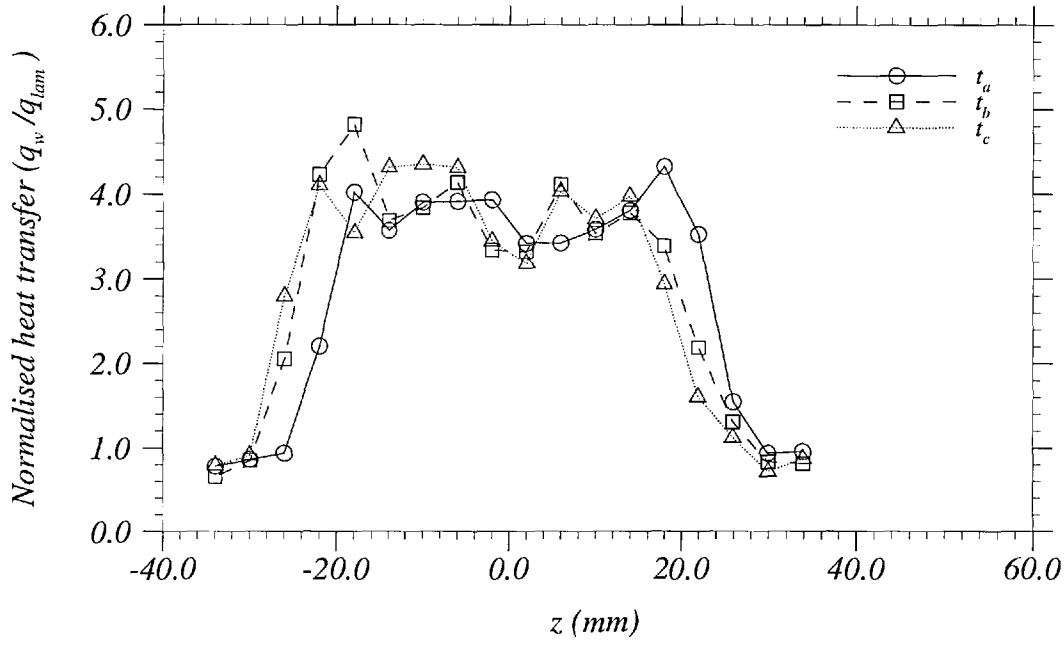

Figure 7.15: Heat transfer spanwise distribution at three various times t_a, t_b, and t_c (as shown in figure 7.10); $x = 279$ mm.

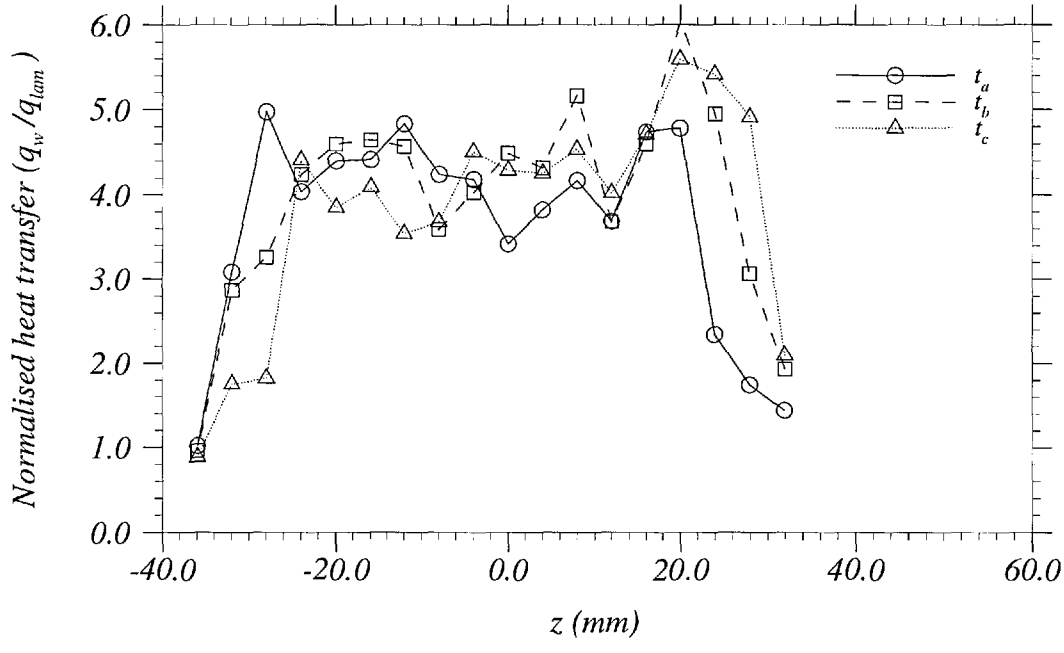

Figure 7.16: Heat transfer spanwise distribution at three various times t_a, t_b, and t_c (as shown in figure 7.10); $x = 334$ mm.

The undulation of the wedge boundaries is further demonstrated in figures 7.13 to 7.16, which present the spanwise distributions of heat transfer at three various times, t_a, t_b, and t_c, for each axial location. The first observation to make is the clear lateral shift with time of the turbulent wedge. Through this time shift, the transverse length scale of the wedge is virtually maintained, suggesting a somewhat organised wedge edge structure at least at a local level. The figures also reveal a variation in heat transfer level across the wedge similar to individual spots spanwise heat transfer distributions reported in chapter 6 (e.g., figures 6.23, 6.25, 6.27, 6.29 and 6.31). This variation does not only represent large turbulent fluctuations, but also internal structures as their scale and magnitude vary quite dramatically with axial distance (as discussed in chapter 6). The figures also show a clear local peak heating around the wedge edges (also observed in the time-averaged distributions shown in figure 7.3).

The wedge internal structure is a result of a highly complex flow pattern which takes place in the vicinity of the roughness trip and flows downstream along the measurement region. A schematic of a suggested flow structure surrounding the trip is illustrated in figure 7.17. There is formation of a curved detached shock wave ahead of the roughness element within the supersonic region of the boundary layer. The actual three-dimensionality of the shock system creates an axial vorticity, as it interacts with the spanwise vorticity lines existing within the boundary layer, which takes the form of a *horseshoe* vortex encircling the roughness element as shown in figure 7.17. The two side-ends of this vortex grow circumferentially downstream of the trip and eventually undergo transition. Within the subsonic region of the boundary layer, two counter-rotating vortices form and shed from each of the two wing-tips of the trip (figure 7.17) as a result of flow separation over its leading edges. The two *trailing* vortical structures expand laterally and eventually undergo transition at a certain downstream location. The flow separated over the central region of the trip reattaches behind it, exhibiting a *hairpin*-vortex structure which ultimately breakdowns to turbulence. These conjectures agree with the findings of

Zanchetta[112] from his examination of roughness-induced transition of a supersonic boundary layer.

The three different vortical structures mentioned above, namely *horseshoe, trailing,* and *hairpin* vortices, may take place simultaneously. The two off-centreline 'trains' of turbulent spots (figure 7.11) are believed to be the result of the transitioned trailing vortical structures generated from each side of the roughness trip. The centred third 'train' is associated with the evolved hairpin vortices formed within the reattached flow behind the trip. The contribution of the horseshoe vortex, on the other hand, is believed to take the form of peaks in heat transfer level around the edges of the turbulent wedge, as witnessed in figures 7.3 and 7.13 to 7.16.

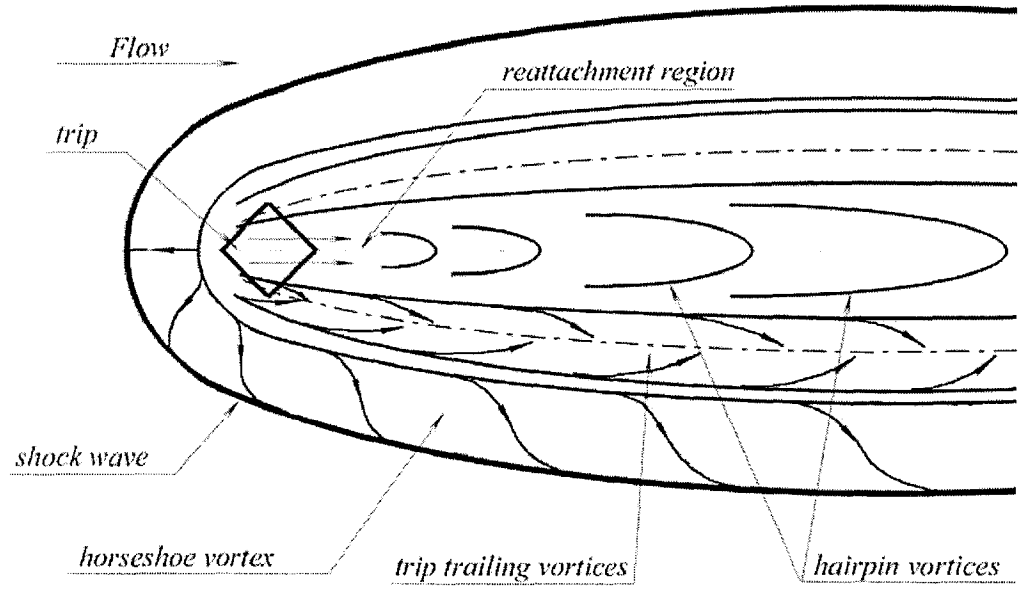

Figure 7.17: Schematic of an exaggerated scale of a suggested flow structure surrounding the roughness trip.

7.2 Effects of roughness trip size

The analysis presented thus far proposed a possible wedge internal structure consisting of 'trains' of amalgamated turbulent spots generated at a very high rate downstream of the roughness trip. The clarity of the spots within these 'trains' was not sufficient to substantiate their existence. Consequently, the investigation of the trip size, in terms of both height k and width w_k, aimed at decelerating the process of spot formation within the turbulent wedge so that individual, or at least 'near-coalescing' spots, could be made visible. As the variation in flow properties is more significant in the wall-normal direction (y), the effect of roughness height k was first examined. This constituted experimental set 2, whereas set 3 was dedicated to the investigation of the trip width w_k.

7.2.1 Effect of trip height

In this set of experiments (experimental set 2), the same trip width as in set 1 (i.e., $w_k \approx 2$ mm) was used, with a gradual reduction in the trip height k as summarised in table 7.3. This reduction corresponds to a decrease in the local Reynolds number based on the trip height Re_{kk} and the local Mach number M_k, two possible important factors in the transition process. The heat transfer measurements were made using the circumferential module positioned at $x = 279$ mm axial distance from the model leading edge.

x (mm)	w_k (mm)	k (mm)	k/δ	k/δ_1	k/δ_2	Re_{kk}	M_k	Re_{kk}/M_k
279	1.950	0.24	0.64	2.96	4.42	1620	2.24	724
279	1.950	0.12	0.32	1.48	2.21	695	1.77	393
279	1.950	0.08	0.21	0.99	1.47	390	1.41	277
279	1.950	0.04	0.11	0.49	0.74	143	0.91	157

Table 7.3: Experimental set 2; gradual reduction in the roughness height k. $w_k = 1.95$ mm, $k = 0.64\delta$, 0.32δ, 0.21δ, and 0.11δ. The trip axial position is $x_k = 37.75$ mm.

Time-averaged heat transfer

Figure 7.18 presents the time-averaged distributions of heat transfer obtained using the four different roughness trip heights, $k = 0.64\delta$, 0.32δ, 0.21δ, and 0.11δ. Two to three repeated tunnel runs were performed for each trip height in order to verify the repeatability of the result. The figure shows a significant decrease in the spanwise extent of the turbulent wedge as the trip height is reduced from 0.64δ to 0.32δ. There is also a small reduction in the intermittent region spanwise extent, within the experimental uncertainties however. Further decrease in trip height to 0.21δ resulted in virtually no variation in heat transfer distribution, hence, a similar wedge circumferential width as for 0.32δ. On the other hand, the height of 0.11δ maintained a laminar flow downstream of the roughness trip.

The decrease in wedge spanwise extent between $k/\delta = 0.64$ and $k/\delta = 0.32$ suggests two possible scenarios. Firstly, and most likely, the reduction in trip height yields a significant decrease in the local flow properties, Re_{kk}, M_k, and Re_{kk}/M_k (table 7.3), which in turn delays transition, hence the formation of the turbulent wedge. Using the same wedge lateral spreading half-angle, α_c, determined in section 7.1.3, the delay in transition is estimated as being approximately 80 mm axial distance downstream of the roughness element, which corresponds to a position, x_{tr}, of approximately 120 mm. Secondly, and less likely, the trip remains effective, which means that the wedge forms immediately behind it, but grows at a different lateral spreading half-angle α_c'. The latter is estimated at approximately 2.8 degrees, a value which is significantly lower than those suggested by the present study (section 7.1.3), by Fischer,[28] or by Doorly et al.[23] Consequently, it is quite clear that the first scenario is more likely to have taken place, in which case the *minimum effective* trip condition lies somewhere between $0.32 < k/\delta < 0.64$. The increase in heat transfer level within the core of the turbulent wedge from that obtained with $k/\delta = 0.64$ to that with $k/\delta = 0.32$, although within the margin of measurement errors, indicates end of transition characteristics as reported by Bertin[11] and Zanchetta.[112]

The figure shows no significant change in wedge characteristics between $k = 0.32\delta$ and $k = 0.21\delta$. No obvious explanation can be given as the variation between the intermittent zone extents in the two cases is within the margin of experimental uncertainties. However, the figure clearly reveals a fully laminar or near-laminar flow downstream of the roughness trip of height $k = 0.11\delta$. This trip height did not present a large enough disturbance environment to trigger the transition of the boundary layer. The *incipient* trip height, which is the maximum value allowing to maintain a laminar flow downstream of the trip, lies between $0.11 < k/\delta < 0.21$.

Wedge internal structure

Figure 7.19 shows the 'z-t' plots of heat transfer contours obtained at $x = 279$ mm, using the four trip heights, $k = 0.64\delta$, 0.32δ, 0.21δ, and 0.11δ. Once again, the wedge boundaries (with $k = 0.32\delta$ and 0.21δ) exhibit undulations which, however, do not demonstrate a well organised periodic motion. The bottom plot presents a fully laminar flow with the presence of occasional regions of turbulence.

The spanwise heat transfer distributions at the times t_a, t_b, and t_c, shown in figure 7.19, are plotted in figure 7.20. The undulation of the wedge edges is once more demonstrated by the spanwise shift with time of the turbulent wedge, which retains its width however. The spanwise extent of the wedge diminishes with decreasing trip height as already demonstrated in figure 7.18. Moreover, the figure shows a consistent drop in the peak heating level around the boundaries of the wedge with the gradual reduction in k (and M_k and Re_{kk} as a result). This reduction produces a more 'plateau-like' distribution within the wedge, in contrast to the 'concave-like' distribution observed with $k = 0.64\delta$. The presence yet of the 'spot-like trains' with $k = 0.32\delta$ and 0.21δ suggests that the corresponding local flow conditions, namely Re_{kk} and M_k, are still sufficiently large to generate the trailing vortical structures from the trip side-tips.

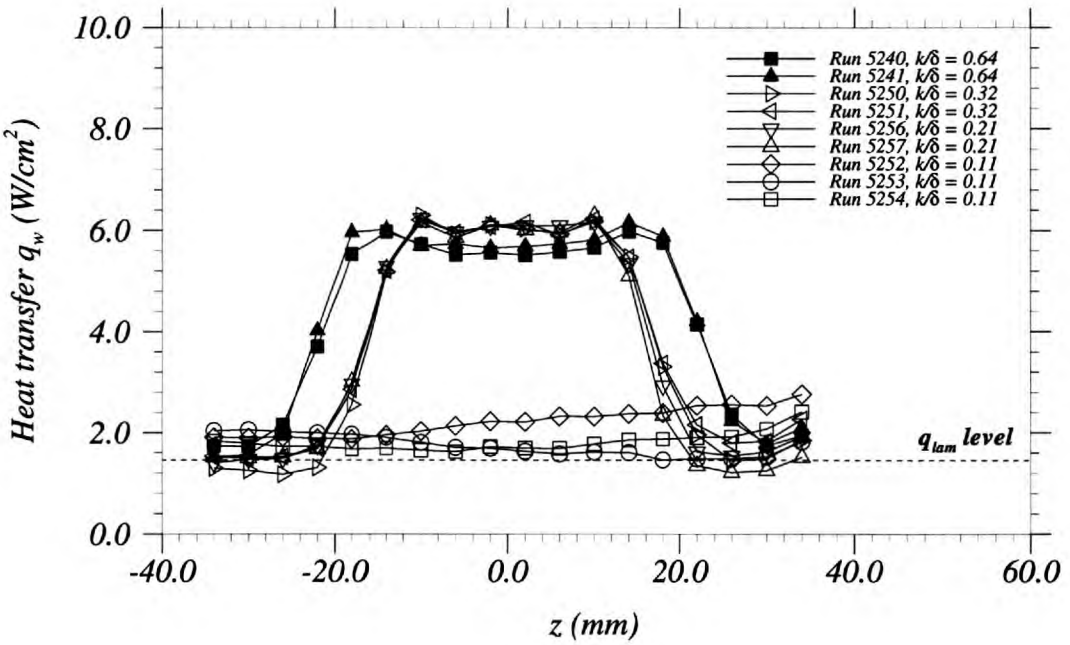

Figure 7.18: Spanwise time-averaged heat transfer distributions together with the laminar CFD value; $x = 279$ mm. Experimental set 2 with $w_k = 1.95$ mm and four various values of trip height; $k/\delta = 0.64$, 0.32, 0.21, and 0.11.

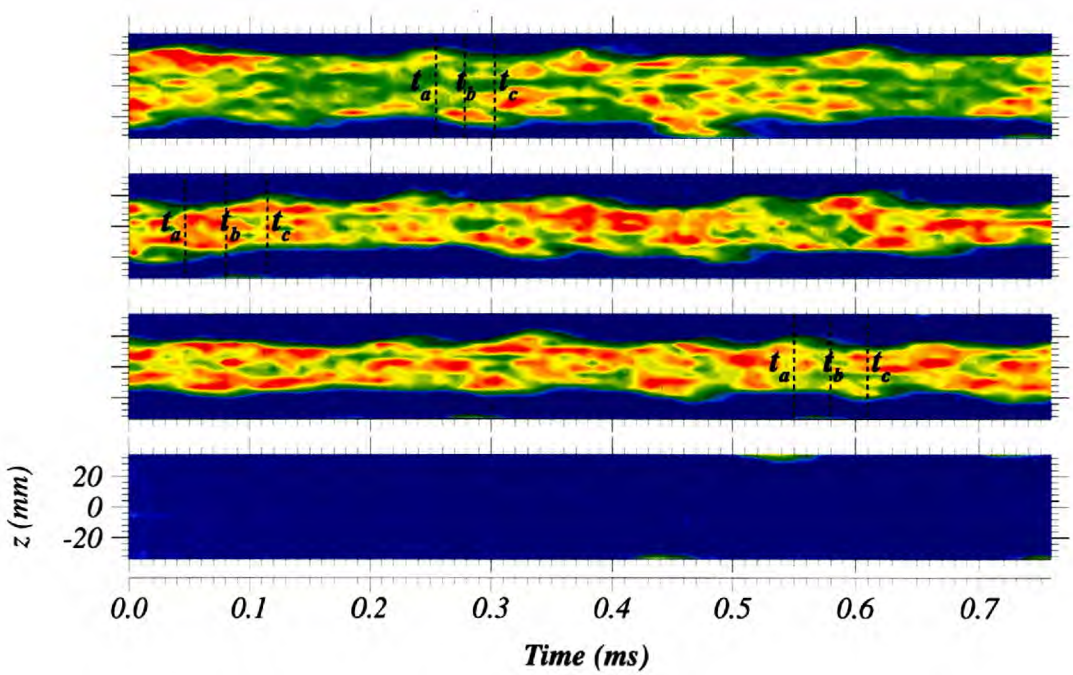

Figure 7.19: 'z-t' plot of heat transfer contours at $x = 279$ mm. $w_k = 1.95$ mm, $k/\delta = 0.64$, 0.32, 0.21, and 0.11 (top to bottom).

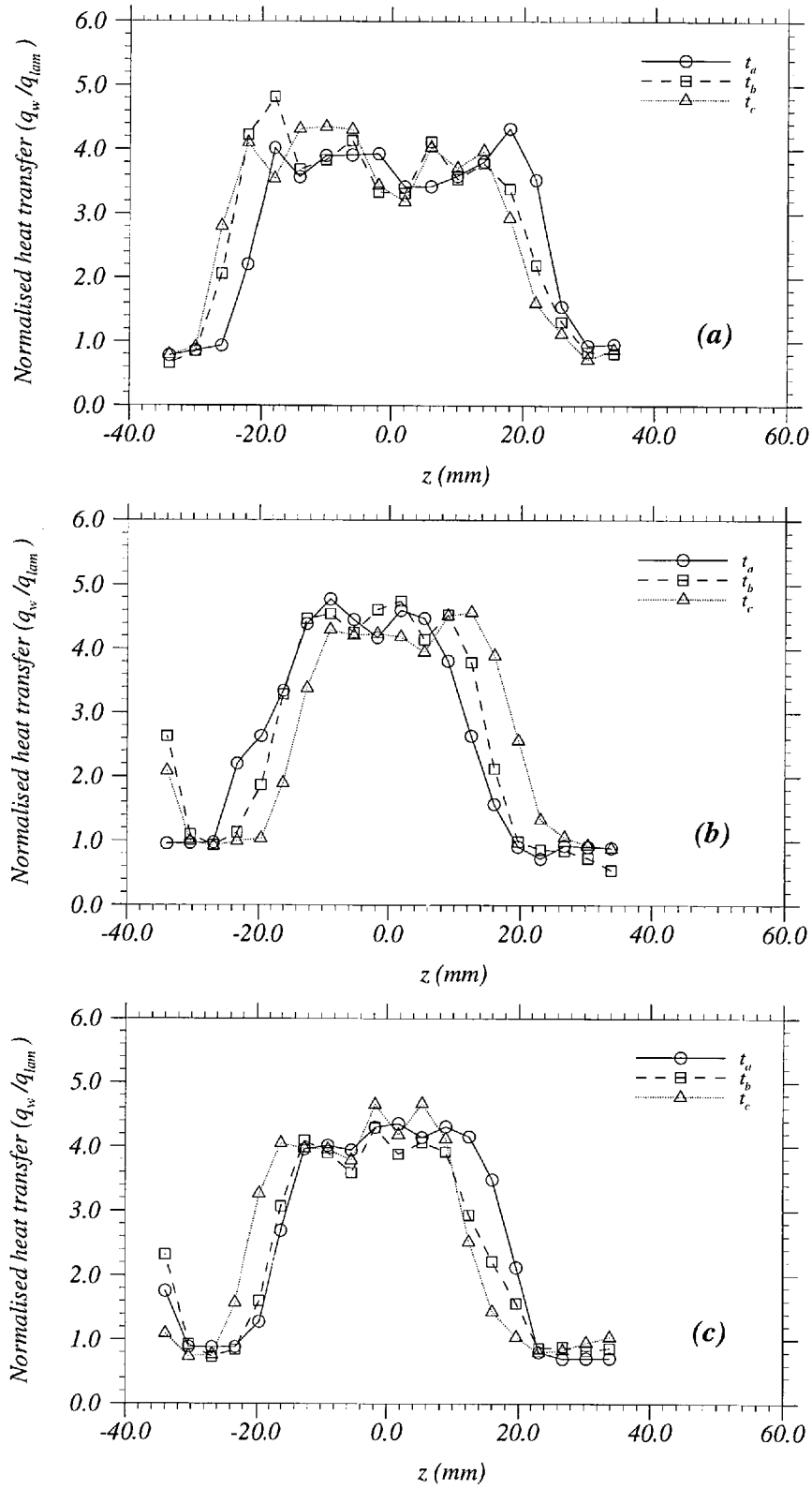

Figure 7.20: Heat transfer spanwise distributions at three various times t_a, t_b, and t_c at $x = 279$ mm (as shown in figure 7.19). (*a*) $k/\delta = 0.64$, (*b*) $k/\delta = 0.32$, and (*c*) $k/\delta = 0.21$.

7.2.2 Effect of trip width

In this set of experiments (experimental set 3), the roughness trip width w_k was reduced to a nominal value of 1.075 mm. Two different trip heights were used, namely $k = 0.32\delta$ and 0.16δ. The incentive behind the choice of the former value was to investigate the effect of trip width by comparison with the data acquired with $k = 0.32\delta$ and $w_k = 1.95$ mm. The latter value, however, was chosen in order to capture an intermediate stage, of individual or near-amalgamating spots, between the fully developed wedge obtained with $k = 0.21\delta$ and the fully laminar flow retained with $k = 0.11\delta$. The heat transfer measurements were made at $x = 279$ mm distance from the model leading edge. Two to three tunnel runs were carried out for each trip height to confirm the repeatability of the result. The experimental setup for this set is summarised in table 7.4, which also includes the CFD conditions based on the trip height.

x (mm)	w_k (mm)	k (mm)	k/δ	k/δ_1	k/δ_2	Re_{kk}	M_k	Re_{kk}/M_k
279	1.075	0.12	0.32	1.48	2.21	695	1.77	393
279	1.075	0.06	0.16	0.74	1.11	257	1.18	218

Table 7.4: Experimental set 3; trip width $w_k = 1.075$ with two different values of trip height $k = 0.32\delta$ and 0.16δ.

Time-averaged heat transfer

The time-averaged heat transfer spanwise distributions obtained with the two various trip heights, $k = 0.32\delta$ and 0.16δ, and width, $w_k = 1.075$ mm, are shown in figure 7.21. There is formation of a fully developed turbulent wedge behind the trip of $k = 0.32\delta$. The two different runs (i.e., 5261 and 5262) display excellent agreement in heat transfer level within the core of the wedge.

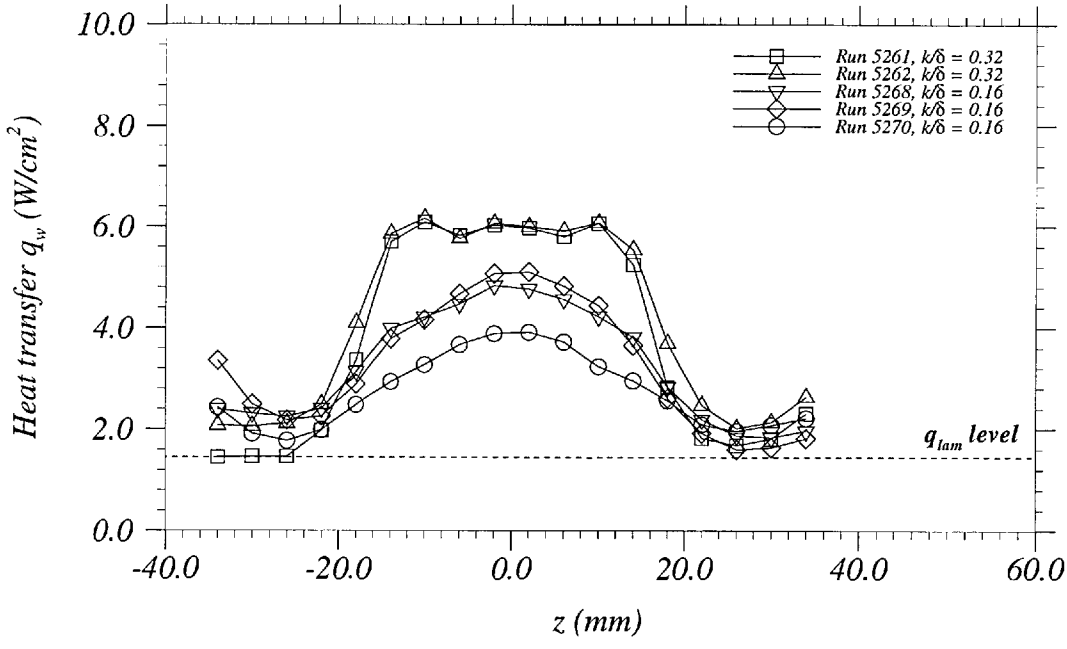

Figure 7.21: Spanwise time-averaged heat transfer distributions together with the laminar CFD value; $x = 279$ mm. Experimental set 2 with $w_k = 1.075$ mm and two various values of trip height; $k/\delta = 0.32$ and $k/\delta = 0.16$ ($Re_{kk} = 695$ and $Re_{kk} = 257$ respectively).

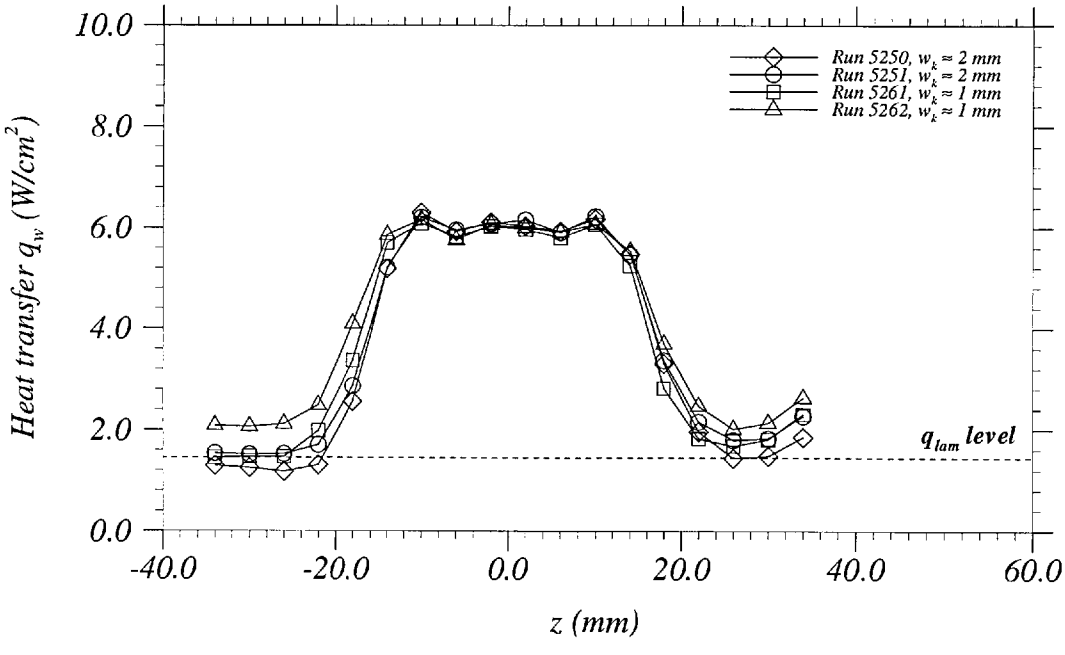

Figure 7.22: Spanwise time-averaged heat transfer distribution at $x = 279$ mm using two roughness trip widths $w_k \approx 2$ mm and $w_k \approx 1$ mm. The trip height in both cases is $k/\delta = 0.32$ ($Re_{kk} = 695$).

The trip height of $k = 0.16\delta$ generated a flow which exhibits an average heat transfer level between the fully laminar and fully turbulent values, suggesting the presence of an intermittent flow, in other words, an *intermittently-turbulent* wedge (figure 7.21). The production of this intermittently-turbulent wedge is merely the result of the reduction in trip height to $k = 0.16\delta$ rather than the reduction in trip width to $w_k = 1.075$ mm, as demonstrated by the time-averaged heat transfer plots achieved with $k = 0.32\delta$ together with $w_k = 1.95$ mm and 1.075 mm (figure 7.22). This figure shows good agreement in terms of both heat transfer level and wedge spanwise extent obtained with the two different trip widths.

Wedge internal structure

The heat transfer contours in the 'z-t' plane, obtained from two different tunnel runs, are presented in figure 7.23. The reduction in trip width, w_k, (to 1.075 mm compared with 1.95 mm) has no major effect on the shape of the wedge boundaries by comparison to figure 7.19. The figure occasionally reveals the 'spot-like' nature of these undulations as can be seen at approximately $0.22ms < t < 0.30ms$ and $0.50ms < t < 0.58ms$ (figure 7.23-a). The undulation of the wedge edges is once more demonstrated in figure 7.24, which illustrates the heat transfer spanwise distributions (obtained from two tunnel runs) at three different times, t_a, t_b, and t_c, as indicated in figure 7.23. The figure shows a spanwise shift with time of the wedge, similarly to the result obtained with $w_k = 1.95$ mm, however, at a relatively smaller amount (about 4 mm shift compared to approximately 6 mm in figure 7.20). Figure 7.24 also shows similar heat transfer distributions within the core of the wedge compared to figure 7.20. In the same manner as in the $w_k = 1.95$ mm case, the formation of the wedge is believed to be the result of the two vortical structures trailing from the trip side-tips, which undergo transition downstream of the trip.

The *intermittently-turbulent* wedge is better visualised in figures 7.25 and 7.26, which present the heat transfer contours obtained from three repeated tunnel runs in the 'z-t' reference frame. Figure 7.26 represents a zoom into the 0.75 ms time

windows indicated in figure 7.25. The latter shows the intermittent nature of the wedge which clearly spreads over the whole 6 ms steady time interval of the tunnel run. The figure also demonstrates the run-to-run variation in intermittency level. The trip height of 0.16δ, which corresponds to $Re_{kk} = 257$, allowed the capture of an intermediate stage of a 'train' of individual and amalgamating turbulent spots that constitute the intermittently-turbulent wedge (figure 7.26). In the present study, this intermediate stage is referred to as the *turbulent spot-to-wedge transition* and covers the range of $0.11 < k/\delta < 0.21$. The spots grow with distance until they entirely coalesce to form a fully developed wedge. The variation of the trip height controls the rate of spot production, hence the streamwise extent of the intermittently-turbulent wedge, which ranges between the transition and fully developed wedge onset locations. The latter is defined with the emergence of a distinct fully turbulent region (i.e., a turbulent core), with a finite spanwise extent within the intermittent flow, in the time-averaged heat transfer spanwise distribution. Consequently, the process of turbulent wedge formation can be captured at different stages, depending upon both the flow conditions at the trip height and the streamwise measurement location.

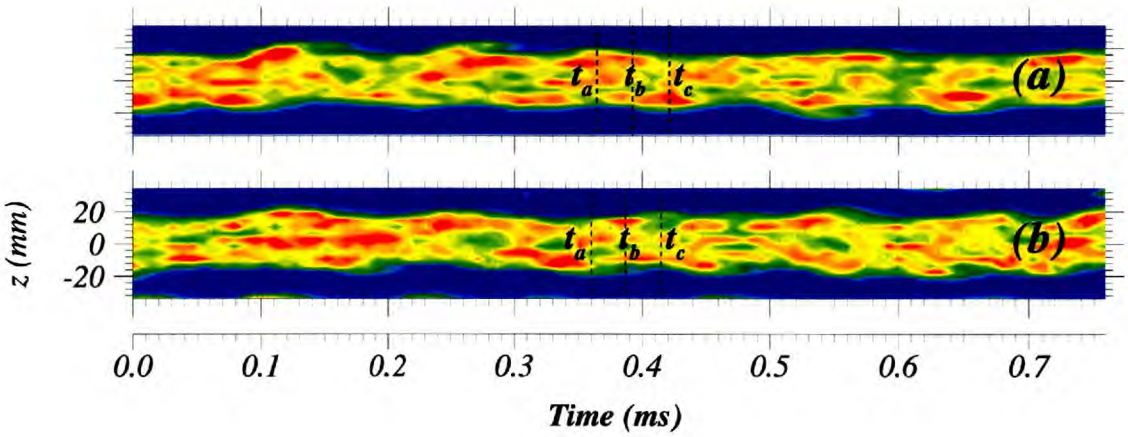

Figure 7.23: 'z-t' plot of heat transfer contours at $x = 279$ mm from two repeated runs. $k = 0.32\delta$ ($Re_{kk} = 695$), $w_k = 1.075$ mm.

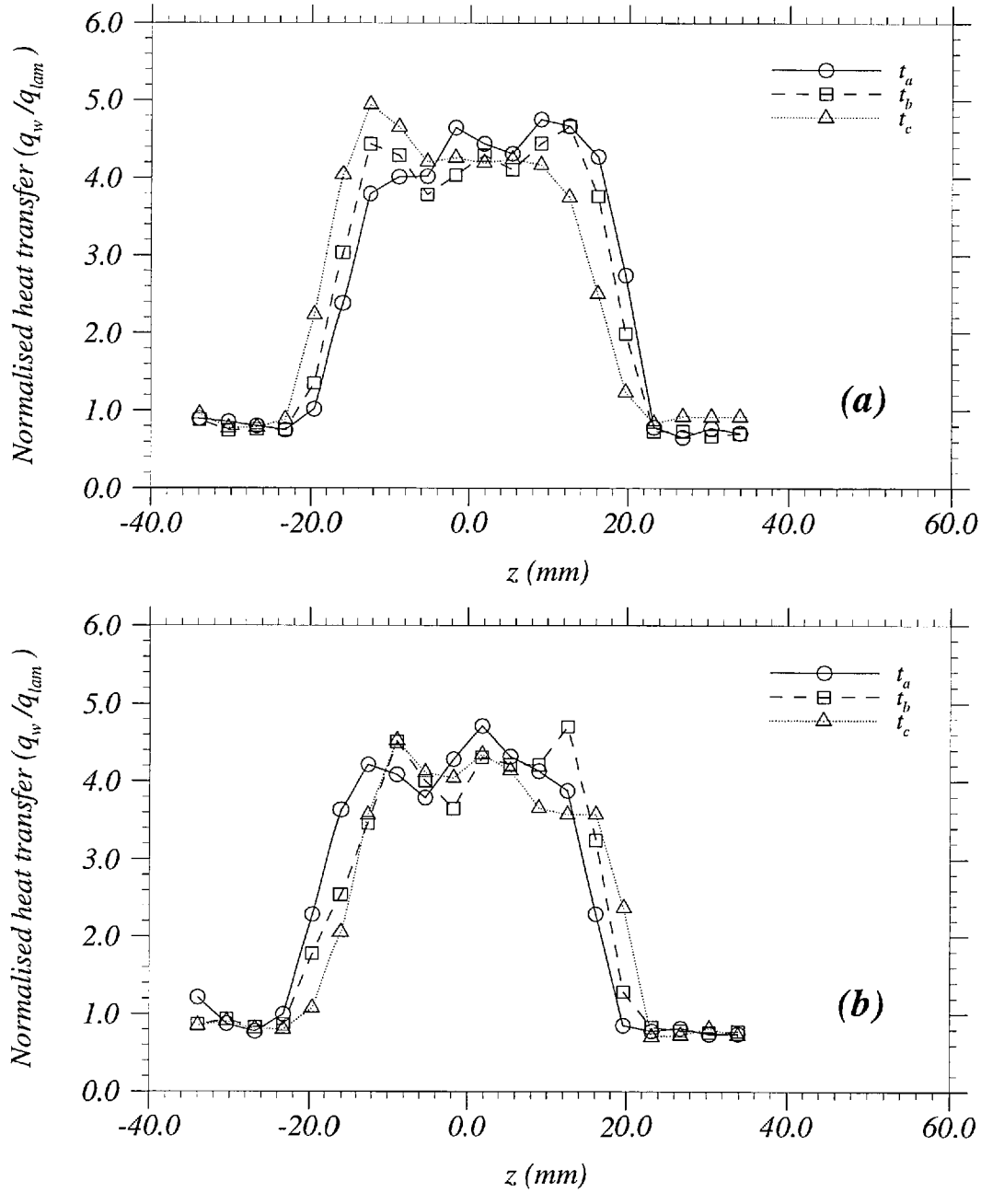

Figure 7.24: Heat transfer spanwise distributions at three various times t_a, t_b, and t_c at $x = 279$ mm (as shown in figure 7.23). $k/\delta = 0.32$ ($Re_{kk} = 695$), $w_k = 1.075$ mm.

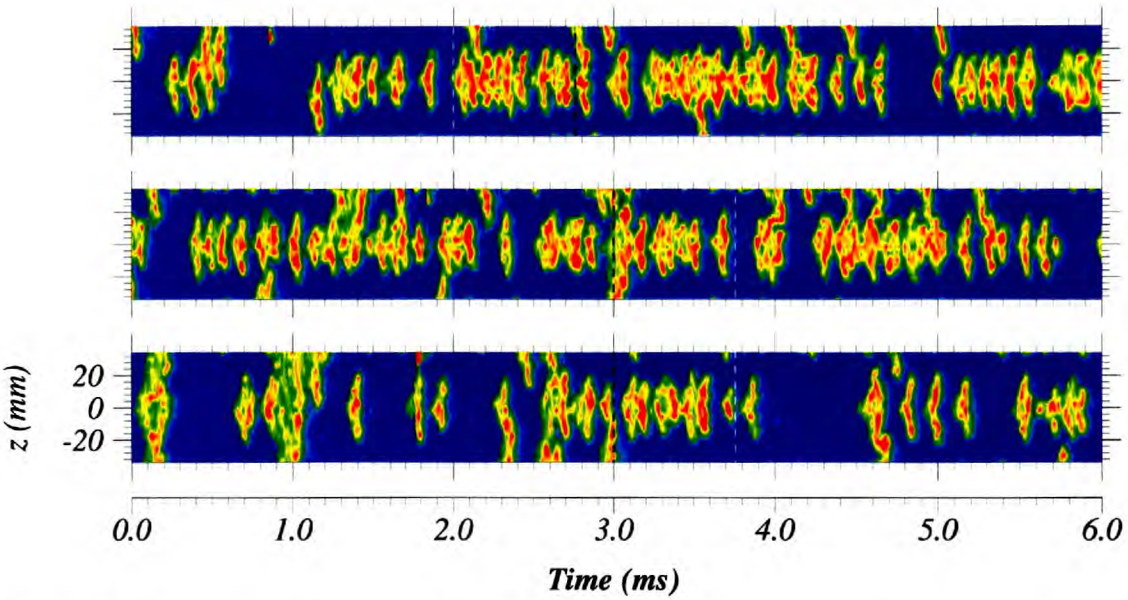

Figure 7.25: 'z-t' plot of heat transfer contours at $x = 279$ mm from three repeated runs. $w_k = 1.075$ mm, $k/\delta = 0.16$ ($Re_{kk} = 257$).

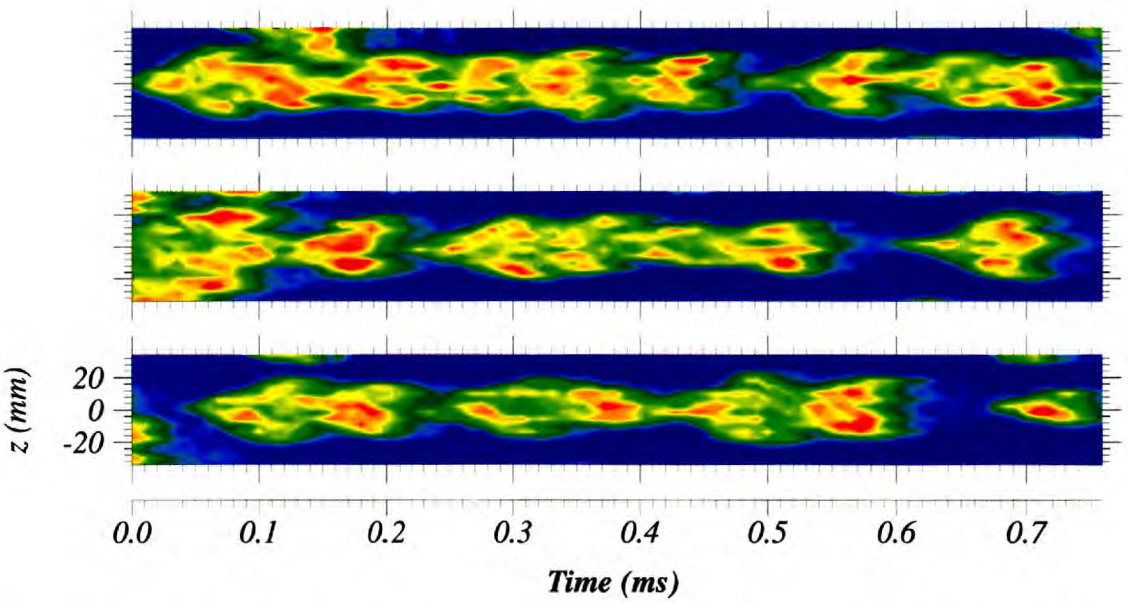

Figure 7.26: 'z-t' plot of heat transfer contours at $x = 279$ mm from three repeated runs (zoom into the window indicated in figure 7.25.

7.3 Transition onset characteristics

The three sets of experiments, that have been presented in this chapter, allowed three different types of flows to be acquired. In experimental set 1, a fully developed turbulent wedge was obtained immediately downstream of the roughness trip, with the height, k, of 0.64δ, demonstrating the effectiveness of the trip (transition front at the trip location). In set 2, the gradual variation in the trip height, k, allowed the localisation of the *effective-trip* condition (i.e., the minimum roughness height above which transition occurs immediately downstream of the trip) within the interval $0.32 < k/\delta < 0.64$. Experimental set 3 enabled the definition of the *incipient-trip* condition (i.e., the maximum roughness height below which laminar flow is maintained), which was found to be in the interval $0.11 < k/\delta < 0.16$. An intermediate stage of individual and amalgamating turbulent spots (referred to as *turbulent spot-to-wedge transition*) exists between the fully laminar (with $k = 0.11\delta$) and fully turbulent (with $k = 0.21\delta$) flows. The transition onset parameters are summarised in table 7.5, including the *incipient*, *spot-to-wedge transition*, and *effective* conditions, together with the corresponding laminar CFD predictions.

	k/δ	k/δ_1	k/δ_2	Re_{kk}	M_k	Re_{kk}/M_k	Re_{s_k}
low *incipient*	0.11	0.49	0.74	143	0.91	157	188073
high *incipient*	0.16	0.74	1.11	257	1.18	218	225780
high *spot-to-wedge*	0.21	0.99	1.47	390	1.41	277	257065
low *effective*	0.32	1.48	2.21	695	1.77	393	305516
high *effective*	0.64	2.96	4.42	1620	2.24	724	355860

Table 7.5: Transition onset characteristics. k is the roughness trip height. δ, δ_1, and δ_2 are the local laminar boundary layer thickness, displacement thickness, and momentum thickness respectively. $Re_{kk} = \rho_k U_k k/\mu_k$ is the Reynolds number based on the roughness height k. M_k is the local Mach number at the trip height. $Re_{s_k} = \rho_k U_k s_k/\mu_k$ is the Reynolds number based on the wetted distance the stagnation point and the trip location $s_k = 52.7$ mm. 'low' and 'high' correspond to the lower and upper limits of the intervals.

Chapter 8

Concluding Remarks

8.1 Conclusions

This present study has consisted in the experimental investigation of turbulent spot and wedge characteristics in a hypersonic blunt-body transitional boundary layer. The aim was to acquire detailed information that would contribute to the better understanding of the flow within the intermittent-transition region, which is of particularly substantial lengths in hypersonic flows. Many crucial flow interactions would therefore occur with such a transitional flow rather than a fully laminar or fully turbulent flow.

The experiments have been performed on an axisymmetric configuration which consists of a blunt-nosed forebody and a number of interchangeable cylindrical afterbody segments, of which two are fitted each with a single instrumentation module that is either axial or circumferential. This has provided good flexibility and precision in the streamwise positioning of the instrumentation module with respect to the model apex. The measurements have exclusively focused upon surface time-dependent heat transfer because it not only represents a critical design parameter for hypersonic vehicles, but it also is a good transition detector via spot and wedge thermal footprints at the body surface.

The experiments have been conducted in a Mach 8.9 flow with a unit Reynolds number of 47.4 million per metre. The laminar computational simulation has demon-

strated a significant reduction in boundary layer edge conditions—a Mach number, M_e, of approximately 3.7 and a unit Reynolds number, Re_e, of approximately 2.7 million per metre—compared with the freestream, a direct consequence of the entropy layer effect associated with the blunt nose.

The time-dependent heat transfer measurements have allowed the acquisition of detailed spot and wedge planform geometries and growth rates and also the determination of the spot convective properties. The spot displays an arrowhead shape with triangular leading edges, a maximum width region and a wake (or calmed) region. The turbulent heat transfer level within a spot and wedge generally agrees with that of a fully turbulent flow. The spot data have revealed the presence of large spot length scales of the order of 150 times the local laminar boundary layer displacement thickness. With these length scales, the spots are regarded as sufficiently grown and thus they are fairly independent of the mechanisms by which they are formed.

The time-dependent and time-averaged data have indicated a significant run-to-run variation in the average intermittency level over the 6 ms running-time window, a fact which is principally due to the low frequency of intermittent events. As a result, long sample windows are judged necessary for statistically average intermittency functions along the intermittent-transition zone to be adequately obtained. The effect of distributed surface roughness, applied on the model nose, has been to significantly increase the spot formation rate and average intermittency level along the measurement length.

Conditional sampling of the streamwise data has been used to identify spot leading and trailing edges and to determine their average convection speeds. The spot leading edge average speed has been estimated at approximately 0.76 to 0.80 of the boundary layer edge velocity, U_e, whereas the spot trailing edge average speed has been estimated at approximately 0.41 of U_e. The resulting spot average speed has been evaluated at approximately 0.58 to 0.69 of U_e. The streamwise measurements have provided no distinction in the spanwise location of the spots with respect to the heat transfer module.

The average spot has a spanwise growth rate of approximately 6.2 degrees, in reasonable agreement with previous studies at similar speeds. This rate, however, is lower than that obtained at much lower speeds, which is generally around 10 degrees, justifying the more elongated intermittent-transition region in hypersonic flows compared with that in low speed flows. The average spot grows in a near self-similar manner at large enough distances downstream of its inception. The resolution of the spot data has been sufficient to indicate a streak or cellular sub-structure which has been associated with a hairpin-vortex structure, more widely observed in incompressible flows.

The discrete roughness-induced experiments have allowed turbulent wedge geometry and spanwise growth characteristics to be obtained. The time-dependent and time-averaged data have revealed two distinct regions within the wedge; that is a wedge core where the flow is turbulent, and an intermittent zone where fractions of laminar and turbulent flow coexist. The presence of this intermittent zone has suggested the irregularity in shape of the turbulent wedge physical edge, which has been related to a 'coalesced-spot' internal structure, whereby spots are generated at a high rate causing the amalgamation to occur at short distances downstream of the roughness element. The wedge core and outer spanwise growth rates have been estimated at approximately 4.3 and 6.9 degrees respectively, enfolding the individual spot value of 6.2 degrees.

On the whole, this present study has produced a unique set of heat transfer data that provide a comprehensive evaluation of spot and wedge geometrical and growth characteristics, and individual spot propagation speeds, very scarce at hypersonic speeds. This study has also demonstrated, for the first time, the existence of an internal structure within a spot and wedge in hypersonic flows. The findings reveal considerable similarities with previous studies at much lower speeds.

8.2 Further work

Several ideas have arisen from the analysis of the data which are worth pursuing. The scatter in the data of the spot front and back propagation speeds has risen the question of whether it only represents measurement uncertainties or also actual variation from one spot to another. This can be verified through the application of a longer streamwise measurement distance. A model which comprises two streamwise heat transfer modules axially aligned has already been constructed. It provides streamwise measurement lengths of up to 210 mm, with half the current gauge-to-gauge resolution.

The scatter in the spot front speed data has suggested a possible variation across the width of a spot, since no distinction has been made with the present measurements regarding the spanwise location of a spot with respect to the gauges (capture of spot centrelines which are on, and off, the heat transfer module centreline). In effect, low speed work (e.g., Wygnanski et al.[106]) showed a spanwise variation in the spot leading edge velocity from the spot apex to its wing-tip. Because simultaneous axial-circumferential measurements are particularly difficult, it is recommended that well controlled discrete roughness-induced transition, using precisely machined and small enough roughness trips, should be used to generate individual spots at fixed spanwise locations. Then using a single axial heat transfer module, positioned at different spanwise locations with respect to the roughness element, the spot leading edge velocity distribution between the spot apex and spot wing-tip can be obtained.

Other avenues include refined spanwise measurements of spots in order to better resolve the spot substructure, with the objective of finding any correlations with the low speed case.

Bibliography

[1] Air Force Studies Board. *Hypersonic Technology for Military Application.* USA, National Research Council, 1989.

[2] ANDERSON, J D. *Hypersonic and High temperature Gas Dynamics.* USA: McGraw-Hill, 1989.

[3] ANDERSON, J D. *Modern Compressible Flow with Historical Perspective, 2^{nd} edition.* USA: McGraw-Hill, 1990.

[4] ANDERSON, J D. *Fundamentals of Aerodynamics, 2^{nd} edition.* USA: McGraw-Hill, 1991.

[5] Antonia, R A., Chambers, A J., Sokolov, M., and Van Atta, C W. **Simultaneous Temperature and Velocity Measurements in the Plane of Symmetry of a Transitional Turbulent Spot**. *Journal of Fluid Mechanics*, 108, 1981, 317–343.

[6] Arnal, D. and Casalis, G. **Laminar-Turbulent Transition Prediction in Three-Dimensional flows.** *Progress in Aerospace Sciences,* 36, 2000, 173–191.

[7] Barrow, J., Barnes, F H., and Ross, M A S. **The Structure of a Turbulent Spot in Blasius Flow**. *Journal of Fluid Mechanics*, 149, 1984, 319–337.

[8] Ben-Artzi, M. and Falcovitz, J. **A Second Order Godunov-Type Scheme for Compressible Fluid Dynamics**. *Journal of Computational Physics*, 55, 1984, 1–32.

[9] Berry, S A., Horvath, T J., Hollis, B R., Thompson, R A., and Hamilton II, H H. *X-33 Hypersonic Boundary Layer Transition.* USA, AIAA Paper 99-3560, July 1999.

[10] Berry, S A. and Hamilton, H H. *Discrete Roughness Effects on Shuttle Orbiter at Mach 6.* USA, AIAA Paper 2002-2744, June 2002.

[11] BERTIN, J J. *Hypersonic Aerothermodynamics.* USA: AIAA Education series, 1994.

[12] BURDEN, R L. AND FAIRES, J D. *Numerical Analysis, 6^{th} edition.* USA: Brooks/Cole Publishing Company, 1997.

[13] Bushnell, D M. **Research status/Requirements and NASA Applications for Wall Layer Transition.** *Transition, Turbulence and Combustion, Vol 1: Transition, 3–12.* Netherlands, Kluwer Academic Publishers, 1994.

[14] Ching, C Y. and LaGraff, J E. **Measurement of Turbulent Spot Convection Rates in a Transitional Boundary Layer.** *Experimental Thermal and Fluid Science*, 11, 1995, 52–60.

[15] Chong, T P. and Zhong, S. **On the Three-Dimensional Structure of Turbulent Spots.** *Proceedings of ASME International Conference TURBO EXPO 2003*, GT-2003-38435, 2003, Atlanta, USA.

[16] Clark, J P., Jones, T V. and LaGraff, J E. **On the Propagation of Naturally Occurring Turbulent Spots.** *Journal of Engineering Mathematics*, 28, 1994, 1–19.

[17] Clark, J P., Jones, T V. and LaGraff, J E. **Turbulent-Spot Propagation in a Decelerating Compressible Flow.** *AMSE Journal of Fluids Engineering*, 118, 1996, 612–614.

[18] Coleman, C P. *Boundary layer Transition in the Leading Edge Region of a Swept Cylinder in High Speed Flow.* USA, NASA Technical Memorandum TM-1998-112224, March 1998.

[19] Cook, W J. and Felderman, E J. **Reduction of Data From Thin Film Heat Transfer Gauges: A Concise Numerical Technique.** *AIAA Journal*, 4(3), 1966, 561–562.

[20] Creighton, S. *Hypersonic Flow Over Non-Rectangular Cavities.* UK, Imperial College of Science, Technology and medicine, Ph.D Thesis, September 2003.

[21] Das, A. and Mathew, J. **Direct Numerical Simulation of Turbulent Spots.** *Computers & Fluids*, 30, 2001, 533–541.

[22] De Lange, H C., Hogendoorn, C J., and van Steenhoven, A A. **The Similarity of Turbulent Spots in Subsonic Boundary Layers.** *Int. Comm. Heat Mass Transfer*, 25(3), 1998, 331–337.

[23] Doorly, D J. and Smith, F T. **Initial-Value Problems for Spot Disturbances in Incompressible or Compressible Boundary Layers.** *Journal of Engineering Mathematics*, 26(1), 1992, 87–106.

[24] Edwards, A J. *Boundary Layer Studies at Hypersonic Speeds.* UK, Imperial College of Science, Technology and Medicine, Ph.D Thesis, 1981.

[25] Emmons, H W. **The Laminar-Turbulent Transition in a Boundary Layer—Part 1.** *Journal of Aeronautical Sciences*, 18(7), 1951, 490–498.

[26] Falco, R. *The Production of Turbulence Near a Wall.* USA, AIAA Paper 80-1356, 1980.

[27] Fedorov, A V. and Malmuth, N D. **Application of Similarity in Hypersonic Transition Prediction.** *AIAA Journal,* 33(8), 1995, 1523–1525.

[28] Fischer, M C. **Spreading of a Turbulent Disturbance.** *AIAA Journal,* 10(7), 1972, 957–959.

[29] Fischer, M C. **Turbulent Bursts and Rings on a Cone in Helium at $M_e = 7.6$.** *AIAA Journal,* 10(10), 1972, 1387–1389.

[30] Garry, K P. *Viscous Flow: Introduction to Boundary layers, Aerospace Dynamics Lecture Notes.* UK, Cranfield University, November 1999.

[31] HAGEN, K D. *Heat Transfer with Applications.* NJ: Prentice Hall, 1999.

[32] Hillier, R., Kirk, D C., Sell, M., and Soltani, S. **Studies of Hypersonic Viscous Flows.** *Theoretical and Experimental Methods in Hypersonic Flows,* AGARD-CP-514, 1993, (32-1)–(32-11).

[33] Hillier R., Kirk, D., and Soltani, S. **Navier-Stokes Computations of Hypersonic Flows.** *International Journal of Numerical Methods for Heat & Fluid Flow,* 5, 1995, 195–211.

[34] Hillier, R., Boyce, R R., Creighton, S A., Fiala, A., Jackson, A P., Mallinson, S G., Sheikh, A H., Soltani, S., and Williams, S. **Development of Some Hypersonic Benchmark Flows Using CFD and Experiment.** *Shock Waves,* 13, 2003, 375–384.

[35] Hillier, R. Private communication. 2003.

[36] Holden, M S. **Experimental Studies of Laminar, Transitional and Turbulent Hypersonic Flows over Elliptic Cones at Angles of Attack.** *Proceedings of the 22nd International Symposium on Shock Waves,* 18-23 July 1999, London, UK, Paper 0840.

[37] HOLMAN, J P. *Heat Transfer, 7^{th} edition.* UK: McGraw-Hill, 1990.

[38] Horvath, T J., Berry, S A., Merski, N R., and Fitzgerald, S M. *X-38 Experimental Aerothermodynamics.* USA, AIAA Paper 2000-2685, June 2000.

[39] Huntley, M. and Smits, A. **Transition Studies on an Elliptic Cone in Mach 8 Flow using Filtered Rayleigh Scattering.** *Eur. J. Mech. B - Fluids* 19, 2000, 695–706.

[40] Iliff, K W. and Shafer, M F. *Space Shuttle Hypersonic Aerodynamic and Aerothermodynamic Flight Research and the Comparison to Ground Test Results.* USA, NASA Technical Memorandum 4499, June 1993.

[41] Itsweire, E C. and Van Atta C W. **An Experimental Investigation of Coherent substructures associated with Turbulent Spots in a Laminar Boundary Layer**. *Journal of Fluid Mechanics*, 148, 1984, 319–348.

[42] James, C S. *Observations of Turbulent-Burst Geometry and Growth in Supersonic Flow.* USA, NACA Technical Note TN 4235, 1958.

[43] Johnson, M W. and Dris, M. **The Origin of Turbulent Spots**. *Journal of Turbomachinery*, 122, 2000, 88–92.

[44] Johnson, M W. **On the Flow Structure within a Turbulent Spot**. *International Journal of Heat and Fluid Flow*, 22, 2001, 409–416.

[45] Kachanov, Y S. **Physical Mechanisms of Laminar-Boundary-Layer Transition.** *Annual Review of Fluid Mechanics,* 26, 1994, 411–482.

[46] Katz, Y., Seifert, A., and Wygnanski, I. **On the Evolution of the Turbulent Spot in a Laminar Boundary Layer with a Favourable Pressure Gradient**. *Journal of Fluid Mechanics*, 221, 1990, 1–22.

[47] Kimmel, R L., Demetriades, A., and Donaldson, J C. **Space-Time Correlation Measurements in a Hypersonic Transitional boundary Layer.** *AIAA Journal,* 34(12), 1996, 2484–2489.

[48] Kimmel, R L. and Poggie, J. *Effect of Total Temperature on Boundary Layer Stability at Mach 6.* USA, AIAA Paper 99-0816, January 1999.

[49] Kimmel, R L., Poggie, J., and Schmisseur, J D. *Effect of pressure Gradients on Axisymmetric Hypersonic Boundary Layer Stability.* USA, AIAA Paper 2000-0538, January 2000.

[50] KUETHE, A M. and CHOW, Chuen-Yen. *Foundations of Aerodynamics: Bases of Aerodynamic Design, 5^{th} edition.* USA: John Wiley & Sons, 1998.

[51] Lachowicz, J T., Chokani, N., and Wilkinson, S P. *Hypersonic Boundary Layer Stability over a Flared Cone in a Quiet Tunnel.* USA, AIAA Paper 96-0782, January 1996.

[52] Macaraeg, M G. **Group Summary: Receptivity.** *Transition, Turbulence and Combustion, Vol 1: Transition, 258–266.* Netherlands, Kluwer Academic Publishers, 1994.

[53] Mack, L M. **The Stability of the Compressible Laminar Boundary Layer According to a Direct Numerical Simulation.** AGARDOGRAPH 97, Part 1, 1964, 329–389.

[54] Malik, M R. *Prediction and Control of Transition in Hypersonic Boundary Layers.* USA, AIAA Paper 87-1414, June 1987.

[55] Malik, M., Zang, T., and Bushnell, D. *Boundary Layer Transition in Hypersonic Flows.* USA, AIAA Paper 90-5232, October 1990.

[56] Mallinson, S G., Hillier, R., Jackson, A P., Kirk, D C., Soltani, S., and Zanchetta, M. **Gun Tunnel Flow Calibration: Defining Input Conditions for Hypersonic Flow Computations.** *Shock Waves*, 10, 2000, 313–322.

[57] Masad, J A. **Relationship Between Transition and Modes of Instability in High Speed Boundary Layers.** *AIAA Journal*, 33(4), 1994, 774–776.

[58] Masad, J A. and Abid, R. **On Transition in Supersonic and Hypersonic Boundary Layers.** *International Journal for Engineering Sciences,* 33(13), 1995, 1893–1919.

[59] Mautner, T S. and Van Atta, C W. **An Experimental Study of the Wall-Pressure Field Associated with a Turbulent Spot in a Laminar Boundary Layer.** *Journal of Fluid Mechanics*, 118, 1982, 59–77.

[60] McDaniel, R D., Nance, R P., and Hassan, H A. *Transition Onset Prediction for High Speed Flow.* USA, AIAA Paper 99-3792, July 1999.

[61] McKeel, S A. *Numerical Simulation of the Transition Region in Hypersonic Flow.* USA, Virginia Polytechnic Institute and State University, Ph.D Thesis, February 1996.

[62] Mee, D J. and Goyne, C P. **Turbulent Spots in Boundary Layers in a Free-Piston Shock Tunnel Flow.** *Shock Waves*, 6, 1996, 337–343.

[63] Mee, D J. *Transition Measurements on a 5 Degree Cone in the T4 Shock Tunnel.* Australia, University of Queensland Research Report Number 2001-2, May 2001.

[64] Mee, D J. **Boundary-Layer Transition Measurements in Hypervelocity Flows in a Shock Tunnel.** *AIAA Journal*, 40(8), 2002, 1542–1548.

[65] Menter, F R. **Eddy Viscosity Transport Equations and Their Relation to the $k-\epsilon$ Model.** *Journal of Fluids Engineering*, 119, 1997, 876–884.

[66] MERZKIRCH, W. *Flow Visualization, 2^{nd} edition.* USA: Academic Press Inc., 1987.

[67] MURTHY, T K S. *Computational Methods in Hypersonic Aerodynamics.* UK: Computational Mechanics Publications, Kluwer Academic Publishers, 1991.

[68] Nagamatsu, H T., Sheer, R E., and Graber, B C. **Hypersonic Laminar Boundary Layer Transition on 8-Foot-Long, 10 Degree Cone, $M_1 = 9.1 - 16$.** *AIAA Journal*, 7(7), 1967, 1245–1252.

[69] Narasimha, R., Subramanian, C., and Badri Narayanan, M A. **Turbulent Spot Growth in Favorable Pressure Gradients.** *AIAA Journal*, 22(6), 1984, 837–839.

[70] Perry, A E., Lim, T T., and Teh, E W. **A Visual Study of Turbulent Spots.** *Journal of Fluid Mechanics*, 104, 1981, 387–405.

[71] Reda, D C. *Boundary Layer Transition Experiments on Sharp, Slender Cones in Supersonic Free Flight.* USA, NSWC/NOL TR 77–59, 1977.

[72] Reda, D C. **Boundary-Layer Transition Experiments on Sharp, Slender Cones in Supersonic Free Flight.** *AIAA Journal*, 17(8), 1979, 803–810.

[73] Reda, D C. **Review and Synthesis of Roughness-Dominated Transition Correlations for Re-entry Applications.** *AIAA Journal*, 39(2), 2002, 161–167.

[74] Reed, H L., Kimmel, R., Schneider, S., and Arnal, D. *Drag Prediction and Transition in Hypersonic Flow.* USA, AIAA Paper 97-1818, July 1997.

[75] Reshotko, E. **Boundary-Layer Stability and Transition.** *Annual Review of Fluid Mechanics*, 8, 1976, 311–349.

[76] Reshotko, E. *Boundary Layer Instability, Transition and Control.* USA, AIAA Paper 94-0001, January 1994.

[77] Reshotko, E. *Progress, Accomplishments and Issues in Transition Research.* USA, AIAA Paper 97-1815, July 1997.

[78] Sabatino, D. and Smith, C R. **Simultaneous Velocity-Surface Heat Transfer Behavior of Turbulent Spots.** *Experiments in Fluids*, 33, 2002, 13–21.

[79] Sankaran, R., Antonia, R A., Bisset, D K., and Sokolov, M. **Flow Patterns and Organization within a Turbulent Spot.** *Physics of Fluids*, 3(6), 1991, 1560–1571.

[80] SCHETZ, J A. *Boundary Layer Analysis.* USA: Prentice-Hall, 1993.

[81] SCHLICHTING, H. and GERSTEN, K. *Boundary Layer Theory, 8^{th} edition.* Germany: Springer-Verlag, 2000.

[82] Schneider, S P. **Effects of High-Speed Tunnel Noise on Laminar-Turbulent Transition.** *Journal of Spacecraft and Rockets.* 38(3), 2001, 323–333.

[83] Schneider, S P. **Hypersonic Laminar-Turbulent Transition on Circular Cones and Scramjet Forebodies.** *Progress in Aerospace Sciences.* 40, 2004, 1–50.

[84] Schook, R., de Lange, H C., and van Steenhoven, A A. **Heat Transfer Measurements in Transitional Boundary Layers.** *International Journal of Heat and Mass Transfer,* 44, 2001, 1019–1030.

[85] Schröder, A. and Kompenhans, J. **Investigation of a Turbulent Spot Using Multi-Plane Stereo PIV.** *Proceedings of the 11th International Symposium on Applications of Laser Techniques to Fluid Mechanics*, Turbulent spot, Session29, July 2002, Portugal.

[86] Schubauer, G B. and Klebanoff, P S. *Contributions on the Mechanics of Boundary-Layer Transition.* USA, NACA Technical Note TN 3489, 1955.

[87] Schultz, D L. and Jones, T V. *Heat-Transfer Measurements in Short-Duration Hypersonic Facilities.* France, AGARD-AG-165, 1973.

[88] Seifert, A. and Wygnanski, I J. **On Turbulent Spots in a Laminar Boundary Layer Subjected to a Self-similar Adverse Pressure Gradient.** *Journal of Fluid Mechanics*, 296, 1995, 185–209.

[89] Sell, M. *Hypersonic Blunt Cone Aerodynamics.* UK, Imperial College of Science, Technology and Medicine, Ph.D Thesis, August 1992.

[90] SETTLES, G S. *Schlieren and Shadowgraph Techniques.* Germany: Springer-Verlag, 2001.

[91] Shell Education series, A Note on the Schlieren Method.

[92] Singer, B A. *Modeling the Transition Region.* USA, NASA Contractor Report CR 4492, February 1993.

[93] Singer, B A. and Joslin, R D. **Metamorphosis of a Hairpin Vortex into a Young Turbulent Spot.** *Physics of Fluids*, 6(11), 1994, 3724–3736.

[94] Singer, B A. **Characteristics of a Young Turbulent Spot.** *Physics of Fluids*, 8(2), 1996, 509–521.

[95] SMITS, A J. AND LIM, T T. *Flow Visualization Techniques and Examples.* Singapore: Imperial College Press, 2000.

[96] Stetson, K F., Thompson, E R., Donaldson, J C., and Siler, L G. *On Hypersonic Transition Testing and Prediction.* USA, AIAA Paper 88-2007.

[97] Stilla, J. **Engineering Transition Prediction for a Hypersonic Axisymmetric Boundary Layer.** *Journal of Aircraft,* 31(6), 1994, 1358–1364.

[98] Thompson, R A. **Review of X-33 Hypersonic Aerodynamic and Aerothermodynamic Development.** *22nd Congress of the International Council of the Aeronautical Sciences*, 27 August-1 September 2000, Harrogate, UK, Paper 323.

[99] Vasudevan, K P., Dey, J., and Prabhu, A. **Spot Propagation Characteristics in Laterally Strained Boundary layers.** *Experiments in Fluids*, 30, 2001, 488–491.

[100] Vidal, R J. *Transient Surface Temperature Measurements.* USA, CAL rep. 114. Cornell Aeronautical Laboratory, Inc. March 1962.

[101] Wendt, V., Simen, M., and Hanifi, A. **An Experimental and Theoretical Investigation of Instabilities in Hypersonic Flat Plate Boundary Layer Flow.** *Physics of Fluids,* 7(4), 1995, 877–887.

[102] WHITE, F M. *Viscous Fluid Flow, 2^{nd} edition.* USA: McGraw-Hill, 1991.

[103] Wijesinghe, S. *Investigation of the Heat Transfer Rate on the Surface of a Blunt Nosed Cylinder in Hypersonic Mach 9 Flow.* UK, Imperial College of Science, Technology and medicine, MEng Project Report, May 1996.

[104] WILCOX, D C. *Turbulence Modeling for CFD, 2^{nd} edition.* USA: DCW Industries, 1998.

[105] Williams, S. *Three-Dimensional Separation of a Hypersonic Boundary Layer.* UK, Imperial College of Science, Technology and medicine, Ph.D Thesis, August 2004.

[106] Wygnanski, I., Sokolov, M., and Friedman, D. **On a Turbulent 'Spot' in a Laminar Boundary Layer.** *Journal of Fluid Mechanics*, 78, 1976, 785–819.

[107] Wygnanski, I., Zilberman, M., and Haritonidis, J H. **On the Spreading of a Turbulent Spot in the Absence of a Pressure Gradient.** *Journal of Fluid Mechanics*, 123, 1982, 69–90.

[108] YANG, WEN-JEI. *Handbook of Flow Visualization.* USA: Hemisphere Publishing Corporation, 1989.

[109] YANG, WEN-JEI. *Computer-Assisted Flow Visualization: Second Generation Technology.* USA: CRC Press Inc., 1994.

[110] YOUNG, A D. *Boundary Layers.* UK: Oxford Blackwell Scientific, 1989.

[111] Zanchetta, M A. and Hillier, R. **Boundary Layer Transition on Slender Blunt Cones at Hypersonic Speeds.** *Proceedings of the 20th International Symposium on Shock Waves*, 699–704, July 1995, Singapore.

[112] Zanchetta, M. *Kinetic Heating and Transition Studies at Hypersonic Speeds.* UK, Imperial College of Science, Technology and medicine, Ph.D Thesis, April 1996.

[113] Zhong, S., Kittichaikan, C., Hodson, H P., and Ireland, P T. **A Study of Unsteady Wake-Induced Boundary-Layer Transition with Thermochromic Liquid Crystals.** *Proceedings of 4th IMechE International Conference on Optical and Data Processing in Heat and Fluid Flows*, IMechE Conference Transactions, London, 1998.

[114] Zhong, S., Kittichaikan, C., Hodson, H P., and Ireland, P T. **Visualisation of Turbulent Spots and Unsteady Wake-Induced Boundary-Layer Transition with Thermochromic Liquid Crystals.** *Optics and Laser Technology*, 31, 1999, 33–39.

[115] Zhong, S., Kittichaikan, C., Hodson, H P., and Ireland, P T. **Visualisation of Turbulent Spots under the Influence of Adverse Pressure Gradients.** *Experiments in Fluids*, 28, 2000, 385–393.

[116] Zhong, S., Chong, T P., and Hodson, H P. **A Comparison of Spreading Angles of Turbulent Wedges in Velocity and Thermal Boundary Layers.** *Journal of Fluids Engineering*, 125, 2003, 267–274.